VT-Forschungsbericht 2014-05

Numerical Modeling of Ignition Processes in Single- and Multiphase Flows

Jan Michael Boyde

Deutsches Zentrum für Luft- und Raumfahrt
Institut für Verbrennungstechnik
Stuttgart

DLR Deutsches Zentrum für Luft- und Raumfahrt

Herausgeber

Deutsches Zentrum
für Luft- und Raumfahrt

**Institut für
Verbrennungstechnik**

Pfaffenwaldring 38-40
70569 Stuttgart

Telefon
Telefax

(0 7 11) 68 62 - 3 08
(0 7 11) 68 62 - 5 78

D93, Stuttgart

Numerical Modeling of Ignition Processes in Single- and Multiphase Flows

A thesis accepted by the Faculty of Aerospace Engineering and Geodesy of the Universität Stuttgart in partial fulfillment of the requirements for the degree of Doctor of Engineering Sciences (Dr.-Ing.)

by

Dipl.-Ing. Jan Michael Boyde

born in Rostock

Main referee:	Prof. Dr.-Ing. Manfred Aigner
Co-referee:	Prof. Dr.-Ing. Nikolaos Zarzalis
Date of defence:	23rd May 2014

Institute of Combustion Technology for Aerospace Engineering
University of Stuttgart

2014

Vorwort

Die vorliegende Doktorarbeit entstand während meiner Tätigkeit am Institut für Verbrennungstechnik des Deutschen Zentrums für Luft- und Raumfahrt (e.V.) in der Abteilung Numerik von 2008 - 2012 in Stuttgart.

Jede Arbeit entsteht im Angesicht des eigenen Schweißes und vereint doch eine Vielzahl von Unterstützern hinter sich, welche hier gebührend Berücksichtigung finden sollen. An erster Stelle danke ich meinem Doktorvater Prof. Dr.-Ing. M. Aigner, dafür, dass er mir die Gelegenheit und den Freiraum für diese Dissertation gegeben hat. Ich habe es immer sehr zu schätzen gewusst, dass ich die Ergebnisse meiner Arbeit auf Projekttreffen und einer Vielzahl von Konferenzen vorstellen durfte und mir so eine große Basis an Projektberichten und Veröffentlichungen zulegen konnte, welche das Zusammenschreiben ungemein erleichtert haben. Herzlich danken möchte ich auch Prof. Dr.-Ing. N. Zarzalis für die Übernahme der Zweitkorrektur und Prof. Dr.-Ing. U. Rist für die Bereitschaft den Prüfungsvorsitz zu übernehmen. Als nächstes möchte ich meinen beiden Betreuern Dr.-Ing. habil. B. Noll und Dr.-Ing. P. Le Clercq meinen persönlichen Dank aussprechen. Durch ihr großes Vertrauen in mein Schaffen und ihre kontinuierliche Unterstützung konnte ich über so manchen schwierigen Punkt gelangen und erst durch die motivierenden Anregungen und Korrekturen beider großartiger Betreuer konnte der rote Faden in dieser Arbeit entstehen. Dr.-Ing. M. Di Domenico danke ich dafür, dass er mir den THETA Code näher gebracht hat und mir bei meinen ersten wissenschaftlichen Arbeiten unterstützend zur Seite stand. Den Kollegen G. Gebel und Dr.-Ing. T. Mosbach möchte ich Danke sagen für die ausgezeichneten experimentellen Erkenntnisse, welche kontinuierlich in die Entwicklung meines Modells geflossen sind. Ebenfalls danken möchte ich allen Kolleginnen und Kollegen am DLR, dass Sie mir die Zeit am DLR so angenehm bereitet haben, besonders J. Fleck und A. Fiolitakis mit welchen ich eine sehr schöne gemeinsame Zeit im Büro hatte. Ohne sie hätte ich mit ziemlicher Sicherheit die eine oder andere Frist versäumt. Auch die Mensaclique und die THETA Gruppe haben jeden Tag bereichert.

Abschließend möchte ich mich bei meiner Frau, meiner Familie und meinen Freunden herzlich bedanken, welche für mich stets eine großartige Unterstützung waren und mir viel Arbeit abgenommen haben, wenn ich mich gerade intensiv in das Schreiben der vorliegenden Dissertation vertieft hatte.

Contents

Abbreviations

CFD	Computational Fluid Dynamics
CFL	Courant Friedrich Lewis Number
CV	Control Volume
DNS	Direct Numerical Simulation
ED	Energy Deposition
LuFo	Luftfahrt Forschungsinitiative
LES	Large Eddy Simulation
ODE	Ordinary Differential Equation
RANS	Reynolds Averaged Navier Stokes
SLM	Standard Liter per Minute
SPRAYSIM	Spray Simulation Solver
TFC	Turbulent Flame Speed Closure
THETA	Thermal Extension for Tau
TIMECOP-AE	Towards Innovative Methods for Combustion Prediction in Aero Engines
URANS	Unsteady Reynolds Averaged Navier Stokes
VOF	Volume of Fluid

Nomenclature

Latin Variables	
A	Cross Section / Cross sectional area (Droplet) [m^2]
c_p	Specific heat capacity at constant pressure [J/kgK]
$C_\nu, C_{\epsilon 1}, C_{\epsilon 2}, \sigma_k, \sigma_\epsilon$	Turbulence Model Constants
C	Drag Coefficient [-]
C_{ig}	Extended TFC Model Constant [-]
D	Diameter [m]
D_Y	Species Diffusion Coefficient [m^2/s]
D_{ij}	Shear Stress Tensor [1/s]
e	Specific Energy [J/kg]
E	Energy [J]
f_e	Vaporization Fraction [-]
f_r	Thermal Reduction Factor [-]
$\vec{F}$	Force [N]
$\vec{g}$	Gravity Constant [m/s^2]
g_{cr}	Critical Stretch Rate [1/s]
G	Quenching Term [-]
h	Specific Vaporization Enthalpy [J/kg]
h_e	Specific Enthalpy [J/kg]
H_e	Vaporization Enthalpy [J]
i	Index Variable [-]
k	Turbulent Kinetic Energy [m^2/s^2]
$l_\int$	Integral Length Scale [m]
$L_{\nu K}$	Karman Length Scale [m]
$\dot{m}$	Mass Flow Rate [kg/s]
M	Molecular Weight [kg/mol]
$\overline{M}$	Mean Molecular Weight [kg/mol]
n	Number of Reactions [$-$]
$\vec{n}$	Normal Vector [m]
N	Number of Grid Cells [-]
N_p	Number of Particles [-]
p	Pressure [Pa]
$\mathscr{P}$	Production Term [m^2/s^3]

Latin Variables ... Continued	
r	Radius [m]
R	Specific Gas Constant [J/kgK]
$\mathscr{R}$	Ideal Gas Constant [J/molK]
S	Source Term [Unit/s]
S_{CV}	Surface Control Volume [m^2]
S_ϵ	Turbulent Dissipation Source Term [$\mathrm{J/s}^2$]
S_m	Mass Source Term [kg/s]
S_L	Laminar Flame Speed [m/s]
S_T	Turbulent Flame Speed [m/s]
S_E	Energy Source Term [J/s]
S_k	Kinetic Energy Source Term [J/s]
t	Time [s]
t_i	Auto Ignition Time [s]
$t_\int$	Integral Time Scale [s]
T	Temperature [K]
T_{ij}	Viscous and Pressure Tensor [1/s]
u	Velocity [m/s]
u_b	Velocity of the boundary [$\mathrm{N/m}^2$]
V	Volume [m^3]
$\vec{x}$	Location [m]
y	Function Variable [Unit]
Y	Mass Fraction [−]
$Y_{\mathrm{CO_2max}}$	Maximum Local CO_2 Mass Fraction [−]

Greek Variables	
β	Current Chemical Reaction Progress [-]
γ	Proportionality Factor [-]
Γ	Turbulent Stretch [1/s]
ζ_1, ζ_2, ζ_3, C_μ, κ, σ_k, σ_Φ	SAS Model Constants
η	Kolmogorov Length Scale
λ	Heat Conductivity Coefficient [W/m K]
μ	Dynamic Viscosity [kg/m s]
ν	Kinematic Viscosity [m^2/s]
ρ	Density [kg/m^3]
σ	Surface Tension [N/m]
Σ_{CV}	Control Volume [m^3]
τ	Relaxation time
ϵ	Turbulent Dissipation [m^2/s^3]
ϕ	Generic Variable [-]
Φ	Mixture Fraction [-]
ω	Turbulent Time Scale [1/s]
$\dot{\omega}$	Reaction Rate [Unit/s]

Non-Dimensional Numbers	
$\mathscr{L}$	Markstein Length for Curvature
Da	Damköhler Number
Ka	Karlovitz Number
Pr	Prandtl Number
Re_t	Turbulent Reynolds Number
Sc	Schmidt Number
We	Weber Number

Indices	
0	Ambiant Conditions
ad	Adiabatic Conditions
c	Current Cell
D	Drag
g	Gas
gr	Gravity
i,j,k	Sum Indices
l	Liquid
p	Particle
rel	Relative (e.g. between phases)
s	Spark
sgs	Subgrid Scale
S	Surface
t	Turbulent
u	Unburnt
V	Volume
x,y	Number of Atoms
η	Kolmogorov Length Scale

Systematic	
$\bar{}$	Reynolds Average
$\tilde{}$	Favre Average
$'$	Reynolds Fluctuation
$''$	Favre Fluctuation
∂	Partial Differential Operator
d	Differential Operator
$\vec{}$	Vector
$\bar{\bar{}}$	Matrix

Throughout this work the Einstein sum convention is employed, meaning that indices i,j,k represent the x,y and z direction if not stated otherwisely.

Abstract

Ignition of an aircraft engine is a fundamental requirement for safety and airworthiness. Despite the fact that until now, ignition of an aircraft engine is accomplished by means of well established ignition techniques, the trend in developing combustors which are run under lean conditions will also entail substantial changes concerning the ignitability of these configurations. The motivation to implement a lean-burn combustion system into aircraft engines originates from more stringent pollutant emission regulations which limit the amount of tolerable pollutants concentrations. Enabled by, in general, lower temperatures in the combustion chamber, the production of pollutant is significantly suppressed. In contrast, the widely employed rich-burn quench lean-burn combustion approach cannot be sufficiently improved to meet the emission targets which has enhanced the interest in developing lean-combustion operated aircraft engines. However, the new combustion concept so far lacks a similar broad basis of experience and knowledge as is present for the conventional concepts which requires new efforts to achieve a similar comprehensive level of confidence.

This work's objective is to develop numerical tools which can be employed to elaborate new combustion concepts from the perspective of ignitability for the above given reasons. Numerical studies regarding the simulation of ignition processes are up to now relatively scarce in the literature. Due to the comparably high level of reliability of ignition techniques in conventional combustion systems, the main focus of research was dedicated to topics such as pollutant emission reduction and predictions concerning the temperature strain of walls and turbine blades. In addition, the modeling of ignition events comprises several challenging aspects which have to be considered. The process of ignition is intrinsically transient which demands a time-resolved computation to capture the underlying instationary phenomena. A large spectrum of time and length scales is present in a full ignition sequence which spans the evolution of a first flame kernel, induced by the release of ignition energy into the domain, until the stabilization and stable burning of the flame at subsequent stages. Characteristics of the flame, primarily, the flame propagation and the temperature of the flame, which drives the heat expansion, need to be well approximated for an accurate flame growth prediction.

To meet these requirements, the turbulent flame speed closure model (TFC model) which is available from literature is identified as a suitable means. In the scope of this work, the standard version of the TFC model is subjected to several modifications to achieve, firstly, an extension of its range of applicability to also comply with multiphase conditions and, secondly, to allow the model to incorporate auto-ignition as a fundamental part of the ignition sequence. The TFC model in its standard formulation offers advantages for the simulation of transient flames. Through the derivation of the source term from the laminar flame speed, the model is apt to accurately describe flame propagation processes. Due to the low number

of required transport equation, the computational effort of simulations which employ the TFC model remains comparably low. In this work, in order to capture multiphase phenomena, such as fuel droplet evaporation which induces mass sources in the domain, the model formulation based on the mixture fraction is substituted by including transport equations for major species. Additionally, an auto-ignition term is added to the source term of the flame progress variable. Both modifications guarantee to resolve the development of a flame kernel, generated by forced ignition, until the flame stabilization within a multiphase environment.

This work is structured as follows. At first, the governing equations of the flow solver and the combustion model are presented. Subsequently, the modifications applied to the original combustion model are validated by a series of fundamental test cases. The numerical integrity of the model is verified through a Bunsen burner simulation which is characterized by a typical flame cone angle that is suited for comparison. Secondly, the grid independency is established by a repetition of the Bunsen burner simulation for two grid refinements which show that the results remain nearly unaffected and converge to a grid-independent solution. The physical and chemical accuracy of the model for the flame propagation and temperature are further evaluated in the remaining test cases which also include multiphase conditions. Then, the model predictions are assessed for complex test cases for which comprehensive experimental data sets are available. Initially, only gaseous test cases are investigated. The flame propagation and ignition probability in the domain are distinguishing features which are compared between experiment and simulation. It is demonstrated that, both, the development of the flame is resolved correctly and that regions characterized by a high ignition probability are identified in the simulation. To establish the reliability of the model for complex stationary configurations exhibiting levels of turbulence which can cause flame quenching, a highly turbulent enclosed jet flame is simulated. The results of the simulation point out that the model is capable of capturing detrimental and beneficial effects of turbulence by the incorporation of a proposed quenching term. For the last investigated test cases which involve burner-like multiphase conditions, it is confirmed that the model also succeeds in capturing the measured trends of the ignition statistics concerning the ignition location and the impact of the boundary conditions. In addition, the transient flame behavior is predicted satisfyingly.

In conclusion, a combustion model is developed and presented in this work which is made applicable to a wider range of conditions through the accomplished modifications. The model predictions show that for all examined test cases, a satisfying agreement with available experimental data is achieved. This underlines the usefulness of numerical tools for the investigation of ignition processes in the context of aircraft engines.

Kurzfassung

Das Zünden eines Flugtriebwerks, selbst unter widrigsten Bedingungen, stellt eine Grundvoraussetzung für den Betrieb eines Triebwerkes dar. Auch wenn bisher die Zündbarkeit eines Triebwerks durch aktuelle Techniken zufriedenstellend beherrscht wird, so hat doch die Absicht in Zukunft Triebwerke basierend auf einem Magerverbrennungskonzept einzusetzen, zu einer Hinterfragung bisheriger Zündmethoden geführt. Die Entwicklung von magerverbrennenden Fluggasturbinen hat durch strengere Vorschriften aus der Politik in Bezug auf maximale Grenzwerte des Schadstoffausstosses stark an Interesse gewonnen. Durch die insgesamt geringeren auftretenden Temperaturen können auch in Zukunft die auferlegten Grenzwerte eingehalten werden, was mit einer Verbesserung des bisher eingesetzten Rich-Quench-Lean Konzepts in dieser Größenordnung nicht mehr möglich gewesen wäre. Die Zündbarkeit des Triebwerkes basierend auf einem mageren Verbrennungskonzept ist noch relativ wenig untersucht und es bedarf deshalb Anstrengungen, um Wissen und Erfahrungen auf diesem Gebiet zu sammeln.

Aus dieser Motivation heraus, die Entwicklung neuer Verbrennungskonzepte auch unter dem Aspekt der Zündbarkeit voran zu treiben, ist diese Arbeit entstanden. Es wird ein Verbrennungsmodell vorgestellt, welches geeignet ist, den gesamten Prozess der Zündung numerisch abzubilden. Dieses Feld im Bereich der Strömungssimulation ist noch relativ wenig untersucht, da bisherige Schwerpunkte, wie die Schadstoffvorhersage und Temperaturabschätzungen, eine höhere Priorität eingenommen haben. Die Simulation von Zündprozessen beinhaltet zahlreiche Phänomene, welche in der Entwicklung des Verbrennungsmodells berücksichtigt werden müssen. Zum einen ist der Vorgang der Zündung an sich ein transienter Prozess, welcher somit zeitaufgelöst behandelt werden muss. Daneben spielt das breite Spektrum an auftretenden zeitlichen und räumlichen Skalen während der Entwicklung des Flammenkerns zu einer voll ausgebildeten Flamme eine wichtige Rolle. Auch die Ausbreitungsgeschwindigkeit und die Temperatur, welche in die Wärmeausdehnung eingeht, als elementare Eigenschaften der Flamme müssen zufriedenstellend wiedergegeben werden.

Um diesen Anforderungen Rechnung zu tragen, wird in dieser Arbeit das bereits in der Literatur beschriebene “Turbulent Flame Speed Closure” (TFC) Modell aufgegriffen. Das TFC Modell bietet bereits Eigenschaften, die für die Simulation von transienten Flammenverläufen vorteilhaft sind. Die Herleitung des Quellterms basierend auf der Flammengeschwindigkeit garantiert eine intuitive Beschreibung der Flammenausdehnung. Weiterhin ist das Modell durch seine geringe Anzahl an benötigten Transportgleichungen für Parameterstudien, welche zur Erstellung von Zündkarten notwendig sind, gut geeignet. Um dieses Modells für Zündprozesse, insbesondere für mehrphasige Strömungen zu adaptieren, wurden der Standardformulierung zentrale Erweiterungen hinzugefügt. Die wesentlichen Punkte sind, ein Aus-

tausch des bisher benötigten Mischungsbruch mit den am Verbrennungsprozess grundlegend beteiligten Spezies und der Zusatz eines Zündverzugsterms zur Standardform des Quellterms der Flammenfortschrittsvariable. Beide Anpassung ermöglichen es dem Modell, sowohl in reinen Gasgemischen als auch unter Mehrphasenbedingungen, eine Flamme von der erzwungenen Zündungen, durch das Einbringen von Zündenergie, bis zum Erreichen eines quasistationären Zustandes abzubilden.

In dieser Arbeit wird zunächst auf die Grundlagen des Strömungslösers und des Verbrennungsmodells eingegangen. Die am Originalverbrennungsmodell vorgenommen Veränderungen werden dann durch eine Reihe von Standardtestfällen validiert. Die Integrität des Modells bezüglich seiner numerischen Implementierung wird durch eine Gitterunabhängigkeitsstudie und eine Untersuchung des sich einstellenden Flammenwinkels für eine Bunsenbrennerkonfiguration belegt. Die richtige Beschreibung der physikalischen und chemischen Vorgänge wird ebenso durch eine Reihe von elementaren Testfällen, welche auch mehrphasige Bedingungen aufweisen, evaluiert. Im Anschluss an die Validierung wird die Vorhersagequalität des Modells für komplexere Testfälle, für welche eine breite experimentelle Datenbasis verfügbar ist, untersucht. Als erstes werden reine gasphasige Konfigurationen simuliert. Vergleichbare Größen, wie die Ausbreitungsgeschwindigkeit der Flamme, die Zündwahrscheinlichkeit im Rechengebiet sind dabei charakteristische Größen, welche eine Aussage über die Genauigkeit der numerischen Ergebnisse zulassen. Es wird demonstriert, dass sowohl das Verhalten der Flamme, als auch die Zündwahrscheinlichkeitsverteilung in der Domäne gut wiedergegeben werden. Um die Zuverlässigkeit des Modells für stationäre komplexe Flammen zu belegen, wird außerdem ein stark turbulenter Jet simuliert. Hierbei wird das Verlöschen der Flamme in Gebieten mit sehr intensiver Turbulenz, in welchen die hohe Streckungsrate keine weiteren chemischen Reaktionen zulässt, vom Modell korrekt vorhergesagt. Für die zuletzt untersuchten Testfälle wird verdeutlicht, dass das Modell auch unter brennkammerähnlichen mehrphasigen Bedingungen treffende Vorhersagen, hinsichtlich der zeitlichen Ausdehnung der Flamme, sowie der Lage von Gebieten mit hoher Zündwahrscheinlichkeit, liefert.

Zusammenfassend wird im Rahmen dieser Arbeit ein Verbrennungsmodell vorgestellt, welches durch die vorgestellten Veränderungen für ein breites Spektrum an Einsatzmöglichkeiten geeignet ist. Die Vorhersagen, die mit dem Modell erstellt werden, erweisen sich in den durchgeführten numerischen Untersuchungen als sehr zufriedenstellend, was den Nutzen von numerischen Werkzeugen für die Untersuchungen von Zündprozessen in Fluggasturbinen unterstreicht.

1. Introduction

1.1. Problem Statement & Motivation

Ignition of the engine, especially under adverse conditions, is a rising issue, due to the shift of the combustion chamber design to leaner conditions to fulfill policy requirements of pollutants emissions. The interest of the aircraft engine original equipment manufacturers (OEM) regarding this topic is demonstrated through studies published by Stow *et al.* [170], Mosbach *et al.* [122] and Fyffe *et al.* [62]. With the combustion systems' concept changing from rich-burn toward lean-burn primary zone combustion in order to address policy measures regarding pollutant emission reduction, in particular nitrogen oxides (NO_x), the issue of ignitability of the engine is more pronounced. Actually, lean-burn low NO_x combustors have an operating envelope closer to the stability limits with respect to rich-burn systems. Especially high altitude relight and cold start where adverse conditions prevail are thoroughly investigated experimentally in dedicated facilities during OEMs lean combustion system research programs [62]. Thus, there is a growing interest in dealing with this matter at an early stage of the combustor design cycle entraining a demand for numerical tools to support the development and allow several simultaneous computations. In aircraft engine combustors, ignition is typically achieved by a spark plug, located at the top of the chamber. Levebvre [96] remarked that ignition is successfully accomplished if three phases are mastered.

The first phase concerns the establishment of an initial kernel. This depends mostly on the characteristics of the spark and the current mixture properties in the vicinity of the plug itself. In case no fuel vapor is generated at the spark location, the deposited energy is likely to be dissipated shortly afterwards. In contrast, in case too much fuel vapor is created at the ignition location, the mixture becomes too rich which also has a detrimental impact on the flame establishment. Once an initial flame kernel has developed, the second phase relates to the spreading of the generated flame kernel. This process is still considerably influenced by local mixture characteristics. Concurrently, the impact of the flow-field grows. The local conditions determine the growth of the flame which is dominated by the flame speed and turbulent quantities. The turbulence can act twofold, as an enhancement and as an impairment to the flame growth as turbulence can wrinkle the flame front, leading to higher burning rates or quench the flame by disturbing elementary reactions in the inner flame zone. In contrast to the flame kernel growth, the path the flame takes is governed by macroscopic flow-field

characteristics. They determine whether the flame is transported out of the domain or to a region which permits a sustainment of the flame. The third stage describes the stabilization of the flame. For the flame to stabilize it is essential that a position is reached which can serve as flame holder. Once the flame has established at this location, this marks the successful ignition of a single sector combustor. Obviously, when one considers full annular combustors, then successful ignition is marked by the stabilization of all single combustors around the ring.

Due to the complexity of the underlying processes, an experimental investigation of the ignition procedure is a troublesome task. This motivates the development of numerical tools through which significant phenomena can be analyzed more thoroughfully, thus, enabling a deeper understanding of the ignition process. In particular, a failed ignition requires a comprehensive data set to examine the relevant causes.

1.2. State-of-the-Art

This thesis presents a low-order combustion model for simulations of ignition and flame propagation in multiphase flows. Low-order methods for the treatment of combustion processes in numerical simulations have a long history. With low-order it is referred to combustion models in contrast to those using a detailed description of the gas phase chemistry, e.g. Blacha *et al.* [15], Di Domenico *et al.* [44] or Michaelis and Bragg [116], which consider complex kinetic schemes and require the transport of a multitude of species. Indeed, since the development of global reaction schemes, e.g. Westbrook and Dryer [186] and Jones and Lindsted [77], the use of such models is widely acknowledged. Concurrently, the demand of numerical work for investigating problems involving complex fluid dynamics has increased. Due to the improvement made in LES modeling [67, 118] a large part of modeling strategies focuses on implementing a multiphase combustion model within a LES context to simulate full-scale gas turbine combustion chambers [148, 154]. However, as this essentially proves very costly in terms of computation time, a large number of calculations on supercomputers is usually out of scope. Specifically, studies involving parameter variations, such as finding the optimal position of an igniter, are predestined for a fast and efficient computation for which simplified combustion models as for example the eddy dissipation model [168] or the flamelet model [189] and simplified turbulence modeling (e.g. URANS) can be utilized.

In the context of identifying favorable igniter locations, a significant number of experimental investigations which aim at determining the ignition probability for simplified geometries have been recently published [2, 3, 4, 5, 105]. The starting point in such a series of experiments is marked with the analysis of the basic gaseous jet-flame configuration [4] for the development of numerical tools. Then, technically relevant applications as for example a swirl-stabilized spray flame [105] are investigated.

Some numerical work has been done concerning the ignition probability of the experiment of a lifted jet flame [4, 5]. Based on an approach with LES, as carried out by [88, 177, 185] a good agreement for distinct points was achieved in terms of the ignition probability of that specific location and the subsequent flame behavior. In general, it was prohibited to repeat the simulations in a grid like pattern [1] identical to the experimental procedure due to the computational cost which was remarked in the work of Lacaze *et al.* [88]. One solution to overcome this restriction is to use the multitude of data which is gathered in the course of a LES simulation in a post-processing step to derive quantitative information about the ignitability of the domain. This can be done by evaluating the time dependent flow-field with respect to a set of relevant conditions such as the probability of finding burnable mixture or a beneficial mean velocity. However so far no valid criteria could be found to yield a reliable prediction of the ignition probability for the investigated numerical domain, see e.g. Lacaze *et al.* [88]. In summary, the numerical studies involving a LES-based approach were limited to a very small number of calculations. As a consequence, the results only comprised a confined set of locations at which the ignitability could be elucidated and can therefore, at the current state of still restricted computational power, not be employed to yield a complete spatial map of the ignitability of a combustor.

Recently, ad-hoc ignition models such as those proposed by Neophytou *et al.* [126] and Weckering *et al.* [184] were developed in the context of numerical ignition studies. These models offer the advantage that they are very time efficient and allow a large number of computations. The shortcoming of these models is that they depend on strong modeling assumptions. The model by Neophytou *et al.* [126] assumes a frozen LES flow-field as basis of the flame propagation evaluation which leads to a model dependency on the choice of the initial flow-field.

In conclusion, the available models achieve reasonable results for the simulation of ignition events. However, due to their lack of the ability to determine the ignitability in the entire domain or the sensibility to initial conditions, a model based on a URANS approach is proposed in this work.

1.3. Contribution of this work

In order to bridge the gap until the computational power becomes available to allow LES computations for numerous stoichiometric and air flow rates at the igniter positions, a reacting combustion model for multiphase flow is presented which is applicable to a standard RANS / URANS environment. The approach is based on the Turbulent Flame Speed Closure

[1] By grid like pattern it is meant that the whole domain is divided into evenly vertical and horizontal intervals. At these locations, the ignition probability is determined which yields a spatial distribution of the ignition probability for the entire domain.

model, hereafter termed TFC-model, which was first proposed by Zimont [196] and offers the advantage that it is of a very reasonable accuracy and robustness. This was successfully demonstrated by the work of Zimont *et al.* [200], Polifke *et al.* [135], Flohr and Pitsch [60] and Knudsen and Pitsch [80] among others. Usually, low-order models are optimized for a single characteristic of the combustion process, for instance certain species concentrations and pollutant emissions or ignition delay times or soot prediction. In this work, the TFC model offers the essential advantage that it captures the flame propagation speed. Precisely, the source term in the reaction progress variable transport equation is closed using a velocity scale dependent upon the physical-chemical properties of the local mixture. With the inclusion of the laminar flame speed as an intrinsic chemical property and the local turbulence quantities, a correlation is derived which approximates the propagation behavior of the flame also in laminar and turbulent regimes. Through the dependence on the laminar flame speed, detailed chemistry effects are taken into account yet retaining the simplicity of the model.
The TFC model itself has undergone a series of enhancements since its formulation by Zimont [196]. One of the improvements made by Zimont and Lipatnikov [199] limits the turbulent flame speed needed for the source term in the presence of high turbulence. Formerly, the increase of turbulence fluctuations would also cause a rise in the absolute value of the turbulent flame speed, which is only valid for Karlovitz numbers [2] less than one. Up to this conditions the small eddies of the size of the Kolmogorov length scale are larger than the inherent reaction zone of the flame front. Beyond that point, for Karlovitz numbers greater than one in case of stronger turbulence, the chemical reactions are affected by the small scale turbulence, which reduces and ultimately quenches the flame. A further contribution to the flexibility of the model was accomplished by Polifke *et al.* [135] and also Cokljat *et al.* [37] who proposed the transport of the mixture fraction and the sensible enthalpy in order to adapt the model to non-premixed environments and to incorporate non-adiabatic effects. The model is also being used in the context of LES simulations, as demonstrated by Knudsen and Pitsch [80].

To the best of the authors knowledge, simulations involving the TFC-model for multiphase flows are not present in the literature, nor the common model implementation apt to incorporate multiphase reactants phenomena. Thus, the contribution of this thesis is the extension of the model formulation to allow the treatment of multiphase reactants in turbulent flows [3]. Furthermore, the extension avoids some shortfalls associated with the standard model implementation. A numerical study performed by Wood and Moss [191] revealed that problems arise for example in situations where a fully burnt lean mixture connects with pure air. Under these circumstances, the definition of the reaction progress variable becomes a challenge, as the dilution by air should not alter the reaction progress variable considering

[2] The Karlovitz number is defined as the ratio of the chemical time scale divided by Kolmogorov time scale: $\mathrm{Ka} = \chi_\mathrm{u} \, / S_L^2 / t_\eta$.
[3] The assumption of the standard TFC-model of a local homogeneous reaction applies.

that a further chemical reaction cannot occur. It is demonstrated that this dilemma is solved by applying the extended model formulation presented in this thesis. The proposed approach demands the transport of selected species which enables the determination of the physical reaction progress and avoids an erroneous influence of mixing effects. Although this renders the model more costly in terms of computational time, it will be elaborated that the advantages and the possibilities of the model far outweight this issue. The second model improvement developed within this work is the ignition interface, which is also not yet available for the standard model. In the original version of the model, a flame kernel is initiated through setting the reaction progress variable to unity at the designated ignition location. This approach neglects the prevailing local conditions at the ignition location (it is automatically assumed that the mixture is burnable) and implicitly presumes an ignition delay time of one simulation time step. The methodology derived in this work to correlate the reaction progress variable evolution to the auto-ignition time, offers a more physical description of the initial stages of the flame kernel development. With the main objective of the model to study ignition problems, this represents an essential and valuable extension of the model abilities.

Enabled through the introduced model extensions, a series of ignition test cases are examined in the scope of this work. With the findings of the simulation, the process starting at the heat release from the ignition device until the establishment of a fully developed flame can be understood more thoroughly. Available experimental data for all considered set-ups indicate that for each test case, the outcome of the ignition sequence changes fundamentally depending on the flow boundary conditions and the ignition location. The results presented in this thesis help to shed light upon what are the most significant causes for a successful / failed ignition.

The model quality and adequacy is underlined by a series of publications. The model derivation is accepted for publication in Combustion and Flame [24]. Another part of the model background concerning the laminar flame speed and the ignition delay time polynomials which constitute input parameter to the model is also available in the literature [18]. Ignition studies employing the extended TFC model which demonstrate the applicability of the model are published in the Journal of Engineering for Gas Turbines and Power [22] and in the Proceedings of the ASME [17, 20, 21], AIAA [19, 23] and, ISABE [24].

2. Governing Equations and Numerical Methods

The underlying principles of the model formulations are discussed in this chapter. Additionally, the elementary framework of the governing equations of the flow solver will be covered as well as a detailed background of the combustion model. The chosen approach to treat combustion processes in this work is based upon a well established model from literature which has been modified and extended to be applicable to ignition in multiphase flows. Further contents of this chapter are the major characteristics of the employed turbulence models and the background of the Lagrangian liquid-phase solver.

2.1. System of Equations for Turbulent Flows

This part is dedicated to the fundamental equations of the CFD (computational fluid dynamics) solver. They are crucial for the computation of the primitive variables of the flow-field which serve as basis for the description of combustion processes.

2.1.1. Fundamentals

The CFD solver is based upon the principle of conservation. For mass this means that a given quantity of matter cannot be created or destroyed [59]. Within a finite control volume, the gain or loss of mass must be the same as what traverses the boundaries of the control volume, which yields for the temporal change of mass:

$$\frac{\mathrm{d}m}{\mathrm{d}t} = 0. \tag{2.1.1}$$

For any other given intensive quantity, source terms can exist which increase or decrease the absolute amount. This leads to the second type of conservation equation:

$$\frac{\mathrm{d}(\rho\phi)}{\mathrm{d}t} = \sum_k f_{\phi,k}, \tag{2.1.2}$$

where ϕ represents an arbitrary intensive variable and $f_{\phi,k}$ the corresponding source term. These two kinds of conservation equations provide the inherent structure for the CFD code algorithm. Since the finite volume method is very appropriate for the requirements arising from the conservation equations, this approach has been utilized throughout this work. The

finite volume approach regards the computational domain as accumulation of small sub-volumes for which the conservation equations can be solved with satisfying accuracy. For any quantity the complete formulation may be written in the following form:

$$\frac{\partial}{\partial t}\int_{\Omega_{\mathrm{CV}}} \rho\phi \mathrm{d}\Omega + \int_{S_{\mathrm{CV}}} \rho\phi(\vec{u}-\vec{u_b})\cdot\vec{n}\mathrm{d}S = \int_{S_{\mathrm{CV}}} \rho\frac{\nu}{\mathrm{Sc}_\phi}\nabla\phi\cdot\vec{n}\mathrm{d}S + \int_{\Omega_{\mathrm{CV}}} f_{V_\phi}\mathrm{d}\Omega \tag{2.1.3}$$

where $\vec{u}$ constitutes the velocity at the boundary and $\vec{u_b}$ the velocity with which the surface itself moves. $\vec{n}$ denotes the surface normal vector pointing outwards of the control volume. ν is the kinematic viscosity and Sc_ϕ the Schmidt number for ϕ. For the conservation equation of mass, the terms on the right-hand side remain zero for the above given reason that matter cannot be destroyed nor created.

In the following, the conservation equations in a non-moving computational domain for the respective flow variables are stated, providing insight into the general form of the governing equations. For the mass conservation equation this yields:

$$\frac{\partial}{\partial t}\int_{\Omega_{\mathrm{CV}}} \rho\mathrm{d}\Omega + \int_{S_{\mathrm{CV}}} \rho\vec{u}\cdot\vec{n}\mathrm{d}S = 0 \tag{2.1.4}$$

With the Gauss theorem applied to convert the surface integral into a volume integral, the final form is achieved:

$$\frac{\partial\rho}{\partial t} + \nabla(\rho\vec{u}) = 0. \tag{2.1.5}$$

This form is accomplished by integrating over the control volume which cancels the integral for both terms and leads to the final partial differential equation. The same procedure is carried out for the momentum conservation which leads to the following conservative form:

$$\frac{\partial}{\partial t}\rho u_j + \frac{\partial}{\partial x_i}\rho u_i u_j = \sum_k f_{u_j,k}, \tag{2.1.6}$$

The right hand side which contains the source terms is explained in more detail. Forces that can affect the momentum are:

- **Surface Forces**: Surface tensions, pressure, normal and shear stresses, etc..
- **Body Forces**: Gravity, electromagnetic, Coriolis, etc..

In this work only Newtonian Fluids appear, thus, the theoretical background remains confined to this type of fluids. For a more thorough description of the source terms, the reader is referred to textbooks on this topic [7, 32]. The source term for the momentum equation reads:

$$\sum_k f_{u_j,k} = \nabla \underline{\underline{T}} + \rho g_j \tag{2.1.7}$$

In Eq. (2.1.7), g_j denotes the j-th component of the gravitational acceleration, whereas $\underline{\underline{T}}$ represents a general stress tensor in two dimensions which combines pressure and viscous stresses:

$$T_{ij} = -\left(p + \frac{2}{3}\mu\frac{\partial u_j}{\partial x_i}\right)\delta_{ij} + 2\mu D_{ij}. \tag{2.1.8}$$

The shear stress tensor D_{ij} is calculated as follows:

$$D_{ij} = \frac{1}{2}\left(\frac{\partial u_i}{\partial x_j} + \frac{\partial u_j}{\partial x_i}\right). \tag{2.1.9}$$

The next essential transport equation relates to the energy conservation equation:

$$\frac{\partial}{\partial t}\rho e + \frac{\partial}{\partial x_i}\rho u_i e = \frac{\partial}{\partial x_i}\lambda\frac{\partial T}{\partial x_i} + \dot{\omega}_e \tag{2.1.10}$$

Energy losses that occur in the simulation through wall heat losses and/or the evaporation of droplets are accounted for in the $\dot{\omega}_e$ term. This is outlined in more detail in the multiphase solver section, see Sec. 2.3. The last relevant conservation equation concerns the transport of the species. This is expressed as:

$$\frac{\partial}{\partial t}\rho Y_j + \frac{\partial}{\partial x_i}\rho u_i Y_j = \frac{\partial}{\partial x_i}\rho D_{Y_j}\frac{\partial Y_j}{\partial x_i} + \dot{\omega}_{Y_j} \tag{2.1.11}$$

with j being the increment running from the first to the $n-1$ species. The last species Y_n is obtained via:

$$\sum_{i=1}^{n} Y_i = 1. \tag{2.1.12}$$

The source terms for the species transport equations are given in the section about the combustion model, see Sec. 2.2. To determine the thermodynamic state of the mixture, it is assumed that the ideal gas law is valid for all investigated test cases as the prevailing pressures and temperatures remain close to atmospheric conditions. The ideal gas law reads:

$$p = \rho\mathscr{R}/\overline{M}T \tag{2.1.13}$$

2.1.2. Turbulence

As turbulence is an immanent part of complex fluid dynamics, the underlying theory and corresponding modeling approaches are described in this subsection. Turbulence can result from various disturbances in the flow that cause the generation of vortices, which will collapse

into smaller and smaller self-similar structures. This phenomena is called turbulence and represents a large challenge in CFD modeling. Major fundamental insight on this topic was provided by Kolmogorov [81] who carried out elementary research on turbulence and proposed essential theories which are still valid nowadays. His concept comprises a scale separation which conveys the occurring vortex like structures into an energy cascade context. The largest vortices that appear on the entry of the scale are broken-up continuously into smaller vortices until the very small structures are finally dissipated by viscous effects. This is illustrated in Fig. 2.1.1. The left hand side of Fig. 2.1.1 displays the energy containing eddies. On the right hand side the inertial range is depicted which shows the decrease in eddy size until the viscous scales are reached. The difficulty that arises in the simulation is to have grid cell sizes which resolve all scales presented in Fig. 2.1.1. In that case, the grid cell size needs to be of the order of the smallest eddies. By introducing the turbulent Reynolds number $\mathrm{Re}_t = u' l_t / \nu$, an equation for the number of required grid cells can be derived. In the turbulent Reynolds number formulation u' corresponds to the magnitude of the velocity fluctuations and l_t to the largest occurring eddies. The concept of fluctuations in the state variables is described in more detail later in this subsection. The smallest scales are defined according to Kolmogorov [81] as:

$$\eta = (\nu^3/\epsilon)^{1/4}, \text{ Length Scale} \tag{2.1.14}$$

$$u_\eta = (\epsilon \cdot \nu)^{1/4}, \text{ Velocity Scale} \tag{2.1.15}$$

$$t_\eta = (\nu/\epsilon)^{1/2}, \text{ Time Scale.} \tag{2.1.16}$$

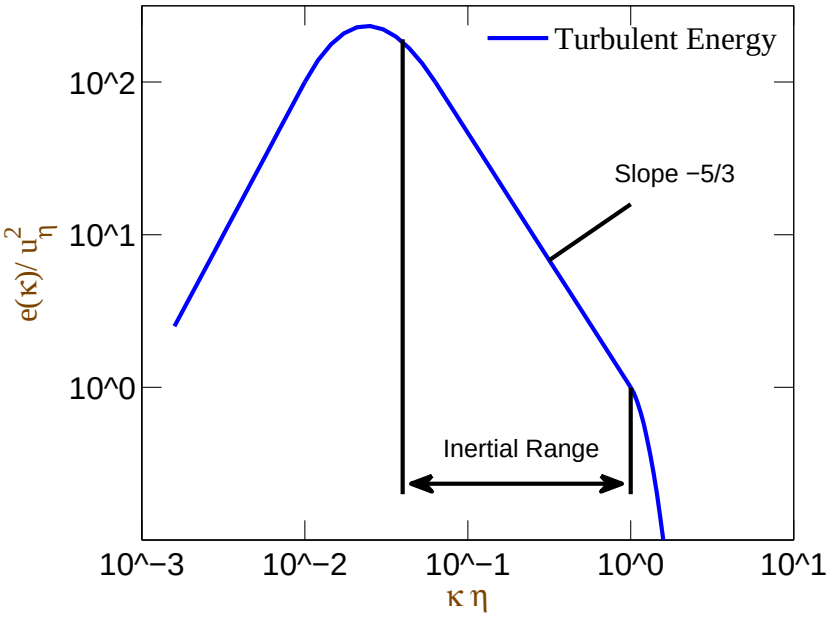

Figure 2.1.1.: **Plot of the turbulent energy cascade.**

On the one hand, the computational domain must be large enough to contain the largest eddies (l_t) and on the other hand be sufficiently small to capture the so called Kolmogorov scale structures (η), which correspond to the smallest eddies. Hence, the number of grid points in one direction, termed N, must fulfill the condition:

$$N\eta > l_t \tag{2.1.17}$$

By using the turbulent Reynolds number the correlation:

$$N > \mathrm{Re}_t^{3/4} \tag{2.1.18}$$

is obtained. This defines the spatial resolution required to capture all turbulent structures. For three dimensional problems, the number of grid points raises to:

$$N > \mathrm{Re}_t^{9/4}. \tag{2.1.19}$$

The example of a simple self-similar round jet, for which the characteristic quantities can be established approximately, shall highlight the issue of grid resolution. A jet with an inlet velocity of $u = 20$ m/s emerging through a nozzle diameter of $D = 0.01$ m corresponds to a Reynolds number of: Re$= Du/\nu \approx 16300$ (with $\nu = 1.2^{-5}$ m/s^2). This represents a moderate Reynolds number compared to technical applications with much higher mean flow velocities. With $l_t = 0.01$ m and $u' \approx 25\%$ $u = 5$ m/s (see Pope [138]), the turbulent Reynolds number amounts to roughly 4,000. To resolve the flow about 127 million grid cells are needed. Thus, for configurations exhibiting higher turbulence levels, resolving all turbulent length scales becomes computationally very costly.

Furthermore, as turbulence needs a transient scheme for its description, requirements regarding the temporal resolution appear. For a stable explicit scheme the CFL (Courant-Friedrich-Lewis) number has to remain smaller than one, yielding:

$$\Delta t = \mathrm{CFL}\Delta x/U, \tag{2.1.20}$$

with Δx denoting the smallest grid cell size and U the corresponding velocity magnitude. Thus, the time step imposes a stringent constraint to the temporal advancement of the simulation, limiting it to very small time steps. This also adds to the computational effort. In summary, this clarifies why resolving all occurring length scales, usually referred to as DNS (Direct Numerical Simulation), is out of scope in the context of relevant technical applications and why a modeling approach needs to be introduced to reduce the computational costs.

2.1.3. Governing Equations

The most common way to account for turbulence is accomplished by splitting the state variables into a mean non-fluctuating part and a fluctuating part [32], which results in:

$$\phi = \overline{\phi} + \phi' \tag{2.1.21}$$

with ϕ representing an arbitrary variable. Consequently, by following this approach all variables can be substituted with their composed counterparts which leads to the averaged Navier-Stokes Equations. As the separation in Eq. (2.1.21) originates from the work of Reynolds, the procedure is called Reynolds averaging. In combustion, as density variations through the progress of reactions occur, Favre averaging is favored [57, 190] as it simplifies correlations involving the density fluctuation ρ'. Thus, each quantity is expressed as:

$$\phi = \tilde{\phi} + \phi'' \tag{2.1.22}$$

where $\tilde{\phi}$ corresponds to:

$$\tilde{\phi} = \frac{\overline{\rho\phi}}{\overline{\rho}} \tag{2.1.23}$$

This leads to the final form of the governing equations written in Favre notation, according to [134]:

Continuity Equation:

$$\frac{\partial\overline{\rho}}{\partial t} + \frac{\partial}{\partial x_i}\left(\overline{\rho}\tilde{u}_i\right) \tag{2.1.24}$$

Momentum Equation:

$$\frac{\partial\overline{\rho}\tilde{u}_i}{\partial t} + \frac{\partial}{\partial x_i}\left(\overline{\rho}\tilde{u}_i\tilde{u}_j\right) = \frac{\partial}{\partial x_i}\left(\overline{\tau}_{ij} - \widetilde{\overline{\rho}u_i''u_j''}\right) \tag{2.1.25}$$

For τ the expression derived in Eq. (2.1.8) is employed.

Energy Equation:

$$\frac{\partial\overline{\rho}\tilde{h}_s}{\partial t} + \frac{\partial}{\partial x_i}\left(\overline{\rho}\tilde{u}_i\tilde{h}_s\right) = \frac{\partial}{\partial x_i}\left(\overline{\lambda}\frac{\partial\tilde{T}}{\partial x_i} - \widetilde{\overline{\rho}u_i''h_s''}\right) + \overline{\dot{\omega}}_T \tag{2.1.26}$$

Note that the specific enthalpy is used for the energy equation (Eq. 2.1.10) and that some terms have been neglected following [134] due to the assumption of incompressibility and due to their relative lower order. Secondly, as for all test cases a constant Lewis number of unity is assumed, the contribution of differential diffusion to the energy equations is omitted. Furthermore, simplification are introduced for the modeling of the diffusion term for which a non-fluctuating diffusion coefficient is prescribed.

Species Transport Equation:

$$\frac{\partial \overline{\rho}\tilde{Y}_j}{\partial t} + \frac{\partial}{\partial x_i}\left(\overline{\rho}\tilde{u}_i\tilde{Y}_j\right) = \frac{\partial}{\partial x_i}\left(\overline{\rho D_j \frac{\partial Y_j}{\partial x_i}} - \overline{\rho}\widetilde{u_i''Y_j''}\right) + \overline{\dot{\omega}}_j \tag{2.1.27}$$

for all $n-1$ species.

Note, that in the above equation unknown terms have arisen, namely the so called Reynolds stress terms which are average products of two fluctuating quantities, e.g. $\widetilde{u_i''Y_j''}$. As these terms cannot be determined during the simulation, a modeling approach is needed to approximate the so called Reynolds stress terms by means of the known average values. The closure of the Favre Averaged Navier-Stokes equations represents the immanent challenge in turbulence modeling. A widely acknowledged approach to model the unknown terms is the Boussinesq approximation [16, 73, 175]. It is assumed that turbulence velocity fluctuations have a similar effect on a transported quantity as laminar diffusion. This intrinsically implies that turbulence acts isotropic which is also a main assumption of the utilized turbulence models. Although isotropy of turbulence is not always given in the examined cases it represents a widely used and reasonable approach. The Boussinesq approximation allows to correlate the turbulent flux to the gradient of the mean values times the turbulent viscosity. The turbulent viscosity is derived from turbulent quantities which are modeled by the turbulence model which is explained in more detail in the next section. Using the Boussinesq approximation, this yields for the turbulent flux of the species transport equation:

$$\widetilde{u_i''Y_j''} = -\frac{\nu_t}{\mathrm{Sc}_{Y,t}}\frac{\partial \tilde{Y}_j}{\partial x_i} \tag{2.1.28}$$

In Eq. (2.1.28) ν_t denotes the turbulent viscosity and $\mathrm{Sc}_{Y,t}$ the turbulent Schmidt number for which a value of 0.7 is prescribed. The above described procedure can be applied to the remaining turbulent fluxes in the same manner.

2.1.4. Turbulence modeling

The previous paragraph outlined that through averaging the Navier-Stokes equations unclosed parts appear in the formulation. The treatment of these terms poses an elementary challenge in turbulence modeling. In this work, three different types of turbulence modeling appear. A RANS (Reynolds Averaged Navier-Stokes) steady state simulation is the numerical approach which has been applied to all steady test cases. For these scenarios, the bias is on obtaining a converged steady state solution. A transient adaptation of the first method, termed URANS (Unsteady Reynolds Averaged Navier-Stokes) is the second turbulence modeling type which is used for most numerical ignition studies. Under these circumstances, the time resolved solution of mean flow quantities is of major interest to capture the flame development. In this framework flow motions larger than the integral length scale are tem-

porarily resolved. The third numerical approach is SAS (Scale Adaptive Simulation) which is also utilized to resolve transient phenomena. This method combines a URANS mode and an LES (Large Eddy Simulation) mode depending on the level of local turbulence. A LES simulation captures turbulent motions larger than a defined filter length scale, which allows it to resolve a part of the turbulent spectrum. All three approaches share the fact that the turbulence and its effects are described based on modeling assumptions.

In the following, the elementary background of these turbulence models is elaborated. The commonly chosen closure in a RANS context relies on a two-equation model. Two-equation model means that two additionally transported quantities are introduced which aim at representing the global effect of turbulence. For the SAS, a subgrid closure is needed in dedicated regions of the flow in which the LES mode is enabled to model the impact of turbulence length scales smaller than the grid size.

2.1.4.1. k-ϵ Model

Being the most widely used complete turbulence model, the k-ϵ approach has also been applied to most of the test cases in this work. Its development can be largely attributed to the research of Jones and Launder [76] with subsequent improvements made to the model constants by Launder and Sharma [91]. The underlying theory is based upon the assumption that the effect of turbulence can be described by introducing a turbulent viscosity in accordance to the Boussinesq approximation as stated in Eq. (2.1.28). This implicitely presumes that the turbulence is isotropic, even for large scales, which is the reason why for direction biased test cases as for example a jet flame, corrections need to be applied. The turbulent viscosity ensures an increase in the diffusion which seeks to capture the net effect of the turbulent velocity fluctuations. In order to determine the turbulent viscosity, the kinetic energy and the turbulent dissipation need to be known. Thus, two additional transport equations are introduced for the kinetic energy and the turbulent dissipation.

The notation is taken from Pope [138]. The equations given here under serve as look-up for the test cases section in which the respective turbulence model is used and help to understand modifications to the model constants which are necessary for some specific configurations.
For the turbulent kinetic energy, the transport equation reads:

$$\overline{\rho}\frac{\partial \tilde{k}}{\partial t} + \overline{\rho}\frac{\partial \tilde{u}_i}{\partial x_i}\tilde{k} = \nabla\overline{\rho}\left(\frac{\nu_t}{\sigma_k}\nabla\tilde{k}\right) + \mathscr{P} - \overline{\rho}\tilde{\epsilon}. \tag{2.1.29}$$

The production term in Eq. (2.1.29) is specified as:

$$\mathscr{P} = C_\nu\overline{\rho}\nu_t\left(\frac{\partial \tilde{u}_i}{\partial x_j} + \frac{\partial \tilde{u}_j}{\partial x_i}\right) \tag{2.1.30}$$

The turbulent dissipation is modeled as:

$$\overline{\rho}\frac{\partial\tilde{\epsilon}}{\partial t}+\overline{\rho}\frac{\partial\tilde{u}_i}{\partial x_i}\tilde{\epsilon}=\nabla\overline{\rho}\left(\frac{\nu_t}{\sigma_\epsilon}\nabla\tilde{\epsilon}\right)+C_{\epsilon1}\frac{\mathscr{P}\tilde{\epsilon}}{\tilde{k}}-C_{\epsilon2}\frac{\tilde{\epsilon}^2}{\tilde{k}}. \tag{2.1.31}$$

The turbulent viscosity needed for Eq. (2.1.29) and Eq. (2.1.31) is obtained via:

$$\nu_t=C_\nu\tilde{k}^2/\tilde{\epsilon} \tag{2.1.32}$$

In the standard k-ϵ model, the constants pertain to:

$$C_\nu=0.09, C_{\epsilon1}=1.44, C_{\epsilon2}=1.92, \sigma_k=1.0, \sigma_\epsilon=1.3. \tag{2.1.33}$$

The implementation of a turbulent viscosity allows the closure of the afore unknown terms in the transport equations which involve a cross-correlation with velocity fluctuations. These expressions can be substituted with the turbulent viscosity term which acts as an enhanced gradient diffusion. Hence, the energy, the momentum and, the species transport equations as described in Eq. (2.1.25, 2.1.26, 2.1.27) are closed by omitting the cross-correlation fluctuation terms and, subsequently, adding the turbulent viscosity to the laminar viscosity.

2.1.4.2. k-ω Model

In order to complete the subsection regarding RANS turbulence models, the k-ω model is presented which is used in test cases with either low turbulence or with a high degree of wall confinement. This additional two-equation turbulence model developed over many years by Wilcox [188] has nearly the same structure as the k-ϵ model. The k-ω is superior as compared to the k-ϵ model as the treatment of the viscous near-wall regions and the accounting of streamwise pressure gradients is improved according to Wilcox [188]. The k-ϵ model suffers from the fact that it predicts a non-physical turbulent time scale close to the wall. As the turbulent time scale is defined as k/ϵ in the k-ϵ model, its value tends to zero close to the wall. In the k-ω model this shortcoming is avoided since the inverse of the turbulent time scales is transported in the second equation. This allows values other than zero at the wall and enables to predict the correct development of the turbulence close to the walls. This entails some changes in the derivation of characteristic turbulent quantities which are given later. The equation for the inverse of the turbulent time scale reads:

$$\overline{\rho}\frac{\partial\tilde{\omega}}{\partial t}+\overline{\rho}\frac{\partial\tilde{u}_i}{\partial x_i}\tilde{\omega}=\nabla\overline{\rho}\left(\frac{\nu_t}{\sigma_\omega}\nabla\tilde{\omega}\right)+C_{\omega1}\frac{\mathscr{P}\tilde{\epsilon}}{k}-\overline{\rho}C_{\omega2}\tilde{\omega}^2. \tag{2.1.34}$$

By defining two turbulent quantities, the purpose to derive a correlation for the turbulence viscosity that allows a closure for all other transport equations in accordance to the approach as described in the k-ϵ turbulence model part is fulfilled. The turbulent dissipation can be obtained directly from k and ω through: $\tilde{\epsilon}=\tilde{k}\tilde{\omega}$. The expression for ν_t in the k-ω model reads:

$$\nu_t = \frac{1}{C_\nu}\tilde{k}/\tilde{\omega}. \tag{2.1.35}$$

The modeling constants correspond to:

$$C_{\omega 1} = 0.44, C_{\omega 2} = 0.92. \tag{2.1.36}$$

2.1.5. Scale Adaptive Simulation

Test cases which involve high levels of turbulence and are significantly influenced by coherent turbulent structures as is frequently the case for realistic technical problems are often unsatisfactory resolved with a RANS approach. Consequently, the application of a LES (Large Eddy Simulation) technique to these configuration becomes necessary. This technique has been successfully established for both non-reacting [58, 97, 131] and reacting flows [41, 113]. In LES, large structures containing most of the energy (> 80 %) are explicitly resolved. The strong assumption of isotropy of turbulence velocity fluctuations, which introduces a significant error into RANS modeling, is avoided for the larger scales. Only the smaller scales for which sub-grid scales models are implemented, are taken to be isotropic in the LES context. This is in accordance with the theory of Kolmogorov [81] stating that in the inertial range of turbulence, motions exhibit a more and more universal character.

The development of LES models can be attributed to the field of meteorological research [160] in which a great interest on capturing the time resolved motions of the large scales persists. These models have been refined by several scientists [40, 67] and have been applied successfully to combustion modeling. Standard LES simulation entail a large computational effort as they require a fine resolution in all parts of the grid. Secondly, issues concerning near wall modeling occur. To circumvent these problems, several other LES based techniques have been developed. For instance, to avoid the difficulty of near wall modeling, the detached eddy simulation (DES) was proposed by Spalart [167]. In the present work the SAS (Scale Adaptive Simulation) model is utilized. This hybrid LES / URANS model, developed by Menter and co-workers [55, 114, 115] offers the advantage that it distinguishes the level of turbulence present in the flow. This leads to a LES-like behavior in regions with high turbulence and to a URANS mode in areas in which low levels of turbulence pertain. Therefore, it allows to design the grid according to the expected levels of turbulence, refining it, for example, in highly turbulent shear layers, yet, avoiding to do so in the entire domain. This also circumvents issues regarding near wall flows as the model adopts a URANS mode in these regions.

In the following only the important details concerning the SAS model used in the scope of this work shall be outlined. The core of the model is formed by a set of two transport equations.

Table 2.1.: **Model constants for the SAS turbulence model.**

ζ_1	ζ_2	ζ_3	C_μ	κ	σ_k	σ_Ψ
0.8	1.47	0.0288	0.09	0.41	2/3	2/3

One for the turbulent kinetic energy in analogy to the previously discussed two-equation models and a second one for a characteristic diffusion scale (Ψ) which allows to determine a turbulent eddy viscosity. The characteristic diffusion scale ensures that in regions which are well resolved by the grid, the turbulent energy production takes predominantly place within the subgrid scales as the other length-scales are implicitely captured by the flow-field. The final equations read (overbars omitted) in accordance to [114]:

$$\frac{\partial \rho k}{\partial t} + \frac{\partial \rho u_i k}{\partial x_i} = \mathscr{P} - C_\mu^{\frac{3}{4}} \cdot \rho \frac{k^2}{\Psi} + \frac{\partial}{\partial x_i}\left(\rho \frac{\nu_t}{\sigma_k}\frac{\partial k}{\partial x_i}\right) \tag{2.1.37}$$

$$\frac{\partial \rho \Psi}{\partial t} + \frac{\partial \rho u_i \Psi}{\partial x_i} = \frac{\Psi}{k}\mathscr{P}\left(\zeta_1 - \zeta_2\left(\frac{l_t}{L_{\nu K}}\right)^2\right) - \zeta_3 \rho k + \frac{\partial}{\partial x_i}\left(\rho \frac{\nu_t}{\sigma_\Psi}\frac{\partial \Psi}{\partial x_i}\right) \tag{2.1.38}$$

The unknown expressions in Eq. (2.1.37) and Eq. (2.1.38) relate to:

$$L_{\nu K} = \kappa \left|\frac{u'}{u''}\right|, \tag{2.1.39}$$

with

$$u'' = \sqrt{\frac{\partial^2 u_i}{\partial x_i^2}\frac{\partial^2 u_i}{\partial x_j^2}} \tag{2.1.40}$$

and

$$u' = \sqrt{2 \cdot D_{ij} D_{ij}};\ D_{ij} = \frac{1}{2}\left(\frac{\partial u_i}{\partial x_j} + \frac{\partial u_j}{\partial x_i}\right) \tag{2.1.41}$$

The turbulent viscosity is obtained via:

$$\nu_t = C_\mu^{\frac{1}{4}} \Psi \tag{2.1.42}$$

The employed constants proposed by Menter and Egorov [114] are provided in Table 2.1. The expression for $\mathscr{P}$ is the same as the one introduced in Eq. (2.1.30). The derived turbulent viscosity in Eq. (2.1.42) enables the closure of the unknown sub-grid terms in the same manner as described in the k-ϵ turbulence model.

2.1.6. Summary

This section outlines the numerical framework employed for the CFD simulations in this work. The governing equations for the conservation of mass, momentum, energy and, species are

presented. It is illustrated that it is computationally too expensive to resolve all fluid motions from the integral length scale to the Kolmogorov (viscous) length scale which results in the introduction of turbulence models. Turbulence models resolve only a part of the turbulent spectrum and offer a modeling approach for the remaining part of the unresolved turbulent kinetic energy. The so-far presented equations allow the description of a non-reacting flow-field, however, do not account for chemical processes that occur in flames. Chemical processes may act as heat sources which alter the fluid density and as a consequence thereof affect the flow. For this reason, a combustion model to include chemical effects is needed which is the main focus of the next section.

2.2. Derivation of the Extended TFC Model

For the inclusion of combustion processes, an approach based on the turbulent flame speed closure model (TFC model) originally developed by Zimont [196], is employed. With the intention to generate ignition maps for combustors, some important requirements apply to the combustion model. The model needs to be computationally efficient to realize a large number of computations for different ignition locations and boundary conditions settings. This excludes LES based models, such as e.g. used in Lacaze *et al.* [88], as the computational costs until a single ignition event is simulated are too high. Low-order combustion models fulfill the condition of computational efficiency. A second requirement concerns the accuracy with which the model describes the ignition process. The flame kernel evolution is largely depending on flame propagation and flame growth, which sets the focus for the type of low-order model needed in this context. For this reason the TFC model is chosen. The TFC model is convenient for unsteady computations, in particular, ignition studies as it is designed for capturing flame propagation. Since the source term for the reaction progress variable is derived from the laminar flame speed, it enables an intuitive description of the flame spreading behavior. Through improvements and modification to the original model, e. g. through Polifke *et al.* [135] who proposed to include a transport equation for the mixture fraction to enable the utilization of the model for non-premixed conditions, the model became suited for a wide range of applications. However, none of the improvements was designated to multiphase-flow simulations nor to ignition case studies. The contribution made within this work concerns these two limitations of the standard model. A model description is derived which overcomes both limitations and enables the model to be used for ignition case studies under multiphase conditions.

To derive the model equations, the simple form of the transport equation for the reaction progress variable c is needed:

$$\frac{\partial}{\partial t}(\rho c) + \frac{\partial}{\partial x_k}(\rho u_k c) = \frac{\partial}{\partial x_k}\left(\rho D_c \frac{\partial c}{\partial x_k}\right) + \dot{w}_c. \tag{2.2.1}$$

c is an independent scalar which indicates the reaction progress. A major difference to the common approach [60, 135, 191] is that no physical species is assigned to c, such as e.g. the normalized product mass species. The reason for that is elaborated in the further course of this paragraph. The other variables occurring in Eq. (2.2.1) are the density (ρ), the diffusion coefficient (D_c) and the source term ($\dot{w}_c$). Since flows of variable density are considered, Favre averaging ($\overline{\rho c} = \overline{\rho}\tilde{c}$) is applied to Eq. (2.2.1) which yields the following form:

$$\frac{\partial}{\partial t}(\overline{\rho}\tilde{c}) + \frac{\partial}{\partial x_k}(\overline{\rho}\tilde{u}_k\tilde{c}) = \frac{\partial}{\partial x_k}\left(\overline{\rho} D_c \frac{\partial \tilde{c}}{\partial x_k}\right) - \frac{\partial}{\partial x_k}\left(\overline{\rho u_k'' c''}\right) + \overline{\dot{w}}_c \tag{2.2.2}$$

The turbulent flux ($\overline{\rho u_k'' c''}$) is modeled with the usual gradient-diffusion assumption, see e.g. [60] and [191]. Hence, the diffusion term in Eq. (2.2.2) is expanded and the turbulent Schmidt number (Sc_t) is introduced, which allows to relate the turbulent flux with the turbulent viscosity using the Boussinesq assumption [16], see Eq. (2.1.28). It has been observed by many researchers [8, 30, 137] that counter gradient diffusion can also occur. However, this phenomenon is neglected in this implementation as the envisaged range of the model corresponds to regimes which are characterized by high turbulent Reynolds numbers: $\mathrm{Re}_T = u' l_t/\nu \gg 1$. Under these conditions an analysis of Veynante *et al.* [180] revealed that counter gradient diffusion is not the dominant direction of the turbulent flux as the large velocity fluctuations govern the flame behavior. For validation studies, associated with conditions of weak turbulence, counter gradient diffusion is also negligible as the velocity fluctuations are of very low magnitude, which limits the impact of the turbulent flux in general. This leads to the closed transport equation for c:

$$\frac{\partial}{\partial t}(\overline{\rho}\tilde{c}) + \frac{\partial}{\partial x_k}(\overline{\rho}\tilde{u}_k\tilde{c}) = \frac{\partial}{\partial x_k}\left(\overline{\rho}\frac{\nu_t}{\mathrm{Sc}_{c_t}}\frac{\partial \tilde{c}}{\partial x_k}\right) + \overline{\dot{w}}_c \tag{2.2.3}$$

Note that the diffusion term only contains a contribution from the turbulent diffusion ν_t, as the laminar diffusion part is contained intrinsically in the source term. The expression Sc_{c_t} corresponds to the turbulent Schmidt Number of c, which is equal to 0.7 in all simulations.

The source term in the transport equation for the reaction progress variable is given as:

$$\overline{\dot{w}}_c = \rho_\mathrm{u}\, S_T |\nabla \tilde{c}| + C_\mathrm{ign}\, \overline{\rho}\frac{1}{t_i} \tag{2.2.4}$$

The first part of Eq. (2.2.4) relates to the standard implementation of the TFC model. It links the source term for c to the local turbulent flame speed and to the gradient of the reaction progress variable. One widely employed expression and present in the original formulation for the turbulent flame speed is the one derived by Zimont *et al.* [196]. It has been substantiated that this expression is valid for the wrinkled-thickened flame regime, characterized by $\mathrm{Re}_t \gg 1$ and $\mathrm{Da}_t \gg 1$, which is usually the case in a gas turbine combustor.

The turbulent Damköhler number is defined as: $\mathrm{Da_t} = l_t/u'/\chi_\mathrm{u}\ /S_L^2$. Beyond these regimes and especially for lean conditions, a quenching term becomes crucial which is specified by Zimont [197] and further elaborated in [135]. It ensures, that the turbulent flame speed cannot grow boundlessly for strong turbulence. Other expressions for the turbulent flame speed exist in the literature, e.g. Eickhoff [56] and Schmid *et al.* [147], which, however lack the quenching term and/or the wide range of validity. As parts of the validation with experimental data do not fulfill the conditions $\mathrm{Re}_t \gg 1$ and $\mathrm{Da}_t \gg 1$, the use of an expression which is proposed by Peters [129] is suggested, which covers a larger range of turbulent regimes:

$$S_T^* = S_L(1 + \tilde{\sigma}_t) \tag{2.2.5}$$

with $\tilde{\sigma}_t$ being defined as:

$$\tilde{\sigma}_t = -\frac{0.39}{2}\frac{l_t}{l_f} + \left[\left(\frac{0.39}{2}\frac{l_t}{l_f}\right)^2 + 0.78\frac{u' l_t}{S_L l_f}\right]^{\frac{1}{2}} \tag{2.2.6}$$

The laminar flame thickness l_f is obtained from $l_f = \frac{\nu/\mathrm{Sc_Y}}{S_L}$. Values for the laminar flame speed (S_L) as a function of the equivalence ratio Φ, the temperature and the pressure are prescribed using polynomial expressions for the corresponding fuel which are provided in Appendix A. The turbulent flame speed expression proposed in the original version of Zimont [196] and the correlation from Peters [129] both converge for large values of Re_t and Da_t. The quenching term introduced by Zimont [197] which bounds the value of the turbulent flame speed for extensive turbulence is specified in Section 2.2.1 and can be coupled to both expressions.

The second contribution to the source term in Eq. (2.2.4): $C_\mathrm{ign}\,\overline{\rho}\frac{1}{t_i}$ represents the triggering mechanism for the reaction progress variable. In the original TFC model no interface to capture ignition is present, hence, artificial assumptions are required to initiate a flame kernel front. The ability to prescribe ignition boundary conditions represents one of the major improvements of the proposed model extension. The coupling of the reaction progress variable to the auto-ignition characteristics of the mixture yields a more natural and physical implementation. The additional source term $C_\mathrm{ign}\,\overline{\rho}\frac{1}{t_i}$ follows the reasoning that a mixture is ignited once the condition: $\int_{t_0}^{t}\frac{1}{t_i}dt > 1.0$ is fulfilled. At each time step the ignition delay time is evaluated for each grid cell depending on the local state which gives a corresponding finite rise in the reaction progress variable. C_ign is a model constant which is equal to 1.0 throughout this work. Values for t_i are prescribed using polynomial expressions which are provided in Appendix A. In case the local conditions do not allow auto-ignition the value of t_i is set to $1\mathrm{x}10^6$ s in order to render the second source term of Eq. (2.2.4) negligible.

The transport equation Eq. (2.2.3) allows a basic flame description within a homogeneous

premixed environment. For more complex flame regimes involving several inflows of different composition and multiphase phenomena, the transport of individual species mass fractions Y_i and specific enthalpy h becomes necessary. In the following the derivation of the modeling background which extends the model applicability to multiphase conditions is detailed, since this constitutes a major achievement in this thesis.

Through the definition of the source term given in Eq. (2.2.4), the evolution of c depends on S_L and t_i. Both are functions (see polynomials in Appendix A) of Φ and T_u . Usually, the mixture fraction is introduced to determine Φ, however, it will be elaborated that within a multiphase environment, it is more adequate to use selected elementary species. The specific enthalpy is required to capture heat losses or sources and to account for evaporation in multiphase flows which both influence the unburnt temperature T_u . The transport equation for an elementary species reads:

$$\frac{\partial}{\partial t}\left(\overline{\rho}\tilde{Y}_i\right) + \frac{\partial}{\partial x_k}\left(\overline{\rho}\tilde{u}_k\tilde{Y}_i\right) = \frac{\partial}{\partial x_k}\left(\overline{\rho}D_Y\frac{\partial\tilde{Y}}{\partial x_k}\right) + \overline{\dot{w}}_{Y_i} + \overline{\dot{\Gamma}}_{Y_i} \tag{2.2.7}$$

In the present work, oxidizer, fuel and main combustion products (i.e. CO_2 and H_2O) are transported. N_2 is considered the inert species to fulfill the continuity. The source term $\overline{\dot{\Gamma}}_{Y_i}$ accounts for evaporation and is detailed in Le Clercq *et al.* [94], whereas $\overline{\dot{w}}_{Y_i}$ describes changes related to the reaction progress variable. D_Y constitutes the constant diffusion coefficient of the species, which corresponds to:

$$D_Y = \frac{\nu}{\mathrm{Sc}_Y} + \frac{\nu_t}{\mathrm{Sc}_{Y_\mathrm{t}}} \tag{2.2.8}$$

with the constants Sc_Y and $\mathrm{Sc}_{Y_\mathrm{t}}$ also equal to 0.7. ν and ν_t represent the laminar and turbulent viscosity, respectively. The model extension is meant for configurations in which a single fuel species is present and for which a global reaction with an oxidizer can be derived in the form of:

$$mC_xH_yO_z + \left[m\cdot\left(x+\frac{1}{4}y\right) - \frac{z}{2}\right]O_2 = x\cdot m\cdot CO_2 + m\cdot\frac{y}{2}H_2O \tag{2.2.9}$$

Hence, transport equations are needed for all species which occur in the global reaction. Since the interaction between evaporation phenomena and the TFC combustion model has not been found in the literature, some general considerations on the implications shall be given here. The first consideration concerns the behavior of the reaction progress variable c when fuel droplets evaporate within the flame. In a lean mixture, the increase in fuel vapor concentration due to evaporating droplets should lead to a reduction in c, as the fuel vapor added to the gaseous phase is not consumed yet. To incorporate this process, a dependent variable β is introduced, which is defined as the ratio of local exhaust gas mass fraction, e.g.

Y_{CO_2} to the maximum attainable local exhaust gas mass fraction ($Y_{CO_{2max}}$) corresponding to a complete combustion.:

$$\beta = \frac{Y_{CO_2}}{Y_{CO_{2max}}} \tag{2.2.10}$$

The choice of Y_{CO_2} as marker is arbitrary, as for the underlying global reaction, any linearly dependent species is an adequate choice. The maximum mass fraction of CO_2 can be obtained by solving the global reaction in the form of Eq. (2.2.9). The quantity β is only defined for an equivalence ratio above 0.1 and is set to zero if below this threshold to avoid divergence in regions without any fuel. Contrary to β the "reaction progress variable" c determines where the flame resides ($c > 0.0$) and is unaffected by local fuel vapor sources. However, it does not give details regarding the local composition in this implementation. It can be interpreted as a flame edge marker, similar to the flame edge variable G in the G-equation model, see e.g. [174]. The second consideration concerns the behavior of the reaction progress in mixing processes. The reaction progress variable c is undefined for pure air ($c = 0$ is used). As a consequence, the degree of reaction cannot be deduced when air with $c = 0$ and exhaust gases with $c = 1$ mix.

For exhaust gases stemming from lean combustion the blending with pure air should not allow any further reaction progress. However, in its standard formulation the TFC model fails. It assumes a dilution of the reaction progress variable which represents an independent variable that will therefore take on values between 0 and 1 in the mixing zone. Values of the reaction progress variable other than 0 and 1 indicate that unburnt fuel is existent and the reaction has not finished yet, see Wood and Moss [191]. This issue is overcome by the method presented in this work, as the algorithm includes the transport of elementary species. By transporting the fuel explicitly, the value of its mass fraction is not directly linked to the value of the reaction progress variable.

The presence of fuel vapor sources explains the necessity of the second dependent reaction progress variable β. β ensures that a physically meaningful reaction can occur within the flame zone which is characterized by $c > 0.0$. Through droplet evaporation within a lean flame or through blending of flows, the reaction progress variable does not describe the current chemical state, as the standard definition of $c = 1$ suppresses any further combustion even if fuel and oxidizer are still present. As β is evaluated at the beginning of each time step it reflects the proper chemical state of the reaction. Consequently, by means of comparing β with c it can be deduced whether the current local reaction progress variable state does indeed correspond to the species mass fractions locally present.
The source term of each species is split into one part associated with the liquid phase evaporation ($\overline{\dot{\Gamma}}_{Y_i}$) and one part associated with the combustion process ($\overline{\dot{w}}_{Y_i}$), see Eq. (2.2.7). The

combustion related source term for each species that occurs in the global reaction is modeled as:

$$(\overline{\dot{w}}_{Y_i}) = \gamma \cdot \left(\overline{\dot{w}_c} + \overline{\dot{w}_\beta}\right) \cdot n_{\mathrm{st},i} \cdot M_i / \overline{M}, \tag{2.2.11}$$

where n_{st_i} represents the i-th stoichiometric coefficient according to Eq. (2.2.9), M_i the molar weight of the i-th species and $\overline{M}$ the average molar weight of the mixture. The factor γ is derived by:

$$\gamma = Y_{\mathrm{CO_2max}} \cdot \overline{M} / \left(M_{\mathrm{CO_2}} n_{\mathrm{st,CO_2}}\right) \tag{2.2.12}$$

The expression $\dot{w}_\beta$ is computed as follows:

$$\dot{w}_\beta = \rho \cdot \max(c - \beta, 0.0) / \left(D_Y / S_L^2\right) \tag{2.2.13}$$

which achieves a steady consumption within a typical chemical time scale, expressed by the term D_Y/S_L^2, of fuel and oxidizer in case the local reaction progress variable (c) is higher than the local chemical state of the combustion (β). A simple correlation depending on turbulent diffusion and the laminar flame speed for the time scale suffices, in contrast to more sophisticated correlations as proposed in Ihme and Pitsch [75] and Michel *et al.* [117], since this only affects the burn-up of newly generated fuel vapor in the flame zone.
In order to capture non-adiabatic effects an energy transport equation in accordance with Eq. (2.1.10) is needed. It is proposed to employ the specific enthalpy for which the transport equation reads:

$$\frac{\partial}{\partial t}\left(\overline{\rho}\tilde{h}\right) + \frac{\partial}{\partial x_k}\left(\overline{\rho}\tilde{u}_k\tilde{h}\right) = \frac{\partial}{\partial x_k}\left(\overline{\rho} D_h \frac{\partial \tilde{h}}{\partial x_k}\right) + \overline{\dot{w}}_h + \overline{\dot{\Gamma}}_h \tag{2.2.14}$$

with $D_h = D_Y$, as the unity gas phase Lewis Number assumptions is employed. The source term $\overline{\dot{w}}_h$ accounts for energy sources such as the ignition energy which is described in Sec. (2.2.4) whereas liquid phase contributions such as the fuel droplet evaporation are covered by $\overline{\dot{\Gamma}}_h$, see [94]. In most TFC implementations, see e.g. Polifke *et al.* [135] the temperature is derived from a correlation relating the adiabatic flame temperature to the reaction progress variable. However, outside the flammability limits, the adiabatic flame temperature is undefined, which requires artificial assumptions to be made. By employing (the transported) elementary species, the mixture temperature is obtained by virtue of:

$$h(T) = \sum_{i=1}^{n} Y_i h_i = \sum_{i=1}^{n} Y_i \cdot (h_{0_i} + \int_{T_0}^{T} c_{p_i}(T) dT), \tag{2.2.15}$$

where n denotes the number of species. For c_p the NASA polynomials are employed [110].

The density is subsequently derived by solving the equation-of-state for ideal gas.

Two unresolved tasks remain for the closure of the model. The laminar flame speed needs to be provided for the source term in Eq. (2.2.4) with consideration of Eq. (2.2.5). Furthermore, an expression for the ignition delay time needs to be found for the auto-ignition contribution in Eq. (2.2.4). Both quantities can be defined as a function of p, T_u (unburnt gas temperature) and Φ which allows the use of polynomial expressions. For adiabatic cases, the unburnt gas temperature is obtained through computing the initial conditions prior to combustion. This is achieved by reversing the global reaction as given in Eq. (2.2.9). For non-adiabatic cases, a correction term for the laminar flame speed is introduced as detailed in Sec. 2.2.2. The form of the polynomials for the laminar flame speed and the ignition delay time plus the corresponding coefficients of the polynomials are provided in Appendix A. The validity of the polynomials ranges from $0.6 < \Phi < 1.5$, $293.15\ \mathrm{K} < T_u < 593.15\ \mathrm{K}$ for the laminar flame speed and from $1200\ \mathrm{K} < T_u < 1800\ \mathrm{K}$ for the auto-ignition time. For both quantities the unburnt temperature and the gaseous equivalence ratio are taken as references. The considered pressure range extends from $0.5\ \mathrm{atm} < p < 6\ \mathrm{atm}$. For temperatures rising beyond the maximum temperature of the respective correlation, the value at the maximum temperature is taken.

2.2.1. Quenching Term

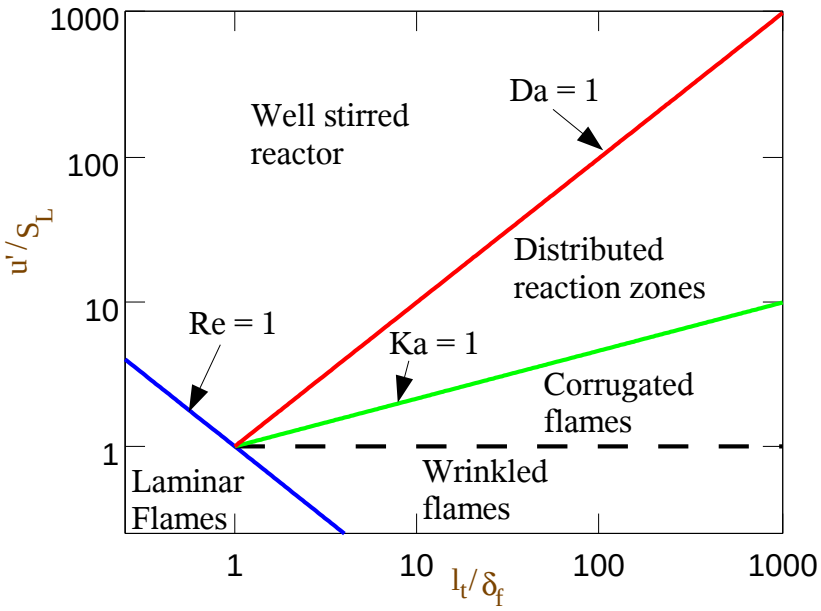

Figure 2.2.1.: **Borghi Diagram.**

The quenching term G is specified in this paragraph. It ensures that the turbulent flame speed remains bounded for high turbulence. For low - medium levels of turbulence with Damköhler numbers: $\mathrm{Da_t} \gg 1$ and Karlovitz numbers: $\mathrm{Ka} < 1$ turbulence enhances the

heat release rate of the combustion due to the wrinkling of the flame. The Damköhler number describes the ratio of the turbulent time scale to the chemical time scale and is defined as: $\mathrm{Da_t} = l_t/u'/\chi_\mathrm{u}/S_L^2$. The Karlovitz number yields the ratio of chemical to the Kolmogorov time scale: $\mathrm{Ka} = \chi_\mathrm{u}/S_L^2/t_\eta$. Thus, it is an indicator, whether the chemical processes are faster than the diffusion processes at the Kolmogorov length scale. To assume a pure enhancement of combustion is only valid while the turbulent eddies are too large to enter the inner reaction zone of the flame. The different regimes are illustrated in a Borghi diagram in Fig. 2.2.1. In the Borghi diagramm, the different lines corresponding to Karlovitz number = 1, to Reynolds number = 1 and, to Damköhler number = 1 are plotted, which allow to characterize separate zones. In case the smallest turbulent structures are able to penetrate the reaction zone of the flame (Ka$\geq$ 1), the combustion is impeded. These regimes are called distributed reaction zones and well stirred reactor which are located above the corrugated flames regime and outside of the laminar flames regime, see Fig. 2.2.1. Under the conditions prevailing in these regimes, flame quenching can occur that may forestall the reaction completely. Zones in a combustor with very intense level of turbulence can be found in the shear layers of the entering fuel and air jets. Consequently, the combustion model needs to distinguish between detrimental and favorable turbulence with respect to the combustion processes. For this reason a quenching term has been added to the correlation for the turbulent flame speed. It does not interfere with its value unless the level of turbulence reaches the quenching limit. The definition of the quenching term, in accordance with Zimont [197] reads:

$$G = \frac{1}{2}\mathrm{erfc}\left[-\sqrt{\frac{1}{2\sigma}}\ln\left(\frac{15\nu g_\mathrm{cr}^2}{\epsilon}+\frac{\sigma}{2}\right)\right] \tag{2.2.16}$$

In Eq. (2.2.16) σ represents the standard deviation of the log-normal distribution of the dissipation which is defined as: $\sigma = 0.28\sqrt{l_t/l_\eta}$ following the proposal of Zimont *et al.* [198]. l_t, l_η correspond to the integral and the Kolmogorov length scales. In Eq. (2.2.16) g_cr is the critical stretch rate and is proportional to the laminar flame speed squared divided by the thermal conductivity at unburnt conditions: $g_{cr} \sim S_L^2/\chi_\mathrm{u}$. The proportionality factor was determined by Polifke *et al.* [135] to be 8.4. G remains unity for low levels of turbulence and approaches zero for turbulence dissipation rates of the order of $15\nu g_\mathrm{cr}^2$.

Since the derivation of the proportionality factor incorporates some uncertainties and, secondly, because the value is not known for most fuels a modeling constant, γ_q, is introduced into Eq. (2.2.16). This yields for the final expression:

$$G = \frac{1}{2}\mathrm{erfc}\left[-\sqrt{\frac{1}{2\sigma}}\ln\left(\frac{15\nu g_\mathrm{cr}^2\,\gamma_q}{\epsilon}+\frac{\sigma}{2}\right)\right] \tag{2.2.17}$$

The factor γ_q increases or decreases the critical dissipation rate, depending whether the flame is affected too much or not enough by turbulence. In later results for the confined jet test case (see Sec. 5.1), the comparison with experimental data points out that the prediction of flame quenching for RANS simulations is well captured without this extra parameter. However, it is also illustrated that the same does not apply for SAS simulations. For SAS simulations, the flame is naturally stretched by the resolved eddies. Consequently, a part of the turbulent spectrum acts directly on the reaction progress. By taking the same quenching factor as for the URANS simulations, the flame is too extensively quenched which results in an underpredicted reaction progress. It is shown that for SAS simulations, employing values of one order higher for γ_q yields a good agreement.

The quenching term is coupled to the value for the turbulent flame speed in the following way:

$$S_T \mathrel{\widehat{=}} G \cdot S_T \tag{2.2.18}$$

2.2.2. Wall Heat Losses

Non-adiabatic walls represent standard boundaries in a combustor. Therefore, it is compulsory to implement the combustion model in such a way that it accounts for wall heat losses. Heat losses affect the energy equation (see Eq. (2.2.14)), however, there is no straight effect on the flame progress variable as opposed to detailed chemistry models. In detailed chemistry models, reaction rates are computed depending on the current local conditions taking changes in the temperature automatically into account. In the TFC model heat losses are not considered straightforwardly since the source term of the reaction progress variable depends on the local unburnt conditions and not directly on the current local conditions. The problem arises through the presence of the laminar flame speed in Eq. (2.2.5), which is a function of the unburnt temperature T_u . The unburnt conditions are difficult to derive once heat is lost at the combustor walls. Under this circumstances, the unburnt temperature cannot be determined by virtue of the mixture fraction and enthalpy. This shall be illustrated by a very simple example: Assuming an initial unburnt temperature of 300 K. In case heat losses of 200 K occur at the wall where the flame connects to the boundary, then reversing the reaction, presuming similar specific heat constants, results in an unburnt state of 100 K for which the laminar flame speed is not defined.

Therefore, to account for heat losses, a correction of the laminar flame speed is introduced. In the extended model implementation, the work of Durand [51] and Wetzel *et al.* [187] is followed. They proposed an enthalpy loss/gain factor for the laminar flame speed which is based on an enthalpy index. The inner layer temperature (T_i) of the adiabatic flame is taken as the reference point for the evaluation. It is obtained from correlations taken

from literature, e.g. [123]. It is argued that once the flame temperature is below the inner layer temperature, the reactions within the flame are disturbed to such an extent that no further flame progress can occur. For flame temperatures in between the adiabatic flame temperature and the inner layer temperature, the enthalpy loss/gain factor takes on values between unity and zero. Two additional temperatures need to be computed. The first one ($T_{\mathrm{ad}_{\mathrm{ref}}}$) corresponds to the adiabatic temperature based on the reference temperature of the domain. The reference temperature is, thus, required as a boundary condition. So far only test cases with inflows and domain being of identical initial temperature have been considered. For complex systems with non-equal inlet and domain temperatures, a further solenoidal transport equation for the initial temperature is needed. The second temperature (T_{ad_l}) is the adiabatic flame temperature computed with the local enthalpy. The reduction factor is then defined as:

$$f_r = \max\left(\frac{T_{\mathrm{ad}_l} - T_i}{T_{\mathrm{ad}_{\mathrm{ref}}} - T_i},\ 0.0\right) \tag{2.2.19}$$

For the resulting laminar flame speed the following equation is evaluated:

$$S_L \ \widehat{=}\ f_r \cdot S_L \tag{2.2.20}$$

The value of the laminar flame speed is multiplied by the reduction factor to yield the final value. For configuration in which all boundaries are adiabatic, the reduction factor will remain unity. In domains where heat losses at the walls occur, the model also captures the phenomena of thermal quenching in case the heat loss at the wall becomes too extensive. Then, the reduction factor approaches zero.

2.2.3. Application to Large Eddy Simulation

In the current development of numerical methods, LES plays an increasingly significant role [145]. LES offers some important advantages as compared to RANS and URANS as it resolves the part of the turbulent spectrum which contains most of the turbulent kinetic energy. In Sec. 2.1.4 the Kolmogorov theory [81] has been elaborated in which the large variety of scales present in a turbulent flow was shown. This requires strong modeling assumptions in a RANS and URANS context, as only scales larger than the integral scale are directly captured. In LES, the modeling assumption are of less influence as scales larger than a certain filter scale Δ are resolved. This reduces the error which enters the calculation by modeling assumptions. Thus, as the energy contained in the smaller scales reduces with nearly the power of two, a decrease of the minimum scale dramatically diminishes the non-resolved turbulent kinetic energy. Nevertheless, a LES model still contains a sub-grid scale model which represents the remaining non-resolved turbulent energy. For simulations with LES the governing equations of the extended TFC model are retained. This is in accordance with the work of Flohr and

Pitch [60]. They remark that the modeling assumptions developed by Zimont [196] are still valid in typical regimes of LES simulations. Their argumentation is based upon the assumption that turbulence wrinkles the laminar flame front. As long as the filter scale in LES is considerably larger than the laminar flame thickness, this condition is still fulfilled.

When applying the extended TFC model to configurations involving very strong turbulence, the turbulent time scale t_t approaches the chemical time scale t_c. The arising similarity of time scales has a significant effect on the combustion processes. This stems from the fact that the smallest eddies of the size of the Kolmogorov scale can enter the inner flame zone in which the reactions take place (see Sec. 2.2.1). Thus, the former undisturbedness of chemical processes which broke-up molecules, recombined them and formed reactants, intermediate species and products is no longer given. This is accounted for in the original TFC model be introducing a quenching factor (see Eq. (2.2.17)). For standard RANS and URANS simulation this approach yields good results. In the scope of this thesis, the SAS model (see Sec. 2.1.5), has been applied to configurations which exhibit high levels of turbulence. This model shifts seamlessly from a LES to a URANS mode and vice versa [55, 115]. It is observed that in LES mode, quenching effects are overpredicted which leads to a too extensive quenching of flame. It was found that a value of 10 for proportionality factor γ_q is adequate which increases the critical strain rate. By raising the critical strain rate a good agreement was obtained for the simulation of a highly turbulent enclosed jet (see Sec. 5.1). A higher value for γ_q to raise the critical stretch rate in the SAS simulation is needed as the resolved turbulent large scale eddies implicitly stretch the reaction progress variable which requires a lower contribution from the quenching term.

2.2.4. Ignition Modeling

This part provides a detailed background of the ignition modeling approach. Here, the term ignition relates to the action of energy deposition within the domain through an ignition device, such as a laser or an electric spark plug. The integration of the ignition process in the combustion model was derived in the previous section, see Eq. (2.2.4). By extending the reaction progress variable transport equation with a secondary term, the value of the reaction progress variable increases when the prevailing conditions allow an auto-ignition of the mixture. The ignition energy represents the heat source which induces the necessary temperature raise up to conditions at which auto-ignition can occur. Due to the enormously concentrated energy provided by the ignition device within a very confined volume, local "temperatures" (although it might not be the standard definition of temperature) over several thousands of Kelvin can occur [28, 102, 103, 104]. This forces the gas to change into a plasma state, which follows the rules of plasma physics. During these initial instances in the range of nano- to micro-seconds, radicals are formed. These highly active and/or catalytic elements provoke two major phenomena. The first one is that chemical processes are significantly accelerated.

This leads to elevated flame speeds as compared to typical flame speeds at the local conditions, see e.g. Bradley*et al.* [29]. Secondly, caused by the high temperature gradients, the flow field is profoundly altered. It is reported that the ignition triggered by a short spark or laser pulse results in a toroidal shaped structure [29, 82, 83]. This toroidal structure evolves and generates an inner flow which also influences the conditions in the ignition volume.

Since the complexity and the highly non-standard flow phenomena associated with the "real" ignition energy release forbid a direct modeling approach within the time- and length scales typical for a CFD solver, a phenomenological methodology is introduced. The spark model which has been applied in the scope of this work is based upon a homogeneous heat release within a defined ignition volume. In the simulated test cases, the released effective energy is known a priori. This energy can be distributed uniformly in the designated ignition zone. For single flow computations, the ignition is modeled by imposing an elevated temperature for the corresponding ignition volume. The necessary energy for the volumetric temperature raise is computed in such manner that it equals the measured effective transferred energy in the experiment. Thus, by prescribing an ignition temperature in correlation with an ignition volume, the delivered energy to the domain between experiment and simulation are of identical order. This is described in more detail in the respective test case sections, see Sec. 4.2.2. The representation of the ignition energy in the above elaborated manner, allows an approximation of the real processes. It is supported by two observations. The physical processes, e.g. the temperature increase, occur almost instantaneously, as illustrated in Fig. 2.2.2. There, due to immense heat losses caused by radiation, shock wave generation and losses at the electrodes for a spark plug, the extensive initial temperatures abate quickly [28, 98, 102]. Therefore, in a numerical simulation where the time steps are of the order of several μs, the presumption that the ignition temperature has decreased to the order of typical adiabatic flame temperatures is justified. Secondly, the developing flow field structures at the edges of the ignition kernel, see e.g [29, 102], lead to enhanced mixing processes. This further mitigates large gradients and promotes the assumption of a homogeneous temperature distribution.

In the test cases concerning the enclosed jet, see Sec. 5.1 and the spray flame, see Sec. 6.2, a slightly more sophisticated ignition approximation has been applied. In an analysis of the results for the methane jet configuration, see Sec. 4.2, it appeared that the gas expansion effects of the ignition kernel which induce a flow field pointing outwards of the ignition kernel can be of importance. Thus, for the studies of the enclosed jet and the spray flame, the ignition energy is not provided to the domain in one time step. A period is defined during which the effective energy is delivered to the domain. This allows that heat convection during the ignition kernel development can be captured as well. Both chosen simplified approach comply with the solver framework in the sense that the maximum temperatures and densities remain

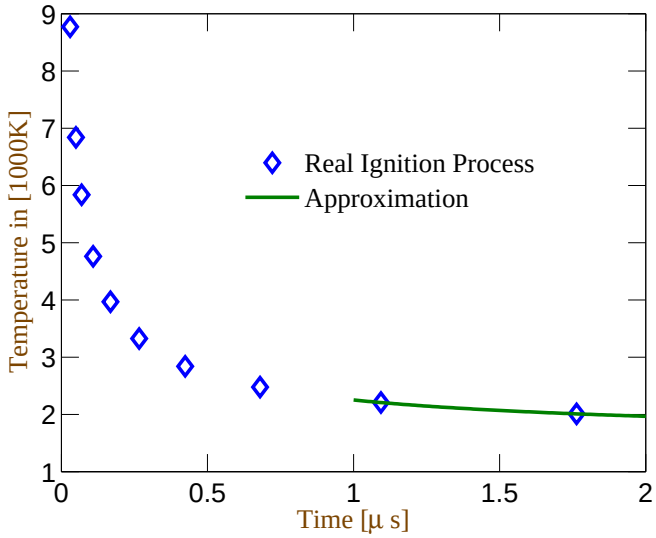

Figure 2.2.2.: **Schematic representation of the temperature course following the ignition by a technical ignition device and the ideal approximation by the numerical approach.**

below plasma states which allows to describe the flow field with the standard Navier-Stokes equations. The employed modeling strategy is similar to widely acknowledged schemes, such as the ED (Energy Deposition) model which has been successfully applied to forced ignition test cases by Chakraborty *et al.* [33] and Lacaze *et al.* [87, 88]. It is also in analogy to an approach proposed by Kravchik and Sher [84] and to modeling assumptions which were established within the automotive industry to treat spark discharges in conventional diesel engines [133].

In case ignition occurs in a multiphase flow, also implications on the liquid phase need to be captured by the CFD solver. Experimental observations reveal that the generated shock wave which is a results of the extreme temperatures, induces a secondary break-up of the droplets [64, 65]. It is found that the droplet diameter decreases considerably in the vicinity of the laser pulse location. This effect is observed in experimental measurements performed by Mosbach and Gebel [121] and is investigated more thoroughly by Gebel *et al.* [65]. The impact of the laser pulse on the flow field and the droplet distribution is perceivable in Fig. 2.2.3, derived from the experimental investigation of the droplet chain flame (Sec. 6.1).

The intensity contour plot (left hand side) of the fuel vapor shows a gap in the droplet streams after only 0.5 μs in the region where the laser-induced breakdown has occurred. This is in accordance with the findings of Gebel *et al.* [64, 65] showing that the droplet evaporation times are considerably shortened as a result of the secondary break-up. Through the break-up into smaller droplets, the surface of the liquid phase has multiplied. The effective liquid phase surface scales linearly with the inverse of the radius. Through the secondary break-up

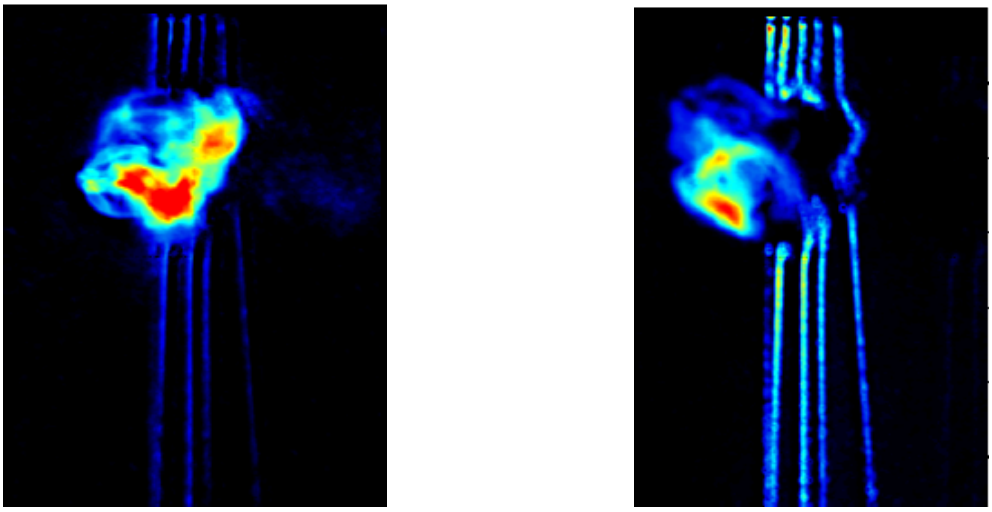

(a) (b)

Figure 2.2.3.: **a) Fuel vapor contour plot and b) OH-distribution of the droplet chain test case, see Mosbach and Gebel [121], 0.5 ms after the laser pulse. The view range length corresponds to the nozzle exit plane to 30 mm downstream position in axial direction. The laser beam direction is from left to right with a slight inclination with respect to the horizontal axis.**

the droplet diameter decreases from 100 μm to 1-5 μm which is a reduction by a factor of 20 up to 100. Another phenomenon is visible on the right hand side in which the OH-field generated by the laser pulse is displayed. The ignition process induces a flow field which points in the direction of the laser pulse as was also observed by Bradley *et. al* [29]. This effect has not been incorporated in the spark representation which leads to small deviations in the flame center movement within the first time instances, see Sec. 6.1.2.4. To account for the almost instantaneous droplet evaporation, a parameter (f_e) has been included in the spark model which defines the fraction of liquid mass currently present in the ignition volume which is instantaneously converted into fuel vapor (see further below in Eq. (2.2.23)). On the droplet side, to account for the evaporated mass, a recalculation of the droplet diameter in the ignition volume is performed. Here it is assumed that all droplets contribute equally to the fuel vapor mass which leads to a respective decrease in the droplet size:

$$V_1 = f_e V_0. \tag{2.2.21}$$

with V being the volume of the droplet and with index 1 representing the state after ignition and 0 referring to the state prior to ignition. Subsequently, assuming spherical droplets, the change in radius for a single droplet can be expressed as:

$$\frac{r_1}{r_0} = f_e^{\frac{1}{3}}. \tag{2.2.22}$$

The value of f_e for the vaporization fraction is obtained by a comparison of the ignition probability results between experiment and simulation. A correct fraction parameter results in a good agreement concerning the corresponding ignitability results. Values ranging between 0% and 20% gave a good approximation for all investigated test cases. The subsequent flame development is largely independent of the initial fuel vapor mass, see Sec. 6.1. It is shown that a flame initiated with two different liquid fuel vaporization fractions, behaves nearly identical with respect to volume and location of the flame kernel at later stages.

The energy which is required for the vaporization of the droplets has to be subtracted from the total available effective energy delivered by the ignition device, so that the total effective energy represents the sum of vaporization plus heating energy. This yields:

$$E_{\text{eff,exp.}} = E_h + E_e = V_\text{s} \cdot (\rho_1 h_1 - \rho_0 h_0) + f_e \cdot h_e m_\text{l} \,, \tag{2.2.23}$$

with f_e denoting the mass fraction of liquid fuel contained in the ignition volume which evaporates and V_s , the volume in which the ignition takes place. h_1, h_0 constitute the specific enthalpy after ignition and prior to ignition, respectively, and ρ_1 and ρ_0 the respective densities. Furthermore, h_e represents the specific evaporation enthalpy of the employed fuel whereas E_e, E_h, $E_{\text{eff,exp.}}$ constitute the evaporation, heating energy and, total effective energy as determined in the experiment.

In conclusion, although the CFD solver is not capable of reproducing the physical temperature evolution as it involves peak temperatures which are outside the limits of the physics captured by the implemented models, appropriate conditions after a typical time step of the simulation can be imposed. Consequently, the initiation of the simulation with a finite temperature and an imposed vapor concentration, represents an adequate approximation which is underlined by the good agreement for all considered test cases.

2.2.5. Polynomials

2.2.5.1. Laminar Flame Speed

This short paragraph contains the methods which were employed to derive the polynomials for the laminar flame speed. A multitude of high accuracy values for the laminar flame speed are needed to establish a valid correlation for the description of these data points. The approach employed in this work for the computation of the nodal points is based on a one-dimensional laminar premixed flame configuration. Several authors, for example Grcar *et al.* [70], Peters [128] and Smooke *et al.* [164] have established valuable knowledge on this field. The underlying equations have the following form:

$$\dot{m} = \rho u A = \text{constant} \tag{2.2.24}$$

$$\dot{m}\frac{\partial T}{\partial x} - \frac{1}{c_p}\frac{\partial}{\partial x}\left(\lambda A \frac{\partial T}{\partial x}\right) + \frac{A}{c_p}\sum_{i=1}^{n}\rho Y_i D_{\mathrm{Y},i} c_{p_i}\frac{\partial T}{\partial x} + \frac{A}{c_p}\sum_{i=1}^{n}\dot{\omega}_i h_i M_i = 0 \tag{2.2.25}$$

$$\dot{m}\frac{\partial Y_i}{\partial x} + \frac{\partial}{\partial x}\left(\rho A Y_i D_{\mathrm{Y},i}\right) - A\dot{\omega}_i M_i = 0 \ (i = 1, \ ..., \ n) \tag{2.2.26}$$

The objective is to find the eigenvalue of $\dot{m}$ which solves the above stated system of equations. For this reason, boundary conditions and an appropriate discretization are necessary. Details on this procedure can be found in Smooke *et al.* [164]. As the whole problem is very sensitive to the initial guess, a multi-staged approach, corresponding to the one proposed by Smooke *et al.* [164] is utilized. The different steps until a converged solution is obtained, can be categorized as:

- 1. Derivation of an initial "cold" solution with a fixed temperature profile and a fixed mass flow. Grid points are inserted at intervals with large fluctuation in each iteration.
- 2. Determination of an initial solution with the chemical reaction turned on. Receipt of a first good guess for further "hot" iterations.
- Continue refining the grid in sections with large deviations until a stable converged solution has been reached.

Through this method, which is implemented in the Cantera code [69], values for the laminar flame speed can be obtained for a desired equivalence, pressure and temperature range. These values are used as nodal points in a subsequent least squares fit function. Concerning the final coefficients of the polynomials, the reader is referred to Appendix A with an evaluation of the accuracy.

2.2.5.2. Ignition Delay Time

The solution process for the ignition delay time is based on the assumption of a perfectly stirred reactor. For the evolution of the chemical reactions a finite rate chemistry solver is employed. Some of the fundamental equations, underlying the approach are described shortly. For any chemical systems, a problem involving n unknowns for the n species and the temperature, whereby the last species can be calculated by $Y_n = \sum_1^{n-1} Y_i$ and m reactions is faced. The entity of unknowns can be written as:

$$\Psi = \begin{Bmatrix} Y \\ h \end{Bmatrix} \tag{2.2.27}$$

In order to increase stability an implicit approach was chosen which also helps to avoid problems with very small time step sizes necessary in an explicit scheme. Thus, this yields

for the ith source term:

$$\omega_i(\Psi^{t+\Delta t}) = \omega_i\left(\Psi^t\right) + \frac{\partial \omega_i}{\partial \Psi}\Delta\Psi + O(||\Delta\Psi||^2) \tag{2.2.28}$$

where $\frac{\partial \omega_i}{\partial \Psi}$ is the i-th line of the Jacobian matrix, calculated at time t. At this point the solution at the new time step can be obtained by performing:

$$\Psi_i^{t+\Delta t} = \Psi_i^t + \omega_i \Delta t \tag{2.2.29}$$

for each unknown. More details on this topic can be found in the work of Di Domenico [42] and Gerlinger [66]. With accurately defined initial conditions, the chemical reaction is started at the time $t = 0$ s with the purpose of extracting the position of the largest incline in the temperature profile. The slow increase shortly before the intense exothermal reaction starts does not influence the procedure neither does the slow balancing-out of the last reactions. By determining the occurrence of the sharpest increase in the profile, an exact value of the ignition delay time for a corresponding data set of T, ϕ and p can be derived.

2.3. Multiphase Flow Solver

Since combustion in aircraft engines is invariably linked to liquid fuel injection, the treatment of multiphase flows is a fundamental part of the numerical approach. In the course of this thesis, a software package called SPRAYSIM has been employed, which has been developed and tested at the DLR under the care of Michael Rachner. The underlying theories, the solver characteristics and the associated abilities of the code are the aspects this paragraph aims at describing.

2.3.1. Lagrangian Approach

For the modeling of the liquid phase, a variety of numerical techniques is available, see Frank [61]. The Eulerian method, in analogy to the transport equations of the gas flow solver, treats the liquid as a continuous phase, see. e.g. Grupta and Bracco [72]. The Lagrangian approach, with a detailed description given in Dukowicz [49], constitutes the opposite practice by treating the droplets as discrete particles within the continuous gaseous phase. In-between these contrary techniques, intermediate models such as the ICAS (Interactive Cross-sectional Averaged Spray model) [182, 183] and other more detailed methods, such as the VOF (Volume of Fluid) in combination with a level set method, exist [74, 99, 155]. These methods are for DNS for a few particles which is not the focus of this work. The advantage of using an Eulerian-Lagrangian framework is the natural description of the droplets and the direct computation of associated properties such as e.g. temperature and velocity. The benefit of an Eulerian-Eulerian methodology lies within the compliance with the already existing solver framework. No additional scheme to track single fluid particles is needed. However, for an

Eulerian approach, Stiesch [169] remarked that the resolution of all parameters governing the behavior of the liquid phase in the entire domain leads to a drastic incline of the computational effort. This is justified in cases where the emphasis is on researching fundamentals of single droplets evaluation or break-up and atomization phenomena [95, 99]. Secondly, an Eulerian approach is appropriate in cases for which the liquid volume fraction is high throughout the domain. In the framework of numerical simulations of combustion chambers in technical applications, the focus is on the macroscopic effect of the droplets such as e.g. the fuel vapor distribution in the domain. Except close to the nozzle exit, where the spray (an explanation is given below) is still dense, the liquid volume fraction (the ratio of liquid volume in a cell to the cell volume) takes on small values [127, 141]. The same reasoning excludes the use of more sophisticated models which also focus on modeling the boundary between liquid and gaseous phase, which is not the primary intention and entails a high computational effort. A spray is a polydisperse distribution of a multitude of droplets. The high number of droplets entering the domain renders the transport of all droplets and the associated properties too expensive. This has lead to the representation of droplets contained within the spray by a multitude of discrete liquid computational particles (called parcels) by a Lagrangian approach. This retains the straightforwardness of the modeling approach of the physical processes at the particle level and mitigates the computational costs, as only a distinct number of parcels (each representing a certain number of real particles) is transported. Thus, the set of governing equations (ordinary differential equations) needs to be solved solely for each parcel present in the domain.

Below, the fundamental equations of the liquid solver for the parcels' motion shall be outlined. The spatial evolution of a single parcel in the Lagrangian framework can be expressed, following Stiesch [169], as:

$$\frac{d}{dt}\vec{x}_{\mathrm{p}} = \vec{u}_{\mathrm{p}} \,. \tag{2.3.1}$$

The change in velocity of each parcel is given by:

$$\frac{d}{dt}\vec{u}_{\mathrm{p}} = \vec{F}/m, \tag{2.3.2}$$

where $\vec{F}$ represents all forces acting upon the fluid particle. By means of these two equations, parcels are tracked within the domain. The major impact on the motion of a parcel originates from the gravity force and the drag force exerted by the continuous phase. The gravity force on a parcel is described through:

$$\vec{F}_g = 1/6\pi D_{\mathrm{p}}^2 \, \rho_{\mathrm{p}} \, \vec{g}. \tag{2.3.3}$$

The drag force depends on the mean Stokes number computed with Eq. (2.3.5). The drag

significantly influences the droplet velocity. It is quantified by:

$$\vec{F}_{\mathrm{D}} = \frac{1}{2}\rho_{\mathrm{g}}\, C_D A_{\mathrm{p}} \cdot |\vec{u}_{\mathrm{p}} - \vec{u}_{\mathrm{g}}| \cdot (\vec{u}_{\mathrm{p}} - \vec{u}_{\mathrm{g}}). \tag{2.3.4}$$

The indices p and g relate to parcel and gas properties, respectively. In Eq. (2.3.4) A_{p} resembles the frontal area of the droplet which is subject to changes due to deformation caused by the drag. The coefficient C_D in Eq. (2.3.4) for the drag computation is obtained from empirical correlations relating it to the parcel Reynolds number defined in Eq. (2.3.8) and the Weber number, see Eq. (2.3.9). The empirical correlations employed in SPRAYSIM can be found in [36]. The drag coefficient allows to determine the drag force as one of the major forces needed in Eq. (2.3.2) for the droplet motion.

Along with the equations for the parcel location and velocity, equations for the parcel diameter D_{p} and the parcel temperature T_{p} in order to account for heating and evaporation of droplets need to be solved. Furthermore, in test cases where multicomponent fuels (fuels consisting of more than one liquid species) are considered, additional ODEs (ordinary differential equations) concerning the liquid fuel composition appear. This framework is described in the next paragraph.

Most test cases are inherently transient in which the number of droplets continuously changes, on the one hand due to the generation of new parcels at the injector and on the other hand, due to droplets being fully evaporated or leaving the domain. This is accounted for by the generation of new parcels at the nozzle and by stopping the parcel tracking outside the computational domain.

In summary, the above equations capture the intrinsic motion of the parcels. Combined with equations for the parcel diameter and temperature, a complete description of the liquid phase is achieved. As a consequence thereof, the exact location of the parcel, its velocity, diameter and temperature are known at each solver time step which allows a formulation of spray feedback source terms for the continuous phase. In turn, the gas phase influences the parcel by the gas-field values at the parcel location. This is called two-way coupling and is implemented in the liquid and continuous phase solver.

2.3.2. Continuous Thermodynamics Model

The previous correlation for the droplet momentum in Eq. (2.3.2) is independent of whether the liquid phase is described as a single component or as a complex mixture of different species. However, the evolution of the droplet diameter directly relates to the physical properties which underlie the droplet modeling. Commonly, the liquid phase in a combustor is represented by a single-component fuel, see e.g. [170, 193, 195]. This is sufficient for many academic test cases [63, 146, 152]. However, applications for aircraft gas turbines usually comprise more complex fuels with a multitude of components, see e.g. [181], that contribute

to the overall characteristics of the fuel. The modeling of the fuel can have a significant effect upon the evaporation behavior of the droplets [52, 92, 140] and thus influence ignition characteristics and more generally the kinetics of the flame. As an approach based on continuous thermodynamics (CT) is employed for the studied multiphase test cases, the basics of the method shall be outlined in the present section.

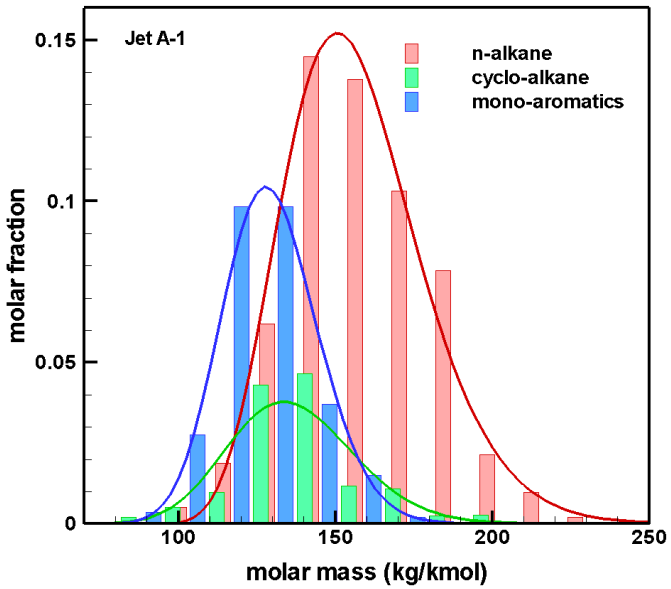

Figure 2.3.1.: **Molar fraction distribution for the different components of Jet A-1, see Le Clercq *et al.* [94].**

Treating the fuel statistically by means of dividing the discrete species of the fuel in component families offers the advantage, that the computational burden associated with a transport of all involved discrete species can be reduced to a great extent [46, 47, 93, 94].

Fig. 2.3.1 highlights the composition of kerosene Jet A-1 which is obtained by a gas chromatography [181]. This demonstrates the large bandwidth of species in common aviation fuels. By an analysis of the composition and in order to find a suitable compromise between accuracy and computational effort, only three out of the initially six component families are retained, as proposed by Le Clercq *et al.* [93]. By neglecting families with small mass fraction and additionally merging the iso-alkanes with the n-alkanes, three resulting families as depicted in Fig. 2.3.1 are obtained. According to Le Clercq *et al.* [93], the initial composition of each of the remaining families can be achieved with good accuracy by a Γ-PDF, see Fig. 2.3.1.

In this work, the droplet evaporation is modeled with the diffusion-controlled model as for example presented in Sirignano [156]. The derivation of this more comprehensive and stable model framework is given in Abramzon and Sirignano [1]. Following their approach, equations for the evolution of the droplet diameter, the droplet temperature and the respective

mass fraction of each of the component families can be derived. These equations complete the liquid phase modeling and allow a description of the temperature and droplet diameter evolution.

2.3.3. Non-dimensional numbers for multiphase flows

An important means to analyze flow conditions for multiphase flows are non-dimensional characteristic numbers. Therefore, the numbers which are used for the classification of the test cases shall be outlined here.

2.3.3.1. Stokes Number

To assess the influence of the gas phase on the motion of the droplets can be very decisive in some cases, as the gas phase might or might not be the governing factor for some configurations. Hence, under certain circumstances, an error in the gaseous flow field without droplets might not even alter the path of the particles as they are independent of the gas field velocities. This is quantified by the Stokes number, which describes the ratio of the particle relaxation time (τ) to a characteristic flow time (t_g).

$$\mathrm{St} = \frac{\tau}{t_\mathrm{g}} \tag{2.3.5}$$

Hence, if the particle relaxation time is very high, the flow field influence on these particles is considerably weakened. The particle relaxation time is derived from the equation of motion (see Eq. (2.3.4)) for a single particle:

$$\rho_\mathrm{l}\, V_\mathrm{p}\, \vec{F}_D = \frac{1}{2}\rho_\mathrm{g}\, C_D A_\mathrm{p}\, \cdot (\vec{u}_\mathrm{p}\, - \vec{u}_\mathrm{g}\,)^2, \tag{2.3.6}$$

with A_p being the frontal area of the particle. Consequently, the relaxation time is expressed as:

$$\tau = \frac{8}{3}\frac{\rho_\mathrm{l}\, r_\mathrm{p}}{\rho_\mathrm{g}\, C_D |\vec{u}_\mathrm{p}\, - \vec{u}_\mathrm{g}\,|}, \tag{2.3.7}$$

where r_p refers to the particle radius. For C_D a value obtained in analogy to the provided correlation in the previous subsection needs to be given. A characteristic time scale for the flow might be the path length for which the influence of the gas field needs to be estimated divided by the transit velocity of the particle. Stokes numbers ≥ 1 correspond to droplets that are marginally influenced by the gas flow field, whereas Stokes number far smaller than one characterize conditions in which the particle motion is strongly dependent on the gas flow field. In a turbulent flow, the turbulent time scale (Kolmogorov time scale) is also used when evaluating the particle interaction with turbulent structures (droplet dispersion). Thus, the expression which is used for the characteristic flow time scale depends on the focus of the analysis, whether the influence of the mean flow or the influence of the turbulent dispersion

is of interest.

2.3.3.2. Parcel Reynolds Number

The parcel Reynolds number describes the ratio of momentum forces to viscous forces acting on the particles. This is employed to define several flow field regimes for which a characteristic break-up behavior of the liquid particles is derived. The parcel Reynolds number is expressed as:

$$\mathrm{Re_p} = \frac{2r_\mathrm{p}\,\rho_\mathrm{g}\,|\vec{u}_\mathrm{g} - \vec{u}_\mathrm{p}\,|}{\mu_\mathrm{g}} \tag{2.3.8}$$

2.3.3.3. Weber Number

The Weber number provides a measure of the relative importance of the fluid's inertia compared to its surface tension. The quantity is useful in analyzing break-up phenomena of droplets and bubbles.

$$\mathrm{We} = \frac{\rho_l v_\mathrm{rel}^2\, D_\mathrm{p}}{\sigma_\mathrm{l}} \tag{2.3.9}$$

3. Combustion Model Validation: Simulation of Simple Flows

In this paragraph, numerical results for basic test cases are presented to ascertain the physical integrity and accuracy of the model. The overall complexity of the first numerical studies is kept at an elementary level to focus on specific aspects of the model. The validation begins with verifying the model's behavior for steady laminar flames. For this reason, results concerning a stationary simulation of a Bunsen flame are shown. In order to prove the correct model prediction concerning transient processes, a spherical propagating flame is examined next. Subsequently, two further configuration are presented. One demonstrates the correct mixing behavior for a fully burnt flow with an unburnt co-flow. The second configuration focuses on the modeling of multiphase flows for which the laminar flame speed is determined in the simulation and compared to results from the literature. The last test case illustrates the model capabilities in a turbulent environment. It is shown that the enhancing effects of moderate turbulence on the flame growth are captured and that the flow-field is considerably influenced by the propagating flame.

3.1. Laminar Flame Propagation

This section evaluates the model ability for well characterized laminar test cases in which the laminar flame speed can be derived in a post analysis step. Several methods to determine the laminar flame speeds by experimental means exist [68, 149, 171, 178]. Values obtained from those measurements for the laminar flame speed are taken as reference for the comparison with the numerical results. The term "laminar flame speed" refers to the speed of a planar laminar flame front that travels relative to the unburnt gas in a direction normal to the flame surface.

In this work, the focus is on two specific configurations, the Bunsen burner flame and the constant volume bomb set-up which have been meshed for the numerical representation. For both assemblies exact correlations are available which allow a deduction of the laminar flame speed from the obtained results. The Bunsen burner configuration is used to validate the model for stationary test cases. In the constant volume bomb set-up, the flame propagates outwardly which allows to validate the model for transient applications.

3.1.1. Bunsen Burner

The Bunsen burner configuration as means to derive laminar flame speeds has been employed in experimental studies for example by Natarajan [124] and Günther and Janisch [68]. In this set-up, an axisymmetric conical premixed flame which stabilizes on the lip of the burner exit is investigated. The flame speed is eventually inferred from either the flame area or the flame angle. In the validation, the flame angle method as described for example in Liberman [101] is utilized. Consequently, from the flame angle which finally evolves in the simulation, the corresponding laminar flame speed is determined, see e.g. [101, 130], which allows a straightforward comparison to the theoretical results. The employed numerical domain is a axisymmetric grid of two co-axially aligned tubes, see Fig. 3.1.1 with the boundary conditions prescribed according to Table 3.1.

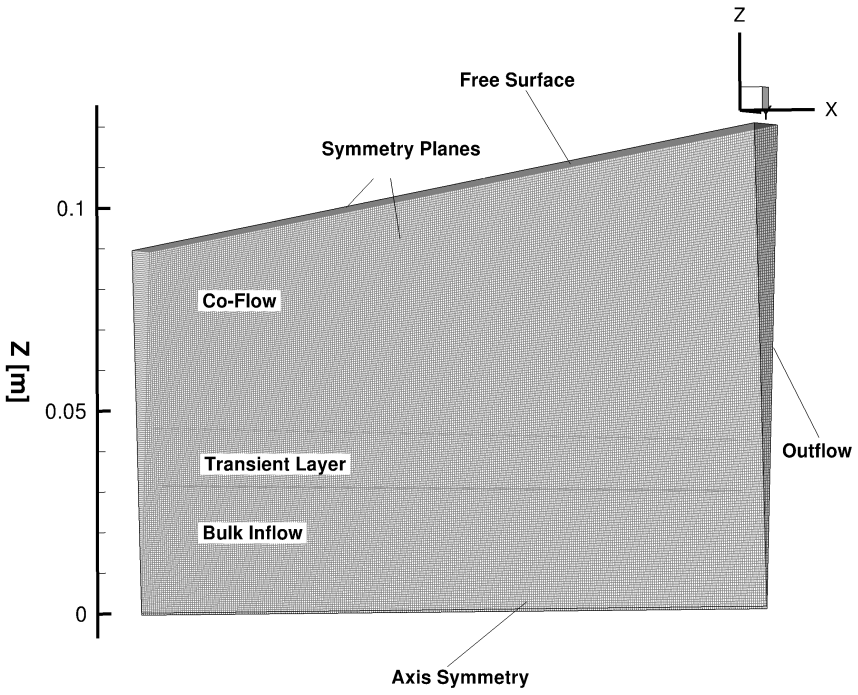

Figure 3.1.1.: **Schematic illustration of the Bunsen burner domain.**

Concerning the inlet boundary conditions, a transition layer is introduced which slowly reduces the velocity from the inner tube to the velocity of the outer tube which improves the solver convergence and behavior. The flame in the simulation attaches approximately at the position at which the prescribed inflow velocity is of the same magnitude as the laminar flame speed. Note that the flame position is not the validation criterion but rather the cone angle which is relative to S_L.

Three grid configurations have been tested to validate the model against grid dependency.

Table 3.1.: **Boundary conditions of the Bunsen burner configuration.**

Inlet	Outer Tube	$y > 0.045$	u: 0.1 m/s
		$Y_{CH_4} = 0.0$	$T = 300$ K
	Trans. Zone	$0.045 > y > 0.03$	u: 0.1 - 0.8 m/s
		$Y_{CH_4} = 0.055$	$T = 300$ K
	Inner Tube	$0.03 > y > 0.0$	u: 0.8 m/s
		$Y_{CH_4} = 0.055$	$T = 300$ K
Outflow	Pressure Outlet		
Symmetry	Symmetry condition on both sides		
Walls	Adiabatic no-slip walls		

Table 3.2.: **Grid configurations for the Bunsen burner test case to verify the grid independency of the extended TFC model.**

Test Case No.	Grid Dimensions
1	161x91 Nodes
2	322x182 Nodes
3	644x364 Nodes

For a second grid independency validation of the model, the reader is referred to [194]. Table 3.2 lists the different test cases. The outcome of the respective simulations exhibits the features as displayed in Figure 3.1.2.
At the central inflow the flame cannot attach as the prevailing mean flow velocity exceeds the laminar flame speed. Consequently, a Bunsen flame cone develops which allows a derivation of the laminar flame speed of the mixture. The relationship between laminar flame speed and Bunsen burner exit velocity reads:

$$S_{\mathrm{L,u}} = v_{\mathrm{u}} \sin\alpha. \tag{3.1.1}$$

$S_{\mathrm{L,u}}$ represent the laminar flame speed of the unburnt mixture and α denotes the opening angle of the Bunsen cone as schematically illustrated in Fig. 3.1.3. For an inlet velocity of 0.8 m/s and a stoichiometric methane/air mixture at 300 K, which has a laminar flame speed of ~ 0.41 m/s according to Müller *et al.* [123], the analytically derived angle equals 31°. The resulting angle in the simulation has been calculated by employing the following procedure:

- Extract cut-plane from converged solution in the domain center ($y = 0$).
- Post-process data file and extract lowest position with respect to z at which the flame progress variable $c = 0.05$.
- Regress x, z data of these data points with a linear function.
- Slope of the linear function corresponds to the angle of the Bunsen burner cone.

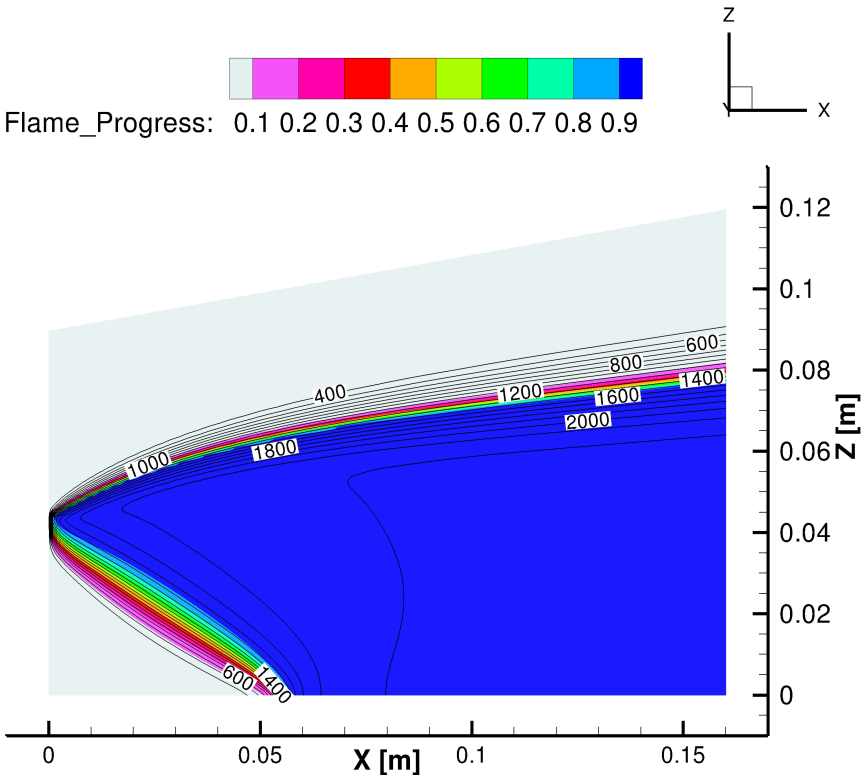

Figure 3.1.2.: **Contour plot of the flame progress variable for the bunsen burner configuration. The iso-lines relate to the computed temperature.**

Table 3.3.: **Bunsen burner angle of the corresponding grid resolution.**

Test Case No.	Computed Angle	$S_{L,\mathrm{u}}$
1	33.6°	0.443 m/s
2	31.2°	0.414 m/s
3	31.2°	0.414 m/s

The procedure has been applied to all three grid configurations which gave the results for the cone angle and the respective laminar flame speed as provided in Table 3.3.

For all grids a very satisfying agreement with the theoretical value is achieved. Moreover, it is demonstrated that the model is consistent despite grid variations and can pertain the high accuracy on coarse grids as well. The results also show that the extended model does not suffer from the inhomogeneities associated with the standard TFC-model in which only the mixture fraction is transported. Under this circumstances the temperature at the shear layer where the jet mixes with the surrounding air is difficult to derive. The flame progress in this region drops to zero, as a consequence of the mixture being too lean to burn, which entrails a very steep non-physical temperature decrease. This originates from the fact that in the original TFC model the flame progress is not subject to laminar diffusion which implicitly sustains high gradients. Since the temperature is directly coupled to the mixture fraction and flame progress, see e.g. Polifke *et al.* [135], this leads to rather unphysical abrupt temperature

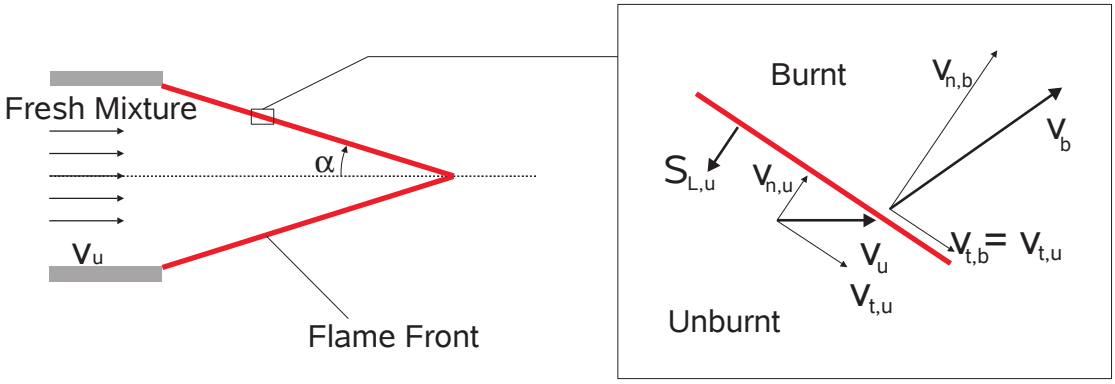

Figure 3.1.3.: **Schematic illustration of the velocity correlation for a Bunsen burner flame.**

declines. This drawback is resolved by the extended model formulation which couples the temperature to the enthalpy and to the present major species. As the transport equation for the major species includes a laminar diffusion term, this leads to a smooth temperature distribution in the vicinity of the flame front. This capability is essential for the model in order to describe the proper laminar flame behavior. Laminar test case can be still regarded as challenging even for more complex models [39] as the diffusion of the species and the reaction mechanism need to be very precise to achieve a good agreement.

3.1.2. Spherical Flame

A second established method to investigate the laminar flame speed is the constant volume method which has been applied for example by McLean *et al.* [112] and Sun *et al.* [172]. With this approach the laminar flame speed is deduced from the spherical expansion of the flame front. In contrast to the bunsen burner configuration which relies on a steady state to measure the flame speed, the constant volume method is entirely unsteady. Therefore, it can be employed to validate the model behavior under transient conditions.

The mesh which is employed for the simulations is depicted in Fig. 3.1.4 with the corresponding boundary conditions as specified in Table 3.4. The number of grid points equals $\sim$ 493,000. The ignition is carried out by prescribing a flame progress of 1.0 for an initial spherical volume with radius 5 mm. This prevents additional energy typically present at forced ignition by a heat source from influencing the flame propagation. The ignition energy leads to enhanced laminar flame speeds [29] within the first milli seconds which impedes the analysis.

The flame speed is evaluated for three sets of imposed boundary conditions. The distance is extracted from the initial diameter of the kernel to the averaged diameter of later time instances which allows to deduce the propagation speed of the flame front. The procedure

Table 3.4.: **Boundary conditions of the spherical flame configuration.**

Sphere Edges	Pressure Outlet
Mixture Composition	$Y_{CH_4} = 0.55$, $Y_{O_2} = 0.215$, $Y_{N_2} = 0.73$
Temperature	$T = 300$ K

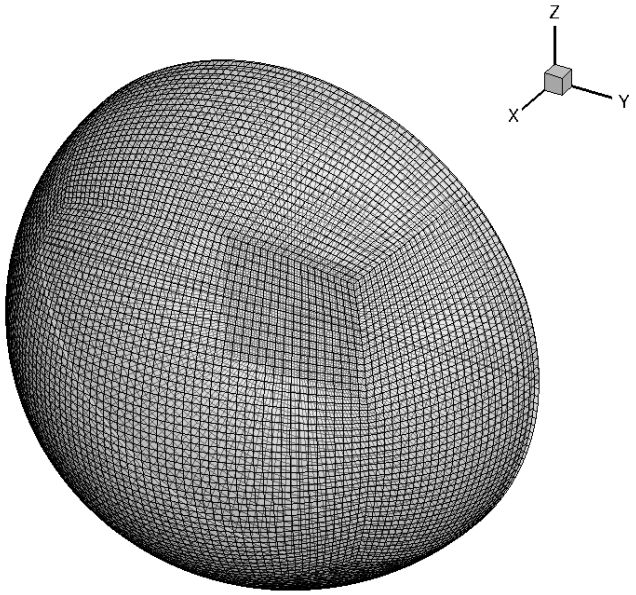

Figure 3.1.4.: **Illustration of the spherical mesh for the constant volume validation test case. Domain radius: 0.1 m**

is highlighted in Fig. 3.1.5. In this configuration gas expansion effects induced by the temperature increase through combustion play a significant role. Therefore, the laminar flame speed (S_L) does not correspond to the propagation speed (S_F) of the flame front, as the flame growth also involves a contribution from the gas expansion. The laminar flame speed can be extracted from the propagation speed through the following correlation:

$$S_{\mathrm{L}} = \frac{\Delta x}{\Delta t} \cdot \left(\frac{T_1}{T_2} \right) \tag{3.1.2}$$

where T_1 and T_2 denote the ambient temperature and the adiabatic flame temperature.

Table 3.5.: **Flame propagation speed and resulting laminar flame speed for three different equivalence ratios ($\Phi = 0.7$, $\Phi = 1.0$, $\Phi = 1.4$).**

Φ	Flame Edge Speed	Corrected (with $\mathscr{L}$) Flame Edge Speed	$S_{L,u}$	Theoretical Value	T_{cold}	$T_{\mathrm{ad.}}$
0.7	1.12 m/s	1.17 m/s	0.190 m/s	0.199 m/s	300 K	1846 K
1.0	2.92 m/s	3.05 m/s	0.399 m/s	0.402 m/s	300 K	2288 K
1.4	1.10 m/s	1.15 m/s	0.157 m/s	0.167 m/s	300 K	2195 K

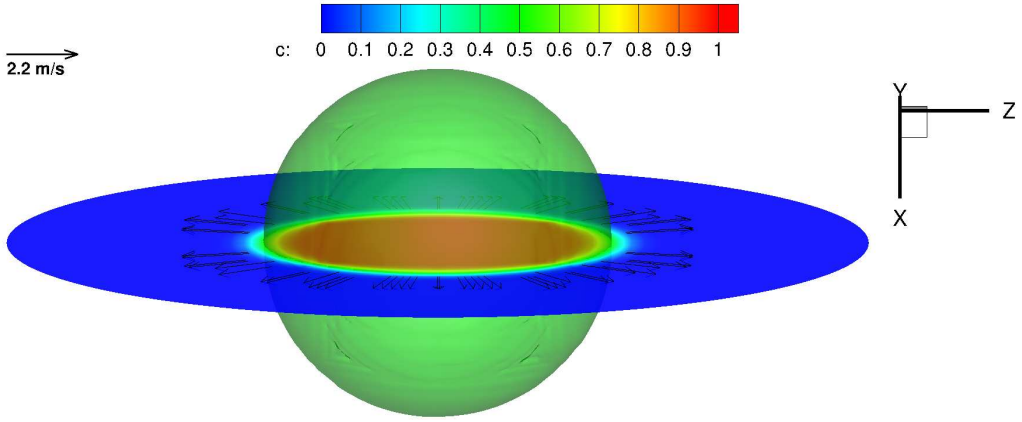

Figure 3.1.5.: **Flame development $t = 0.15$ s after the ignition. The gas velocity in front of the flame front is shown as vectors. The iso-surface relates to the flame progress at 0.5 which is taken as reference value for the determination of the current flame radius.**

The plot in Figure 3.1.6 of time correlated values for the radius demonstrates the correct outcome of the simulation. Table 3.5 lists the respective values from the simulation for

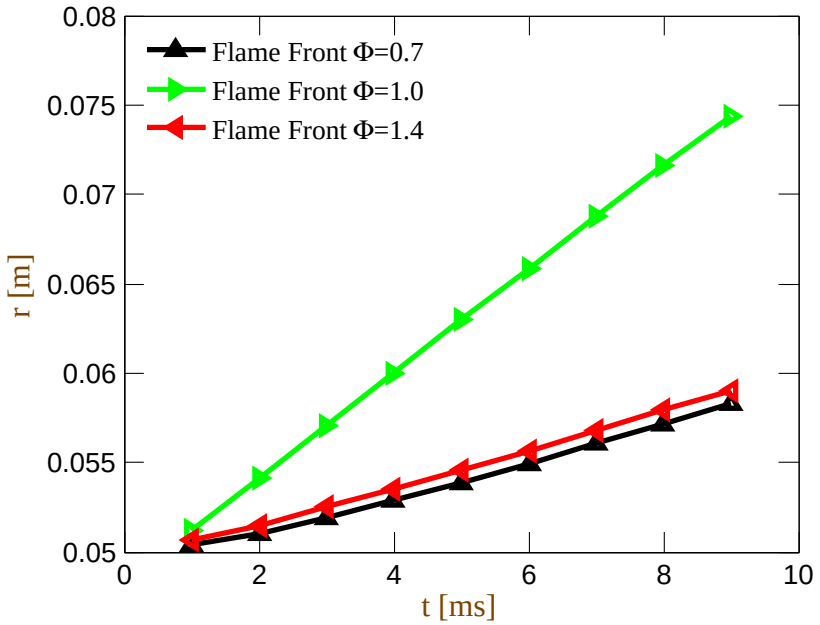

Figure 3.1.6.: **Time correlated flame edge positions for three different equivalence ratios ($\Phi = 0.7$, $\Phi = 1.0$, $\Phi = 1.4$) .**

the propagation speed and the inferred laminar flame speed. The values for the cold flow temperature and adiabatic temperature which is needed for the correlation in Eq. (3.1.2) are also provided.

In general the values for the unburnt laminar flame speed comply well with the theoretical values taken from [123]. Little deviations occur which relate to the non-planar propagation of the flame which results in a slightly slower flame growth. Since the flame front raises in length

due to the increasing volume which is enclosed, the flame speed is diminished by a stretch factor of $1/A \cdot dA/dt = 2/r \cdot dr/dt$ times the Markstein Length $\mathscr{L}$, see Bradley *et al.* [26]. That gives for an initial flame radius of 5 mm a relative decrease in the propagation speed of the order of 2.5 %. Thus, the total difference between the simulated and theoretical value for the derived laminar flame speeds is within 8 %. In conclusion, the model demonstrates that it accounts well for the transient effect of gas expansion and is able to provide an accurate representation of the unsteady nature of a propagating flame.

3.2. Mixing: Counterflow Configuration

This test case comprises a counterflow flame configuration which is frequently employed in combustion modeling validation [163, 165, 166, 179]. The configuration offers convenient means to investigate specific aspects of the flame characteristics, e.g. flame structure [165, 166], flame extinction by stretch [108, 109], by prescribing appropriate boundary conditions. In this work, the test case is utilized to demonstrate the correct mixing behavior in case a burnt and an unburnt flow mix. In the original TFC model [196], some physical inconsistencies are present, which are not observed here with the improved formulation. One is reported by Wood *et al.* [191] who found out that mixing of a fully reacted flow with fresh air leads to an erroneous creation of fuel. This stems from mixture fraction changes in conjunction with changes of the flame progress variable value by which the remaining fuel mass fraction is originally determined. This shows the ambiguity associated with the flame progress variable approach, which is undefined for pure air. Pure air for example, can correspond to a flame progress variable of 1, since no further reaction can occur or to 0 for the reason that no reaction has yet occurred. However, imposing a value of 1 for pure air conflicts with the gradient based formulation of the flame progress variable directing the flame from burnt to unburnt mixture. Secondly, if an unburnt partially premixed flow mixing with pure air is considered, severe problems regarding the resulting value of the flame progress variable emerge as well.

The set-up of the configuration and the boundary conditions are provided in Fig. 3.2.1 and Table 3.6, respectively.

Table 3.6.: **Boundary conditions of the counterflow test case.**

General	$\sim$ 40.000 Grid Points, 5° cake pie		
Left inlet	Temperature 1872 K	Velocity: 2.1 m/s	$c = 1$
	$Y_{H_2O} = 0.1207$	$Y_{CO_2} = 0.1474$	
	$Y_{O_2} = 0.0266$	$Y_{N_2} = 0.70534$	
Right inlet	Temperature 300 K	Velocity: -0.3 m/s	$c = 0$
	$Y_{O_2} = 0.23$	$Y_{N_2} = 0.77$	
Out Flow	Pressure Outlet in the central section of the upper wall. Walls are modelled as adiabatic no-slip boundary condition.		

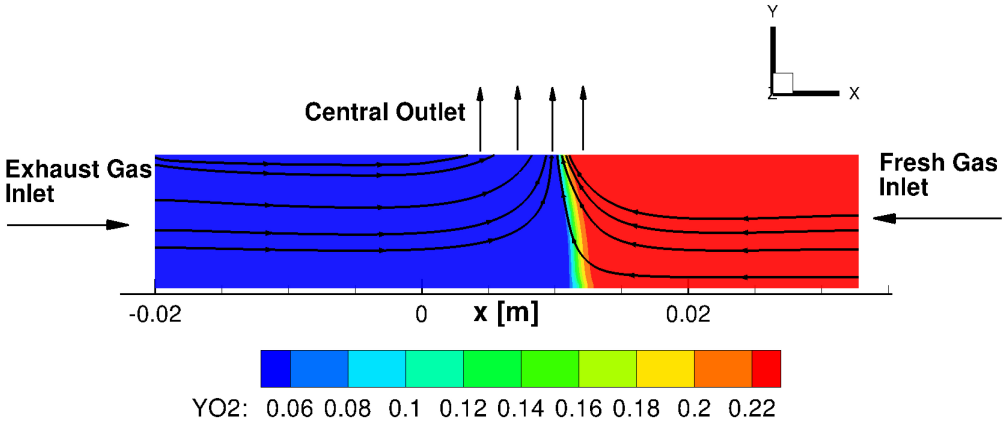

Figure 3.2.1.: **Set-up of the counterflow test case. A contour plot of the mass fraction of O_2 is presented. Stream-lines indicate the direction of the flow. The left inlet provides hot exhaust gases stemming from a lean combustion which mix with the fresh air coming from the right.**

In this set-up, exhaust gases from a lean fully burnt methane/air flame with an equivalence ratio of $\Phi = 0.9$ enter from the left. Fresh air is provided from the right. The inlet velocities have been chosen so that the impulse of both flows is of roughly the same order. A pressure outflow through which the flow can leave the domain is located at the upper boundary in between $x = 0.0$ m and $x = 0.0127$ m. The remaining part of the upper boundary is modeled as a adiabatic no-slip wall. The intention of the configuration is to demonstrate the proper mixing behavior of the proposed model extension. Therefore, the test case has been calculated a second time with a finite rate chemistry (FRC) scheme which employs a detailed mechanism. The finite rate chemistry scheme achieves a very accurate solution for this kind of set-up as the flow regime remains laminar. The GRI 3.0 mechanism [161] has been employed for the comparison. Both results, for the present TFC model extension and the FRC model with respect to the predicted temperature are presented in Fig. 3.2.2 in addition to a third calculation corresponding to the standard TFC model. As opposed to the present TFC model extension, where selected single species are transported, in the standard TFC implementation the mixture fraction is transported. The temperature is then determined using a polynomial of the adiabatic flame temperature for a given mixture fraction and flame progress variable. The polynomials are taken from Müller *et al.* [123].

The temperature profiles from the present TFC model extension show a very good agreement with the values derived from the detailed mechanism as depicted in Fig. 3.2.2. Slight deviations relate to a different equilibrium temperature derived in the extended TFC model. Since the present TFC model extension does not incorporate, for example CO as a major species, which has an impact on the equilibrium temperature, the temperature in general is slightly overpredicted. However, as the TFC model belongs to the low-order models, limitations can-

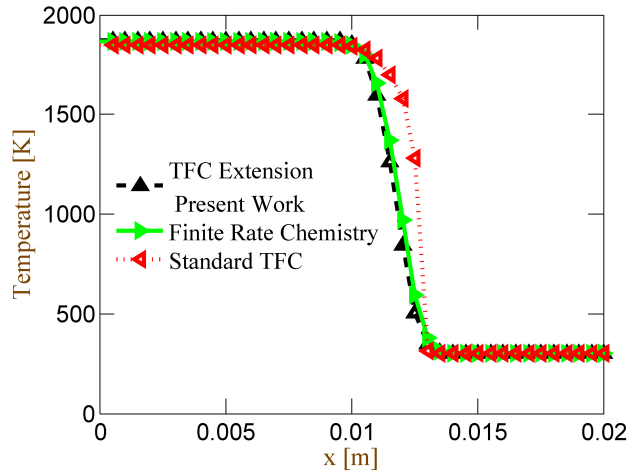

(a)

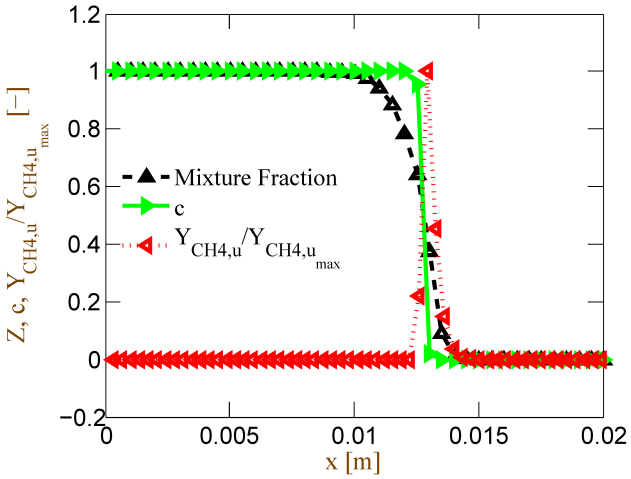

(b)

Figure 3.2.2.: **a) Model comparison for the axis temperature profiles of the laminar counterflow configuration. b) Central axis profiles for the standard TFC model. Note, the unphysical generation of fuel in the standard TFC model. This raise does not occur with the present TFC model extension.**

not be completely avoided. More important, e.g. for ignition modeling, is that the model accurately captures the position of the flame front which was successfully demonstrated by this test case.

In contrast to the new implementation, the plot in Fig. 3.2.2b shows the fuel mass fraction in the standard model, obtained by means of the mixture fraction variable and the reaction progress variable. Fuel is created behind the mixing zone since in this region, the mixture fraction is greater than zero in conjunction with a reaction progress variable less than one.

In summary, the new model implementation resolves the known issues with mixing of burnt gases with a flow of a different composition. This stems from the substitution of the mixture fraction variable with selected independent species. Consequently, the extended model

predicts the correct diffusion of burnt gas into fresh air.

3.3. Multiphase Flow in a Channel

The first multiphase test case represents a very simple configuration of a 1D channel with an inflow at the left-hand side and an outflow at the opposite end. The confinement is modeled as symmetry boundary conditions. In general, the flame speeds, which evolve in such a configuration are quite different from those of pure gaseous flames, which is associated with the occurring evaporation processes. This can cause, in case of a high overall equivalence ratio (liquid and gaseous fuel to gaseous oxidizer), rather beneficial conditions for the flame to propagate as the fuel may slowly evaporate and provide stoichiometric conditions within a confined region. On the other hand, an equivalence ratio of unity leads to a more distributed combustion as the fuel droplets evaporate within a longer part of the channel. This causes the flame to propagate slower, since the gradients in the flame are not as strong as for the high equivalence ratio. This is what was also observed by the numerical study of Neophytou and Mastorakos [125], who applied a detailed chemistry scheme to obtain flame speed results in this configuration. They also excluded single droplets effects which may impact the outcome, since droplet surrounding flames can have a local accelerating effect. A schematic of the test case and the boundary conditions are provided in Fig. (3.3.1) and Table 3.7 respectivly.

Table 3.7.: **Boundary conditions of the 1D multiphase flow channel configuration.**

General	1.000 Grid points Quasi 1D (2 Grid points in y, z direction)
Inlet	Temperature 300 K $Y_{O_2} = 0.23$, $Y_{N_2} = 0.77$
Spray inlet	Located at $x = 0.002$ m Temperature 300 K, Fuel: n-decane.
Out flow	Pressure outlet

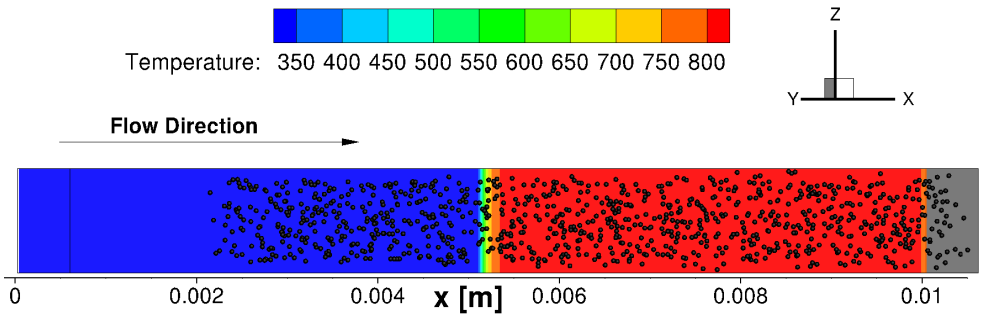

Figure 3.3.1.: **Illustration of the droplet distribution for the quasi 1D channel test case. A representative number of 1,000 droplets is depicted. Ignition in the second half of the channel has just occurred.**

The boundary conditions are provided in Table 3.7. After the down stream end of the channel is occupied by a steady number of droplets, an ignition is accomplished at x=0.0075 m with a radius of 0.0025 m and a total ignition energy of 30.0 mJ. This is shown in Fig. 3.3.1 in which parts of the ignition energy have been already delivered to the domain. Subsequently, a flame kernel develops in the ignition zone. After the ignition effects have abated ($t > 10$ ms), the flame propagation can be measured. The flame front is tracked and through dividing the spatial displacement by the passed time, a value for the laminar flame speed is obtained. The investigation has been carried out for n-decane as liquid fuel, for a set of equivalence ratios and droplet diameters. A comparison to the study of Neophytou and Mastorakos is presented in Fig. 3.3.2.

In summary, the model has demonstrated, that it is capable of offering a reliable prediction for the propagation of a planar flame in a multiphase flow environment. A good agreement can be achieved for this case of a simplified propagating laminar flame due to two reasons. First, the fine grid which is employed captures the flame front reasonably well. Secondly, the high resolution also enhances the accuracy of the thermal diffusion calculation which enables a proper prediction of the heat and mass source terms from the evaporating fuel droplets. Two-way coupling applied in the framework of the present Eulerian-Lagrangian simulation ensures that the vaporized fuel vapor mass fraction is distance-proportionally interpolated to the Eulerian nodes. This is essential as the computation of the laminar flame speed includes the gaseous fuel to air ratio as one parameter in the polynomials. One drawback appears in contrast to the results obtained by Neophytou and Mastorakos [125]. They found that preferential diffusion in conjunction with a detailed chemistry scheme, can cause a laminar flame speed higher than the laminar flame speed at stoichiometric conditions. This

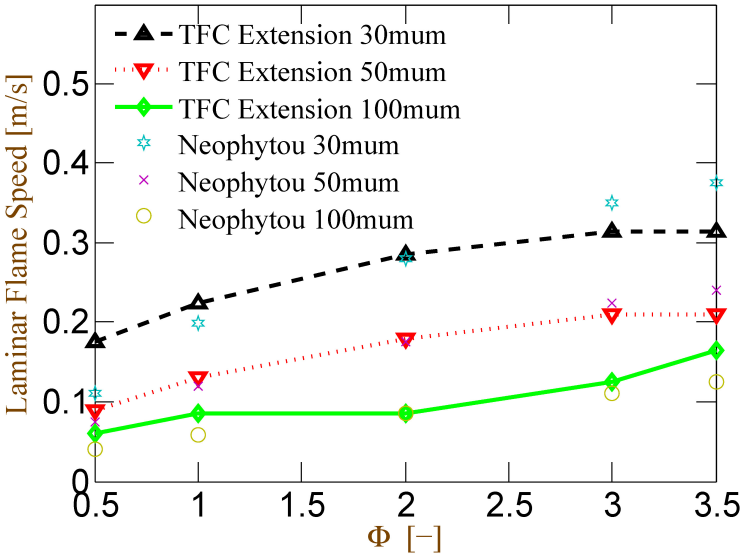

Figure 3.3.2.: **Comparison of predictions for the laminar flame speed for different droplet sizes and equivalence ratios.**

contribution of finite rate effects cannot be resolved with the simplified chemistry approach incorporated in the TFC model formulation.

3.4. Shearless Flow

The set-up of this test case belongs to the category of non-premixed flames category since air and fuel enter separately. Non-premixed mixing-controlled jet flames have been widely studied also in the context of ignition [13, 162]. For this validation study, the focus is on flame propagation in a shearless flow, showing that although an initial flame kernel is generated, the overall outcome of the ignition event can fail. The geometric dimensions of this test case are as described in [2] and outlined in Fig. 3.4.1. Since experimental data is available for this configuration, the model prediction for the flame behavior in a turbulent environment is compared against measurements.

Table 3.8.: **Boundary conditions of the shearless flow test case.**

General	200,000 grid points Quasi 2D (2 Grid points in z direction)
Upper inlet	Fully turbulent profile, Temperature 293.15 K $Y_{CH_4} = 0.138$, $Y_{O_2} = 0.198$, $Y_{N_2} = 0.664$
Lower inlet	Fully turbulent profile, Temperature 293.15 K $Y_{O_2} = 0.23$, $Y_{N_2} = 0.77$
Walls	Adiabatic no slip walls
Symmetry	Symmetry boundary condition in z-direction
Out flow	Pressure outlet

Fuel, diluted with 80 Vol% air, and pure air stream in the domain from two separate inlet channels of 23 mm width. The velocity of both flows is identical. A moderate level of turbulence establishes in the domain middle as both inlet flows mix behind the splitter plate. Subsequently, the mixing layer gets accelerated through the mean flow. This leads to a slow reduction of the turbulent intensity. The boundary conditions of the test case are provided in Table 3.8.

The numerical simulation is performed with two different settings. In the first case, the flow velocity is prescribed as 1.5 m/s which is of the order of magnitude of the turbulent flame speed. It is observed that the initial flame kernel once established is able to overcome the oncoming flow and propagate backward to the splitter plate. In the second configuration, the flow velocity equals 3.0 m/s which exceeds the maximum turbulent flame velocity and no stabilized flame is achieved. Results from the first and second simulation are presented in Fig. 3.4.3. It is very interesting to note that flow field results, gained by a pre-conducted cold flow simulation, indicate that even in the case of the slow mean flow, a backwards propagation of the flame will not happen, since the turbulent flame speed is slightly below the

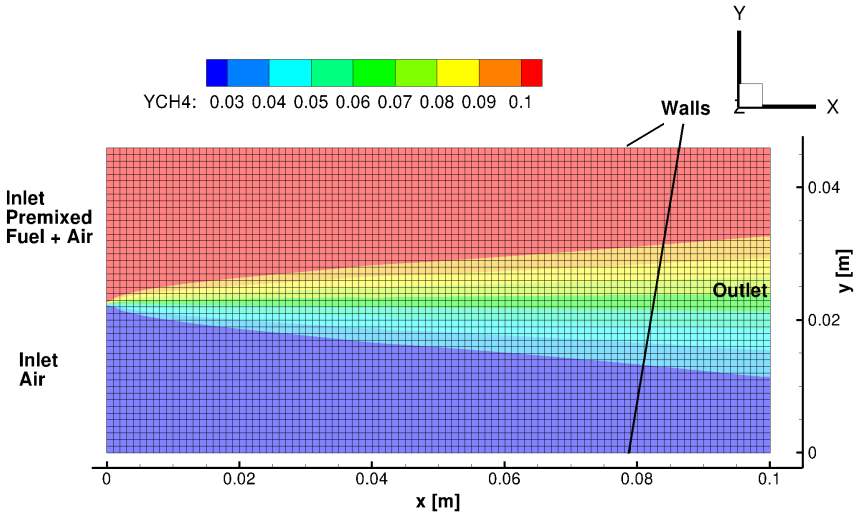

Figure 3.4.1.: **Schematic of the set-up of the shearless flow configuration. Fuel distribution and meshing is indicated.**

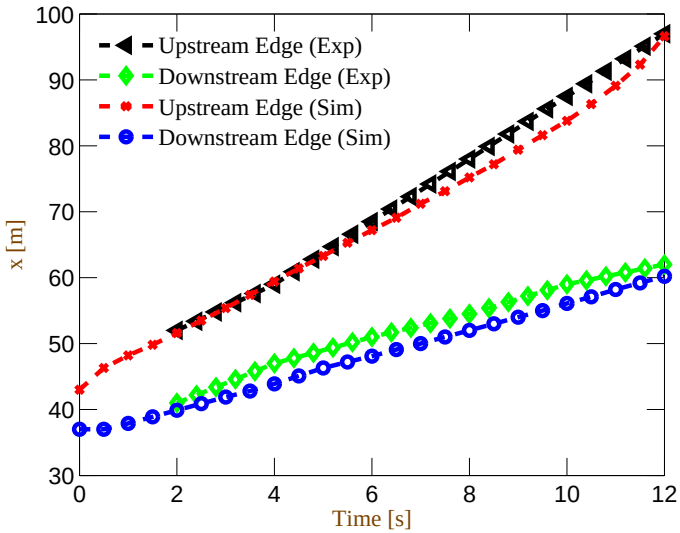

Figure 3.4.2.: **Comparison of flame edge positions. Exp: Refers to experimental data [2]. Sim: Refers to simulation results.**

mean stream velocity. Through dilution of the gas, the local velocities change and, due to heat expansion effects, the flame is able to overcome the mean flow and propagate backwards towards the inlet. In the second scenario, the turbulent intensity is increased throughout the whole domain induced by higher mean velocities. However, as the turbulent flame speed does not scale linearly with the turbulent intensity, the gain in the turbulent flame speed is not sufficient to allow the flame to propagate backwards. The results of the simulation agree well with the findings from the experiments of Ahmed *et al.* [2]. Figure 3.4.2 shows a quantitative comparison between the flame edge positions measured in the experiments and the simulations. As reference point in the simulation, a value of 0.9 of the flame progress variable is taken to determine the upstream and downstream edge position.

The satisfying agreement benefits from the ideal conditions for the TFC-model which prevail in the domain. The level of turbulence in both cases is moderate. Hence, high fluctuations in the mean quantities are not necessarily expected. Thus, the turbulent flame speed is only slightly enhanced by the turbulence. The ignition mechanism plays a minor role in this test case. As flow velocities and turbulence intensities are rather low, the heat from the spark ignition can not be convected or dissipated away too quickly. The heat remains local and leads to very short ignition delay times which facilitates the establishment of a viable initial flame kernel.

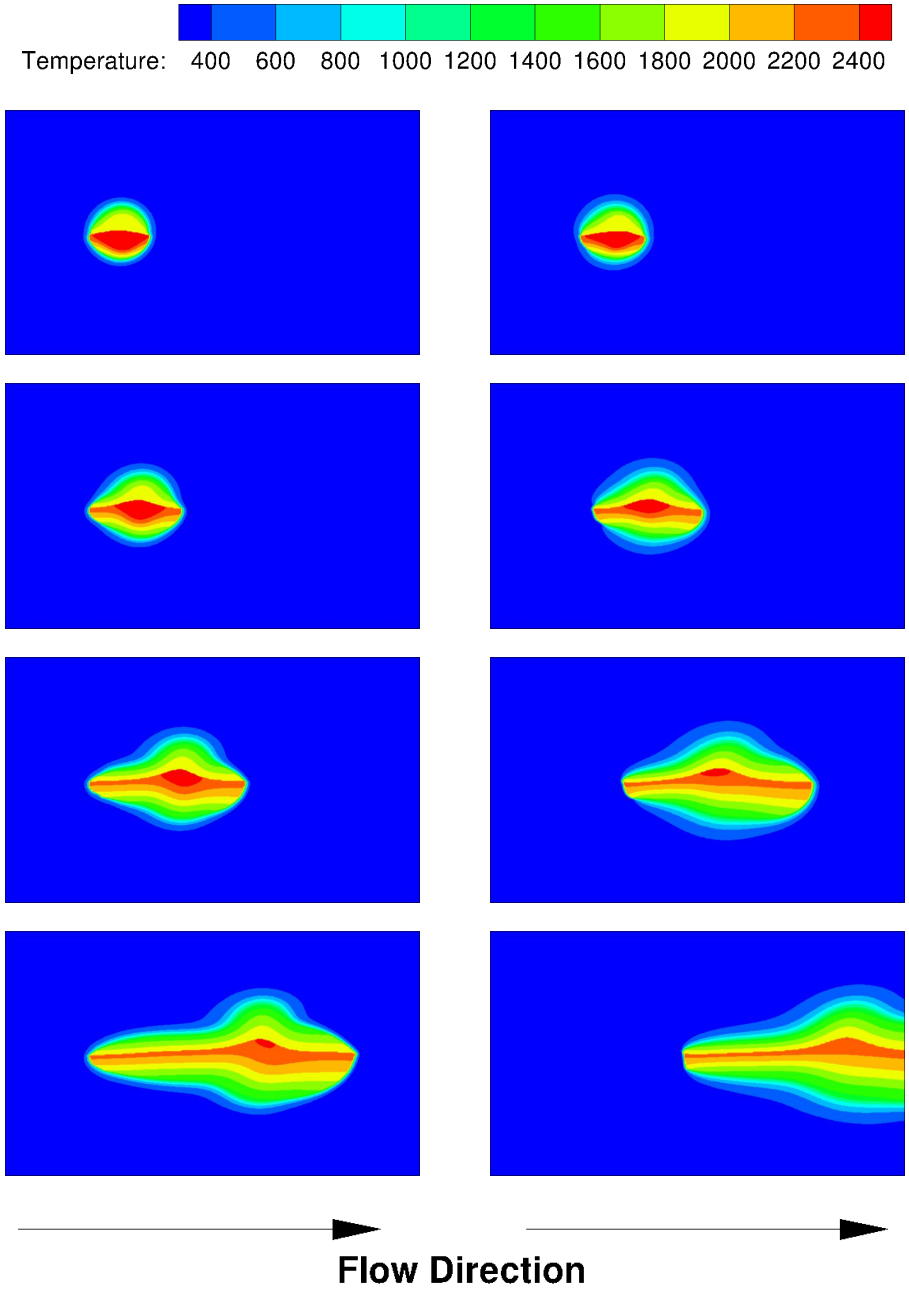

Figure 3.4.3.: **Spark ignition in the shearless flow configuration. Spark at $x = 0.02$ m $r_s = 3$ mm. View range: 100 mm x 46 mm. Rows correspond to $t = 1$ ms, $t = 3$ ms, $t = 7$ ms, $t = 14$ ms. Columns correspond to $u = 1.5$ m/s, $u = 3.0$ m/s.**

4. Numerical Generation of Ignition Maps for Single Phase Flows

This chapter presents two well-characterized single phase test cases for which ignition maps have been generated in dedicated experiments. The task of establishing an ignition map is confined to rather simple geometries, as otherwise, the computational effort to simulate the vast number of possible ignition locations is out of bounds. The two test cases under investigation are experimental set-ups which have been studied at Cambridge university by the team of Mastorakos. The first ignition map is compiled for a counterflow flame for which the ignition probability is computed on the center axis. The second configuration concerns a methane jet injected into a slow air co-flow. For this set-up a two dimensional ignition map is presented. The test cases provide insight into ignition in co-axial and counterflow configurations. The turbulence intensities for both ignition studies are rather low as they are intended for fundamental research purposes, however, especially in the second test case the sometimes detrimental influence of turbulence can be observed. Ignition in both cases is achieved through a spark plug which has been modeled by an increase of enthalpy in the numerical simulations. The results help to elucidate the extended TFC model capability to determine favorable parameter for a successful ignition.

4.1. Counterflow Flame

This section comprises a numerical study of a counterflow flame configuration studied experimentally by Ahmed *et al.* [4, 6]. The counterflow flame as means to derive insight into combustion processes theoretically and practically is widely established as in Cho *et al.* [35], Seiser *et al.* [153] and Smooke *et al.* [166] to name only a few. This set-up has also been used previously by Mastorakos [106] to research the specific flow-field and mixture fraction. An ignition map and data concerning the flame propagation speed has been derived in [4, 6] which will be compared here to the numerical results. In relation to the second investigated jet flame test case, this set-up exhibits a larger stratification of fuel and oxidizer, similar to the prevailing conditions in a full scale combustor. A premixed fuel/air and an air flow entering from opposite sides characterize this counterflow geometry. A comprehensive study concerning the impact of the igniter position and the ignition energy on the outcome of the ignition event is performed. The main finding for this test case is that a successful ignition

of the domain can occur, even in cases in which the ignition energy is not released in an area with flammable mixture. In general, the comparison with experimental data shows a good agreement, both in terms of successful ignition and flame kernel propagation.

4.1.1. Boundary Conditions

Table 4.1.: **Boundary conditions of the counterflow configuration.**

General	Axisymmetric domain. Cake pie of 10°. 320,000 Grid Points
Center Inlets	$r = 12.5$ cm. Fully developed velocity profiles. $T = 293.15$ K. $u = 2.0$ m/s Premixed Air/Fuel inlet on the right-hand side. $Y_{CH_4} = 0.1383$, $Y_{O_2} = 0.1977$, $Y_{N_2} = 0.664$ Air inlet on the left-hand side. $Y_{O_2} = 0.23$, $Y_{N_2} = 0.77$
Outer Inlets	$r = 22.5$ cm. Fully developed velocity profiles. $T = 293.15$ K. $u = 0.6$ m/s. $Y_{N_2} = 0.77$
Outflow	Pressure outlet ($p = 1$ bar) at the top
Side Walls	Symmetry boundaries

A total energy of 100 mJ was quantified by Ahmed *et al.* [4] for the total spark energy. Since most of the energy is directly lost in the form of heat transfer at the electrodes, the assumed effective amount of energy transferred to the flow is considered to be about 30% in the simulation, which is consistent with the original work. This leads to a spark kernel size of $r_s = 3$ mm in the simulation which is derived from:

$$E_s = V \rho_s c_p (T_s - T_0) \tag{4.1.1}$$

with V being the volume heated-up by the spark and E_s being the effective spark energy. Subscripts 0 and s denote ambient and spark conditions, respectively. As the volume is regarded to be spherical, the volume can be expressed via: $V = 4/3\pi r_s^3$. Note that an instantaneous heat release for this configuration is assumed, see Sec. 2.2.4 which is in agreement with a previous performed numerical study of this configuration by Richardson and Mastorakos [144]. For the resulting density in the spark volume, ρ_s is substituted by: $\rho_s = p/(RT_s)$. Solving Eq. (4.1.1) for the spark kernel radius yields:

$$r_s = \left(\frac{3}{4\pi} \frac{R}{c_p p} \frac{1}{(1 - T_0/T_s)} E_s \right)^{\frac{1}{3}} \tag{4.1.2}$$

T_0 and p are the ambient temperature and pressure values, which are taken to be 300 K and 1 bar, respectively. T_s represents a parameter which is set to 1800 K posing a reasonable value for the temperature of the mixture after the initial short-time spark effects have vanished,

see Richardson [143]. The spark is applied to the domain after a well converged cold flow flow-field has established. Additionally, the grid has been designed such that the spark radius is resolved by at least 10 grid points which gave good results in preliminary ignition studies.

In this set-up, fuel and oxidizer enter premixed from the right side. The fuel to air ratio is 20 % by volume, hence above the flammability limit which is taken to be 0.12727 % Vol maximum and 0.06158 % Vol minimum [130]. From the left side a pure air flow streams into the domain. In order to stabilize the flow at the outer radius, a nitrogen co-flow is employed at the top of the domain. The experimental set-up is depicted in Fig. 4.1.1 with the corresponding boundary conditions as specified in Table 4.1. The resulting mass fraction at the symmetry axis are shown in Fig. 4.1.2. For the numerical simulations a grid of $\sim$ 320,000 nodes is utilized. As the flow is axisymmetric, a cake shaped piece of 10° has been extracted from the entire domain. For the side walls in flow direction, symmetry planes are prescribed. The upper boundary resembles the outflow for which a zero-gradient is prescribed. At the inlet, fully turbulent profiles are imposed.

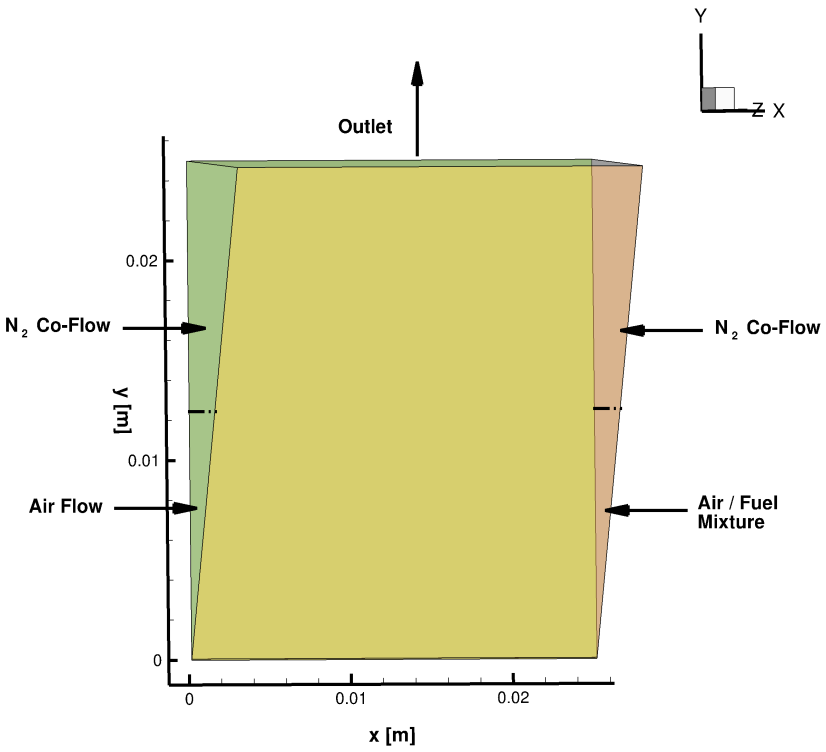

Figure 4.1.1.: **Set-up of the counterflow test case.**

4.1.2. Reactive Flow Results

The simulations have been carried out with several different spark locations and spark properties. At first, the spark ignition is performed in a region with very low ignition probability, according to Ahmed *et al.* [4], with the spark center being located at $x = 4$ mm on the center-

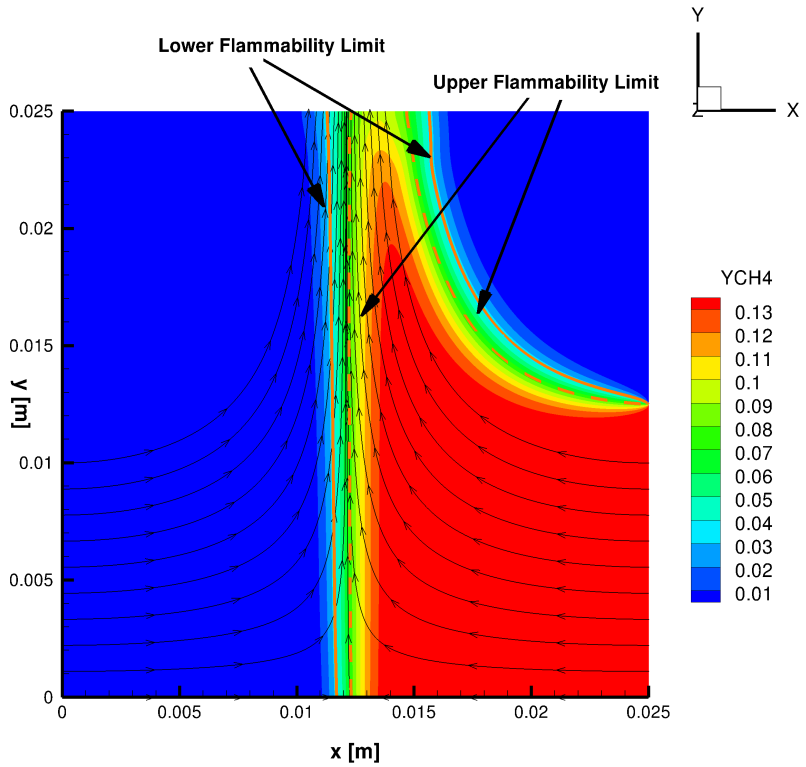

Figure 4.1.2.: **Methane mass fraction and velocity stream lines of the counterflow test case.**

line. The spark energy is convected towards gas mixtures being above the lean flammability limit. However, by the time it reaches the region, most of the initial energy has dissipated, and the mixture is too cold to ignite. The same calculation is repeated with the ignition energy release closer to the region with limited flammability, this time with the spark location at $x = 8$ mm. Although the hot mixture is too lean to ignite at the beginning, a successful sparking of the domain is observed. This is due to the fact that the energy is still contained in a small confined volume when the hot mixture is convected into burnable mixture. This is shown in Fig. 4.1.3 (second column), where at the end of the hot volume, a small flame kernel develops which is further growing as the hot gas is transported towards the domain middle. Finally, the flame kernel can develop into a full flame anchored at the domain bottom. The flame length, taken as the distance from the domain bottom to the end of the hot region ($T > 2000$ K) and the related time correlate well with the results from the experiment, as shown in Tab. 4.2.

A second successful ignition of the test case is achieved when moving the spark location closer to the region with flammable mixture.

Additionally, the influence of the spark energy is investigated. In the second scenario with ignition at $x = 8$ mm on the centerline, the ignition energy has been reduced to $\sim 30\%$ of the previous effective energy. Under these conditions the light-up of the whole domain

Table 4.2.: **Flame evolution in the counterflow flame test case**

Time	Flame Length in Experiment	Flame Length in Simulation
1 ms	2.3 mm	2.2 mm
3 ms	7.0 mm	6.9 mm
7 ms	14.1 mm	19.8 mm
10 ms	25.8 mm	27.1 mm

fails. The spark energy does not suffice to generate a flame kernel, as the initial lower energy has decreased too much when finally encountering flammable mixture. This stresses the importance of the spark energy as a crucial parameter in ignition problems, as was also found in the experiments. Results from each of the simulations can be found in Fig. 4.1.3.

4.1.3. Ignition Map

As pointed out by the obtained results, the closer the spark kernel is located to the stoichiometric center of the configuration, the higher the probability of generating a fully established flame. One advantage of a URANS approach as compared to LES simulations is its high computational efficiency, allowing the realization of a multitude of different simulations, each with a varied set of initial conditions. In the scope of this numerical examination, a set of calculations with the spark being moved on the centerline has been performed. The intention is to determine the range along the centerline within which a successful ignition of the whole domain is feasible. Figure 4.1.4 shows the outcome of the simulations and a comparison with experimental results.

The agreement between both results is satisfying. In the region (0 - 7 mm and 18 - 25 mm) in which the experiment predicts a low to none probability of ignition, the simulation results show failing ignitions as well. Further towards the center of the domain, the ignition probability rises in the experiment to values between 30 % - 60 %. From 8 mm to 17 mm the simulation predicts a successful sparking as well, although parts of the range in which the spark is located do not overlap with the flammability region.

At this point as it is the first occurrence of a comparison between a numerical and an experimental ignition map, characteristics of both maps shall be discussed. The experimental map shows values in between zero and unity, which indicate that at the same location both successful and non-successful ignitions can happen. This is a consequence of the stochastic nature of the flow, which can contain turbulent structures which may alter the local properties of the flow field. At a certain time instance, the conditions for a successful ignition might be improved through, for example, an eddy providing beneficial mixture to the ignition location whereas at a different time instance the conditions might be worsened through an eddy providing non-flammable mixture to the ignition location. This stochastic dependency on

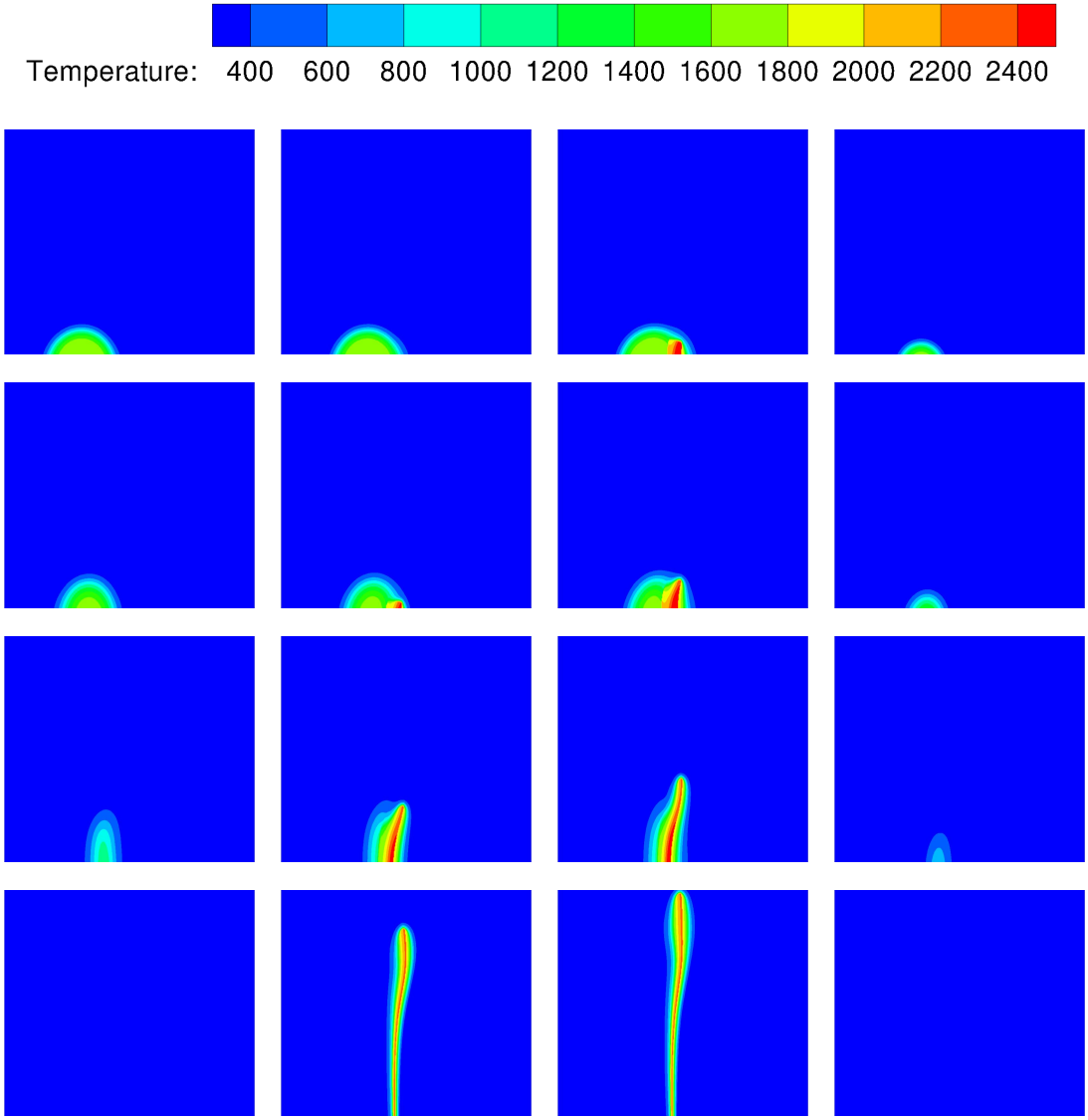

Figure 4.1.3.: **Spark ignition in the counterflow configuration. View range 25 mm x 22 mm. Rows correspond to t =0.3 ms, t = 0.9 ms, t = 3.0 ms, t = 6.9 ms. 1st column: Spark at x = 7 mm, r_s = 3 mm. 2nd column: Spark at x = 8 mm, r_s = 3mm. 3rd column: Spark at x = 9 mm, r_s = 3mm. 4th column: Spark at x = 8 mm, r_s = 2mm.**

turbulence cannot be resolved with the utilized URANS approach. In a URANS simulation, the ignition probability can only take on values of either zero or unity. A URANS simulation inevitably cancels out coherent turbulent structures. As a consequence thereof, the flow field of a URANS simulation has a deterministic nature, meaning that once the solution of the flow-field has converged, the flow-field will not change in time any more. With the flow field being fixed, the outcome of the ignition becomes independent of time. It can either be successful or fail as determined by the local properties of the flow. However, this does not imply that turbulence is completely neglected. In URANS, turbulence is assumed to be isotropic and is considered through the turbulent kinetic energy and dissipation (see Sec. 2.1.4) which

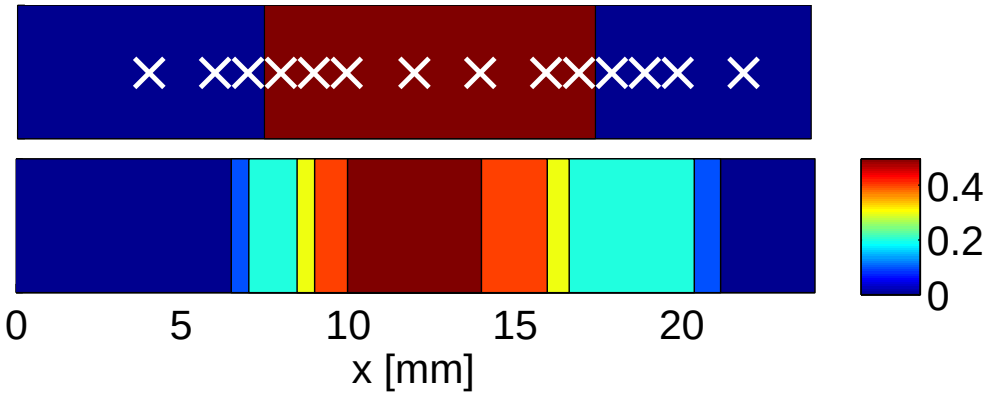

Figure 4.1.4.: **Ignition map for the counterflow case. White crosses symbolize performed simulations. Upper Plot: Simulation results, red: ignitable | blue: non-ignitable. Lower Plot: Ahmed *et al.* [5] experimental results, colorbar denotes the ignition probability.**

also affect the outcome of ignition. Thus, the average influence of the turbulence is captured to a large extent by the simulation, only the stochastic nature is not resolved. From the perspective that the purpose of the simulation is to identify locations which offer beneficial conditions for the majority of time, the limitations of the chosen modeling approach are acceptable. Ultimately, regions which show an ignition probability of unity in the simulation indicate that they are also adequate for successful ignition in the real application. This is underlined by the outcome of this study in which the region with elevated ignitability of more than 30 % corresponds well to the region in which the simulation predicts a successful spark event.

The impact of the second parameter besides the ignition location, the influence of the spark energy onto the ignition map, is presented in Fig. 4.1.5.

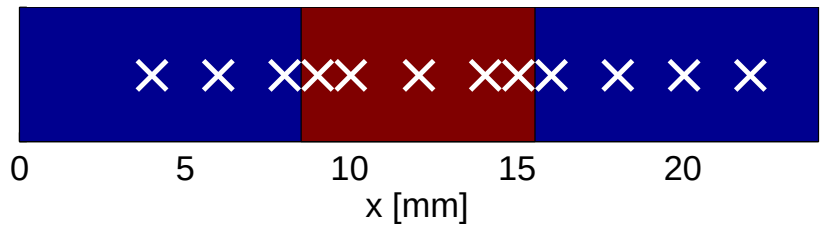

Figure 4.1.5.: **Simulation results with spark radius r_s = 2 mm. White crosses symbolize performed simulations.**

The basic observation is that only spark locations containing a mixture within the flammability limits are able to ignite the whole domain. Due to the low energy of the spark, flame kernels away from the flammable middle section are quenched before they can reach favorable conditions. The assumed magnitude of energy transferred to the gas, using Eq. (4.1.2), amounts to 9.7 mJ which, as stated before, poses approximately a decrease by 2/3 of the ignition energy. Studies by Ahmed *et al.* [5] have confirmed the detrimental effect of a

reduction of the spark energy on the ignition probability. This provides credibility to the obtained numerical results. However, further experimental data is needed for a more detailed quantitative comparison of the influence of the ignition energy. At this point, the importance of an additional implementation of a spark sub-model becomes apparent.
Without an enthalpy equation, ignition outside of burnable mixture represents a situation for which unphysical initial conditions need to be imposed. As remarked by Richardson [143], two ways to model ignition are possible. Possibility one is, to prescribe conditions which correspond to a burning flame at the ignition location and let the flame spread naturally afterwards. The second possibility concerns the prescription of an enthalpy rise at the ignition location and wait for auto-ignition to occur. The first possibility fails in region in which no flammable mixture exists. Under these circumstances no burned state can be deduced which prevents a meaningful initiation of the flame kernel. Furthermore, by employing the enthalpy equation as means to trigger the flame, the effect of the spark energy on the ignitability of a test case can be taken into account.

4.1.4. Conclusion

The test case demonstrates that, by means of the extended TFC model, it is feasible to generate an ignition map for a generic flame configuration. As was argued in the discussion of results, the chosen modeling approach only offers a deterministic result (either zero or unity) for each investigated ignition location. The stochastic nature of the flow (which is reflected by values in between zero and unity for the ignition probability in the experiment), as a consequence of turbulence structures, is lost, due to the employed RANS turbulence model. With the intention of the simulation to identify regions with a high ignition probability for the majority of time, this limitation appears acceptable. The obtained numerical ignition probability map proves this concept as a satisfying similarity to the ignition probability map determined in the experiment is achieved. Spark locations with a high probability to ignite the domain are well captured. In addition, regions with zero ignition probability are also been correctly identified in the calculations which render the method a valuable tool in assessing preferable or non-preferable locations for an ignition device. In contrast to LES simulations, the developed combustion model offers the advantage of low computational costs, making it attractive for design studies of combustion chambers.

4.2. Jet Flame

The test case presented in this paragraph belongs to the extensively studied and acknowledged configurations, involving a number of interesting aspects. In particular the high turbulence and the stratification of the mixture but also the flame stabilization and operation limits are of high relevance concerning modern combustion systems. Besides studies on the interaction between stabilized flame and flow-field [34, 48, 79], several experiments focusing on the igni-

tion of the jet flame have been conducted [9, 10, 11, 12, 173]. The experimental investigations established insight into minimum ignition energy, spark kernel size and flame kernel development. Recently, simulations [88, 185] and experimental work [5, 107] were accomplished to examine the spatial ignitability of the jet flame. On the basis of the experimental results from Ahmed and Mastorakos [5, 107], a series of simulations is performed and evaluated by a comparison with the available data.

The jet-configuration itself represents a difficult environment for standard RANS turbulence models as it exhibits a strong directional bias of the velocity fluctuations. This is caused by the fact that the stream-wise velocity is far higher than the radial components of the velocity. These circumstances contradict the main assumption in the theory of isotropic turbulence, see Sec. 2.1.4, which presumes that the velocity fluctuations are of equal strength in all spatial directions. Consequently, care needs to be taken in simulating the cold flow initial solution, as the mixing of momentum and species, if not captured correctly, will largely influence later ignition results. The derivation of the ignitability for a specific position of the igniter is the key objective of this numerical investigation. Several specific characteristics regarding the distribution of the ignition probability can be observed in this set-up. Due to the incomplete mixing at the beginning of the jet, it is very unlikely to obtain a flame in this region. Secondly, in the far zone of the jet, fuel is very lean which impedes the ignitability in this region.

4.2.1. Test case set-up

Details of set-up are briefly illustrated in this paragraph. The configuration comprises two coaxial tubes with the inner tube carrying a fuel/air mixture and the outer tube providing the air co-flow. The jet diameter d_j equals 5 mm, which yields a Reynolds number of Re$= u_j d_j/\nu$ ranging from $\sim$ 3000 - $\sim$ 8100. The inlet temperature corresponds to 293.15 K. A schematic is provided in Fig. 4.2.1. The air co-flow exits with a velocity of 0.1 m/s which helps to minimize outer influences. The jet velocity in the experiment was varied between three distinct settings. The slowest case corresponding to a velocity of 8 m/s has not been analyzed in the scope of this work. The second case with 12.5 m/s jet velocity and the third case with 25.5 m/s have been simulated. In the experiment, as depicted in Fig. 4.2.1, an igniter was present which can be moved in 1 mm steps within the domain which gives the grid on which the ignition probability map was accomplished. The jet mixture can be adopted as well, whereas in this work it is concentrated on the case of 70 % fuel and 30 % air as benchmark test.

4.2.2. Grid and Boundary Conditions

The grid has been designed according to the characteristics for this type of set-up. These comprise a fine mesh resolution in the entire ignition zone, hence the zone, where the igniter

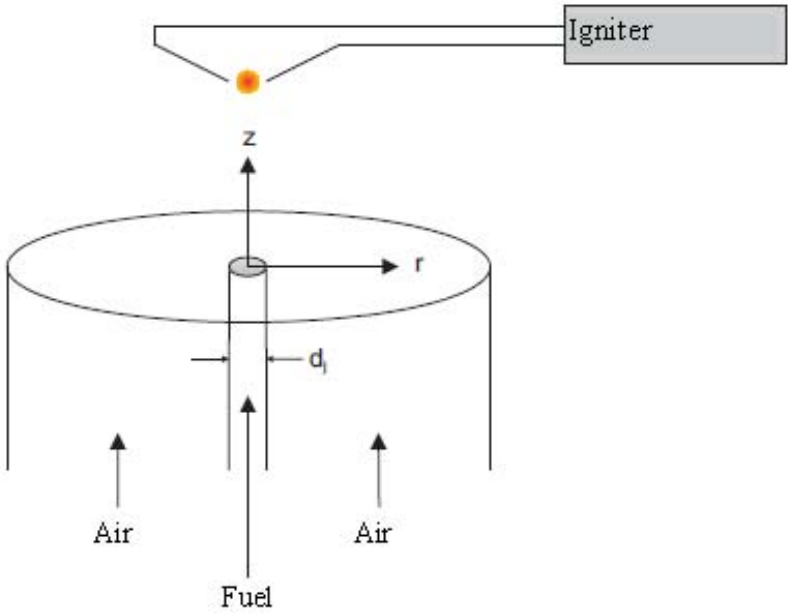

Figure 4.2.1.: **Schematic of the experimental set-up.**

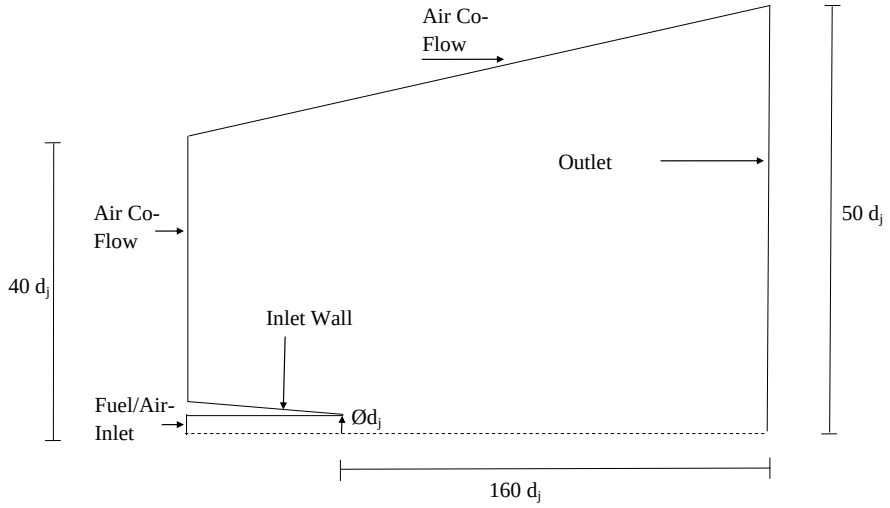

Figure 4.2.2.: **Numerical representation of the jet flame test case.**

has been moved to in the experiment. Additionally, a smooth transition is needed between the inner fine zone and the larger outer cells. The whole 360° domain is modeled, as symmetry walls affect an off-axis ignition simulation. In that case, a non-axisymmetric prescription of the ignition energy would be falsely mirrored by the symmetry axis. The grid has been refined several times to yield a grid independent final version for which a schematic is presented in

Fig. 4.2.2. The prescribed boundary conditions are listed in Table 4.3.

Table 4.3.: **Boundary conditions of the jet flame test case.**

Fuel/Air Inlet	Diameter: $d_j = 5$ mm. 70 % Vol methane and 30 % Vol air. $u = 12.5 - 25.5$ m/s. Fully turbulent velocity profile. $T = 293.15$ K.
Air Inlet	Diameter: $d = 200$ mm. Air (21 % Vol O_2 and 79 % Vol N_2). $u = 0.1$ m/s. Bulk velocity profile. $T = 293.15$ K.
Walls	Adiabatic no-slip walls. Outer domain walls are modeled as inlets with $u = 0.1$ m/s in axial direction to help the solver stability.
Outflow	Diameter: $d = 250$ mm. Pressure (1 bar) outlet.
Ignition Energy	The effective ignition energy corresponds to 30 mJ as determined by Ahmed and Mastorakos [5]. This corresponds to a spherical volume of $r = 3$ mm which is heated up to 1800 K.

4.2.3. Cold Flow Simulation

An emphasis has been put on obtaining the same cold flow results as in the experiment, to start the flame kernel evolution with very similar conditions. It is established knownledge [111, 119, 136], however, that the jet-flow is difficult to simulate with the standard k-ϵ turbulence model. This is referred to as the round jet anomaly, see e.g. Pope [136]. When employing the standard k-ϵ turbulence model for a round jet configuration, the spreading rate of the jet is overpredicted by as much as 40 % [136]. To overcome this issue, several ad-hoc modifications were proposed by [90, 111, 119, 136] to tailor the k-ϵ turbulence model for round jets. For self similar flows it was found that changing the value of the C_{ϵ_1} constant (see Sec. 2.1.4.1) to 1.6 yields the best agreement with experimental data [90, 136]. The adaptation enhances turbulent dissipation and subsequently reduces the turbulent viscosity which leads to a slower spreading of the jet [132]. This necessary procedure indicates a major shortcoming of RANS methods for non-isotropic flows. By assuming isotropy of the turbulence, crucial information about the structure of turbulence is lost. However, for applications which possess a main flow direction such as a round jet, the assumption of isotropy is no longer valid which manifests itselfs in the large deviations from experimental results. Through adjusting the turbulence modeling constants for the specific application, the problem can be alleviated. The satisfying agreement which is achieved with the adjusted C_{ϵ_1} model constant for the axial velocity (top) and the self similarity of the jet (bottom) is displayed in Fig. 4.2.3. Additionally, the correct self-similar development of the velocity fluctutations is illustrated at the top of Fig. 4.2.4. An improvement is achieved for the evolution of the center line velocity as compared to the standard k-ϵ turbulence model. Secondly, the jet behaves properly self-similar, yet, lacks the bouffant shape in radial spreading as observed in expe-

rimental measurements. The numerical results represent a compromise between radial and axial agreement which can be accomplished with the modified turbulence model constant. Regarding the mixing field of the jet, by using a standard turbulent Schmidt number of 0.7, the mixing is underpredicted as a result of the reduced tubulent viscosity. Decreasing the value of the turbulent Schmidt number to 0.4 gave the best comparison with correlations found in the literature. This is shown at the bottom of Fig. 4.2.4.

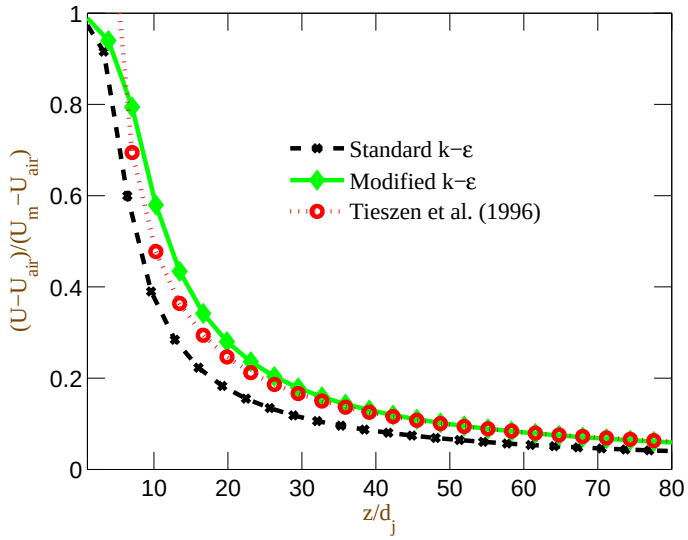

(a)

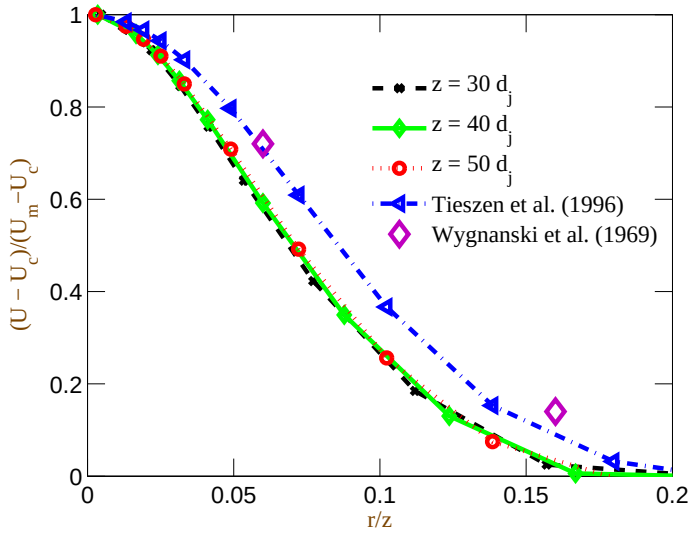

(b)

Figure 4.2.3.: **a) Axial velocity magnitude for the standard k-ϵ and the modified k-ϵ turbulence model in comparison to the correlation by Tieszen *et al.* [176]. b) Radial velocity profiles of the numerical simulations for different axis locations in comparison to the approximation by Tieszen *et al.* [176] and Wygnanski *et al.* [192].**

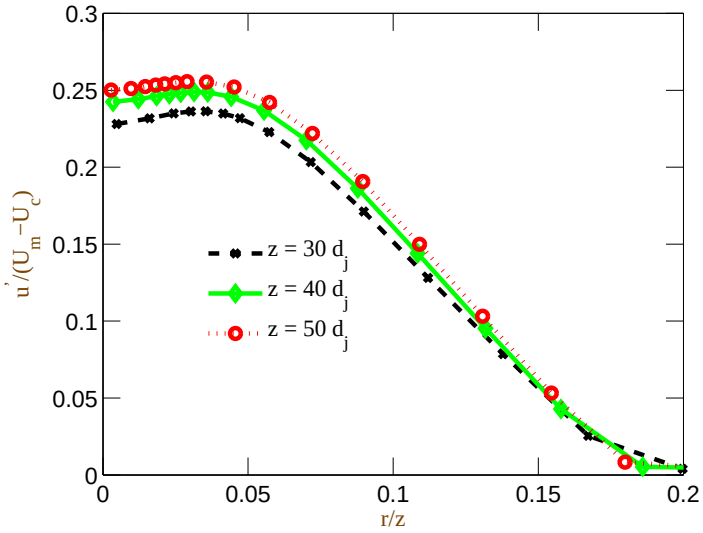

(a)

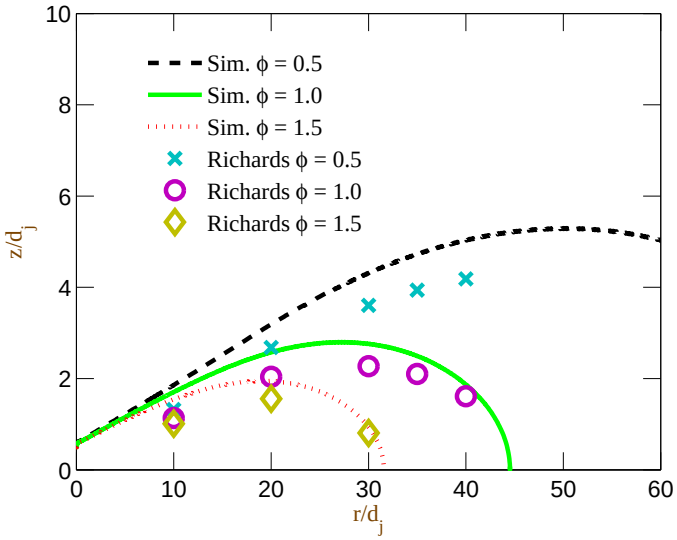

(b)

Figure 4.2.4.: **a) Magnitude of the RMS of the velocity for in correlation with the axial position. b) Comparison of respective equivalence ratios with a turbulent Schmidt number of 0.4 in the simulation to the correlation from Richards and Pitts [142].**

4.2.4. Ignition Maps

Two different inlet velocities have been investigated. The high velocity case with a velocity of 25.5 m/s and the moderate velocity case with 12.5 m/s. The expectations are, that the jet will ignite with a high probability outside of the shear layer between the jet and the co-flow as the turbulence intensity is too high within the layer thus impeding a successful ignition. The numerically derived ignition maps are shown in Fig. 4.2.5 for both respective inlet condition. The evaluation of a successful or non-successful ignition was carried out at the earliest after 20 ms after the spark occurred. Generally, as displayed in the Fig. 4.2.5, three different non-burning regions can be identified. At the jet exit, the mixture composition is too rich to allow an ignition. The second region with no ignitability is located at the jet sides, where no fuel is diffused nor convected to. The third region corresponds to the wake of the jet where the fuel spreads out and the mixture becomes closer to the lower flammability limit and eventually falls below it.

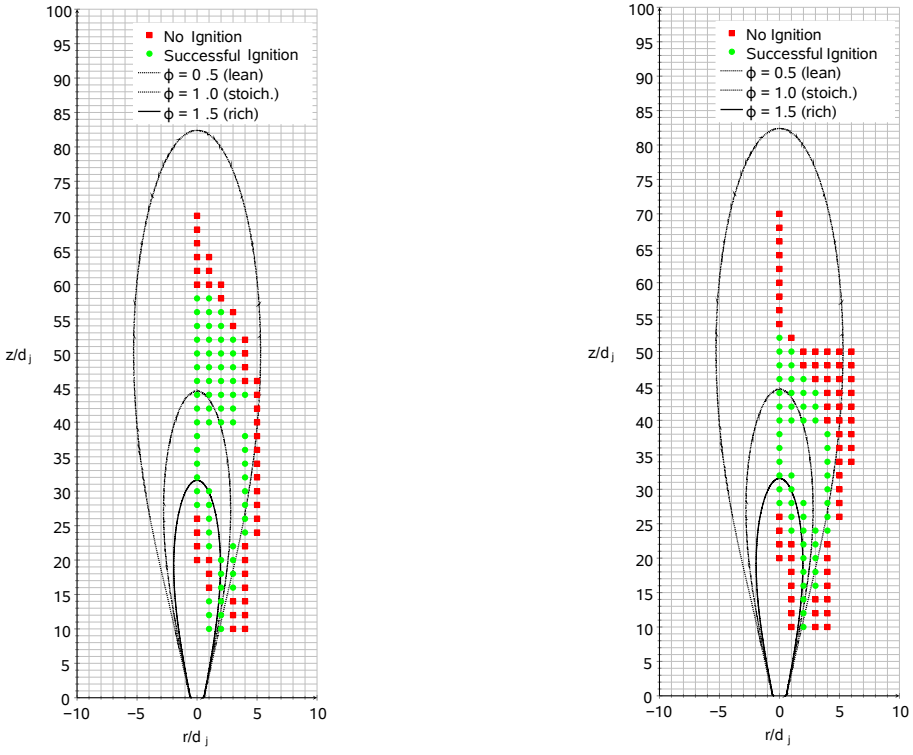

(a) (b)

Figure 4.2.5.: **a) Outcome of the numerical study for the 12.5 m/s jet velocity case. b) Results for the 25.5 m/s jet velocity case.**

4.2.5. Comparison with the experiment

This part presents a comparison of the numerically derived ignition map with the experimental results from Ahmed and Mastorakos [5]. The data is available in a 2-D contour plot as displayed in Fig. 4.2.6. As was remarked in Sec. 4.1.3, a straightforward comparison between

the experimental and numerical results for the ignition map is not possible. This stems from the differences of the stochastic nature of the experiment in which turbulent structures can lead to a successful / failed ignition at the same ignition location for two different time realizations (ignition probability in between zero and unity) and the deterministic nature of the URANS simulation in which the ignition probability can either be zero or unity (no intermediate values). From the perspective that the purpose of simulation is to identify locations for an ignition device where a high ignition probability prevails, a comparison is made between the 50 % ignition probabilty region in the experiment and the successful ignition region in the simulation. This is based on the assumption that the transition from successful to failed ignition in the simulation is likely to correspond to a transition from an elevated to a low ignitability for the real set-up. The agreement, with respect to this assumption, is depicted in Fig. 4.2.7.

In Figure 4.2.7, the comparison obtained close to the jet axis is of very satisfying quality. The first location at which mainly successful sparks can be observed in the experiment is well reproduced. In addition, the indention at the axis location is also well captured, showing that the model, indeed, correctly captures the unfavorable conditions in this area. Regarding the radial confinement of the ignitable region, the achieved agreement is of reasonable accuracy as well. The only discrepancies can be found in the downstream areas, where the model derives an ignition probability which is too high. This part of the ignition map challenges the simulation, as obviously, the gas composition is still within the flammability limits. It is also observed in other numerical studies concerning this experiment, e.g. Lacaze *et al.* [88] and Weckering *et al.* [185], that the derived ignition map spreads out too far when compared to the experimental data.

A reason for the differences shall be given in the following. Favorable conditions for ignition still prevail in this region. That the composition is above the lower flammability limit, hence allowing a flame to sustain, is in accordance to the experimental results. Turbulence as a second parameter may have a growing influence in this region. Due to that the mixture in the far region of the jet is of very lean composition, the ignition delay time increases significantly in magnitude, shifting closer to the time scale of the diffusion processes. As the time scales become of similar order, it becomes crucial whether the deposited energy remains focused long enough for the establishment of a flame kernel. In case too much of the ignition energy has dissipated, the remaining energy and prevailing temperatures do not suffice for auto-ignition. This is largely dependent on the correct prediction of the turbulence level, as lower turbulence levels will entail slower heat dissipation. It was observed in the plot of the mixture field, see Fig. 4.2.4, that, in comparison to well known correlations from the literature, mixing in the simulation is overpredicted. This results in lower turbulence level further downstream. The composition of the gas may be regarded as of minor influence, since

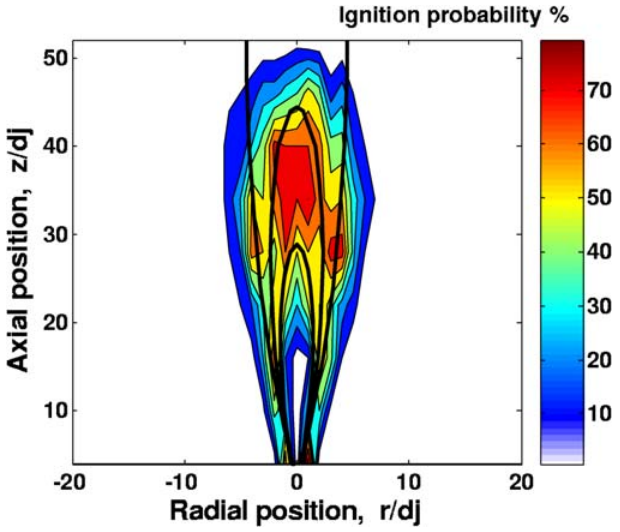

(a)

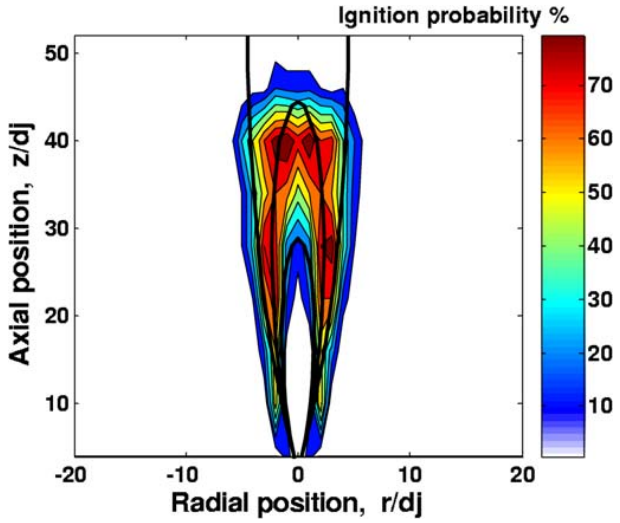

(b)

Figure 4.2.6.: **Experimental results for the ignition probability for (a) the 12.5 m/s case, (b) the 25.5 m/s case derived by Ahmed and Mastorakos [5]. The lines denote from upstream to downstream: upper flammability limit, stoichiometric iso-line and lower flammability limit.**

it also appears from Fig. 4.2.4 that the composition in the simulation is slightly leaner in the far downstream region than in the experiment. This would rather impede the ignition which is evidently not the case. A second important aspect in this sensitive region of the jet may be the assumption of a homogeneous deposition of the spark energy. This might also cause deviations. In the experiment, the deposition of energy by a spark plug is certainly more inhomogeneous, involving higher gradients that enhance diffusive effects and dissolve the ignition energy quicker than in the simulation. Both phenomena, lower turbulence levels and the modeled homogeneous heat release may be probable explanations for the deviations in ignitability between simulation and experiment in the far downstream part of the jet.

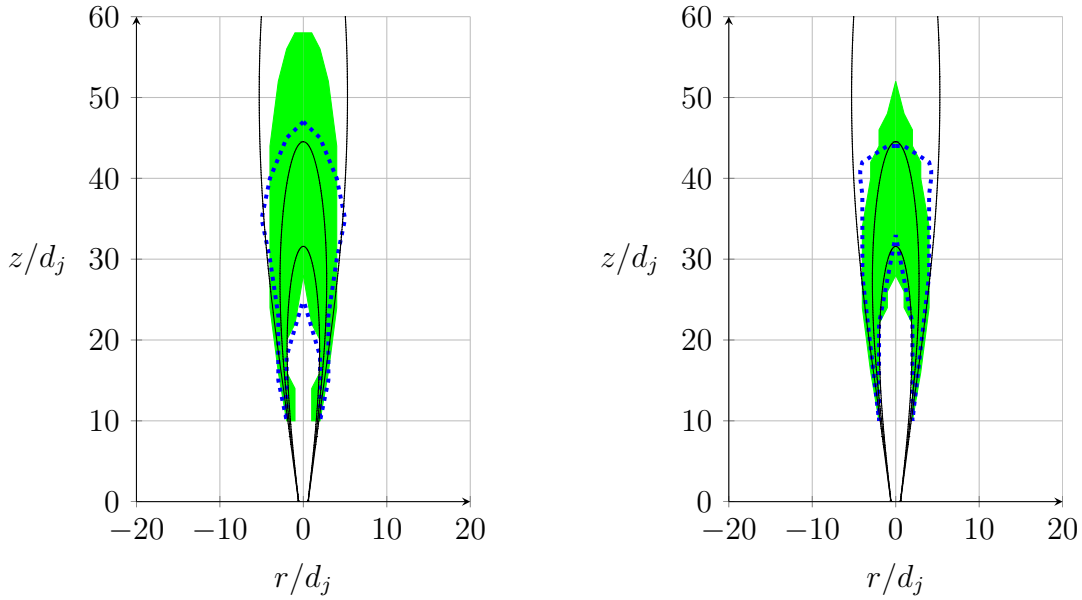

Figure 4.2.7.: **Comparison of the numerical and experimental results for the 12.5 m/s case on the left hand side and for the 25.5 m/s jet velocity case on the right hand side. Solid lines correspond to equivalence ratio isolines. The dotted line represents the measured ignition probability of 50 %.**

Regarding the agreement of the simulation with the experiment in the upstream part; there the shape of zones with high ignition probability is well predicted, as this region is controlled by mixing and the ratio of the flame speed to the local mean flow velocity. Figure 4.2.8 shows a comparison of the turbulent flame speed and the local mean flow velocity. The ignitability is high in parts, where the turbulent flame speed is higher than the flow velocity, allowing an expansion in all directions. With the flow velocity and the mixture becoming richer, both effects impede the expansion of the initial flame kernel and can lead to a failed ignition. This is correctly and accurately captured by the model.

4.2.6. Further Investigations

Beside the data related to the ignition map which provides insight into the transient behavior of the flame kernel, Ahmed and Mastorakos [5] also focused on stationary properties of the flame, namely, the lift-off height. The lift-off height is independent of the location where the ignition occurred. The evolving flame will eventually anchor at a certain displacement to the jet inlet only depending on the initial flow conditions. The lift-off height for 25.5 m/s measured in the experiment equals 9 d_j (4cm) which was found to be the same in the simulation thus showing the good general quality of the model. At the beginning of the jet, the implications of the RANS turbulence model are not as severe as further downstream as the turbulence is only just developing. Therefore the average mean flow velocity and the turbulent flame velocity are the main factors which are reasonably predicted. Deviations can

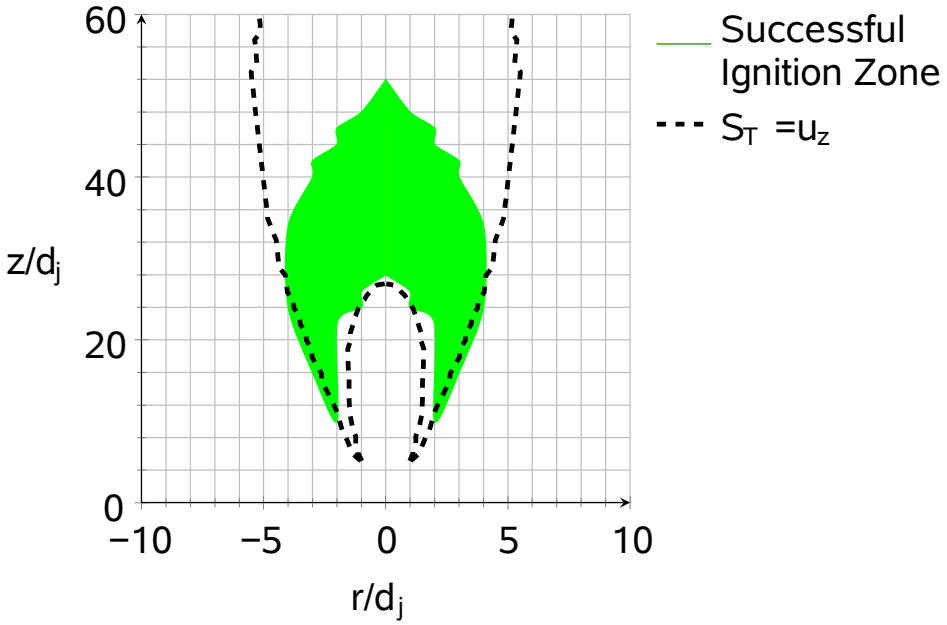

Figure 4.2.8.: **Superposition of the ignitable area determined in the simulation with the dashed line corresponding to $S_T = u_z$ (Turbulent flame speed magnitude equals axial flow-field velocity).**

be observed when looking at the exact time-resolved behavior of the flame. In the simulation the flame almost moves with twice the velocity as extracted from the experiment. However, this may be related to the turbulence modeling which predicts an average level of turbulence and does not include large eddies which can push the flame back or stretch the flame front too extensively and hence slow down the flame propagation. Thus, for the test case of a jet flame where the flow-field is dominated by fluctuations in the steam wise direction, the propagation velocity of the flame is overpredicted. As the turbulent kinetic energy is equally distributed in all three directions, the strong stream-wise dependence is lost, non-accounting for the real influence of the large eddies. In this context a LES can certainly achieve a better agreement.

4.2.7. Conclusion

At first, the objective of gaining comparable cold flow velocity fields between experiment and simulation is accomplished. This is necessary to ensure that the ignition is started with the same initial boundary conditions. To achieve this task, a model constant of the k-ϵ turbulence model is adopted. It is highlighted that the k-ϵ turbulence model has limitations when applied to configurations which possess one main flow direction which are mitigated by the modification. With a reasonable agreement in the cold flow velocity and scalar mixing field, the ignition studies are performed. The comparison between the simulation and the experiment shows that the model delivers a satisfying prediction of the ignition probability within the domain. Zones in which the ignitability remains low in the experiment fail in

the respective computation as well. The lateral confinement of the zone with high ignition probability is correctly captured by the model, just as the increase in ignitability at the frontal zone of the jet. Only the downstream parts exhibit slight deviations in which the ignition probability is overpredicted to a certain extent. Overall, the model demonstrates its appropriateness to provide an adequate picture of favorable and unfavorable locations for ignition. A coupling of the extended TFC model to LES might improve the accuracy of the prediction in the downstream part of the jet.

5. Simulation of Highly Turbulent Flows

This paragraph concerns results of a more complex, highly turbulent, single phase configuration. The presented test case serves as an extension of the envisaged model range from basic flow-field conditions in the previous chapters to flow-field conditions which are relevant to full scale combustors. Two numerical approaches are employed and compared to each other. A URANS simulation is studied first with a subsequent repetition of the simulation with a SAS approach. A comparison with available experimental data is included to allow a thorough assessment of the obtained results.

5.1. Enclosed Jet

In order to evaluate the capability of the model to describe highly turbulent flames, this chapter provides results concerning the outcome of simulations of a high velocity jet flame. Experimental and numerical results related to this configuration have been published by Lammel *et al.* [89] and Di Domenico *et al.* [43, 45]. The previous test cases involved several phenomena which are relevant for aircraft engines, however, the level of turbulence was chosen to be of moderate order for the sake of simplicity. The particular aspect of strong turbulence is highlighted in the following, in which the flame is dominated by turbulence effects which also includes flame quenching. The environment of this test case is purely gaseous, therefore, avoids the issue of droplet modeling. The employed fuel is methane. A series of measurements was performed by Lammel *et al.* [89] for this test case comprising several settings for the inflow conditions. Since this investigations aims at assessing the specific model capabilities with respect to extensive turbulence and the effect of flame quenching, only a single set of boundary conditions, corresponding to the most challenging one, is chosen for comparison. Furthermore, the differences between using a LES technique and a URANS approach are examined. Concerning ignition, as the emphasis of the experimental investigation was not put on deriving ignition statistics, no data is available to compare the flame kernel development. However, in this work, a numerical study is included which comprises three different igniter locations. The differences that occur in the outcome of the ignitions, once more, point out that the selection of the ignition position is crucial for lighting-up a combustor. This contributes to the aim of this work which is to develop numerical tools to efficiently predict

ignition behavior.

5.1.1. Test Case Set-Up

A schematic of the test case is provided in Fig. 5.1.1. The reader is referred to previously published papers by Di Domenico *et al.* [43] and Lammel *et al.* [89] for additional information. In this paragraph only the major characteristics of the burner shall be outlined. The burner comprises a single jet nozzle with an inner diameter D and a rectangular combustion chamber with a cross subsection of $5D$x$4D$ stacked together to a height of $h = 60D$. The nozzle tip is located at $2D$ above the burner base plate. The set-up is non-symmetrical with the nozzle being installed at $3.5D$ with respect to the longer side and $2D$ in perpendicular direction. This is illustrated in Fig. 5.1.3. The purpose of the off-center arrangement is to generate a pronounced recirculation zone at one side of the flow. In the scope of the measurements, Raman scattering was applied to derive information about the species concentration. Additionally, the PIV technique was employed to measure the flow-field.

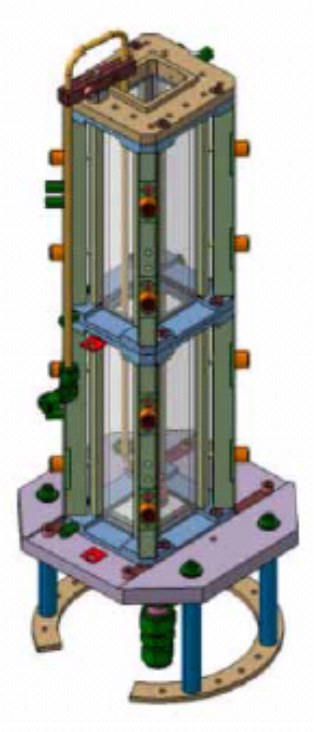

Figure 5.1.1.: **Schematic illustration of the confined jet flame burner, see Lammel *et al.* [89].**

5.1.2. Numerical Representation

The numerical domain is depicted in Fig. 5.1.2. Note that the total length has been chosen in such a way that disturbances from the outlet are minimized. The plots are normalized, according to the scaling quantities as given in Table 5.1, since the absolute values are not

Table 5.1.: **Scaling quantities for the enclosed jet.**

Scaling Quantities	
Length Scale	Nozzle Diameter
Temperature Scale	Adiabatic Flame Temperature with respect to the inlet conditions
Velocity Scale	Inlet Velocity

permitted for publication. The flame within this set-up is stabilized by recirculation zones as no extra flame holder is present. The design is non-symmetrical, which is illustrated in the slice B-B, see Fig. 5.1.3 which is extracted from Fig. 5.1.2. The domain is slightly enlarged in y direction. Through the non-median location of the nozzle in y-direction, a large recirculation zone can develop at the wider side of the channel. Boundary conditions for the numerical simulation are given in Table 5.2. The domain temperature prior to ignition equals the jet inlet temperature. Detailed information of the inflow conditions are also provided in Table 5.2. After the ignition, an isothermal condition for the domain wall with $T = 0.377 \cdot T_{\mathrm{ad}}$ is imposed to account for heat losses as the walls are connected to the cooling ambient air. The chosen temperature gave a good agreement in previous simulations, see Di Domenico *et al.* [45].

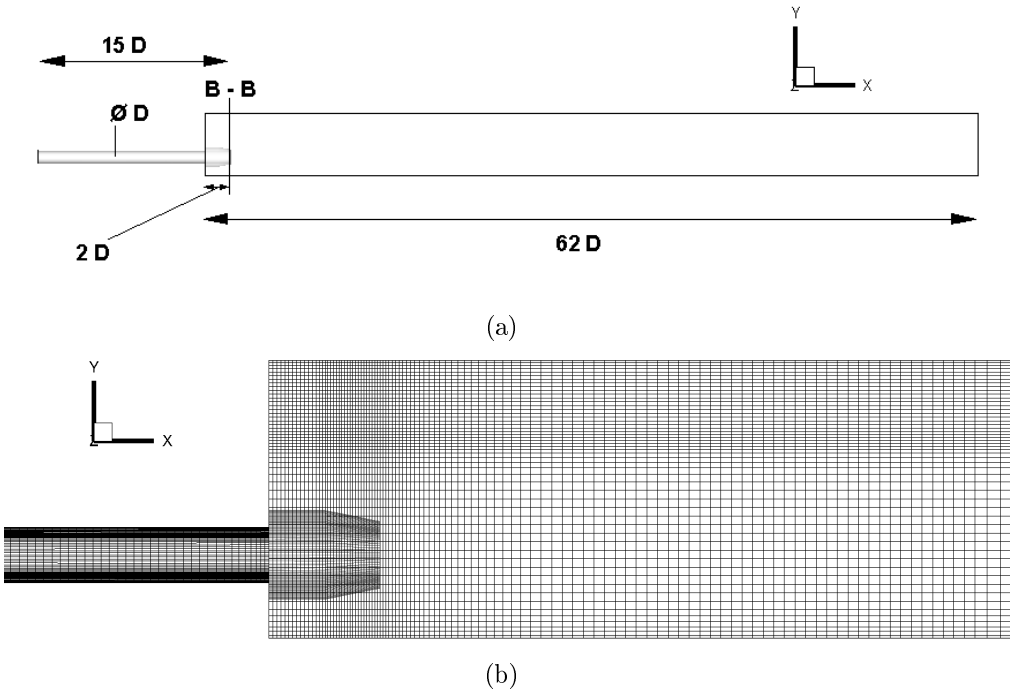

Figure 5.1.2.: **a) Side view of the domain. A part of the inlet tube is included in the calculation to obtain a reasonable turbulent inflow. b) Mesh in the inlet region.**

The total number of cells employed for this domain amounts to $\sim$ 2,000,000 purely hexagonal grid cells which enables a fine resolution in the near exit zone as depicted at the bottom of

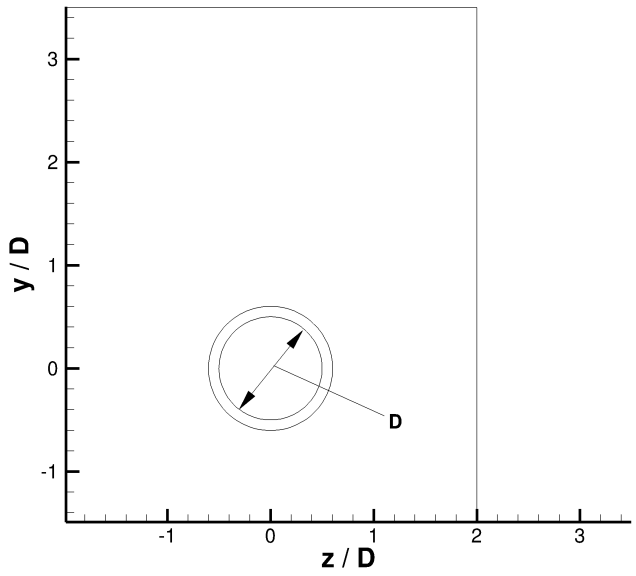

Figure 5.1.3.: **Slice B-B extracted as outlined in Fig. 5.1.2. Note that the test case is highly unsymmetrical. The inlet emerges displaced with respect to the y-axis center. The domain itself is slightly larger in y direction than in z direction**

Fig. 5.1.2. This allows a simulation in either RANS or LES-like mode. Note that the SAS model [114, 115] is employed when referred to a LES-like calculation. The SAS switches to a LES mode in regions which exhibit high turbulence and remains in a URANS mode near the walls and in areas with coarse grid resolution or moderate turbulence. The imposed degree of turbulence at the start of the inlet is rather low which will eventually grow within the pipe. As this test case is highly unsteady only transient simulations have been performed. Attempts with steady computations could not converge to a satisfying level.

Table 5.2.: **Boundary conditions for the enclosed jet.**

General	2,000,000 Grid cells
Inflow Walls	Turbulent, adiabatic
Domain Walls	Adiabatic in cold flow
	Isotherm $T = 0.377 \cdot T_{\mathrm{ad}}$ in reactive flow
Outlet	Pressure outlet
Normalized Jet Inlet Velocity	1 [-]
Normalized Equivalence Ratio (Φ)	1 [-]
Normalized Inlet Temperature	0.266 [-]
Turbulence Length Scale	1 cm
Turbulence Intensity	0.05 %

5.1.3. Cold Flow

A cold flow comparison reveals that smaller changes occur between the URANS and SAS simulation. One finding is that in the URANS cold flow solution only the larger recirculation zone is present which develops in the upper part of the chamber. At the lower part in which the inlet is located, no recirculation zone can evolve between the jet and the close wall. An illustration of the flow-field of the SAS calculation is provided in Fig. 5.1.4 which shows a snapshot of the unsteady flow-field (top) and the averaged converged flow-field (bottom). For a more detailed overview, Fig. 5.1.5 displays the computed normalized averaged x-velocity of the SAS simulation near the jet exit and the recirculation zones.

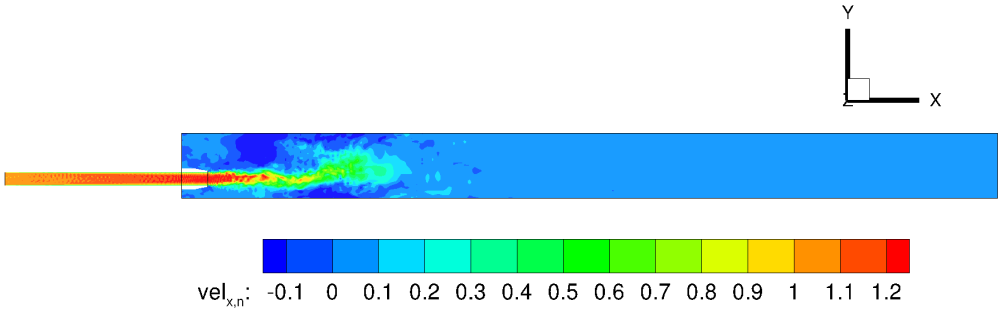

(a)

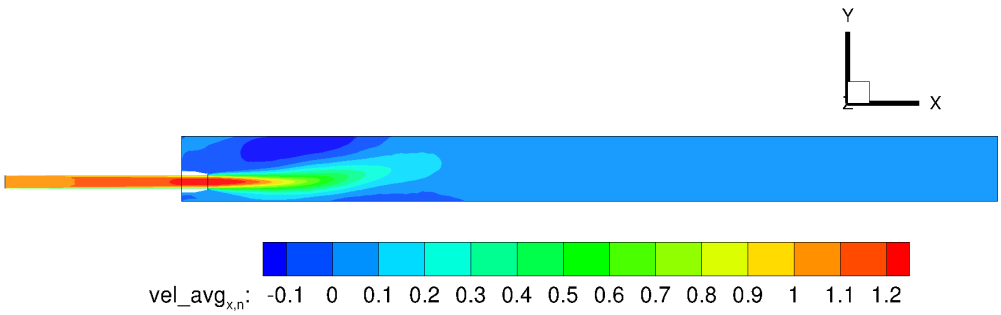

(b)

Figure 5.1.4.: **Cold flow results of the normalized x-velocity for the SAS simulation. (a) Snapshot. (b) Averaged solution.**

Results of the URANS simulation regarding the entire flow-field are presented at the top of Fig. 5.1.6. For a comparison to the SAS results, the recirculation zones in the vicinity of the jet exit obtained in the URANS calculation are highlighted at the bottom of Fig. 5.1.6.

The major difference pointed out qualitatively in the contour plots is the lack of the smaller recirculation zone at the bottom of the domain. The jet in the URANS simulation is not bent upwards which affects the development of the flow-field and causes the absence of the second recirculation zone. Velocity profiles for the axial velocity are presented in Fig. 5.1.7. The plot underlines the findings quantitatively. The largest deviances occur at the $x = 10D$

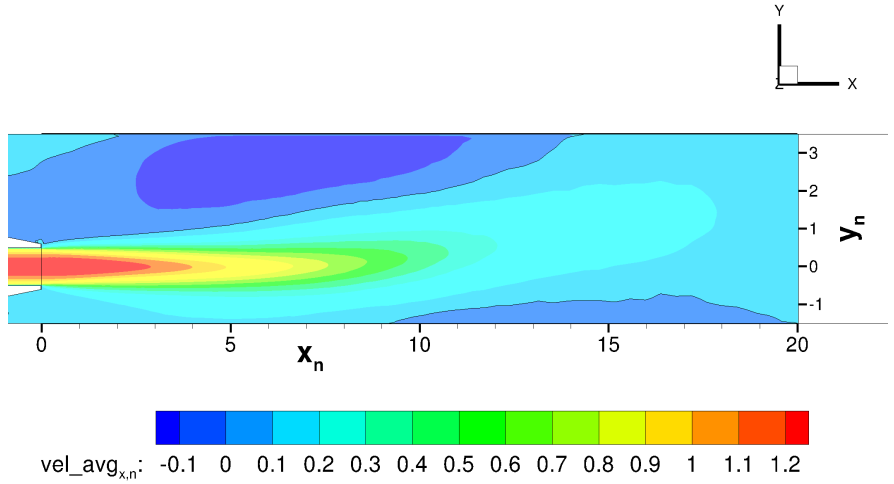

Figure 5.1.5.: **SAS computed detailed contour plot of the normalized x-velocity in the inlet region. Solid lines mark the recirculation zones.**

downstream plane for which the URANS solution does not exhibit the smaller recirculation zone. Therefore, the peak velocity remains almost undisplaced at the nozzle inlet position

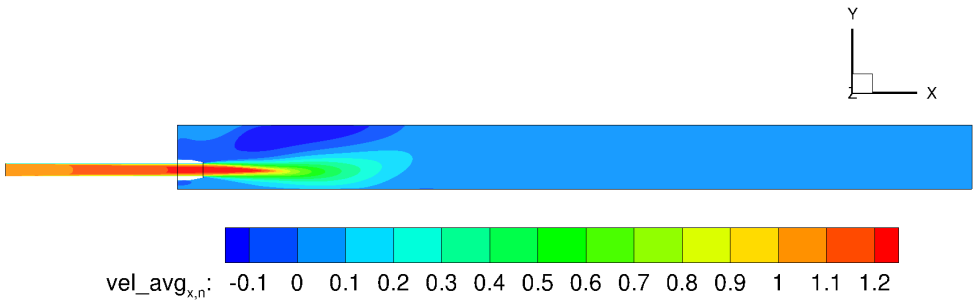

(a)

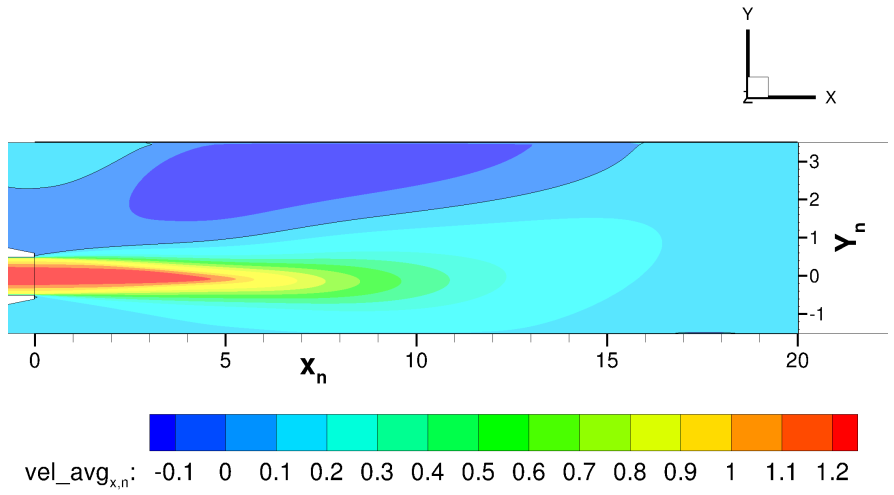

(b)

Figure 5.1.6.: **Cold flow results of the normalized x-velocity for the URANS simulation. (a) Entire domain. (b) Inlet region.**

at $y/D = 0$ whereas the SAS simulation predicts the peak velocity to be slightly displaced in-between $y/D = 0$ and $y/D = 0.5$. The velocities are higher for the regions in which the smaller recirculation in the SAS simulation occur. On the broader side the differences disappear as both simulations predict the establishment of a large recirculation zone in that region which will later stabilize the flame. In total, the differences in velocity between both results are relatively small which enables a good comparability of the reactive flow simulation.

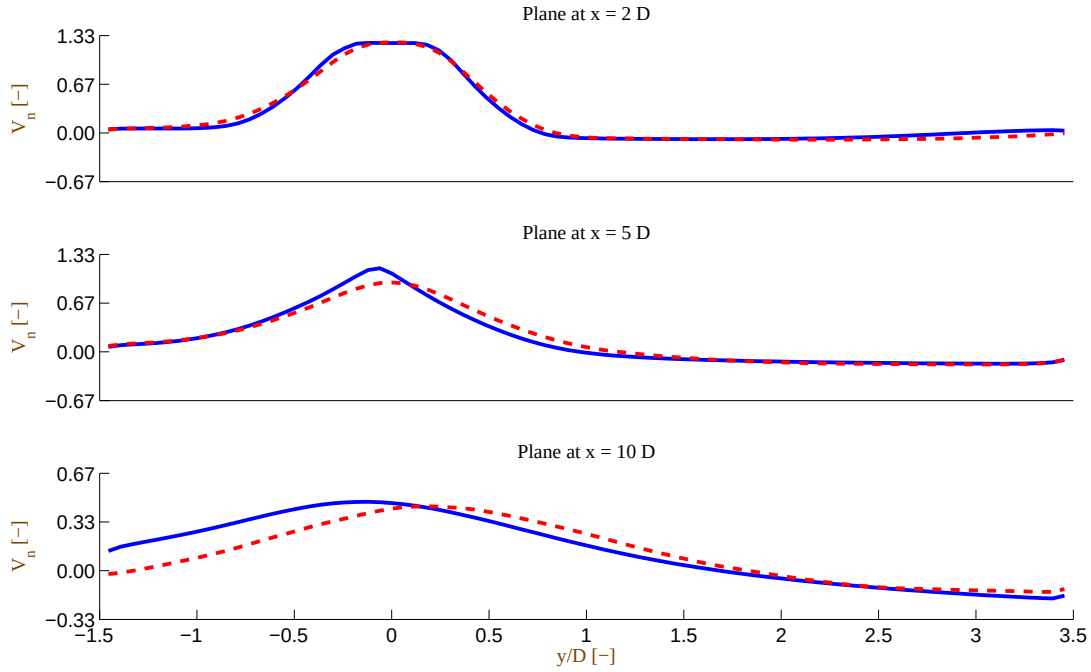

Figure 5.1.7.: **Cold flow comparison for the axial velocity of the averaged SAS and URANS simulation. Solid blue lines correspond to the URANS simulation. Dashed red lines represent the SAS results.**

The corresponding turbulence levels are illustrated in Fig. 5.1.8. Overall the scale of turbulent kinetic energy agrees for all investigated planes. However, a slightly elevated turbulence intensity is observed for the SAS simulation which probably plays a significant role in dissolving the jet momentum. Due to the higher turbulence level, the jet mixes faster with the surrounding mixture which results in a broadening of the jet. The broader jet leads to higher velocity gradients in the vicinity of the lower wall at which the velocity remains zero as a consequence of the no-slip condition. This eventually causes a roll-up of the flow which manifests itself in the recirculation zone. The jet sees the lower recirculation zone as an obstacle which leads to the upward bending of the jet which is not observable in the URANS simulation. The slightly higher turbulence intensity in the SAS simulation also entails a fast dissolution of the turbulence double peak as opposed to the URANS results in which the double peak is still present at the $x = 5D$ plane. For later axial planes the differences decrease as the jet mixes with the surrounding gas in the URANS simulation.

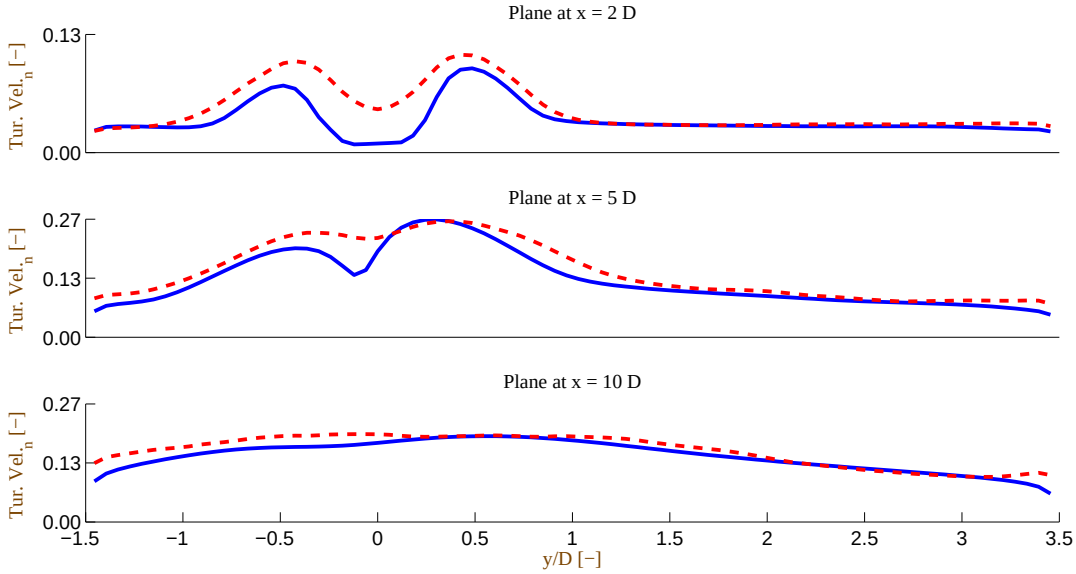

Figure 5.1.8.: **Cold flow comparison for the turbulent intensity of the averaged SAS and URANS simulation. Solid blue lines correspond to the URANS simulation. Dashed red lines represent the SAS results.**

5.1.4. Reactive Flow

The cold flow results have pointed out that although some deviations are present in the flow-field, the initial conditions are overall similar. This supports the expectation that the flame shape and behavior will also be comparable. Once the flame has developed and stabilized in the domain, the time averaging is started. A subsequent section is dedicated to the question of ignitability of this set-up, whereas in this paragraph the focus is on the time-converged solution for the flame. The results from the cold flow point out that the flow is highly unsteady. Thus, for the reactive simulation, again only URANS simulation and SAS simulations are considered. The former observations of the cold flow have indicated that the lower recirculation zone is missing in the URANS simulation. In the results for the reactive flow-field, it is observed that the recirculation zone remains suppressed for both, the URANS and SAS method, which further reduces the remaining influence of the cold flow solution.

The purpose of this test case is to evaluate the quenching mechanism embedded in the model as described in Sec. 2.2.1. It was determined in the experiment that the flame is lifted from the jet exit as the high turbulence and velocities in that region impede the stabilization. The stabilization mechanism of the flame is based on the large recirculation zone at the top of the domain. This flow structure ensures that the flame can propagate backwards and remain in the domain albeit the very high mean velocities. The objective is to evaluate whether the prediction from the simulation is able to capture the flame shape and stabilization mechanism.

Several combinations are investigated which are listed in Table 5.3 with their corresponding

Table 5.3.: **Inlet conditions for the confined jet test case.**

	Identifier
URANS SST - Quenching Factor of 1.0	CJ1
URANS SST - Quenching Factor of 2.0	CJ2
URANS SST - No Quenching	CJ3
SAS SST - Quenching Factor of 10.0	CJ4

identifier. The quenching factor relates to a multiplier present in the correlation for G, see Eq. (2.2.17). It scales the quenching term which is proposed by Zimont [199]. The quenching term ifself acts as a pre-factor for the turbulent flame speed. This factor guarantees that the value for the turbulent flame speed does not increase infinitely with increasing turbulence which would be physically wrong. On the contrary, once the turbulence level is too high, turbulence impairs the combustion which is caused by small eddies penetrating the reaction zone. This effect has to be incorporated in the correlation for the turbulent flame speed to account for flame quenching by turbulence. However, it was remarked by Polifke *et al.* [135] that the determination of the critical dissipation rate which governs the quenching term is still an open issue. In their work, a critical strain rate for methane was suggested which is tested in the scope of this numerical study. In order to obtain more experience with the model, especially in the context of SAS simulations, variations of the critical strain rate by the multiplication with a quenching factor are included.

Figures 5.1.9 and 5.1.10 contain results of the URANS SST simulations and a comparison with experimental data for the temperature of different x-planes for the configurations CJ1 and CJ2. In general for URANS simulations including a quenching term which are shown in Fig. 5.1.9, the flame for $x < 5D$ covers the top half ($y/D > 0.7$) of the domain whereas the flame is quenched in the jet center ($0.7 > y/D > -0.3$) and burns with reduced temperature due to wall cooling effects for $y/D < -0.3$. The flame cannot enter the jet as the high mean velocity does not allow the flame to propagate backwards. Additionally, the flame cannot enter the jet from the sides, as the high strain rates in the shear layer quench the flame. The large recirculation zone represents the stabilization mechanism for both URANS cases. This is in accordance to the experimental findings which also indicate that no reaction occurs in the jet itself and further point out that the temperature is significantly reduced at the lower side of the burner ($y/D < -0.3$). The experimental data shows even lower temperatures for $y/D < -0.3$ suggesting that the thermal flame quenching is more pronounced than in the simulation for $x =< 5D$. This could be related to the wall temperature which might have a significant influence at the beginning of the domain. It was found out by Di Domenico *et al.* [45] that a constant wall temperature of ~ 800 K yields a good agreement in terms of flame behavior for the reactive flow. Measurement of the wall temperature from the experiment are not available. However, it appears more realistic that the wall temperature takes on a

non-constant profile with lower temperatures at the beginning of the domain, taking into account that the jet inlet walls will probably have the same temperature as the jet itself and may act as a heat sink. The wall temperature might than increase with the burner length. This non-constant wall temperature could explain the reduced flame temperatures at the beginning of the domain. This is not resolved in the simulation as a fixed iso-thermal value of 800 is prescribed for the burner walls. After $x = 5D$ this effect diminishes and the agreement improves. After $x = 15D$, both the experimental data and the numerical results show that the flame spreads over the entire cross sectional area of the domain. The outcome is promising since the simulation correctly predicts the absence of the flame in the jet and the reduced temperatures below the jet ($y/D < -0.3$) which shows that the critical strain rate determined by Polifke *et al.* [135] is of satisfying quality. It further demonstrates that the model is able to capture promoting and detrimental effects of turbulence and wall heat losses. The differences between quenching multiplication factor of 1 and 2 are not very large which would allow to omit this factor in further URANS studies. This is explained by the different regimes which evolve in this test case. Due to wall cooling effects the effective laminar flame speed is significantly reduced in near wall regions which suppresses the flame in conjunction with detrimental turbulence effects. Consequently, both configurations predict a reduced proceeding of the reaction at the lower side ($y/D < -0.3$) of the combustor. Most of the reaction takes places further downstream where the turbulence levels have abated. The onset of the reaction is only marginally influenced by the quenching multiplication factor. Only slightly higher temperatures can be observed for the factor 2 than for the factor 1.

At the top of Fig. 5.1.10 in which the results of the unquenched flame are illustrated, the consequences of not accounting for negative turbulence effects become apparent. In case the quenching factor is missing in the correlation for the turbulent flame speed, turbulence always acts as an enhancement to the flame speed value. This is physical within the wrinkled and corrugated regime, however, becomes more and more inapplicable for the high turbulence levels beyond these regimes. Once the smallest turbulent structures are able to enter the reaction zone of the flame, they will impede the ongoing reactions which will at first reduce the flame speed and for stronger turbulence completely prevent the combustion. Without quenching, the agreement of the temperature profiles with respect to experimental data is very poor. High temperatures occur in the shear layer as the high turbulence in this region boosts the reaction. Therefore, the flame is not lifted as in the unquenched RANS simulation in which the hottest temperatures occur further downstream. Furthermore, the flame can also sustain in the smaller part of the channel at the bottom. For all other configurations lower temperatures are observed in this region which result from quenching effects and wall cooling.

The SAS simulation, as shown at the bottom of Fig. 5.1.10, exhibits very similar features as the URANS computation in the temperature profiles. It also correctly predicts the quench-

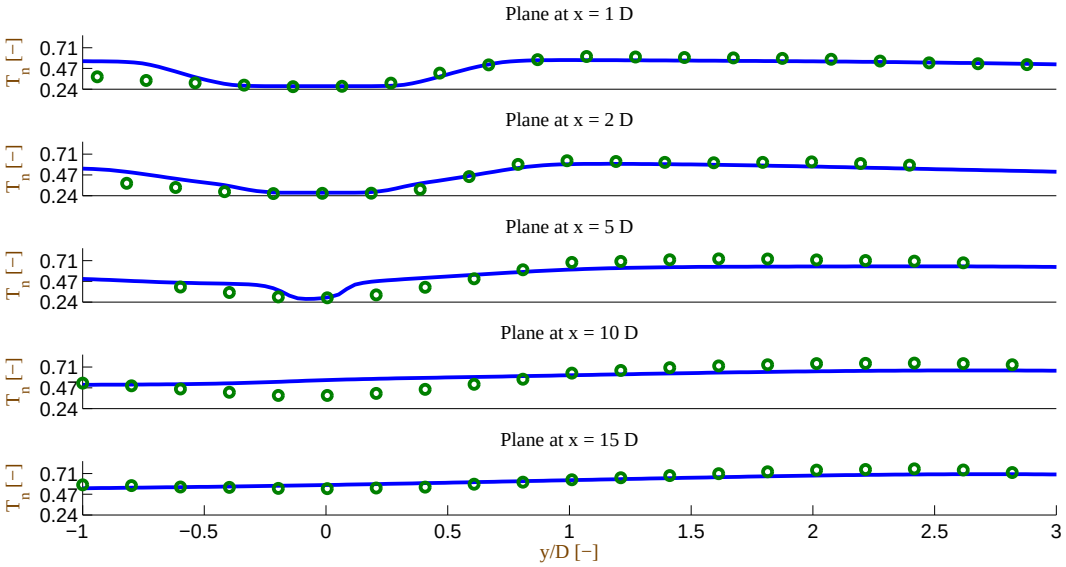

(a)

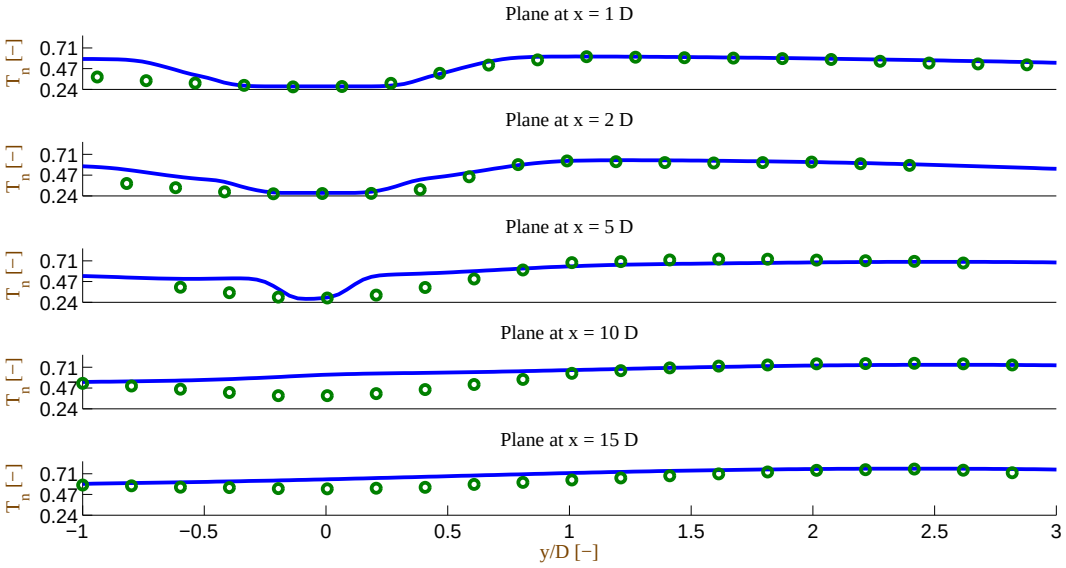

(b)

Figure 5.1.9.: **Comparison of the normalized temperature for the configuration CJ1 and CJ2. The profiles are extracted at several x-planes in y-direction. Dots represent the experimental data [89]. (a) Plot for the CJ1 configuration. (b) Plot for the CJ2 configuration.**

ing of the flame in the shear layer and shows a smooth temperature increase towards the combustor walls. The same finding that the temperature at the lower side of the domain ($y/D < -0.3$) is overpredicted as is observed in the URANS simulation is made. As is remarked in the URANS results, reduced wall temperatures at the beginning of the domain in the experiment may be the cause for these deviations. The jet temperature increases a little

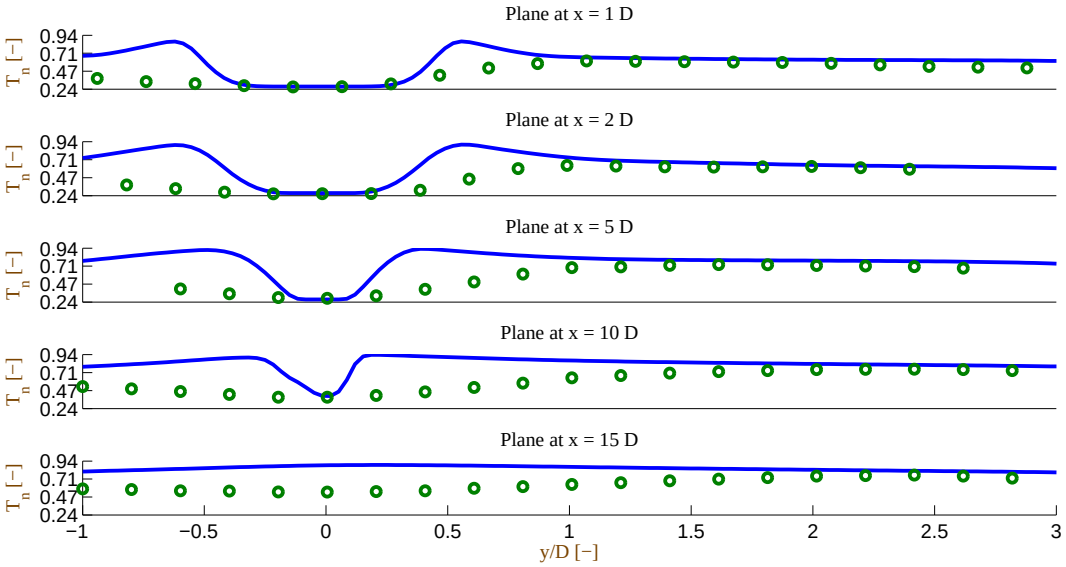

(a)

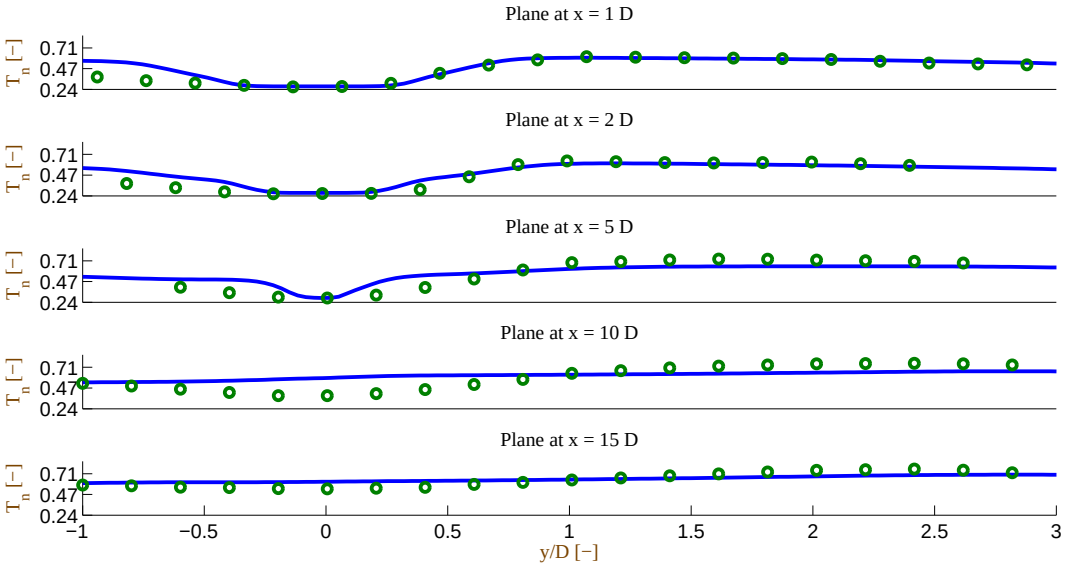

(b)

Figure 5.1.10.: **Comparison of the normalized temperature for the configuration CJ3 and CJ4. The profiles are extracted at several x-planes in y-direction. Dots represent the experimental data [89]. (a) Plot for the CJ3 configuration. (b) Plot for the CJ4 configuration.**

too early (at $x = 5D$) as was also seen in the URANS results. The reduced temperatures at the lower side of the domain ($y/D < -0.3$) can be one reason for this. Additionally, the jet in both, the URANS and the SAS simulation mixes slightly too early as is apparent from the velocity comparison (see Fig. 5.1.11 and Fig. 5.1.12) which can also result in a flame position which is more upstream than in the experiment. Concerning the modified value of

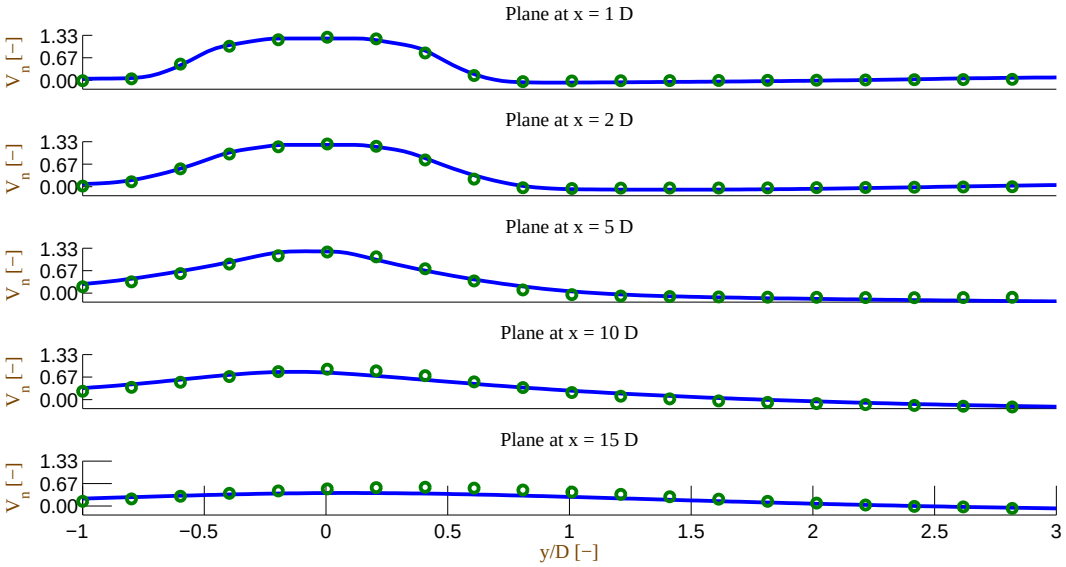

(a)

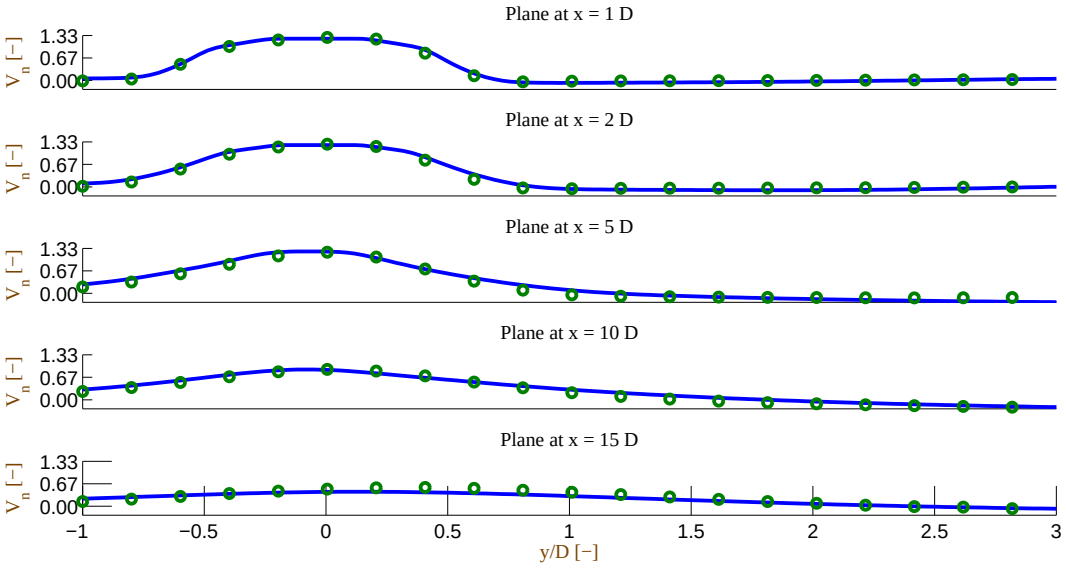

(b)

Figure 5.1.11.: **Comparison of the normalized axial velocity for the configuration CJ1 and CJ2. The profiles are extracted at several x-planes in y-direction. Dots represent the experimental data [89]. (a) Plot for the CJ1 configuration. (b) Plot for the CJ2 configuration.**

the quenching factor, the explanation given in Sec. 2.2.1 applies. Due to the reason that in SAS, a large part of the turbulent spectrum is modeled, the resolved eddies intrinsically diffuse the flame and, thus, contribute to flame quenching. Therefore, the quenching factor is set to 10, reducing the influence of the quenching term, which shows a good agreement with the experimental data. The quenching factor cannot be omitted completely as the

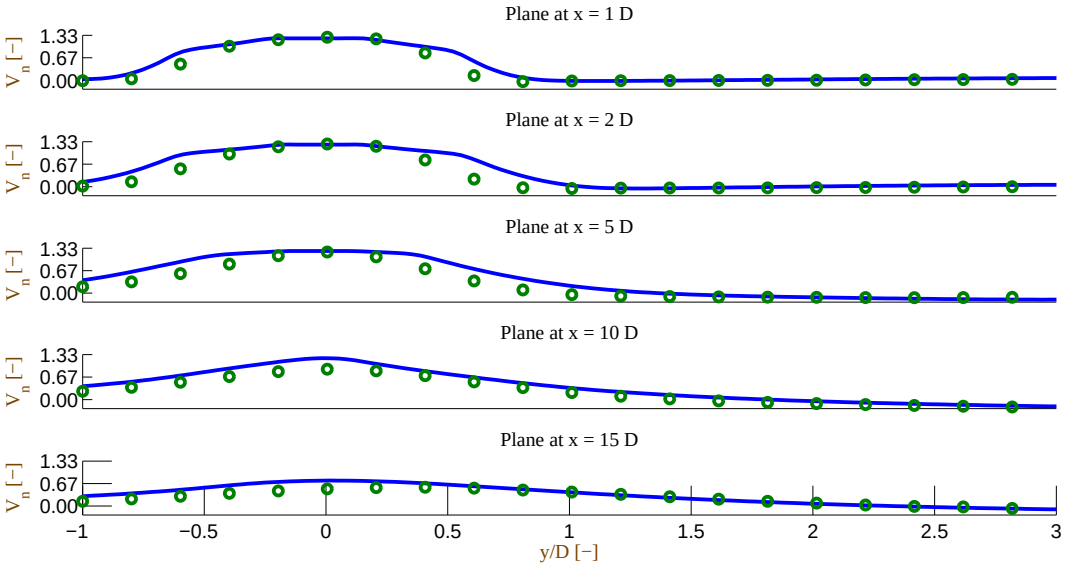

(a)

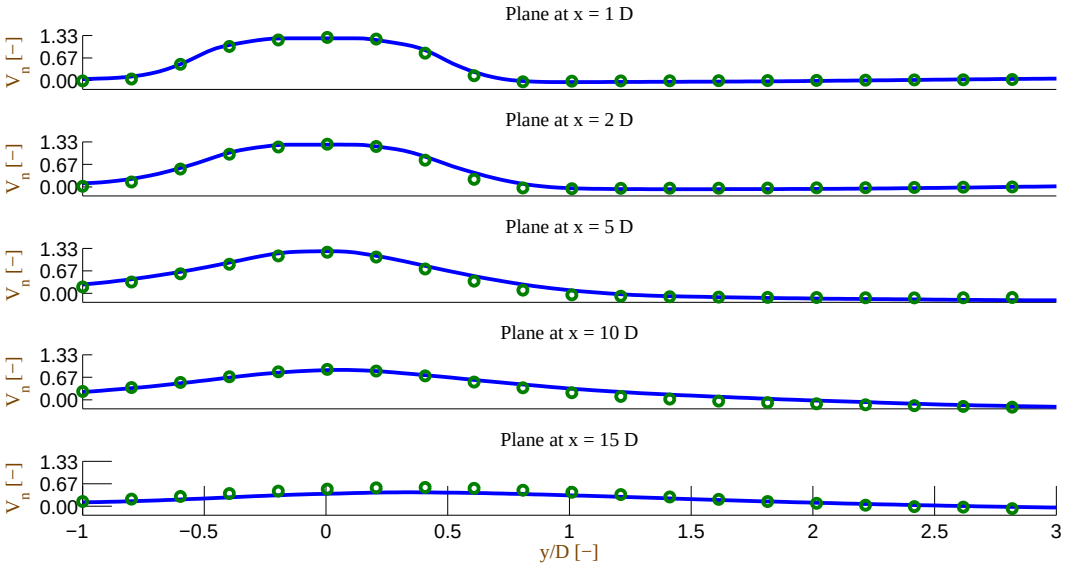

(b)

Figure 5.1.12.: **Comparison of the normalized axial velocity for the configuration CJ3 and CJ4. The profiles are extracted at several x-planes in y-direction. Dots represent the experimental data [89]. (a) Plot for the CJ3 configuration. (b) Plot for the CJ4 configuration.**

sub-grid turbulence needs to be accounted for. SAS results without quenching factor have shown that the temperatures are slightly overpredicted, however far less than for the URANS simulations.

A comparison of the velocity profiles for different x-planes is provided in Figs. 5.1.11 and 5.1.12. The agreement is satisfying for configurations involving a quenching term. Larger

deviations are observable in the URANS simulation without quenching at the top of Fig. 5.1.12. The region of high velocity is considerably overpredicted as compared to the other simulation as a consequence of the high shear layer temperatures. Concerning the other configurations, the differences which were present in the cold flow have partly vanished. In particular, the recirculation zone at the bottom has ceased to exist. This is due to the lower densities within the flame which have reduced the turbulence and, thus, decreased the momentum exchange which was essential for the formation of the lower recirculation zone.

5.1.5. Ignition Location Study

A study concerning three ignitions performed at different locations shall highlight the model capabilities of describing the flame development process in the context of complex flow-fields. This set-up, involving a high velocity jet, exhibits features that are also typical for real combustors in aero-engines. Therefore, the investigation contributes to shedding light on how to select the location of the igniter in a technical combustor. For the example of a high velocity jet in a confined domain, two aspects play a major role, which are the strong recirculation zones at the sides of the jet and the high mean flow velocity which is adapted further downstream. Ignition is essentially promoted in the recirculation zone as the mean flow direction allows the kernel to travel upstream towards the jet exit. Ignition becomes more difficult the further downstream the igniter is located since the flame kernel has to travel a long distance until it reaches the supply with fresh fuel. However, ignition is still accomplishable beyond the axial position of the recirculation zones as the prevailing high levels of turbulence lead to a significant enhancement of the turbulent flame speed.

The ignition in this numerical examination is performed at $x = 10D$, $x = 20D$ and $x = 30D$ axial position and at $3D$ in perpendicular direction. The total energy delivered to the domain equals 1 J which is released in a spherical volume of r=7.34 mm. To illustrate the different prevailing conditions, Fig. 5.1.13 presents normalized contour plots of the velocity of the turbulent flame speed minus the mean flow velocity. Hence, a positive value means that at this location the flame can overcome theoretically propagate against flow.
The results point out that close to the nozzle exit at $x = 10D$ the larger part of the cross subsection allows the flame to travel backwards. The region becomes smaller for $x = 20D$ and for the furthest downstream location, the flame can only transverse upstream close to the walls. However, due to the heat losses at the wall the flame cannot successfully propagate against the mean flow. The non-adiabatic conditions cause wall heat losses which eventually reduce the laminar flame speed, see Sec. 2.2.2, and lead to thermal quenching of the flame.

The x-locations of the flame edges and the flame center are depicted for all ignition sequences in Fig. 5.1.14. The results show that for the further upstream locations the flame kernel succeeds in lighting the entire domain. The fastest flame growth is observable for the $x = 10D$

ignition. The location is completely inside the recirculation zone which allows the kernel to travel upstream close to the nozzle exit. Furthermore, since high velocities persist in the jet and in the layers around the jet, once the combustion has reached those zones, the reaction is also convected downstream rapidly.

The same phenomena apply to the ignition at $20D$. The ignition is significantly enhanced after 3ms when the combustion zone touches the area with high bulk velocity and is subsequently convected with the mean flow. Concerning the ignition at $30D$: The mean flow velocity exceeds the turbulent flame speed apart from near wall regions. However, since this describes the state before ignition, no heat losses have occurred, yet. Furthermore, both, the mean flow velocity and the turbulent flame speed are rather small at the sides of the domain. In the near wall region, the velocity of the mean flow tends to zero due to the no-slip boundary condition. The laminar flame speed eventually also approaches zero, once the thermal losses at the wall have become too large. This hinders the flame from propagating backwards. The flame center rapidly shifts towards the end of the channel, since the downstream flame edge spreads and is convected at the same time. In the subsequent stages, also the upper flame edge is slowly transported out of the domain. This underlines the importance of the location of the ignition in order to successfully light the domain. Without the knowledge of a suitable position, the ignition kernel, although the total energy amount may suffice, cannot produce a fully stabilized flame.

5.1.6. Conclusion

The test case of a high velocity jet flame is successfully simulated with the extended TFC model. The good agreement in the temperature profiles points out that the model is capable of resolving quenching processes and suppresses unphysical burning of the flame in regions with too extensive turbulence. It is shown that the outcome of the simulation is only little influenced by the value of the quenching factor which scales the quenching term. Due to the large differences in turbulence intensity between regions with extensive turbulence, such as shear layers, and homogeneous flow regions, the scaling of the quenching term has no large impact for a specific type of simulation. For SAS simulation, the quenching factor is increased to a value of 10 to decrease the influence of the quenching term. It is argued that in SAS, the flame is naturally stretched by the resolved eddies which requires a lesser contribution by the quenching term in the combustion model. Both, the URANS and the SAS simulation, correctly predict the shape and stabilization mechanism of the flame. Subsequently, an ignition study is conducted which illustrates the large influence of the position of the igniter on the outcome of the ignition. Solely an ignition kernel which can proceed into the recirculation zone generates a fully self-sustained flame.

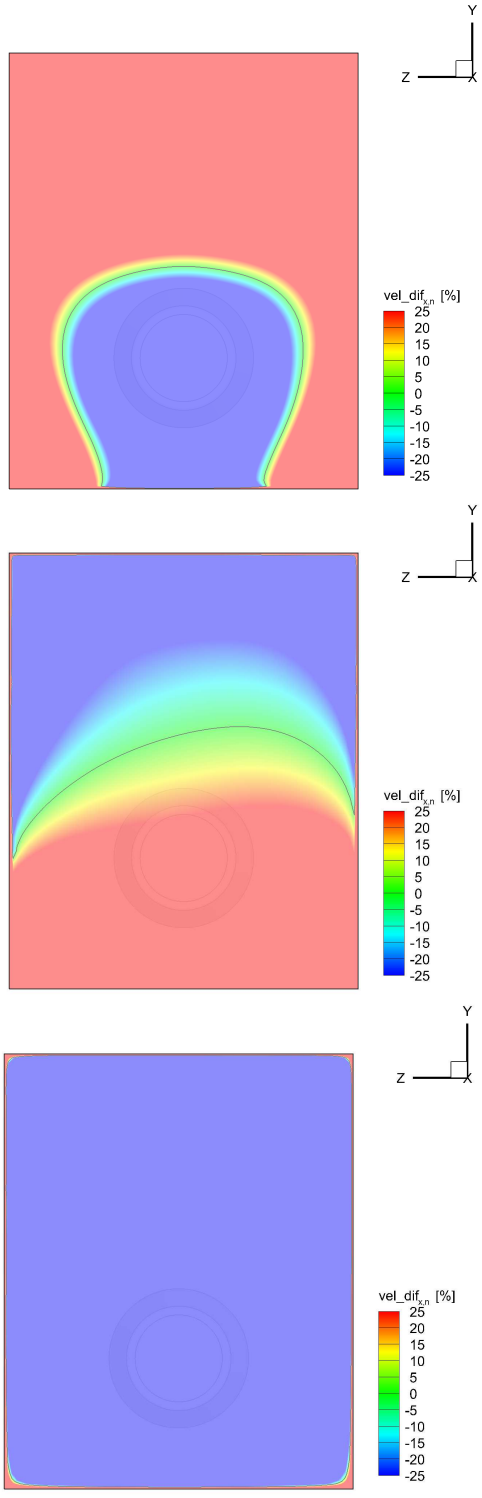

Figure 5.1.13.: **Velocity differences at three x-planes calculated with vel_dif$_{x,n}$ = $(S_T - v_x)/S_T \cdot 100$. The contour plots display the conditions prior to ignition. Top: at $x = 10D$. Center: at $x = 20D$. Bottom: at $x = 30D$. The iso-line corresponds to the value of 0. Yellow to red values indicate that the turbulent flame speed is higher than the mean flow velocity. The blue colors indicate that the mean flow velocity is higher than the turbulent flame speed.**

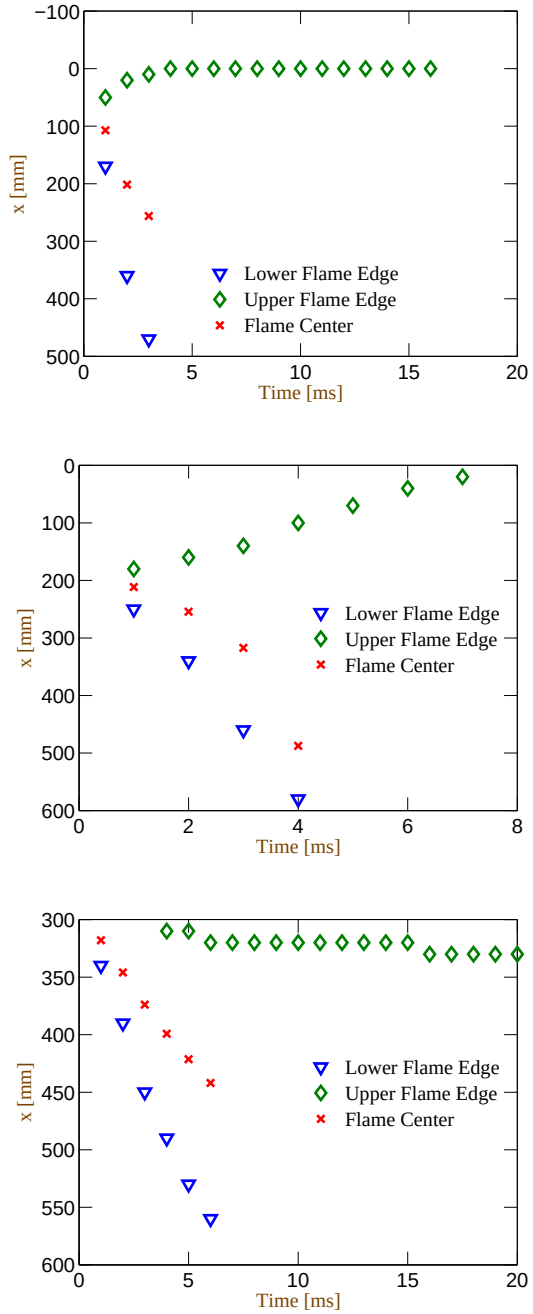

Figure 5.1.14.: **Flame edge and flame center positions following ignition at $t = 0$s. Note that the y-axis is inverted to comply with the wording of "lower" flame edge. Top: Ignition carried out at $10D$. Center: Ignition carried out at $20D$. Bottom: Ignition carried out at $30D$.**

6. Simulation of Ignition in Multiphase Flows

The previously presented test cases, apart from one multiphase configuration in the validation, were intended to establish the reliability of the new model formulation for single phase flows. However, the standard implementation of the TFC model offers also an appropriate capability to accomplish satisfying predictions for single phase flows in complex geometries. Thus, the advantages of the developed model extension could not be explicitly assessed. An improvement was shown by incorporating an energy source as means to establish an initial flame kernel which enables a closer modeling of the physical relevant processes. The most significant new capability of the model, however, is its adaptation to multiphase flows. The elementary integrity of the multiphase extension was illustrated in the validation part in Sec. 3.3. To further underline the multiphase applicability, the last chapter presents two sophisticated test cases to demonstrate the model performance for complex multiphase configurations. The first test case is a set-up which has been studied experimentally at the DLR in the scope of the TIMECOP-AE project which has yielded a profound data set. The second configuration involves higher Reynolds numbers and a technical spray nozzle which renders this test case as the most engine-like application of the model testing. Through the LuFo IV project, a broad experimental data base for comparison is also available for this set-up.

6.1. Droplet Chains

This first examined multiphase test case serves as benchmark for the model capabilities concerning ignition under multiphase conditions. Detailed numerical results have been published in [18, 20]. The previous test cases showed that a good agreement is achieved for purely gaseous configurations in terms of predicting favorable igniter positions. In a multiphase environment, ignition can become more difficult as it may occur that insufficient fuel vapor is present to sustain a flame. This problem becomes evident for example at high altitude relight at which the prevailing conditions allow only a very limited amount of the kerosene to evaporate. Hence, the flame kernel generation by a heat source must entail an evaporation of surrounding droplets and a subsequent auto-ignition of the mixture. To approach the topic of multiphase ignition, the investigated test case operates with a droplet generator as fuel supply which is mounted in a rectangular channel. These rather basic geometric conditions

ensure that the phenomena of flame kernel generation can be studied without disturbances stemming from complex boundary conditions and facilitate the reproducibility of the results. Mosbach and Gebel [121] performed a comprehensive measurement campaign which is the ground for the presented comparison. The major aspects of the accomplished experimental investigation were the determination of the location of the flame kernel, the growth and convection of the flame kernel and the ignition probability. For these purposes, the spatial evolution of the OH and fuel concentration were captured using a planar laser-induced fluorescence (PLIF) technique. The ignition conditions were kept constant with the laser being focused on a volume containing 240 ± 10 droplets. The key findings of the experimental study were as follows. The ignition probability decreases strongly with the fuel mass flow and does not depend on the air co-flow for volume flows above 120 SLM. The fuel vapor in the region of the laser-ignition is far below the lower flammability limit for safety precautions. Fuel vapor and radicals necessary for the flame initiation are produced during the ignition process, see Fig. 2.2.3. A flame kernel is established in the droplet-free region generated by the laser ignition. Due to the short residence time of the fuel droplets in the flame, the droplets are able to pass the flame and generate vapor outside the ignition zone. Therefore, a successful flame generation depends on the initially deposited heat, e.g. the thermal area loading and the droplet velocity, e.g. the droplet residence time in the flame. These characteristics define the observed flame in the experiment and constitute the framework of the evaluation for the numerical simulation.

6.1.1. General Features

The set-up of the investigated test case is displayed in Fig. 6.1.1 which contains a frontal view and illustrates the dimensions. The channel has a cross section of 6200 mm^2 along its length of 1 m. For the numerical study, the length is limited to 500 mm as measurements were not taken after that point.

A lot of emphasis was put on the clarity regarding the boundary conditions. Therefore, the experiment was designed to offer well defined characteristics. This comprises a channel length of moderate dimensions, as the droplets, with increased way length, start being affected by the fluctuations of the main flow which complicates the liquid phase modeling. The shape of the channel is rectangular in order to support the laser measurements by providing perpendicular entry planes. The air inflow enters the chamber from one side. This non-axisymmetric set-up induces transition effects and leads to low level of turbulence intensity. The fuel nozzles sit in the lower half of the experiment which helps the development of the flow and to damp the transition effects. In Fig. 6.1.2 details of the fuel lance are highlighted. Five injection holes with a displacement of 1.05 mm are located at the bottom plane of the fuel lance.

In the further course of this section, the expression injector shall stand for the injector plane from which the droplets emerge. The injector is equipped with five fuel nozzles, each of

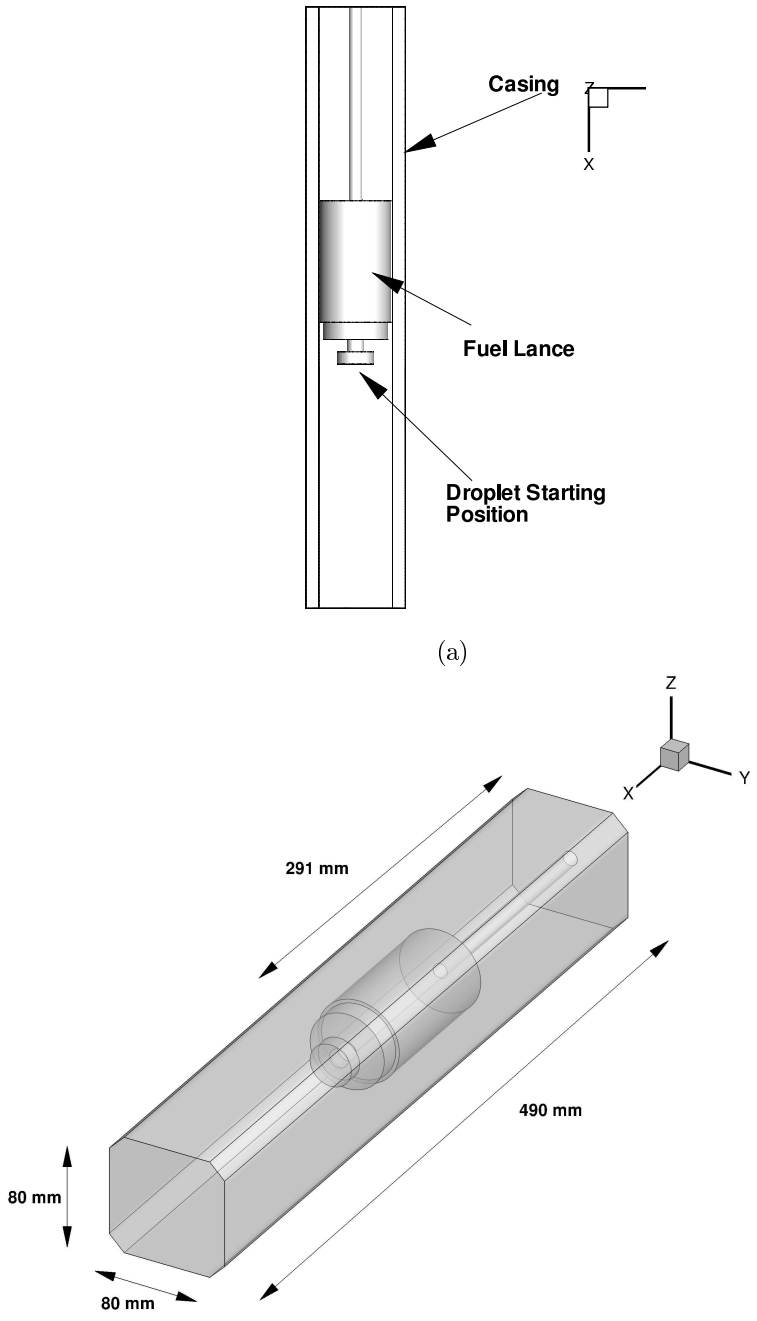

Figure 6.1.1.: **a) Frontal view of the droplet chain combustor. b) Dimensions of the test case.**

diameter 50 μm. The droplet size, which is generated with this configuration corresponds to circa 100 μm. The measured droplet diameter in the experiment ranges from 96 μm for the smallest to 99 μm for the largest droplets. Hence, assuming a droplet size of 100 μm in the simulation represents an appropriate approximation.

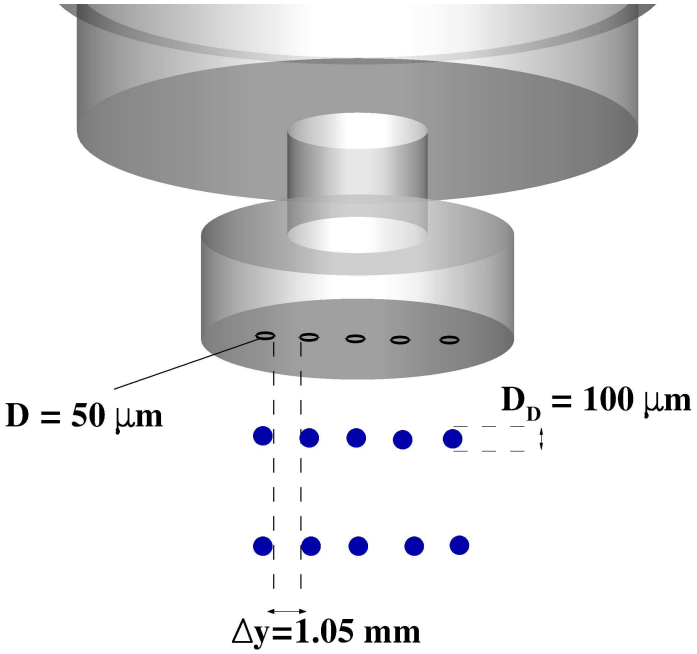

Figure 6.1.2.: **Injector plane and schematic droplet illustration.**

6.1.1.1. Numerical Grid

Developing and optimizing the grid for this test case was a delicate task. On the one hand, small grid cells in the ignition zone constitute one major requirement to accurately adjust the focus of the laser pulse zone. On the other hand, the point-in-cell method adopted for the Lagrangian tracking of the droplets is valid only for droplet sizes negligible with respect to grid cell sizes, which opposes the former. For this reason the grid cells in the region just below the injector are of adequate small size of the order of 0.25 mm, representing a compromise between the two demands. The top of Fig. 6.1.3 zooms on the grid at the injector plane.

An additional reason for choosing small grid cells in the vicinity of the injector is imposed by the very small distance between the injector holes. The distance equals only 1.05 mm. It needs to be avoided that one grid cell encompasses two injector holes as this impedes the accuracy of the calculation. The entire utilized numerical grid is shown at the bottom of Fig. 6.1.3.

The air inlet velocity at the inlet of the channel ranges from 0.18 m/s to 1.79 m/s. The slow velocities justify the rather coarse discretization at the top of the channel. In total, the number of cells is of the order of 450,000. This enables an efficient calculation with a URANS approach with the main features being well resolved.

6.1.1.2. Boundary Conditions

This paragraph provides an outline of the boundary conditions utilized in the different simulations. The experiment comprised numerous variations in inflow velocities and fuel mass

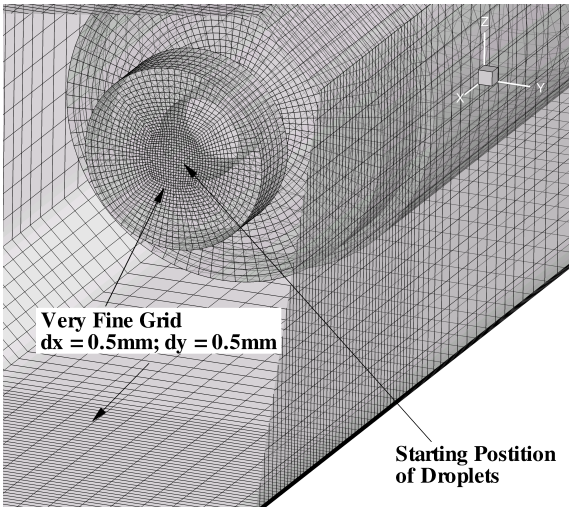

(a)

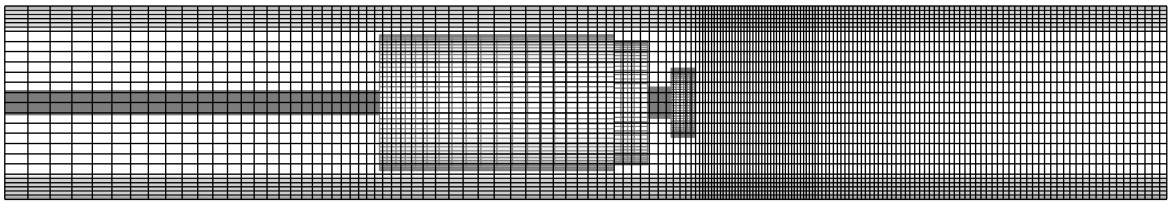

(b)

Figure 6.1.3.: **a) Injector grid design. b) Computational grid.**

flow rates and in the employed fuel. Thus, a selection had to be made for a concise comparison. Table 6.1 lists the different boundary conditions used throughout this numerical study. The droplet initial velocity in conjunction with the impact of the gas field flow on the droplet velocity yield a droplet inertia of the same order as gravity which requires the inclusion of the gravity force.

6.1.1.3. Numerical Treatment of the focused Laser Pulse

It was outlined in Sec. 2.2.4 that the effective laser pulse energy can be separated into heating energy and vaporization energy. Two approximations for the modeling of the laser-induced breakdown are made in this simulation.

- Constant effective ignition energy: The focused laser pulse energy is treated as a given quantity known from the experiment which amounts to 60 mJ.

- Hot volume temperature of 3000 K: It is assumed that the laser spark leads to a heated volume for which a temperature of $T = 3000\text{K}$ is prescribed.

Table 6.1.: **Boundary conditions for the respective simulations of the droplet chain test case. () Brackets denote the fuel used in the experiment.**

Section	Air inflow velocity	Fuel inlet mass flow rates	Description
6.1.2.1	0.7 m/s	-	Cold flow Validation
6.1.2.2	0.7 m/s	3.4 g/min	Cold flow including droplets
6.1.2.4	1.07 m/s	1.9 g/min, 3.4 g/min	Ignited n-decane (Exxsol D80) droplet stream
6.1.2.5	1.07 m/s	1.9 g/min, 3.4 g/min, 5.2 g/min	Ignited ethanol (ethanol) droplet stream
6.1.3	1.07 m/s	1.9 - 5.2 g/min	Single and multicomponent Jet A-1 (Jet A-1) ignitability study
Walls	Adiabatic no slip walls		
Air Inlet	Block velocity profile		
Outlet	Pressure outlet, $p = 1.01325$ bar		

Both assumptions are regarded to yield an adequate approximation of the real conditions after the laser energy deposition. The first assumption is derived from an energy balance in the experiment. Initial processes entrained by the focused laser pulse lead to a highly enhanced temperature exchange which supports the second assumption. The ignition is carried out with a displacement of 10 mm to the injector. In an additional ignition probability study which is shown later in see Sec. 6.1.3, the determination of the split of the ignition energy into heating and vaporization energy which yields the best agreement with the ignition probability data is presented. It is shown that the ignitability measured in the experiment is well reproduced by using the entire ignition energy for the heating of the gas. This results in an ignition volume with radius $r = 4$ mm and height $h = 11.4$ mm without prescription of instantaneously vaporized fuel vapor.

Concerning the results for the flame propagation, it is elaborated that the conditions employed for the spark modeling have a very small to negligible influence on the later flame propagation. This is illustrated in Fig. 6.1.4 which displays the flame position for an ignition with 0% initial fuel vapor and with 100% initial fuel vapor. Deviations only appear at the top and at the tip of the flame, whereas the structure of the flame and the flame dimensions remain very similar, thus, do not influence the evaluation of the flame center and edge speeds.

6.1.2. Results

This section presents a detailed comparison of the simulation results with data available from the experimental measurements. It is sorted as follows: At the beginning, a cold flow verification is given. Afterwards, the influence of the droplets on the flow-field is investigated. The velocity changes due to the interaction of the droplets with the gas phase have a large

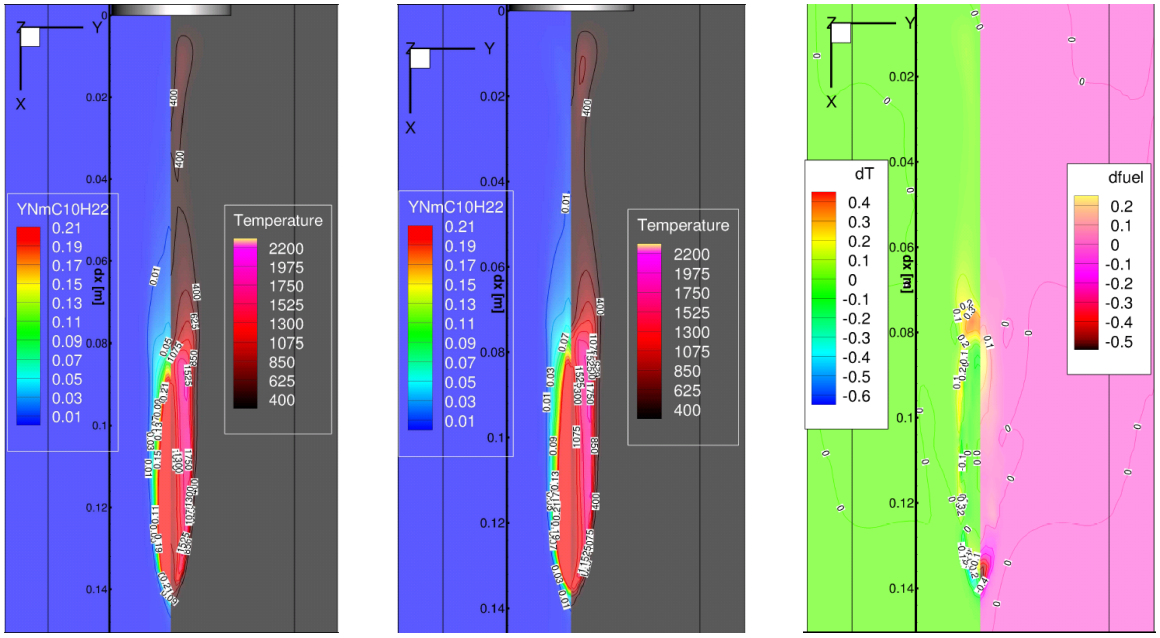

(a) (b) (c)

Figure 6.1.4.: **Snapshots at $t = 20$ ms after ignition. a) 0 % vapor in the laser pulse domain. b) 100 % vapor in the laser pulse domain. c) Deviation as a fraction of the maximum value.**

effect on the ignitability in this test case. Subsequently, the main flame characteristics are examined. The focus is on flame properties such as the flame center velocity and the flame edge velocity which were captured experimentally. Two fuels are considered in the flame center velocity simulation. Detailed data is presented for n-decane which is used as surrogate fuel for Exxol D80, a low aromatic blend of kerosene. It is shown that the experimental results and the numerical simulations are in satisfying agreement which confirms the chosen modeling approach. For the second fuel, ethanol, a comparison of the flame edge velocity between simulation and measurements is given. The study closes with an ignition probability study in which the influence of the employed boundary conditions and spark parameter are examined with respect to the outcome of the ignition sequence.

6.1.2.1. Cold Flow

The verification of the cold flow simulation has been carried out for a single set of conditions. As aforementioned in Sec. 6.1.1, the experiment is equipped with a one-sided inflow with a subsequent sinter plate to harmonize the flow. This induces small asymmetries in the flow which are not accounted for in the simulation. In total, the recirculation zone under the injector varies slightly in length between experiment and simulation due to the flow asymmetries. The recirculation zone persists for a maximum of 60 mm in the simulation (see Fig. 6.1.5). This yields a Stokes number (see Sec. 2.3.3.1) of: $\mathrm{St} = (\rho_L D^2/(18\mu g)) \cdot (u_\mathrm{p} - u_\mathrm{g})/0.06 = 2$ in this region. $\mathrm{St} > 1$ characterizes multiphase flows where droplets are unaffected by the mean

flow-field. It is expected that the droplet streams remain stable within and long outside the injector region, which is conform with the experimental observation. Moreover, the droplet velocity (6.26 m/s) is one order of magnitude larger than the flow velocity (0.7 m/s) which indicates that flow velocity will be significantly influenced by the liquid phase.

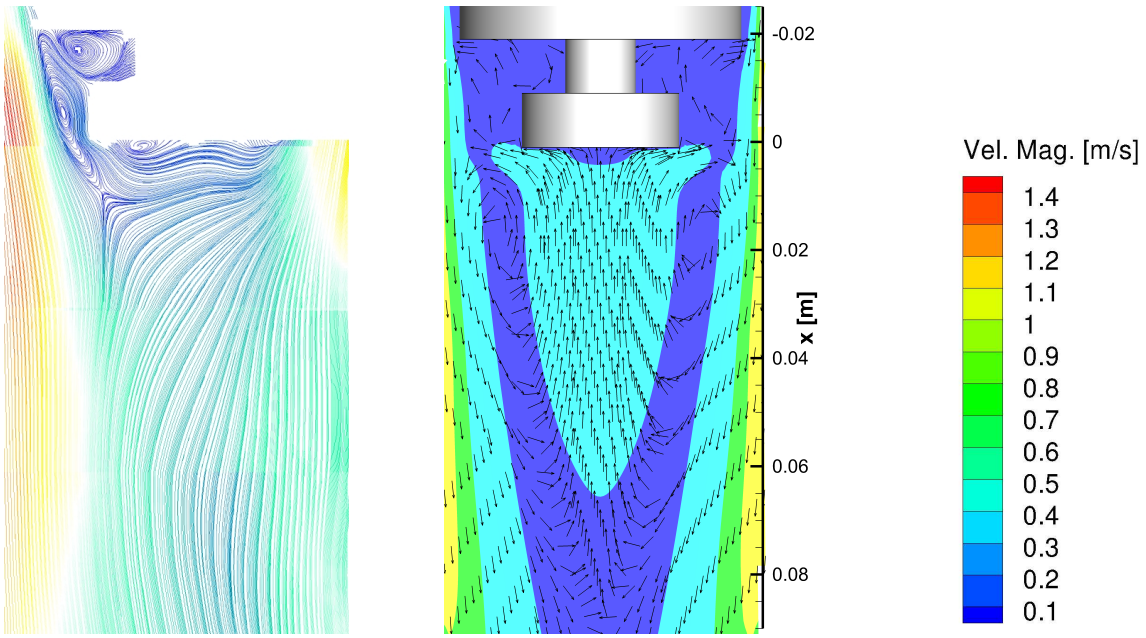

(a) (b)

Figure 6.1.5.: **Results for the cold flow velocity field for an air inlet of 250 SLM ∼ 0.7 m/s inlet velocity. a) Averaged experimental measurements from Mosbach and Gebel [121]. b) Numerical simulation (arrows indicate the mean flow velocity and magnitude).**

As depicted in Fig. 6.1.5, both flow-fields agree well in their general characteristics. The small recirculation zone is visible just below the injector plane. In terms of quantitative agreement, both results plots exhibit the same order of velocities and about the same length of the recirculation zone. The turbulence intensity remains of low order in the entire domain which is indicated by the Reynolds number of the mean flow. The highest velocities occur at the end of the fuel nozzle main body where the cross sectional area is the smallest. The Reynolds number corresponding to this segment amounts to: $\mathrm{Re} = \frac{u_{\max} L}{\nu}$, with $u_{\max} = 1.4$ m/s and $L = 0.0119$ m, denoting the gap width between the outer wall and the injector and $\nu = 1.46\text{x}10^{-5}$ m^2/s, which gives: $\mathrm{Re} = 1140$. By using non-dimensional characterizing numbers, it is demonstrated that the mean flow as well as the large periodical structures developing downstream the injector plane do not affect the droplet streams trajectory and stability. Although the flow is not fully turbulent from an experimental perspective, the k-ϵ turbulence model is employed to capture the slow break-up of the droplet chains.

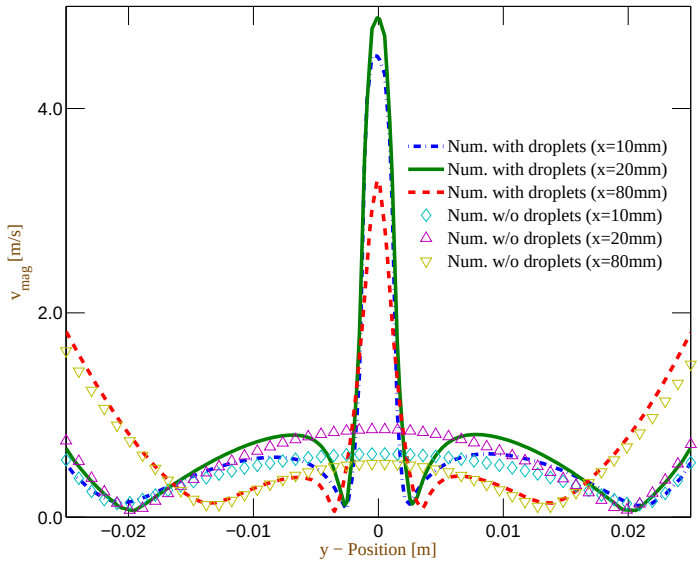

Figure 6.1.6.: **Comparison of the flow-field with droplets and without droplets. Droplet inertia significantly alters the flow-field characteristics.**

6.1.2.2. Cold Flow including Droplets

This paragraph details the influence of the droplets on the main flow features. Figure 6.1.6 shows the large impact of the injected droplets on the flow-field. More specifically, the recirculation zone decreases and the domain becomes less turbulent in the vicinity of the fuel lance. The results illustrated in Fig. 6.1.6 also reveal steeper velocity gradients below the injector plane where the gas in the vicinity of the middle axis is accelerated. The recirculation zone is split into an outer cylinder still dominated by negative velocities and an inner core with flow velocities of the order of 2 m/s. In a later section (Sec. 6.1.3) concerning the ignitability of this set-up, it is shown that the resulting velocities of the droplets govern the probability of a successful flame kernel generation.

Both results displayed in Fig. 6.1.7 are obtained from converged simulations. It shall highlight the differences between a transient and a stationary droplet simulation. In the steady-state treatment the simulation passes pseudo time steps to advance the final solution. The equations for the liquid phase are solved only every five time steps which yields adequate results. Within the liquid phase calculation, trajectories of the parcels which represent a number of identical droplets are computed. The parcel is, thus, completely tracked from its origin until it has left the domain or fully evaporated. Consequently, no single particles are present in the domain, only trajectories. The number of parcels necessary to gain the presented results is 20,000, which leaves 4,000 particles for each injector hole. Within a transient simulation, the particles propagate only the respective distance related to the simulation time step which provides an exact position of all particles at each time step. Nevertheless, a "steady" solu-

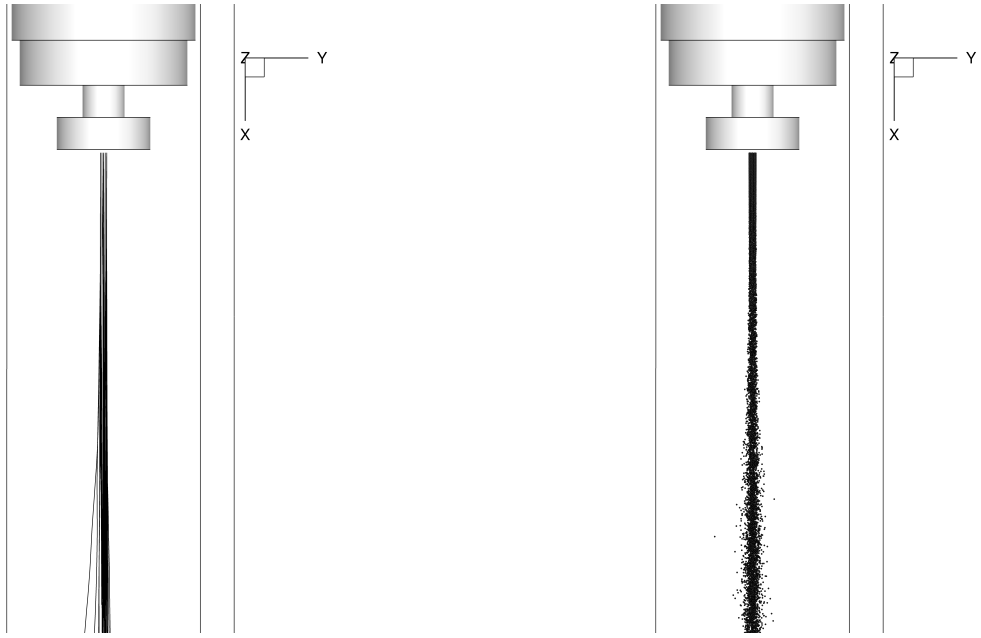

(a) (b)

Figure 6.1.7.: **a) Droplet trajectories obtained in a steady state solution. b) Scatter plot of a transient run.**

tion can be obtained, once large transient phenomena such as the particle acceleration due to the flow-field have vanished. The steady simulation offers the advantage that it achieves the converged solution with lesser computational effort. The initial runs for this numerical study started with a computation of the steady solution. Subsequently, the simulation mode is changed to transient and restarted with the previous converged solution. Since the source terms of the spray trajectories are not kept after the restart of the simulation, the gaseous flow-field at first restores its old state. For this reason, it is eventually decided that purely transient computations are considered which simplified the numerical procedure and did not result in a large increase of the computation time.

Consequently, for deriving the "steady state" of the transient simulation, approximately 80 ms of pure droplet injection without ignition are necessary. This is roughly three times the time a droplet needs to transverse the domain. The left of Fig. 6.1.8 and the snapshot on the right of Fig. 6.1.8 show the droplet evolution. The first particles encounter a large drag force from the gas phase as the initial velocities underneath the injector are negative. This leads to the generation of a cloud as the particles accumulate at the tip of the droplet stream. Subsequently injected droplets with their initial high momentum induce a further acceleration of the flow-field until the continuous phase in the vicinity of the droplet streams has a velocity of similar order of magnitude. At this time, the droplets propagate almost undisturbed until they leave the domain. As no experimental results concerning the cold multiphase flow-field prior to the laser pulse exist, a quantitative comparison cannot be provided.

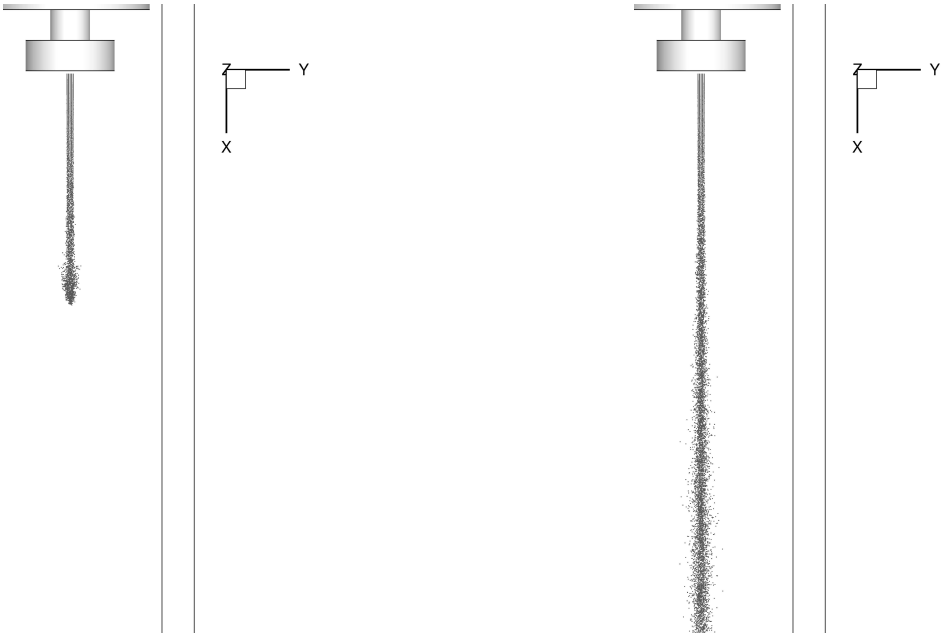

(a) (b)

Figure 6.1.8.: **a) Droplet cloud at the beginning at $t = 2$ ms. b) Smooth droplet distribution after $t = 80$ ms.**

6.1.2.3. Ignited Flow

The cold flow validation focused on establishing appropriate boundary conditions to start the reactive simulation. The impact of the liquid phase on the resulting flow-field was described. The flow-field velocities were significantly increased which will affect the flame propagation following the forced ignition.

6.1.2.4. Exxsol D80

This paragraph covers the results of the numerical simulations concerning Exxsol D80 as employed liquid fuel. A comparison with experimental data with respect to flame characteristics such as the time-dependent flame center and flame edge positions is provided. Exxsol D80 which is a low aromatic blend of kerosene is modeled as n-decane within the liquid and gas phase which is one of the major components of kerosene. Volume averages of the OH-Chemiluminescence were evaluated in the experiment to determine the flame center position. For the flame edges, a linear method was utilized to infer the position. The same methods are applied to the data from the numerical simulation. This allows a one to one comparison with experimental data. Before outlining this data, a qualitative comparison of the flame development is given. Fig. 6.1.9 and Fig. 6.1.10 contain snapshots from the simulation which are compared with ensemble averaged images from the experiment. In Fig. 6.1.9 the temporal evolution of the fuel vapor is illustrated whereas Fig. 6.1.10 depicts the temperature gradient for the same time instances.

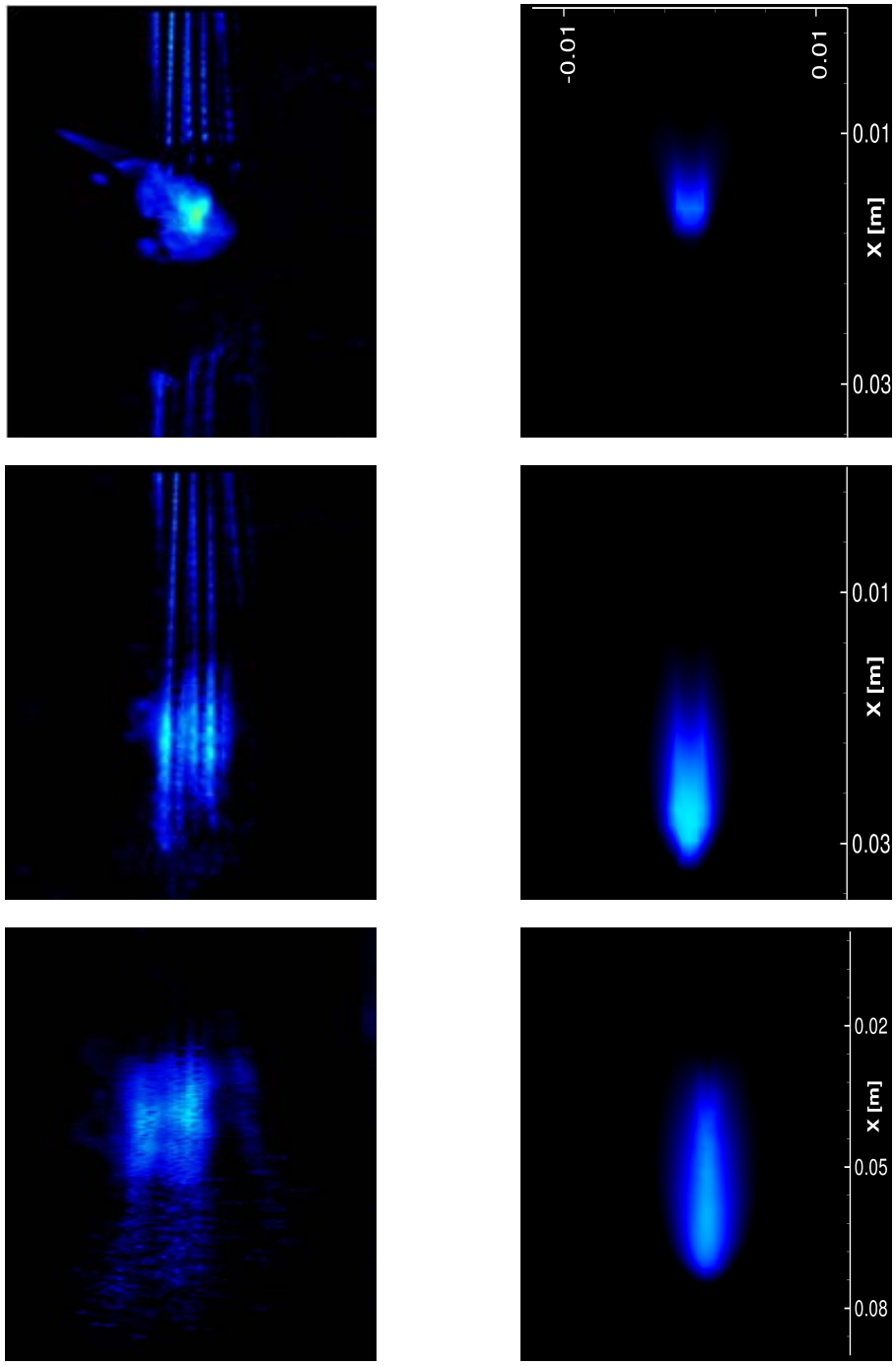

Figure 6.1.9.: **Fuel contour plots for different time instances. Left column: Experimental results [121]. Right column: Numerical results. 1st row:** $t = 3$ **ms. 2nd row:** $t = 8$ **ms. 3rd row:** $t = 30$ **ms.**

Both time series clearly show similar main characteristics of the flame. As observed experimentally, the flame is convected first in stream wise direction. Beside the convection, the flame also stretches and grows in stream wise direction as a result of the flame front burning up newly generated fuel vapor. Opposed to that, the flame cannot expand greatly in cross-stream direction as the fuel vapor remains confined to the droplet axis vicinity. These

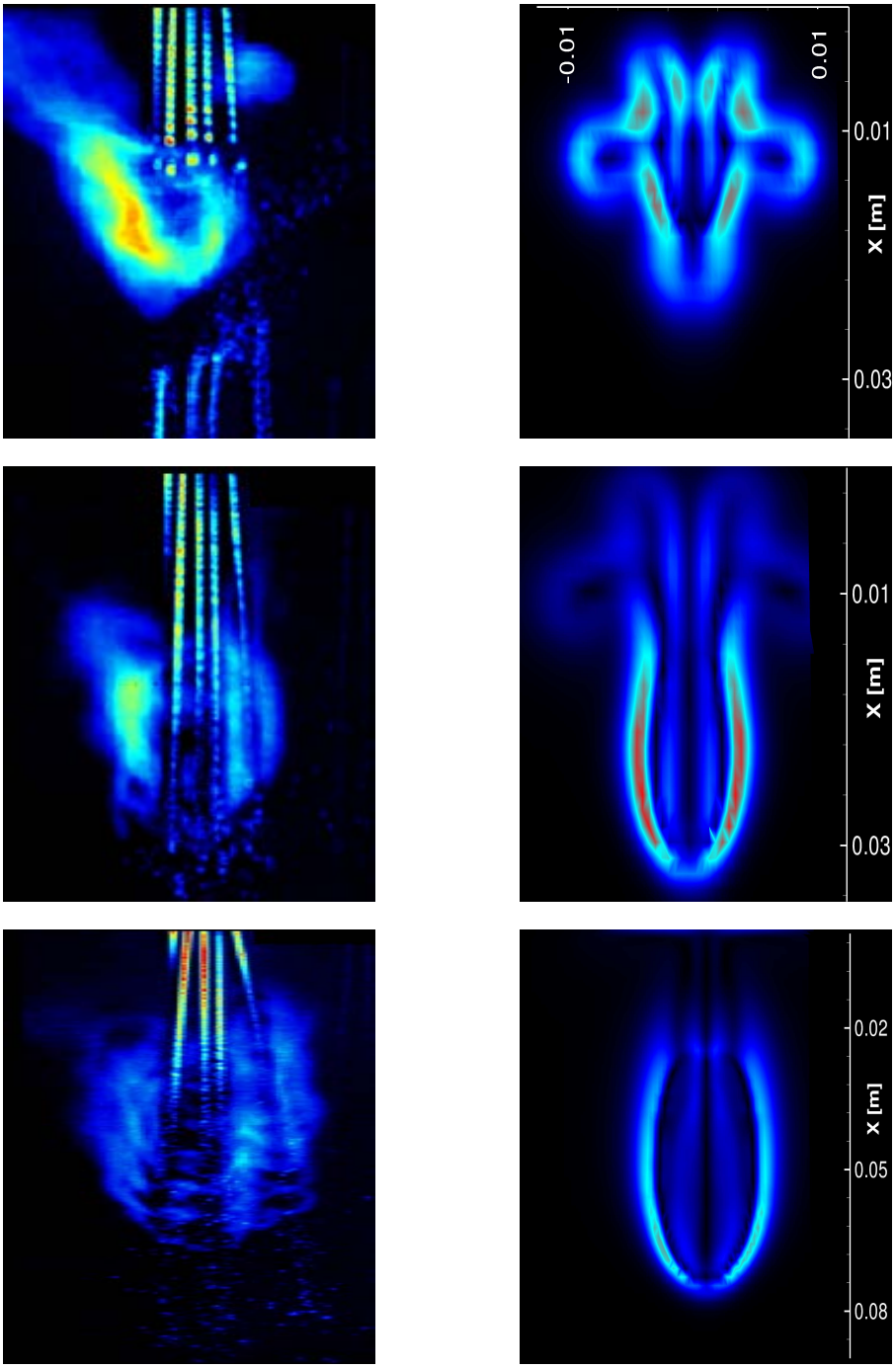

Figure 6.1.10.: **OH/Temperature gradient contour plots for different time instances. Left column: Experimental results [121]. Right column: Numerical results. 1st row:** $t = 3$ **ms. 2nd row:** $t = 8$ **ms. 3rd row:** $t = 30$ **ms.**

two findings are also observed in the simulation in which the flame exhibits a similar flame behavior. It is found in both studies, that the fuel vapor is created within the flame zone which, through diffusion, generates favorable conditions for the combustion. This can be further illuminated by a simultaneous look at plots of the fuel vapor concentration and the

gradient of the temperature. This is presented in Fig. 6.1.11.

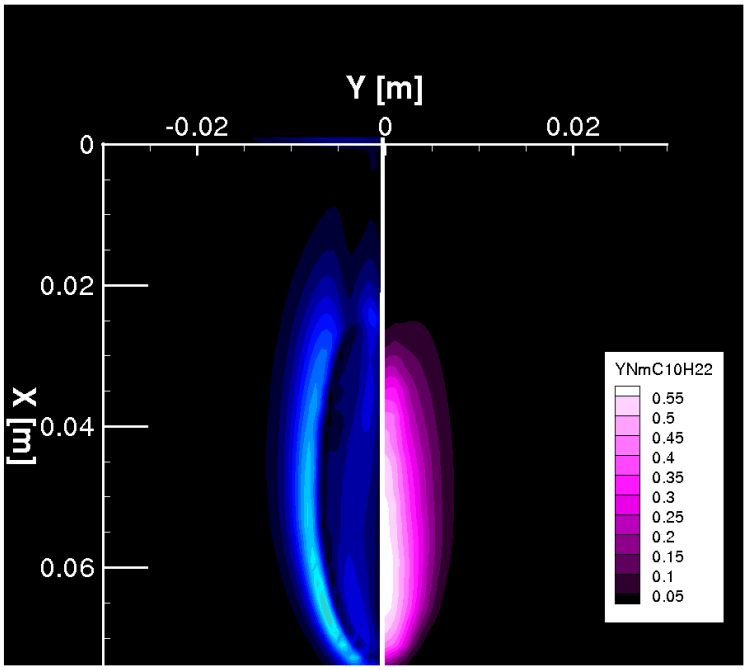

Figure 6.1.11.: **Schematic illustration of the flame after $t = 20$ ms. Left: Gradient of the temperature. Note that light colors indicate high gradients whereas low gradients are indicated by darker colors. Right: Fuel vapor concentration.**

The fuel vapor is generated in the inner region of the cylinder flame through the evaporation of droplets entering the flame zone which leads to a fuel-rich core around the center axis. In this zone the flame cannot burn as the mixture composition is above the rich flammability limit. The contour plot of the gradient of the temperature supports this conclusion as the sharpest intensities appear further away from the centerline, where the fuel vapor concentration abates to more advantageous conditions. To this outer zone, the fuel vapor diffuses to form a composition which is approximately of stoichiometric ratio, hence, providing viable conditions for the combustion. As the fuel vapor is not able to pass this stoichiometric iso-line much further, since it is burned up within this zone, a steep gradient is perceivable at this radial position, see Fig. 6.1.11.

The snapshots presented in Fig. 6.1.9 and Fig. 6.1.10 are not adequate for a quantitative comparison of experimental and numerical results. This stems from the resolution discrepancies and from the uncertainties in the intensity scale of the measurements. Hence, a more elaborate evaluation of the numerical results can be given by comparing the flame center velocity data. Figure 6.1.12 presents the data taken from Mosbach and Gebel [121]. The data derived from the numerical simulations is depicted in Fig. 6.1.13. An overview to summarize the experimental and numerical results is provided in Table 6.2 also underlining

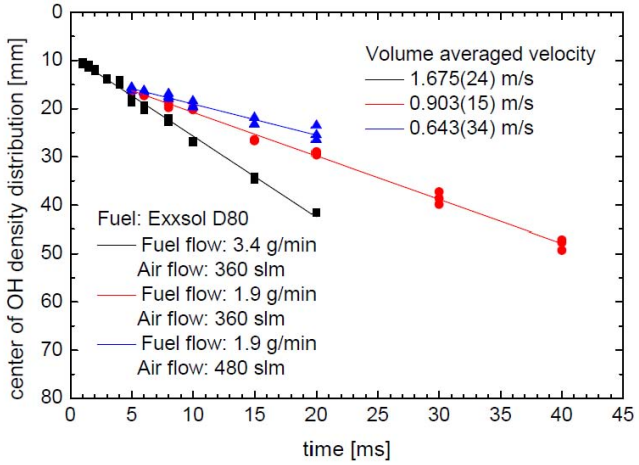

Figure 6.1.12.: **Flame center velocities measured in the experiment [121].**

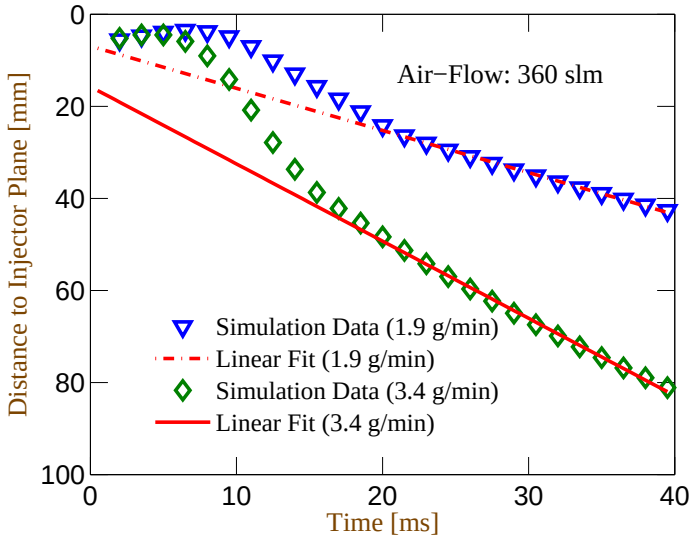

Figure 6.1.13.: **Numerically derived flame center velocity for fuel inflow rates of 1.9 g/min and 3.4 g/min.**

the satisfying agreement between both. The test case confirms that the numerical approach employed for this configuration is able to capture the flame behavior accurately and provides a precise prediction of the flame propagation under multiphase conditions.

Table 6.2.: **Comparison of experimentally and numerically derived flame center velocities.**

Fuel Inlet Velocity	Flame Center Velocity (Experiment)	Flame Center Velocity (Simulation)
1.9 g/min	0.90 m/s	0.91 m/s
3.4 g/min	1.68 m/s	1.68 m/s

One remark concerning the small deviations in the early stages of the flame development for

Exxsol D80 is necessary. In the experiment, nearly no influence of the laser pulse on the initial movement of the flame can be perceived, whereas the numerical results predict a small acceleration through the addition of the laser pulse energy to the domain. This can be due to flow-fields effects caused by the dynamics of the laser pulse which has been researched by several groups, e.g. Bradley *et al.* [29]. The laser generates a flow-field which points in the opposite direction of the laser beam. Since the laser is inclined with respect to the main flow and is pointing slightly in the main axis direction, the generated flow-field can counteract the acceleration effects, caused by the gas expansion effects in the laser pulse region. This might explain the smoother beginning in the experiment as observed in Fig. 6.1.12. To incorporate this laser-induced effect is outside of the solver's capability as discussed in Sec. 2.2.4. However, the modeling approximation has only a very small impact as the correct flame center velocity is achieved shortly after the spark effects have abated.

Moreover, the results point out that the flame center velocity is dominated by the fuel mass flow rate. Both flame center velocities scale well with the increase in the axial velocity which is due to the higher momentum of the droplets at higher fuel inlet rates. Hence, the forced ignition, by an additional energy source, only initially influences the flame behavior. In the further progress for this specific set-up, the propagation becomes a function of the droplet-stream driven flow parameters. Thus, the laminar flame speed plays a minor role as compared to the mean flow characteristics, which scale with the droplet velocity. This is explained by the fact, that the flame propagates almost evenly in both directions, which is shown in the flame growth plot in Fig. 6.1.10. Consequently, the kinetics of the flame do not affect the flame center position much whereas they have a significant impact concerning the upper and the lower flame front position. This is elaborated in the results for ethanol in the next subsection. To conclude this part, a time series of the flame kernel development for Exxsol D80 is given in Fig. 6.1.14.

6.1.2.5. Ethanol

The same numerical set-up as used in the previous paragraph is applied. The main difference is that ethanol is used as liquid fuel in this paragraph. Ethanol is more volatile than the previously investigated Exxsol D80 which allows higher fuel inlet rates that can still be successfully ignited with the same laser pulse energy. Thus, the range of flow parameters, which can be studied is enlarged and offers the possibility of generating a more comprehensive data set as for Exxsol D80. The focus in this part lies on the comparison of the lower flame edge speed which represents a further important characteristic of the flame. As discussed in the previous subsection, capturing the flame edge velocity is a more challenging task as compared to resolving the flame center velocity, since more effects need to be taken into account. As mentioned in the previous section, the laminar flame speed does not affect the flame center position to a large extent. This is due to the almost symmetric growth of the flame. The

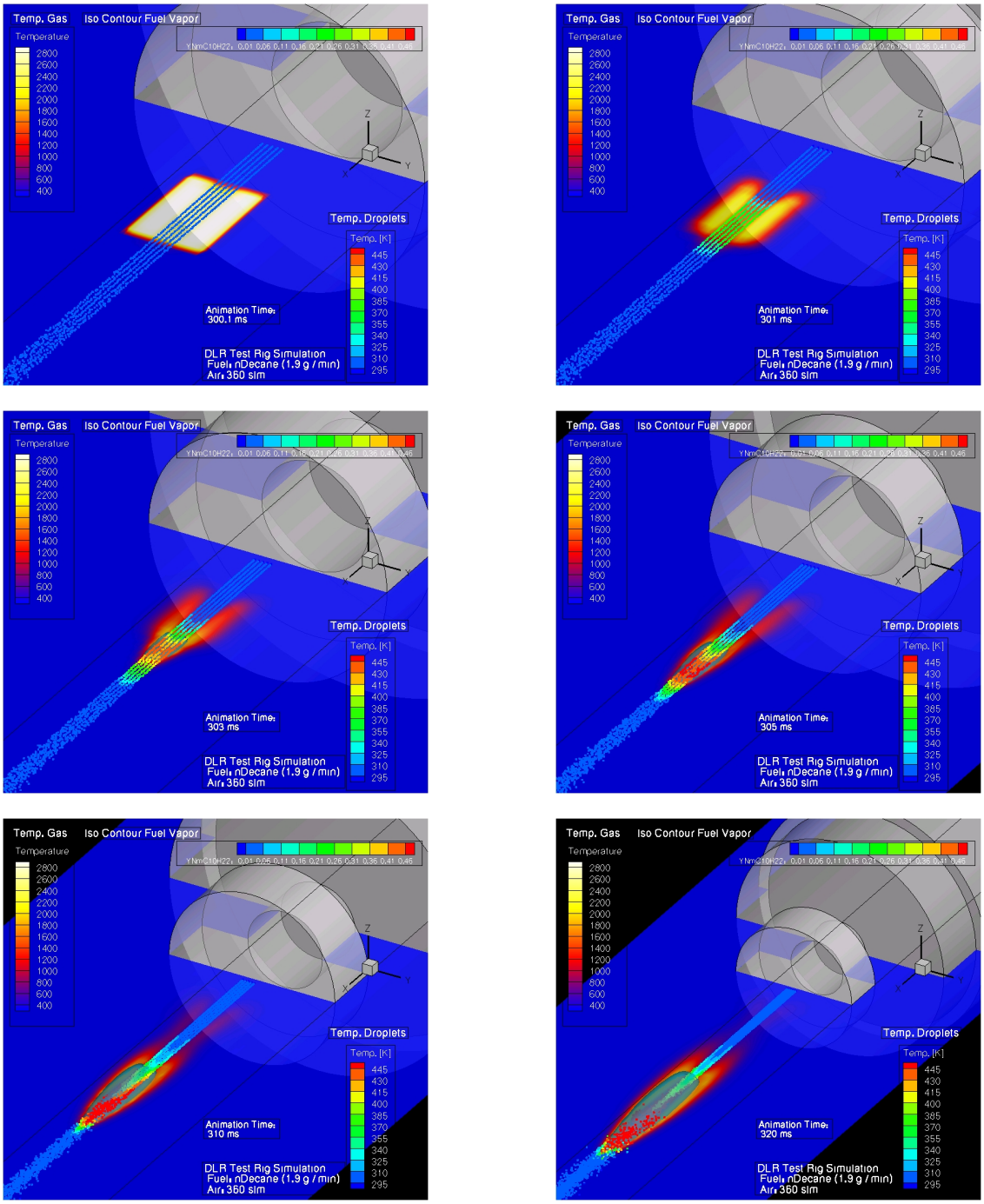

Figure 6.1.14.: **Time evolution of the flame subsequent to the laser pulse. The figures correspond to, from left to right, from top to bottom: 0.1 ms, 1 ms, 3 ms, 5 ms, 10 ms, 20 ms. The temperature contour (in K) is depicted. Additionally the temperature of the droplets is indicated by their color. The iso-surface relates to the fuel vapor mass fraction.**

propagation of a single front, however, is intrinsically governed by the kinetics of the flame. Therefore, the results allow an assessment of the modeling accuracy of the underlying kinetics.

The outcome of the experiment is depicted at the top of Fig. 6.1.15. The numerical results, for the same conditions, are presented at the bottom of Fig. 6.1.15 with a subsequent quantitative comparison in Table 6.3.

Table 6.3.: **Comparison of experimentally and numerically derived flame edge velocities.**

Fuel Inlet Velocity	**Flame Edge Velocity (Experiment)**	**Flame Edge Velocity (Simulation)**
1.9 g/min	2.15 m/s	1.91 m/s
3.4 g/min	2.70 m/s	3.47 m/s
5.2 g/min	3.05 m/s	4.60 m/s

The error bars correspond to the different air inlet velocities which slightly affect the solution. By taking an average air velocity in the simulation which lies in-between the lowest and the highest investigated air velocities, the numerical results are comparable with the average of the experiment. The conclusion can be drawn, based on the findings illustrated in Fig. 6.1.15, that the air velocity is of minor importance in any case, as even a large change does not have a major impact. Generally, an overall good agreement is achieved. The overprediction of the flame edge velocity can be attributed to the absence of the acceleration for the laser-induced breakdown in the experiment. As discussed in Sec. 6.1.2.4, the real laser induces an initial counterflow opposed to the main flow direction. Consequently, the course of the flame edge is smoother in the experiment which is visible within the first milliseconds at the top of Fig. 6.1.15. The numerical results clearly show a deceleration after the initial effects have worn off, which leads to approximately a constant velocity as observed in the experiment.

6.1.3. Ignitability Study

In the scope of the experiment, the air and fuel mass flow were varied in order to gain insight in how this influences the ignitability of the set-up. In the numerical study, the spark parameter are determined by comparing the outcome of a number of ignition sequences with experimental data for a single set of boundary conditions. The parameters with the best agreement are used in further simulations. Parameters which are taken into account are the initial fuel vapor content and the spark height. The energy and the temperature are fixed to the values given in Sec. 6.1.1.2. The spark height is used to specify an energy split between the energy dedicated for heating and the energy dedicated for vaporization yet constraining the total effective energy of the ignition to 60 mJ. This is illustrated in Fig. 6.1.16.
When prescribing a high percentage of vaporization, the ignition volume decreases as less energy is available for the heating of the gas. The radius of the cylindrical volume equals 4 mm as the experimental figures show that the spark spreads rapidly over all five droplet chains, see Fig. 2.2.3. This explains a radius of 4 mm which corresponds approximately to

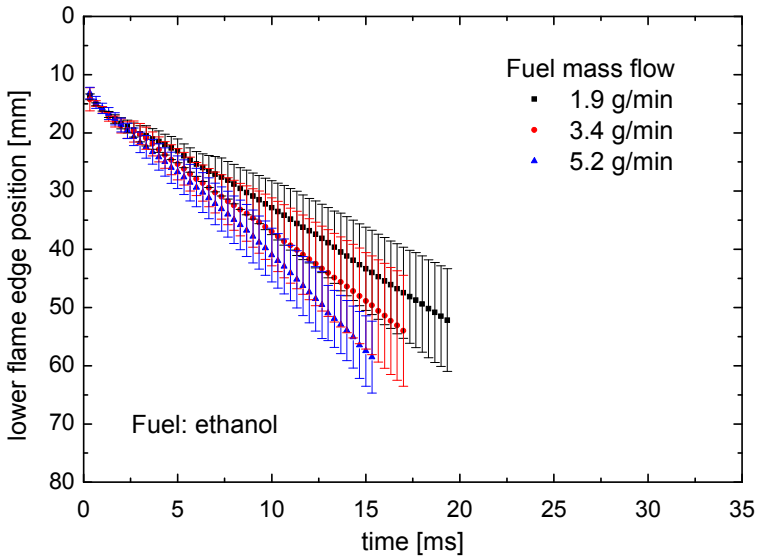

(a)

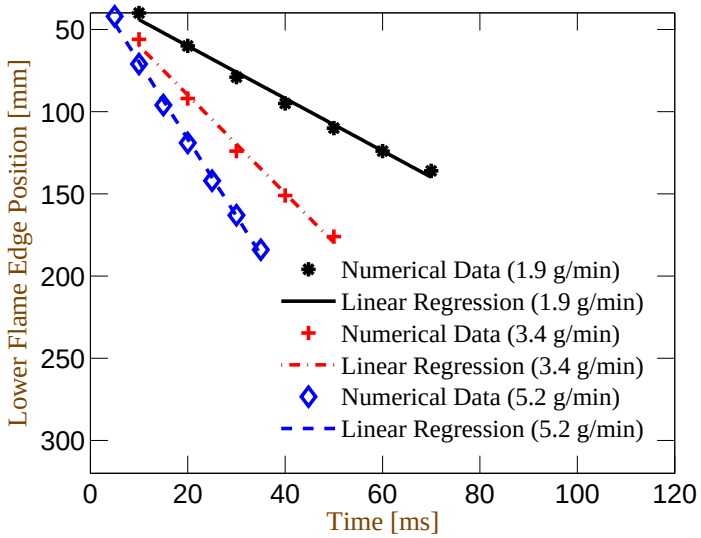

(b)

Figure 6.1.15.: **a) Flame edge velocity of the lower edge of the ethanol flame measured in the experiment, see [121]. Error bars are included. b) Numerical results of the flame edge speed. Air inlet velocity corresponds to 360 SLM.**

the position of the outer injection holes. The height ranges, according to the fraction of fuel which is instantaneously vaporized, from 7 mm to 11 mm which is in good agreement with the estimate from the experimental measurements. A sketch of the modeled laser ignition volume is presented in Fig. 6.1.17.

The underlying equations for the calculation of the ignition kernel height shall be presented

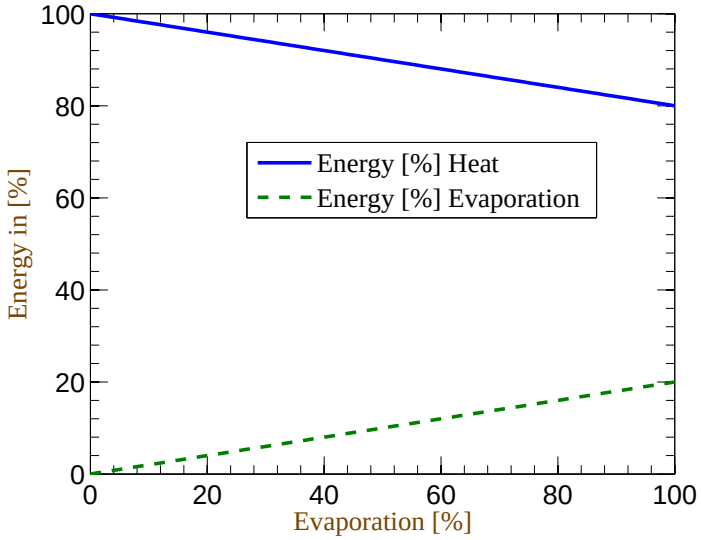

Figure 6.1.16.: **Energy split of the total effective ignition energy. The ignition energy is distributed among the heating of the corresponding ignition volume and the vaporization of the droplets contained in the ignition volume. 0 % instanteneously vaporized fuel relates to a spark height of 11.4 mm. 100 % instanteneously vaporized fuel relates to a spark height of 8.4 mm.**

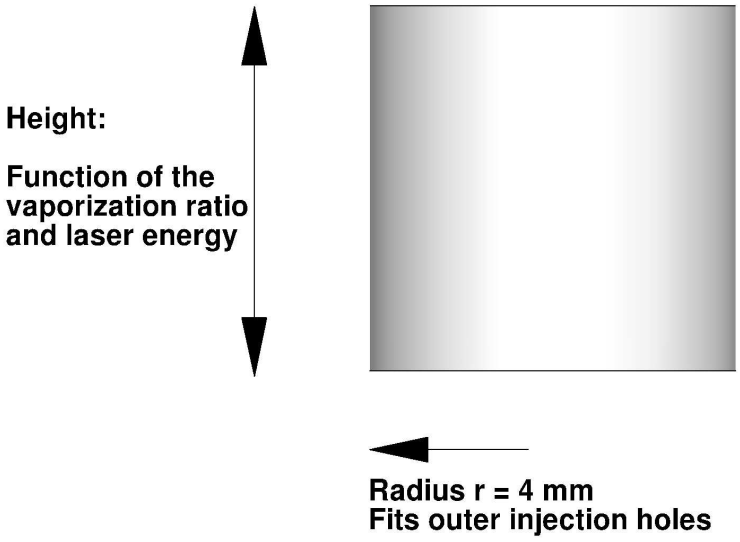

Figure 6.1.17.: **Ignition kernel dimensions.**

briefly. The expression for the heating energy of the gas reads:

$$E_h = \pi r^2 \cdot h \cdot (\mathrm{cp}_{3000\mathrm{K}} \rho_{3000\mathrm{K}} 3000[\mathrm{K}] - \mathrm{cp}_{300\mathrm{K}} \rho_{300\mathrm{K}} 300[\mathrm{K}]). \tag{6.1.1}$$

Regarding the evaporation energy the following expression is employed:

$$E_e = f_e H_e \frac{\dot{m}_\mathrm{d} \cdot h}{u_\mathrm{d}}, \tag{6.1.2}$$

where f_e represents the fraction of fuel which is instantaneously evaporated inside the laser pulse volume and H_e denotes the enthalpy needed for the phase change. $\dot{m}_\mathrm{d}$ is the fuel mass flow, h, the spark height and u_d constitutes the outflow velocity of the droplets. Both energies added yield the effective laser pulse energy by which the height of the cylinder is inferred:

$$E_e + E_h = h \cdot (f_e H_e \frac{\dot{m}_\mathrm{d}}{u_\mathrm{d}} + \pi r^2 \cdot (\mathrm{cp}_{3000\mathrm{K}} \rho_{3000\mathrm{K}} 3000[\mathrm{K}] - \mathrm{cp}_{300\mathrm{K}} \rho_{300\mathrm{K}} 300[\mathrm{K}]). \tag{6.1.3}$$

Table 6.4 provides an overview of the values for the height which are computed with Eq. (6.1.3) exemplary done for n-decane. The resulting dimension of the initial kernel compare well with the data available from the experiment.

Table 6.4.: **Spark heights for n-decane.**

Per Cent of Fuel evaporated	Resulting Height
0 [%]	11.4 mm
50 [%]	9.76 mm
100 [%]	8.40 mm

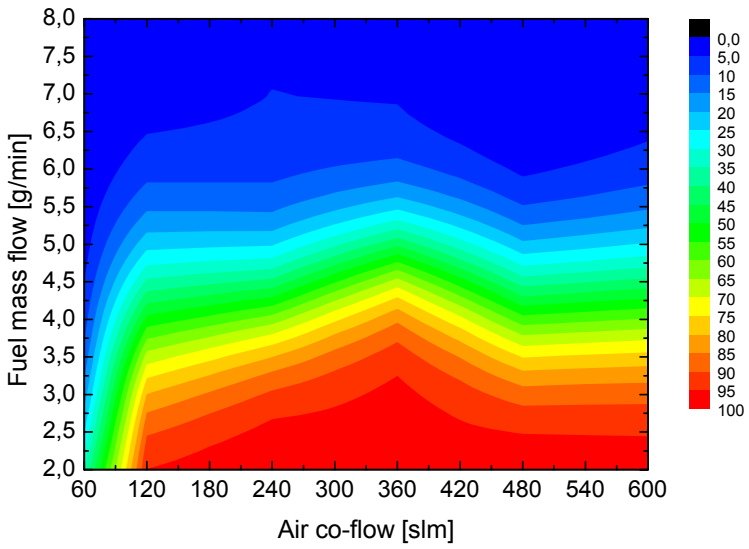

Figure 6.1.18.: **Ignition probability map derived in the experiment, see Mosbach and Gebel [121], with respect to fuel and air mass flow rates.**

The approach taken to derive the most appropriate setting for the numerical representation of the laser pulse utilizes the ignition map generated in the course of the experimental study.

In the ignition map, flow conditions are correlated with the ignitability of the mixture. Figure 6.1.18 displays the ignition map derived in the experiment for Jet A-1. Jet A-1 is treated as a multicomponent fuel using continuous thermodynamics in accordance to Le Clercq *et al.* [94], see also Sec. 2.3. The maximum fuel mass flow rate at which a successful ignition is still achieved is determined in the simulation with different values for the spark height for a single air flow rate. The value of the spark height which agrees best with the experimental results is taken as adequate boundary conditions for the spark modeling.

A large influence of the initial fuel vapor content and the length of the ignition zone becomes apparent in the simulation. On the one hand, if the length becomes smaller, less fuel from the droplets is capable to evaporate fast enough to provide fuel vapor to flame. On the other hand, if initial vapor is present, a flame kernel can develop faster provided that the mixture is within the flammability limits. In case too much vapor is prescribed, it may lead to an impairment of the auto-ignition once the mixture approaches the upper flammability limit. Additionally, the hot zone through which the droplets travel becomes shorter.

To illustrate the large differences which arise from different settings, an example of a failed and a successful ignition is presented in Fig. 6.1.19. In the first column, a failed ignition with 0 % fuel vapor is depicted. An important aspect of the flame kernel development can be observed. It is crucial that the hot gas and the fuel droplets do not exhibit too large velocity gradients. In the first scenario, fuel droplets pass the ignition zone, get heated up, yet no successful ignition occurs, as the fuel vapor is convected outside of the hot zone. This is due to the fact that the axial velocity close to the droplet streams is much higher than further away from the droplets where most of the hot gas is located. In the second scenario, an initial vapor content of 50 % of the fuel droplets mass is present. Under these conditions, a flame establishes within the burnable mixture. The flame kernel is located right in the middle of the droplet streams and is, thus, convected with a high mean velocity. Newly approaching droplets therefore remain long in the zone of the flame kernel and are able to provide new fuel vapor to the combustion. The comparison with the experimental ignition map for a single air flow reveals that without prescribing an initial fuel vapor content, a good agreement with the experimental data is achieved. It is found that with an initial vaporization, the ignition probability is overpredicted. A reason why the spark representation is well modeled without initial vaporization might originate from an overestimation of the total effective ignition energy. The value of 60 mJ represents a first estimate from the experiment, however, in a later experiment and numerical investigation concerning spray flame ignition (see Sec. 6.2) within a similar experimental set-up, it is decided that a total effective ignition energy of 20 mJ might be more adequate.

With the derived spark setting, a comparison with the experimental ignitability data is performed. It is assumed that the transition from a successful to an unsuccessful ignition in

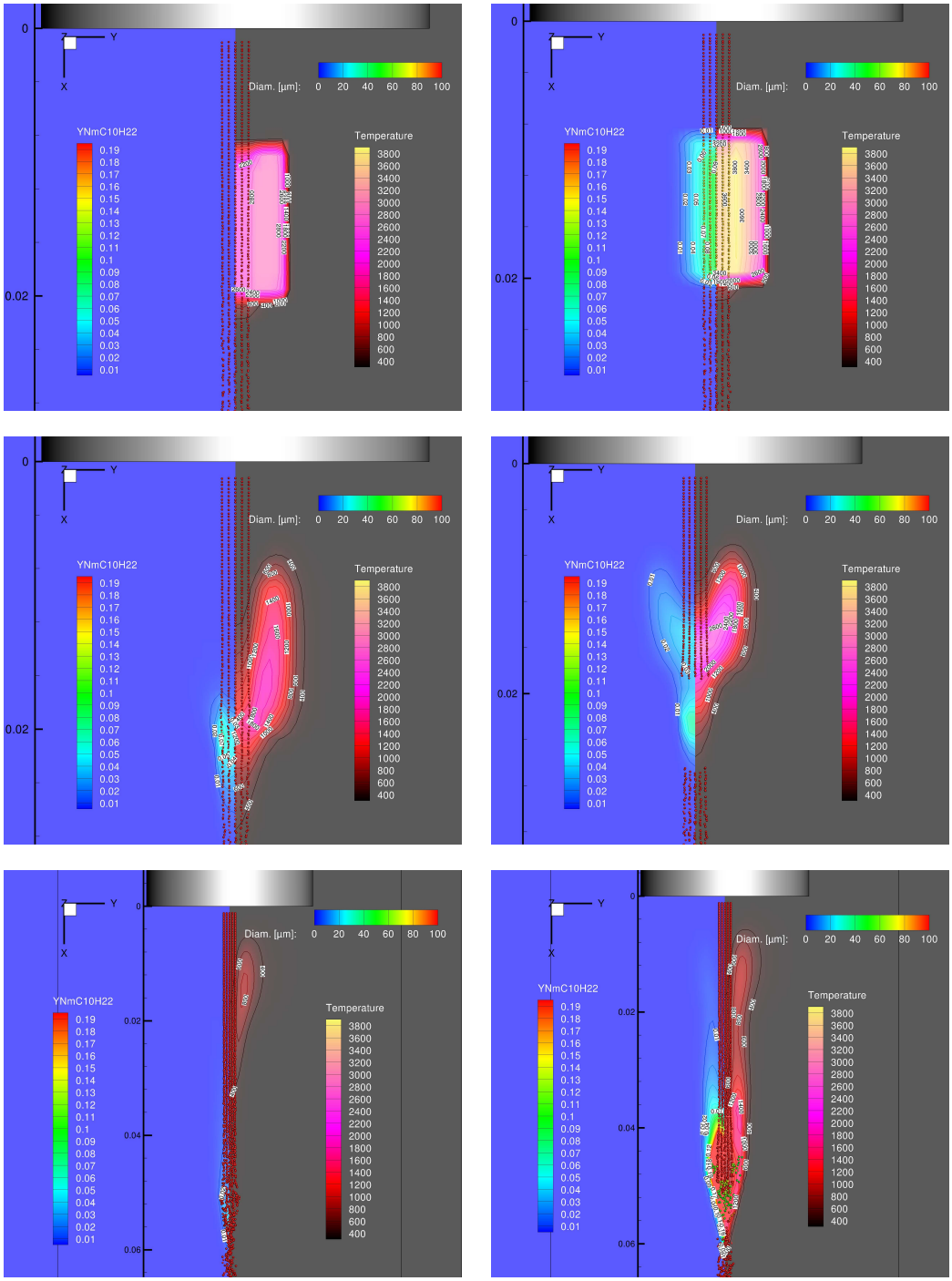

Figure 6.1.19.: **Flame and fuel evolution triggered with two different ignition settings. Columns: Correspond to 0 % vapor / 50 % vapor present in the ignition zone. Rows: Time passed after the laser-induced breakdown. 1st Row: 60 μs. 2nd Row: 2 ms. 3rd Row: 10 ms. Note that for 0 % vapor the ignition fails. 50 % vapor leads to a successful ignition and to a self-sustaining flame.**

the URANS simulation corresponds to an ignition probability of 50 %. Since the outcome of the computation has a yes/no character, probabilities cannot be compared directly. However,

the purpose of the simulation is to identify boundary conditions that are favorable for ignition, which justifies the association with the 50 % iso-line. A comparison of experimental and numerical results is presented in Fig. 6.1.20. The results point out that the transition from a successful to failed ignition in the computation complies well with the ignition probability of 50 % in the experiment. This indicates that the 50 % iso-line in the experiment also marks the conditions for which a successful ignition of the domain becomes more and more difficult. Since the URANS simulation considers an averaged flow-field solution (apart from mean flow variations) without resolving the turbulent stochastic motions, it cannot capture the entrained mixture and flow-field fluctuations which are important at a lower ignitability. Especially for a lower ignitability, turbulent structures which may carry favorable mixture to an otherwisely not suitable ignition location, are crucial. With the determined parameters, however, the URANS simulation is able to deliver a good prediction of locations which provide stable and reliable conditions associated with an ignition probability of above 50 % in the experiment.

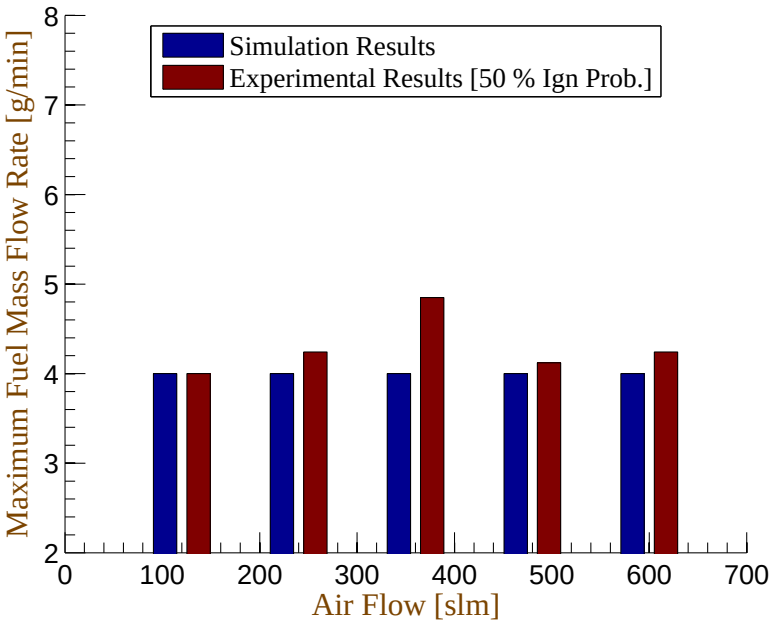

Figure 6.1.20.: **Comparison of the ignition probability between the experimental results [121] and the simulation.**

6.1.3.1. Influence of the Fuel Evaporation Characteristics

So far, the large relevance of the modeling of the laser-induced breakdown has been discussed. A second significant aspect is the fuel evaporation model. As considerable differences occur in the ignition probability which depend on the initial vapor content, the same effect is observed regarding the liquid fuel treatment. The liquid fuel treatment is a very complex subject as most technical fuels consist of a large variety of different elements. For example Jet A-1 is

considered to comprise many different n-paraffins, iso-paraffins, cycloparaffins, and various types of aromatics [38, 181]. This can introduce quite a significant model error if the liquid fuel is described as a single component fuel. This is investigated in the following.

The largest impact of the liquid fuel modeling is expected to occur at the beginning of the ignition sequence, when only a very confined volume contains the energy from the laser pulse. In the later stages of the flame development, the influence of the evaporation model decreases, as the hot conditions with the flame zone almost certainly lead to a vaporization of the droplets. Hence, an accurate evaporation model is required to describe the evaporation process subsequent to the energy deposition. It becomes crucial that also the volatile components of the multicomponent fuel are included as they evaporate quickly and provide fuel vapor to the flame kernel. The differences of the evaporation models are captured in Fig. 6.1.21 in which a hot air flow is prescribed at the inlet which leads to a homogeneous temperature distribution of 1800 K within the domain.

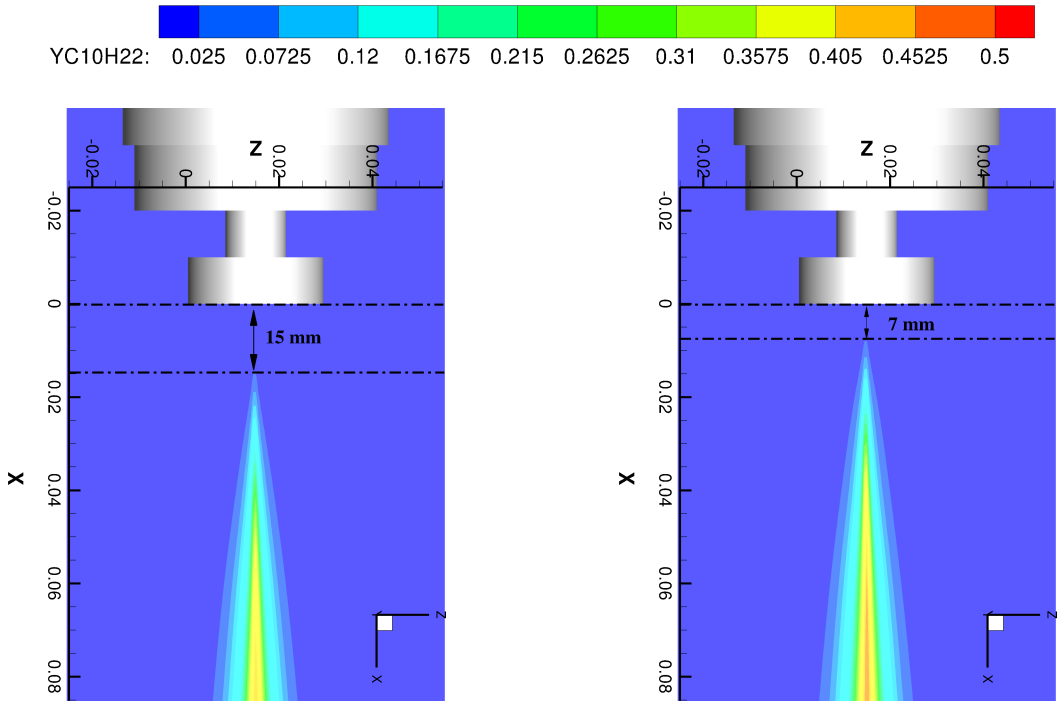

Figure 6.1.21.: **Contour Plots of the fuel mass fraction for a hot environment of $T = 1800$ K for $\dot{m}_\mathbf{f} = 3.4$ g/min and 260 SLM air flow. Left: Jet A-1 modeled with a single component fuel approach. Right: Jet A-1 modeled with a multicomponent fuel approach.**

The interesting information in the figures is the lift-off height of the fuel-rich region. As the gas field temperature is fixed at 1800 K, both numerical kerosene fuel types evaporate rather quick under the imposed boundary conditions. However, a difference in way length can be observed which amounts to several mm until the first concentration of the fuel vapor mass fraction above 7.5 % is found. The multicomponent fuel treatment on the right side predicts

an earlier and increased evaporation as also the more volatile components are modeled. Opposed to that, the single-component fuel model predicts a slower evaporation as the fast evaporating components are not included. This results in a major difference in the fuel vapor content within the very confined hot volume generated by the laser pulse. Therefore, a fuel which requires several mm longer to evaporate sufficiently to sustain a flame can lead to a failed ignition in the simulation. For this reason it is of high priority to provide a realistic behavior of the fuel by incorporating a continuous component distribution, which comprises the characterizing species families of the real fuel.

6.1.4. Summary

At first, the numerical set-up is presented. Subsequently, an assessment of the chosen boundary conditions is performed by means of cold flow comparison of the simulation results with experimental data. A fairly good flow-field agreement is achieved and additionally, the large influence of the droplets is quantified. Afterward, the focus is shifted to the flame development. A first qualitative comparison shows that the experiment and the simulation predict a similar evolution of the flame. The flame remains attached to the droplet chain area after the ignition since this represents the only fuel source in the domain. Due to an increasing fuel vapor content resulting from the evaporation of the droplets the flame in later stages abandons the inner layer and burns at the outside of the fuel vapor zone. The nature of the flame is in both, the numerical and experimental study, identified to correspond to a diffusion flame. Another major finding is the independent behavior of the flame with respect to the parameter of the laser-induced breakdown modeling. A comparison of two differently initiated simulations reveals that only minor deviations occur. In the scope of a subsequent quantitative comparison, it is demonstrated that the flame propagation is captured with reasonable agreement in the numerical simulation. Concerning the flame center propagation, the results are of high accuracy as kinetic phenomena and the evaporation do not affect the solution to a large extent. The flame edge velocity, however, shows a deviation between experiment and simulation as the growth of the flame relies on kinetic quantities such as the local laminar flame speed and the evaporation which also influences the local burning conditions. The obtained propagation speeds of the lower flame edge are slightly overpredicted for which the absence of laser-induced effects may be one reason. These effects in general counteract the initial volume expansion of the heated gas as a flow-field in opposite direction is induced.

Regarding the ignitability of the investigated set-up, a satisfying agreement with the experimentally derived ignition map is achieved. By means of a parameter study it is found, that a larger ignition zone without an initial vapor content leads to a good approximation of the real conditions. The importance of the liquid fuel modeling is emphasized as a critical factor in the flame development as it governs the evaporation length of the first droplets. It is shown that the way length until burnable conditions are reached varies quite significantly,

depending on the employed liquid fuel composition and evaporation model. This aspect also constitutes one of the major findings for generating a viable flame kernel. The ignition zone must be of sufficient size to allow an evaporation of the droplets within the heated-up volume to entail an auto-ignition of the fuel vapor.

6.2. Spray Combustion

In order to increase the technical relevance for this numerical study, the same rectangular combustor set-up as used in the previous section is fitted with a Delavan spray nozzle, which belongs to the air assisted pressure atomizer nozzle types. That allows to investigate the impact of droplet size, velocity distributions and spray cone angle on the flame development, which are also important factors for ignition in a full-scale engine combustor. The geometry which has a significant impact on the flow-field remains of a concise design to enhance the comparison with the experimental results obtained by Mosbach and Gebel [120]. Additionally, the utilized spray nozzle was well characterized in the experiment allowing the numerical approach to be precisely calibrated to the correct boundary conditions. This is a crucial requirement to enable a reasonable comparison. With the accomplished agreement for the boundary conditions it is possible to investigate phenomena which were beyond the scope of the experimental measurements, such as the underlying causes for failed ignition sequences.

The experimental data from Mosbach and Gebel [120] offers two major parts for comparison. The first part relates to the characteristics which distinguish the general behavior of the flame in terms of flame position and flame growth, provided that the ignition was successful. The second part of data comprises measurements aiming at determining the ignition probability of the set-up. For this purpose, different boundary conditions were prescribed with the intention of quantifying the influence of those on the probability of generating a fully developed flame. The laser energy was therefore kept constant which allowed to repeat the ignition procedure several times and extract the number of successful ignitions in correlation with the number of total ignitions. A further aspect was the location of the laser focus. The chance of generating a self-sustained flame is also largely dependent on the exact position where the energy is deposited. Both independent experimental results were compared to the outcome of the simulations. It is demonstrated that the agreement for both, the flame kernel development and the prediction of the ignitability is very satisfying which further promotes the usefulness of numerical tools regarding the investigation of ignition processes.

6.2.1. Experimental Set-Up

The numerical examination is carried out on a grid resembling the experimentally investigated configuration of a rectangular flow channel as depicted in Fig. 6.2.1. The channel has a cross section of 6200 mm^2 along its length of 1 m. In the course of the simulations the channel length is limited to 500 mm as below approximately 450 mm no experimental data

was taken. This unambiguous design was intended to minimize influences stemming from the geometry.

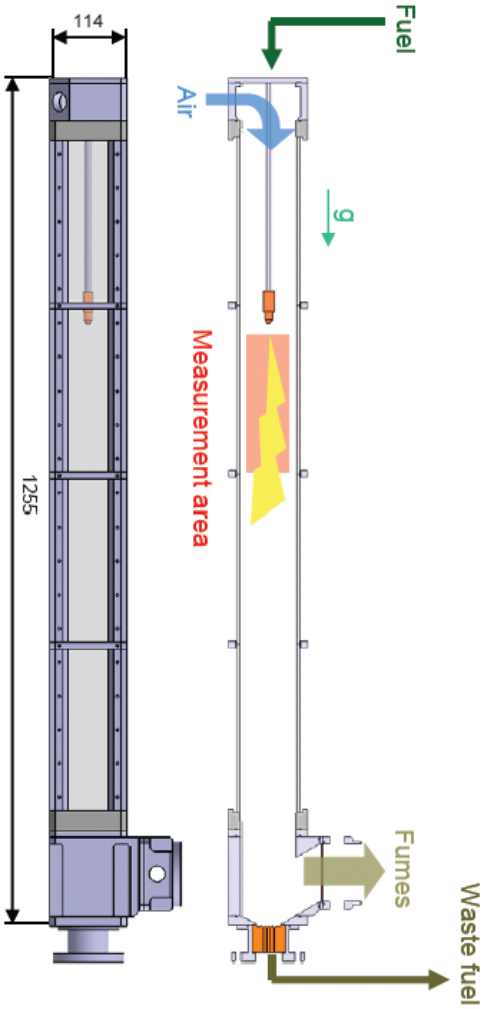

Figure 6.2.1.: **Sketch of the domain, see [120]. Air entering from the top with the fuel droplets emerging from the injector in the upper half of the channel. The laser ignition zone is located at a displacement of** 4 **mm to the middle axis.**

A fuel injector is embedded in the middle of the channel extending from the channel inlet to 320 mm axial position. From the fuel injector, which corresponds to a Delavan Spray Technologies nozzle (model SN 30609-2), a spray with droplet sizes ranging from 20 - 50 μm exits with velocities ranging from 5 - 40 m/s. The employed fuels were Jet A-1 and Exxsol D80, a low aromatic blend of kerosene. A qualitative description of the spray features is provided in Fig. 6.2.2. The spray nozzle belongs to the air-assisted atomizing type, meaning that the air and fuel mix internally. By a slightly swirled flow within the nozzle, the fuel is atomized and a solid cone spray pattern with a fine droplet size distribution is produced. The ignition is carried out with a frequency-doubled Nd:YAG laser which is able to generate pulse energies

up to 400 mJ in single shot mode. The laser focal point is located at 20 mm below the injector tip with a displacement of 4 mm with respect to the center axis. Prior to the laser ignition event the vapor concentration is low due to the imposed atmospheric conditions. Hence, the laser fulfills two tasks: Heating up the gas and generating enough fuel vapor for auto-ignition to occur. In the course of the experimental examination, simultaneous PLIF measurements of the fuel and OH density distribution were accomplished. Additionally, simultaneous high-speed imaging of the chemiluminescence from the OH* and CH* radicals was performed to capture the flame growth and stabilization. The co-flow and spray droplet velocities were determined by using a high-speed PIV technique. For a detailed description of the PLIF, chemiluminescence and PIV experimental devices and techniques, the reader is referred to the experimental report [120]. The air volume flow rate can be varied, ranging from 20 m^3/h to 80 m^3/h, whereas the fuel mass flow can be prescribed from 15 g/min up to over 35 g/min.

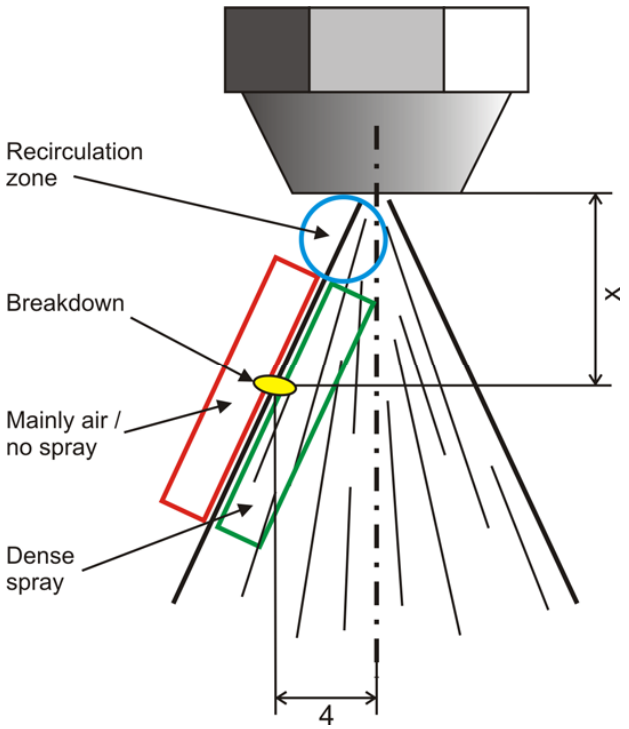

(a)

Figure 6.2.2.: **Illustration of the spray zones taken from Mosbach and Gebel [120].**

The intention of the experimental study was to investigate the flame propagation and flame growth simultaneously. In addition, the fuel evaporation is captured, which gives an insight into the processes governing the flame behavior. The high-speed OH* and CH* chemiluminescence provides further details about the exact position of the flame kernel. Both methods were utilized to yield a good spatial and temporal resolution of the reaction zones. In order to determine accurate boundary conditions for the spray, a Mie-scattering technique was applied to measure the droplet number density and the spray cone angle.

6.2.1.1. Numerical Grid & Boundary Conditions

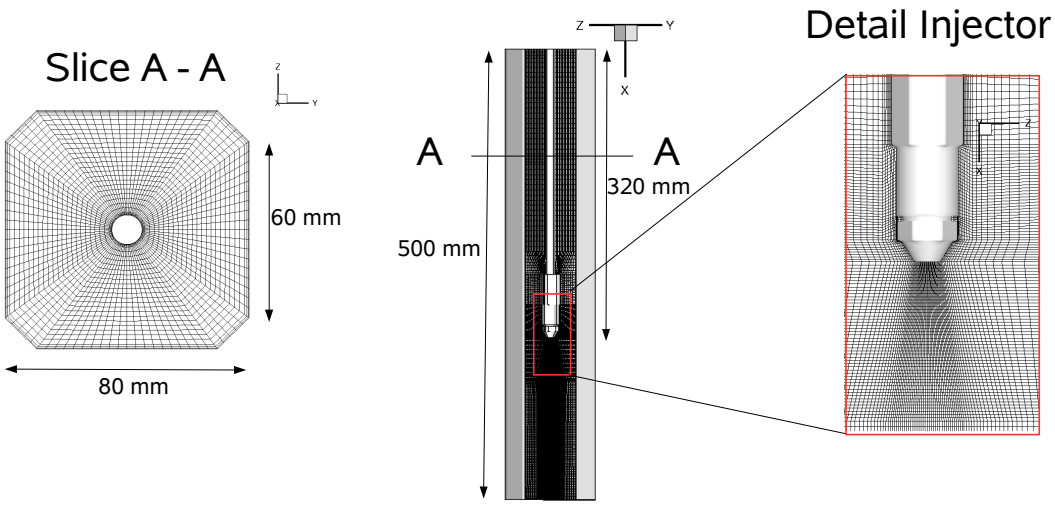

Figure 6.2.3.: **Numerical domain and injector detail.**

Small grid cells in the ignition zone, as discussed in the previous test case (see Sec. 6.1.1.1), constitute one major requirement for being able to accurately define the laser pulse ignition location. However, the modeling requirement due to the presence of a dispersed phase imposes grid cells larger than droplet sizes, which opposes the former condition related to the ignition kernel. For this reason the grid cells in the part just below the injector are of adequate small size of about 0.25 mm as the smallest edge length, representing a compromise between the two demands. Fig. 6.2.3 depicts the grid and a detail of the injector. As the inlet velocity at the beginning of the channel ranges from 0.96 m/s to 3.95 m/s, the coarse discretization at the top of the channel is justified. In total, the number of cells is of the order of 680,000. This enables an efficient calculation with a URANS approach with the main features being well resolved. Table 6.5 provides some major numerical background information about the simulation of this test case.

Table 6.5.: **Numerical background of the spray combustion test case.**

Computational time	
Converged single-phase flow-field	Sim. time step: Steady State (SIMPLE scheme). CPU time: 1.5 days x 4 Knots x 8 CPUs (Intel Nehalem).
Converged multiphase flow-field	Sim. time step: $1x10^{-5}$ s TBP (Three Point Backwards scheme). CPU time: 1 day x 4 Knots x 8 CPUs (Intel Nehalem).
Ignited Flow	Sim. time step: $5x10^{-6}$ s TBP (Three Point Backwards scheme). CPU time: 2-3 days x 4 Knots x 8 CPUs (Intel Nehalem).
Turbulence statistics	
Integral length scale	$l_{\int} = 0.03$ m.
Integral time scale	$t_{\int} = 0.067$ s.

Table 6.6.: **General numerical boundary conditions.**

General Properties	
Air Inflow	Bulk velocity profile. Temperature 293.15 K.
Fuel Injector	Location: $x = 0.32$ m. $r = 8.5$ x 10^{-4}m. Sinusoidal velocity distribution (maximum on the axis). Linear mass distribution (0.0 on axis, maximum at outer radius r of the nozzle). Temperature: 293.15 K. Sauter mean diameter: 35 μm. (Value specified by the manufacturer.) Root normal distribution of droplet sizes.
Side Walls	Adiabatic no slip boundaries.
Outlet	Pressure outlet, $p = 1.01325$ bar
Fuels	Experiment: Exxsol D80, Jet A-1 / Simulation: n-decane

Regarding grid independency, a former study conducted on a similar grid, see [25], points out that the chosen grid resolution is of appropriate quality and changes to the grid do not affect the solution. For this study, the number of computational parcels injected into the domain has been varied to analyze the influence on the simulation results. The standard value for the number of particles per second has been set to: 1.5 x 10^6 [parcels/s]. An increase of this value by a factor of four has not changed the outcome by more than 4 % regarding the flame center and edge locations. The prescribed boundary conditions for the numerical domain can be found in Table 6.6. The specific boundary conditions such as the mass flows and the spray cone angle concerning the respective test cases are given in Table 6.7. Note that, although it is referred to an assisting air co-flow in the nozzle, only its impact on the droplet characteristics as stated in Table 6.7 is modeled. It is assumed that the influence of the additional air mass concerning the gas phase flow-field is negligible. The mass flux and Sauter mean diameter radial distributions from the simulation for different x-planes are given in Fig. 6.2.4. In addition, the exit velocity at the nozzle is illustrated at the bottom on Fig. 6.2.4.

Table 6.7.: **Test case specific boundary conditions.**

Test Case Identifier	C1	C2
Boundary conditions	Air mass flow: 20 m^3/h v_{air} = 0.96 m/s Fuel mass flow for 6 SLM assisting air flow in the nozzle: 17.0 g/min v_{axis} = 23 m/s, v_{edge} = 5 m/s Half spray angle: 19.5°	Air mass flow: 40 m^3/h v_{air} = 1.92 m/s Fuel mass flow for 15 SLM assisting air flow in the nozzle: 17.82 g/min v_{axis} = 35 m/s, v_{edge} = 15 m/s Half spray angle: 16.75°

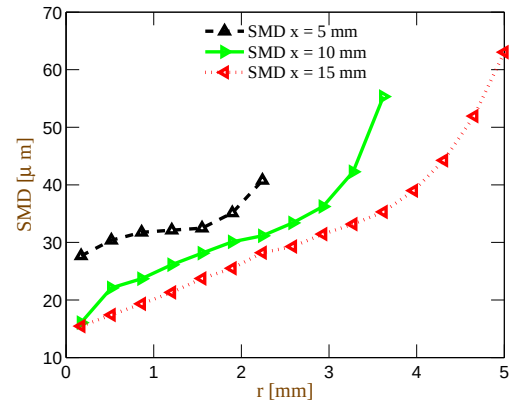

(a)

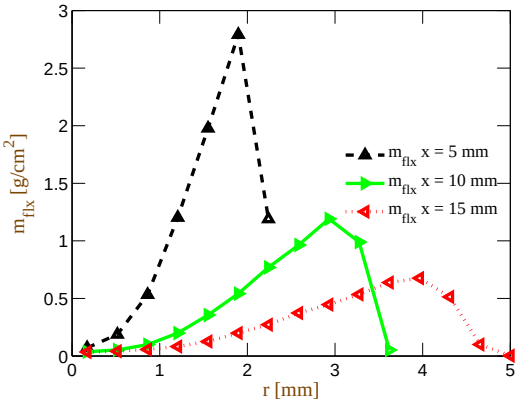

(b)

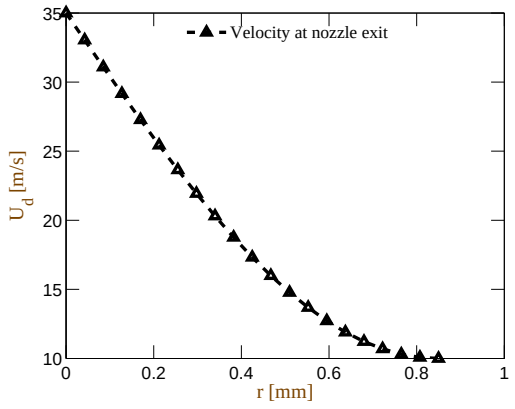

(c)

Figure 6.2.4.: **Results for the C2 case. a) Sauter mean diameter from the simulation for different planes underneath the injector plane. b) Mass flux from the simulation for different x-locations. c) Absolute droplet velocity at the nozzle exit.**

6.2.2. Results

At first, a cold flow comparison is presented which is split into a single-phase part and a second multiphase part in which the spray velocities are compared to the experimental data. After establishing the flow-field agreement, the simulation results including combustion are compared to the experimental outcome with regard to flame position and flame extension.

6.2.2.1. Cold Flow

With the velocity data from the experimental work, a cold flow comparison of the single-phase flow-field without the injection of droplets is performed. In the experiment, a one sided inlet with a downstream sinter plate was prescribed. For the computations, this rather complex boundary condition is simplified. Expectations are that this only slightly affects the solution. In principle, the flow-field without droplets is of only minor importance. Results for the flow-field including spray point out that the flow-field downstream of the injector in which the flame establishes, is dominated by the liquid phase velocity. The results for the single-phase flow-field are depicted at the top of Fig. 6.2.5. Discrepancies in the flow-field occur in the prediction of the recirculation zone, which is overestimated by the simulation. This originates from a more stable flow-field in the simulation which promotes the establishment of a larger recirculation zone. In the experiment, the recirculation zone is shortened, due to coherent structures which develop through the asymmetric inflow. The differences in terms of a relative error decrease from C1 to C2. This stems from the employed turbulence model. URANS models are designed for developed turbulent flows which applies more to the C2 case since higher velocities occur for the same geometry. However, for both cases, the general agreement is still satisfying and should not impede the reactive simulation.
PIV measurements have been accomplished in the course of the experiment. The data can be used to compare the spray velocities obtained from the particle solver. Generally, the velocity distribution is well reproduced, as illustrated at the bottom of Fig. 6.2.5. The derived droplet velocities from registration planes in the simulation exhibit the same features as the experimental curves. The droplet velocity on the axis amounts to ~ 28 m/s, being the maximum observed velocity declining to ~ 7 m/s at the spray cone edge. The spray cone half-angle of $\sim 16.75°$ remains nearly constant within the first 20 mm, supporting the assumption that the flow-field is dominated by the liquid phase and hence no large deformation of the spray pattern occurs. In general, the boundary conditions before the ignition are very similar which confirms that no large error has been introduced.

6.2.2.2. Ignition Kernel Development

In the experiment, the ignition of the spray was carried out with a laser-induced breakdown. The results from the previous droplet chain test case (see Sec. 6.1.1.3) have verified that on one hand, the proper modeling of the laser ignition can be achieved with rather basic

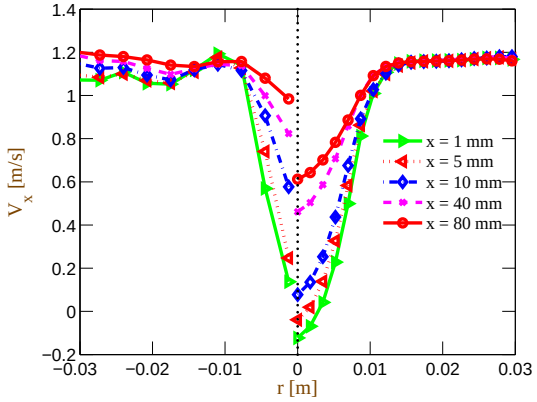

(a)

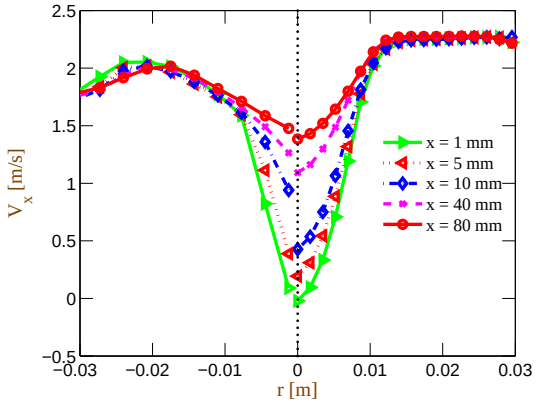

(b)

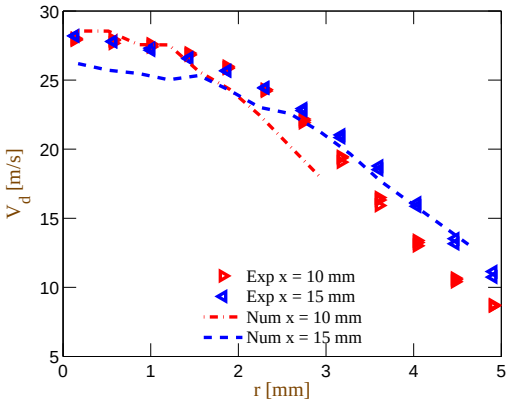

(c)

Figure 6.2.5.: **a) Results for the C1 case: Comparison of measured velocities [120] (left half) and simulated velocities (right half) for the axial velocity of the single-phase flow. b) Results for the C2 case: Comparison of measured velocities (left half) and simulated velocities (right half) for the axial velocity of the single-phase flow. c) Results for the C2 case: Droplet velocities in the experiment and simulation.**

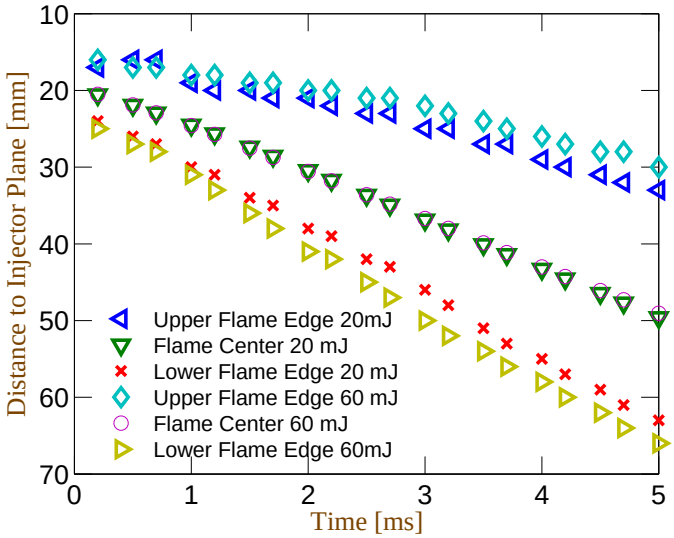

Figure 6.2.6.: **Positions of the flame center and flame edges for two different ignition energies (C2 case). The first three curves correspond to the low energy case with a total ignition energy of 20 mJ. The last three curves relate to an ignition energy of 60 mJ.**

assumptions of a heat source and an initial vapor fraction. On the other hand it has also been confirmed that the laser ignition properties do not influence the later flame propagation to a large extent. This is underlined anew in Fig. 6.2.6 in which the flame position and edge locations are plotted in correlation with the simulation time for two different ignition energies. For the first ignition a total energy of 20 mJ over a period of 0.1 ms is transferred to the gas phase and for the second case an energy of 60 mJ over the same time interval. The flame center remains almost completely unaffected, supporting the fact that the flame location is nearly independent of the spark parameter. Concerning the flame edge positions, small differences for the two cases are noticeable. For the low energy ignition the flame edges do not spread as fast as in the high energy case, as the higher energy entails an increase in the flame speed.

Having clarified that the laser ignition does not alter the flame behavior significantly, the ignition in the following is modeled phenomenologically by providing an energy source of 25mJ over a period of 0.2 ms in a spherical volume of r=2.0 mm. The time scale in which the energy is provided is certainly larger than that in the experiments, yet the absolute value of the effectively transferred energy to the surrounding gas corresponds to the experimental estimate. Based on an energy balance calculation, it was determined in the experiment that from the 400 mJ total laser pulse energy, roughly 20 - 30 mJ remain in the ignition zone. In addition, a fraction of 10% of the fuel droplets mass contained in the ignition volume (sphere with r=2.0 mm) is prescribed to be instantaneously vaporized in the simulation. An almost instantaneous evaporation is also observed in the experiment as a shock-wave induced by the

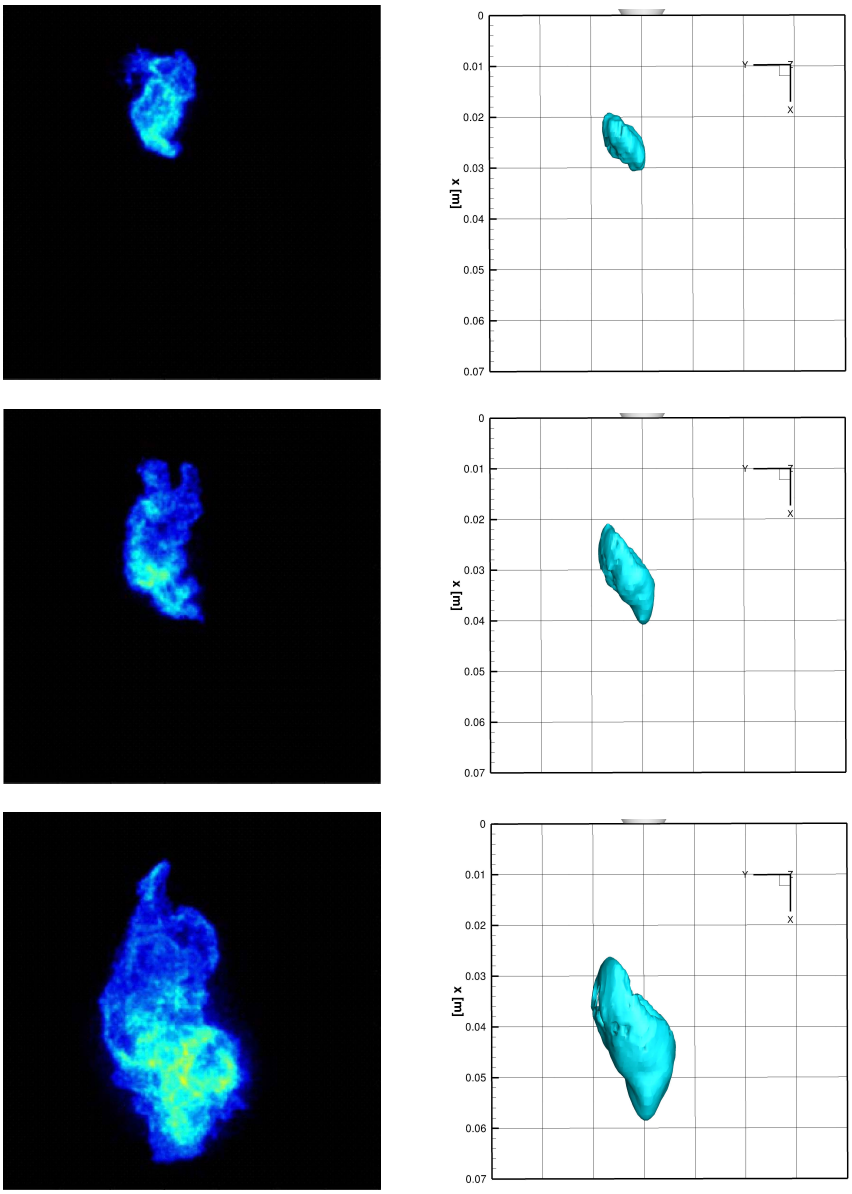

Figure 6.2.7.: **Results for the C2 case. Qualitative comparison of flame shape (Left: Experimental OH-chemiluminescence distribution [120]; Right: Simulation (Iso Surface of 1000 K)) for three different time instances. 1st row: 1 ms. 2nd row: 2 ms. 3rd row: 4 ms.**

laser breakdown causes a secondary break-up. This leads to very small time scales for the evaporation. Once the ignition energy is provided, a first ignition kernel establishes, which is fueled by the initial vapor. The temporal development of the flame is depicted in Fig. 6.2.7 which also contains a qualitative comparison with experimental data [120]. The iso-contour of 1000 K is selected as basis for the comparison with the OH-chemiluminescence since this temperature approximately equals the inner layer temperature of the flame.

Figures 6.2.8 and 6.2.9 show contour plots of the temperature and of the fuel vapor mass fraction from a typical ignition cycle. In the first row, a temperature contour plot and a

fuel vapor mass fraction contour plot are shown corresponding to a simulation time of 1 ms after the ignition. The flame grows due to the provided vapor which is generated by the hot temperatures within the ignition kernel region. Afterward, the temperature in this region starts dropping, since too much fuel has evaporated with insufficient oxidizer being present. Fuel vapor mass fractions of 40 % can be observed in the laser pulse zone which is above the upper flammability limit. This suppresses the sustainment of the flame in the laser zone. The flame therefore spreads to the channel axis as droplets of smaller mean diameter are bound to that regions which allow a fast vaporization and favorable conditions for the combustion to continue. In the second row, the flame tip has reached the center. The center is characterized by higher velocities of both, the droplets and the gas-field, with respect to the outer regions of the spray cone. Since the droplets are still considerably faster than the continuous phase, the droplet evaporation takes place during a longer way length as compared to the outer regions of the spray. This is indicated by the long column of white colored droplets (representing hot droplets) in the middle of the domain which is shown at the top right of Fig. 6.2.8.

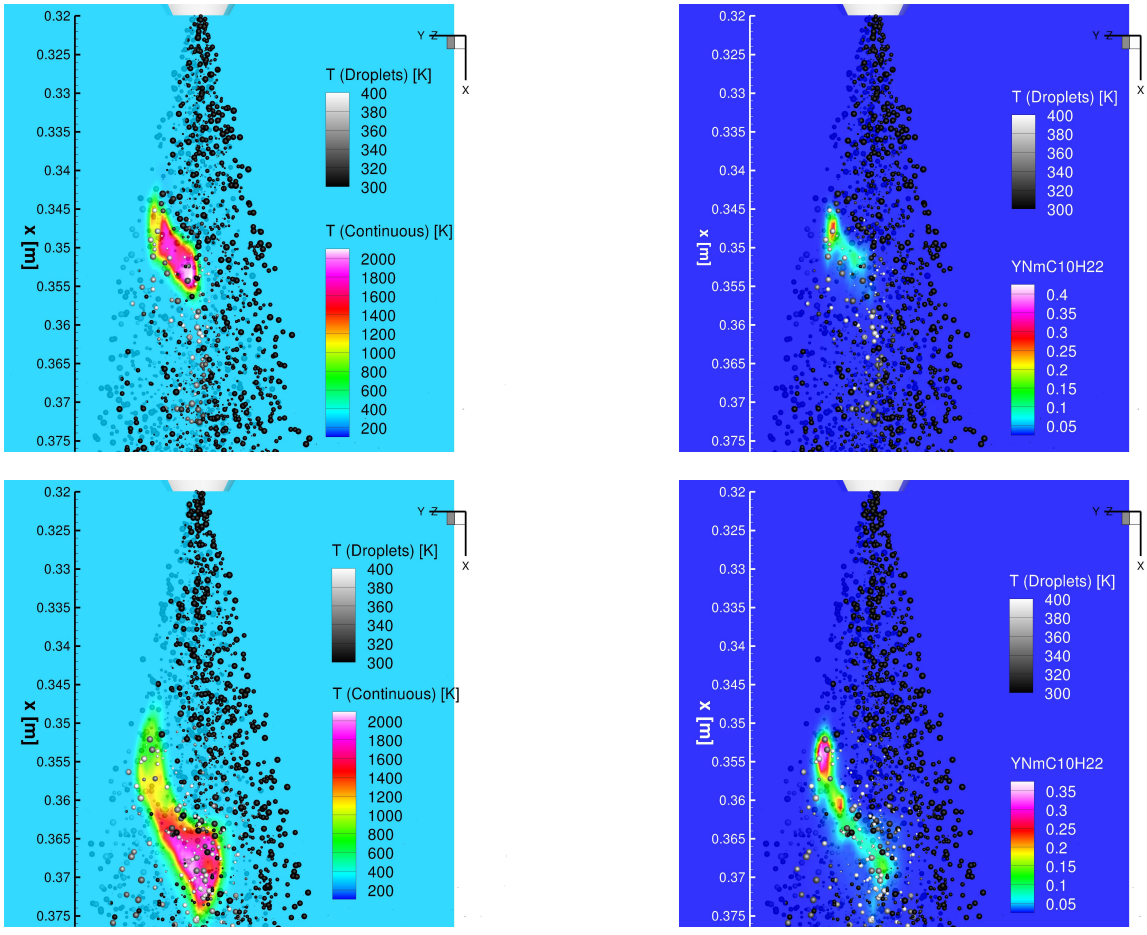

Figure 6.2.8.: **Results for the C2 case. Left column: Flame front location and droplet temperature. Right column: Fuel vapor concentration and droplet temperature. Depicted droplet sizes scale with droplet diameter. 1st Row: $t = 2$ ms. 2nd Row: $t = 4$ ms.**

The more spatially distributed evaporation prevents that too much fuel accumulates in the flame zone and that the fuel vapor mass fraction reaches levels which impede the combustion process. Consequently, the flame can sustain near the channel middle axis and transverses to the other side of the spray cone opposite to the initial off-axis location of the ignition. The beginning of this process is illustrated in the first column of Fig. 6.2.9. Finally, once the very high vapor concentrations have abated at the outskirt of the spray cone, the flame can reattach to the cone surface. The flame eventually adopts a shape which resembles a reverse hollow cone with the center being promoted through the high axial gas velocities and the edges kept back by the slower spray cone shear layer velocities.

To establish a quantitative assessment, general features, such as the flame center position and the flame edge locations are analyzed. This allows a one to one comparison with experimental data, which is presented in Table 6.8 and Fig. 6.2.10.

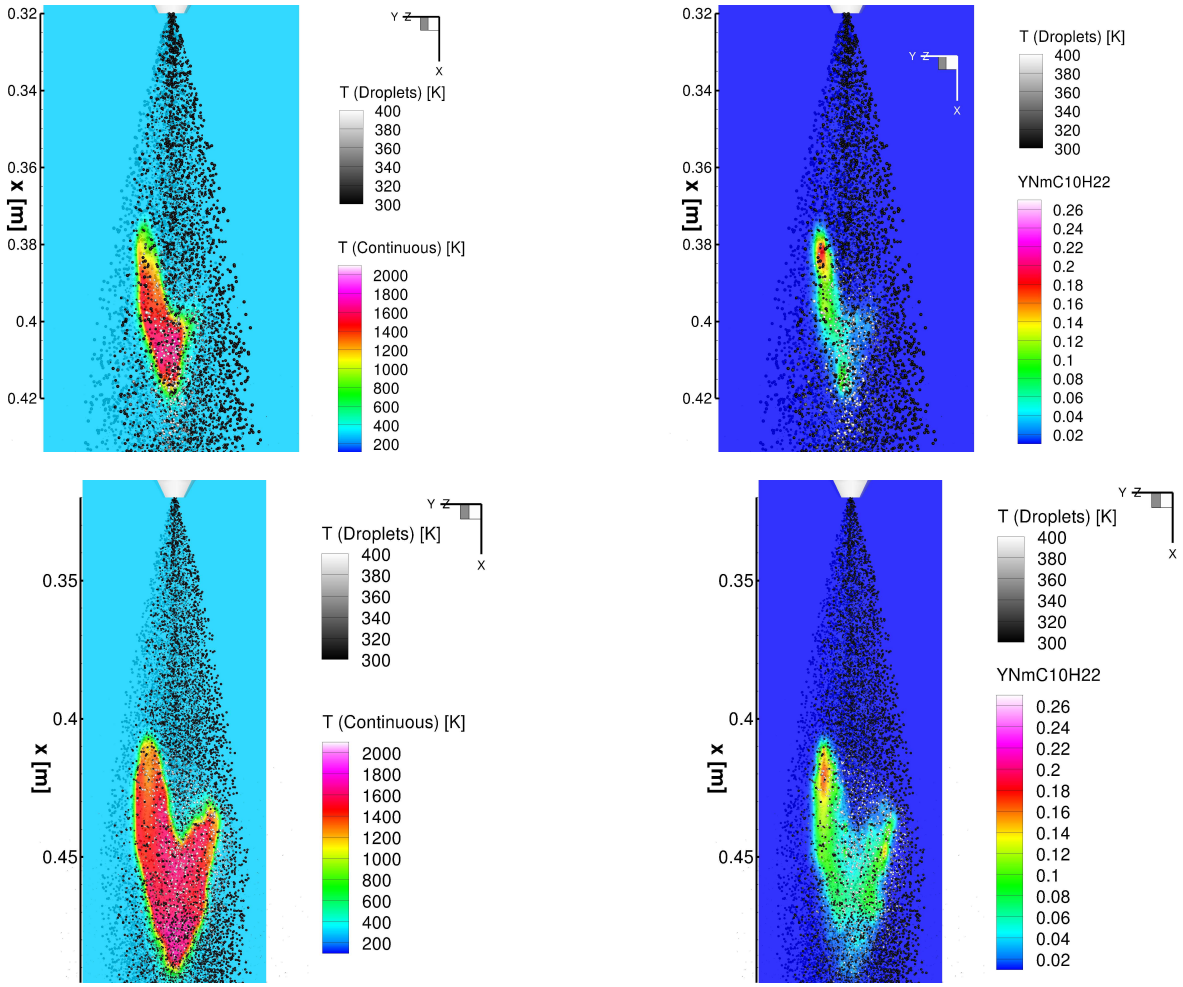

Figure 6.2.9.: **Results for the C2 case. Left Column: Flame front location and droplet temperature. Right column: Fuel vapor concentration and droplet temperature. Depicted droplet sizes scale with droplet diameter. 1st Row: $t = 10$ ms. 2nd Row: $t =$20 ms.**

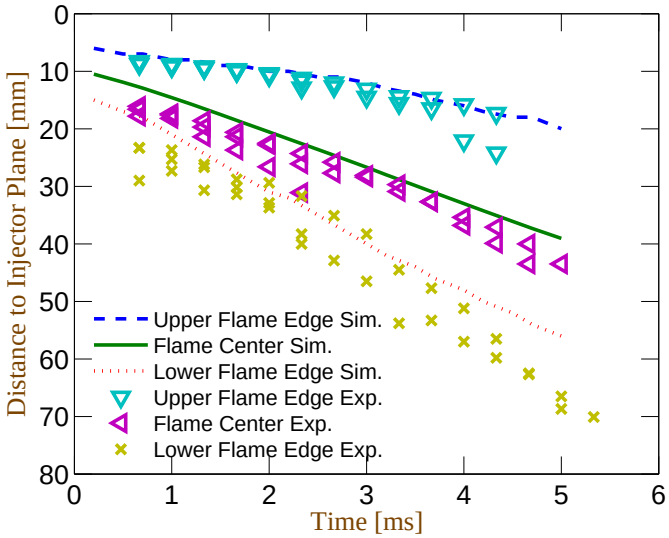

Figure 6.2.10.: **Results for the C2 case. Flame edges and center positions in comparison between experiment [120] and simulation.**

The flame center propagation is captured very accurately, as the convection of the flame itself is governed by flow characteristics which are more easily computed by the numerics. The former evaluation of the flow-field has pointed out that the overall agreement is very satisfying which results in a sound description of the flame location. Regarding the flame edge speed, some slight deviations occur, which can be attributed to the spray characteristics. These are not contained in all detail in the experimental data, as for example the Sauter mean diameter has not been measured. A mean value is given by the manufacturer which has been used as boundary condition in the simulation. However, a tendency to smaller droplets for example would lead to a faster evaporation and could result in an enhanced flame speed, see Sec. 3.3. A second study accomplished by Neophytou et al. [125] has also confirmed that in droplet mist under rich conditions smaller droplet diameter increase the laminar flame speed. In addition, the fuel used in the experiment corresponds to a blend of kerosene. As kerosene also exhibits some more volatile components, the treatment of the liquid fuel as a single component fuel n-decane can cause a deceleration of the computed flame front as well.

6.2.2.3. Conclusion

In general, both the flame center location and the flame edge propagation are predicted with very satisfying precision, which supports the chosen modeling strategy and the spark representation. The assumption is confirmed that the spark parameters with respect to energy and initial vapor content have only a minor influence on the subsequent locations of the flame center and flame edges. Additionally, the representation of the spark through a constant energy source guaranteed that the simulation remained within resolvable temperatures. The numerical results are further evaluated to shed light on the flame structure. It appears that

Table 6.8.: **Comparison of numerical and experimental results [120] of the flame characteristics.**

	Flame Center Speed	Upper Flame Edge Speed	Lower Flame Edge Speed
C1 Case			
Experimental Results	3.62 ± 0.13 m/s	1.01 ± 0.07 m/s	6.24 ± 0.19 m/s
Numerical Results	3.8 1m/s	2.32 m/s	5.4 5m/s
C2 Case			
Experimental Results	6.04 ± 0.23 m/s	5.26 ± 0.69 m/s	10.08 ± 0.40 m/s
Numerical Results	6.43 m/s	3.5 m/s	9.19 m/s

the initial ignition induced very high vapor concentrations within the ignition zone which causes the flame to evade to the central region of the spray cone as there, high velocities and a smaller droplet concentration prevent the generation of detrimental vapor concentrations. Furthermore, it is pointed out that once the high temperatures and fuel vapor concentrations above the rich extinction limits caused by the ignition event have abated, the flame spreads out in circumferential direction again. The final shape which the flame adopts resembles a reversed hollow cone with a promoted flame tip on the axis. Regarding the flame center and edge results, the influence of both the air mass flow and the fuel mass flow combined with changes in the nozzle configuration is elaborated. It is shown that high droplet velocities have a large impact on the mean flow-field and lead to an increase of the convection speed of the flame.

6.2.3. Ignition Map

The good agreement in terms of the flame propagation characteristics has verified that the chosen assumptions are adequate to simulate the ignition kernel development. Furthermore, the boundary conditions were well matched as was illustrated in Fig. 6.2.5. One aspect which has not been fully contemplated so far is the envelope of the ignition with respect to location of the laser pulse focus and imposed boundary conditions. Both are important factors in a real combustor for the success of an ignition sequence. In this paragraph, the capability of the model to support the determination of favorable conditions for the generation of a viable flame kernel in a fuel spray environment is elaborated. The outcome of the simulation is assessed on the basis of the experimental data available for different conditions and locations.

6.2.3.1. Spark Representation

The effective energy from the laser-induced breakdown was quantified in the experiment to equal approximately 20 mJ. In addition, it was observed that a part of the liquid mass present in the ignition volume was almost instantaneously vaporized. These findings comply with experimental studies of laser-ignition that a shock-wave is generated, which induces a

secondary break-up of the droplets and drastically reduces the evaporation time scales, see Gebel *et al.* [64, 65]. It was also found in the previous configuration, see Sec. 6.1.1.3 and Fig. 2.2.3, that within μs after the occurrence of the breakdown, fuel vapor was generated which cannot be explained with typical evaporation rates for the original droplet diameters. In the simulation an instanteneously vaporized fuel mass content of 10% is prescribed with the intention to account for effects that are caused by shock-waves in the experiment which cannot be simulated with the CFD code. The duration in which the total energy of 20 mJ is fed to the computational domain equals 0.1 ms. This guarantees solver stability as very high spatial and temporal gradients are avoided. To capture the laser pulse temporarily and spatially is beyond the scope of a standard CFD solver as the gas takes on plasma states. The associated phenomena cannot be resolved with a standard implementation of the Navier-Stokes equations. However, it was shown for example by Bradley et al. [29] that additional coherent structures are induced by the laser energy. They cause a stronger mixing of the air in the vicinity of the laser pulse, which supports the assumption that the energy release in the domain can be treated approximately homogeneously.

Table 6.9.: **Test case specific boundary conditions for a variation of the assisting air mass flow in the nozzle. SLM stands for Standard Liter per Minute. $V_{d,\mathbf{max}}$ represents the magnitude of the droplet velocity on the centerline and $V_{d,\mathbf{min}}$ the velocity at the outer radius of the fuel nozzle. A linear distribution is prescribed in-between.**

Quantity	10 SLM	15 SLM	20 SLM
$\dot{m}_{\text{fuel}}$ [10^{-3} g/min]	18.56	17.82	17.08
Half Cone Angle [°]	19.5	16.75	15.6
$u_{d,\text{max}}$ [m/s]	28.0	35.0	40.0
$u_{d,\text{min}}$ [m/s]	10.0	15.0	20.0

6.2.3.2. Ignition Parameter Variation

In this ignition study, two aspects have been contemplated. One point is the difference of ignitability with respect to the prescribed boundary conditions of the fuel nozzle. The different settings which are investigated are listed in Table 6.9. Note that, although it is referred to as an assisting air co-flow in the nozzle, only its impact on the droplet characteristics as stated in Table 6.9 is modeled. The gaseous flow from the nozzle is not included, since the mass from the assist air ($\sim$ 1-2 % total gaseous mass) is negligible compared to the mean flow. The other facet is the impact of the location of the energy source on the overall outcome of the ignition event. The investigated ignition locations are presented in Fig. 6.2.11.

For the situation that the assisting air flow in the fuel nozzle is varied, the top of Fig. 6.2.12 depicts the maximum temperature after the ignition energy deposition at 1 cm. It is apparent that only for the 10 SLM case a successful ignition is accomplished. For the other

two settings, the temperature plots also show the peak shortly after the ignition, yet, no sustainable flame can be generated.

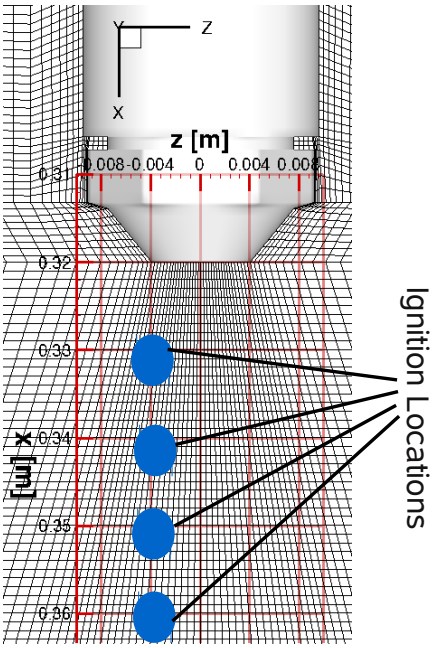

Figure 6.2.11.: **Investigated ignition locations. The cross-axis displacement is kept constant at $z = -4$ mm. For the axis location four distinct distances to the nozzle exit plane are chosen: $x =$ 1 cm, 2 cm, 3 cm, 4 cm.**

At the bottom of Fig. 6.2.12 the temporal evolution of the peak temperature for a fixed assisting air flow in the fuel nozzle of 15 SLM is presented. As mentioned afore, the ignition with the shortest distance to the fuel nozzle fails. It is observed that moving the energy source to locations further downstream leads to successful ignition events with the exception of the location at 4 cm downstream. At this specific point, the ignition is only partially successful. The flame temperature is significantly lower as for the 2 cm and 3 cm case, however, not showing the steep decline as for the 1 cm ignition.

Regarding the results derived in the experiment, they exhibit a very similar behavior, see Fig. 6.2.13. In particular, the impact of a change in the nozzle air flow is well captured. The experimental data also shows a drastic drop of the ignition probability for an increased nozzle air flow. Another observation also made in the experiment is the raise of ignition probability when moving the igniter to a more downstream position. However, it was also denoted that the trend does not continue for the location at 4 cm downstream of the nozzle exit plane.

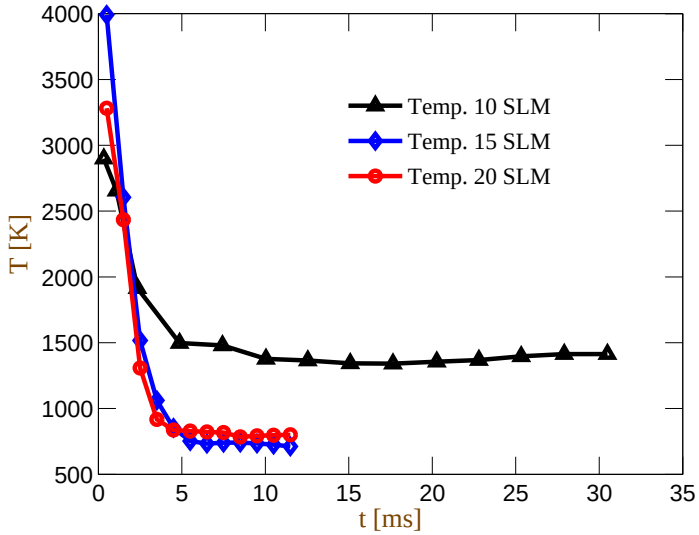

(a)

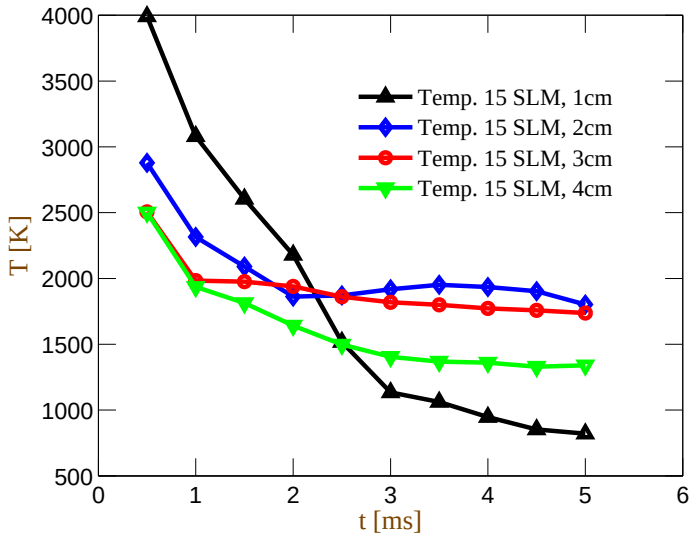

(b)

Figure 6.2.12.: **a) Maximum temperature for the ignition occurring 1 cm downstream location for three different nozzle air flows. b) Maximum temperature for a fixed nozzle air flow with the ignition location varied between 1 cm, 2 cm, 3 cm and 4 cm downstream position.**

6.2.3.3. Discussion

The agreement demonstrated in the previous paragraph allows to analyze more thoroughly the reasons which cause the differences in the ignitability. A first parameter under investigation is the fuel mass contained in the spherical ignition volume. In Table 6.10, the respective fuel masses are listed for the case of a fixed igniter position and different fuel nozzle air flows. It appears that the more fuel present in the ignition volume, the higher the chance of obtaining a successful ignition. This trend continues in Table 6.11 in which the fuel masses

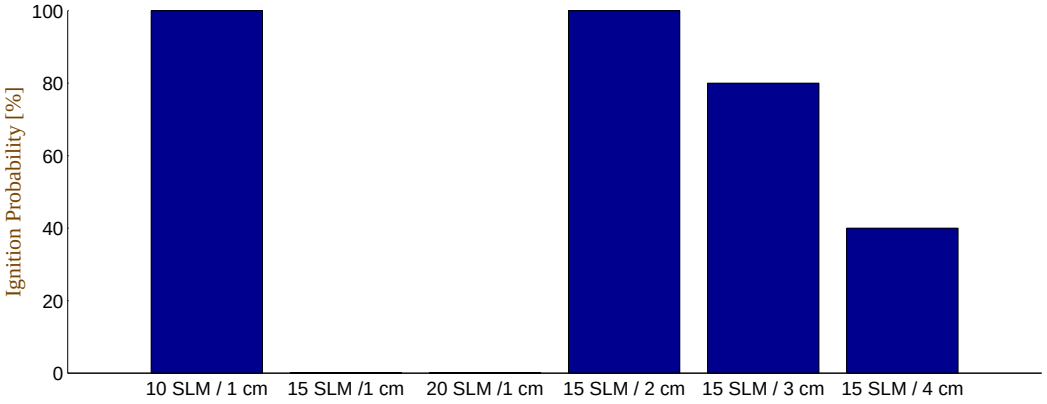

Figure 6.2.13.: **Experimentally derived ignition probability for all investigated conditions and igniter positions, see Mosbach and Gebel [120].**

for the case of a fixed nozzle air flow with varied igniter location are depicted. The ignition probability is also increased when the amount of fuel within the ignition volume is high. However, it is also evident that for all cases the equivalence ratio Φ is above stoichiometric conditions which in principle allows a sustainable combustion.

The first pursued hypothesis is that in cases without successful ignition, the fuel vapor within the flame kernel region raises too strongly and, leads to fuel vapor mass fractions above the rich flammability limit. This does in fact appear quite plausible for ignitions near the nozzle exit plane, where the spray is rather dense. The flammability limits for n-decane have been taken from Cato et al. [31]. In the volume in which the ignition occurs the reference temperature of the cold mixture raises to approximately 2300 K. This leads to very high flammability limits ($>$ 50 % fuel vapor mass fraction) since the upper flammability limit at 200 degree Celsius already denotes 25 % Vol. as investigated by Cato et al. [31]. However, as the high local temperatures also entail a very fast evaporation, high vapor concentration are likely to occur. In Fig. 6.2.14 the maximum and mean fuel vapor mass fraction (averaged over the entire volume) are illustrated. It is pointed out that for the 10 SLM case with an ignition at 1 cm the highest maximum fuel vapor mass fraction is generated and also the highest average value. This essentially opposes the first hypothesis as the flame generation is successful despite the highest fuel vapor concentration. Depositing the energy at 1 cm and

Table 6.10.: **Total contained fuel mass and total equivalence ratio in the ignition zone. The ignition occurred 1 cm downstream for three different nozzle air flows.**

Quantity	10 SLM	15 SLM	20 SLM
Total Mass [μg]	20.59	13.21	7.121
Φ	5.8	3.7	2.0

Table 6.11.: **Total contained fuel mass and total equivalence ratio in the ignition zone. The ignition location is varied between 1 cm downstream to 4 cm downstream for a fixed nozzle air flow (15 SLM) setting.**

Quantity	1cm	2cm	3cm	4cm
Total Mass [μg]	13.21	17.13	15.21	13.47
Φ	3.7	4.8	4.3	3.8

2 cm for 15 SLM nozzle air flow does not lead to a considerable difference in the maximum fuel mass fraction. However, after 3 ms the curve for the average fuel mass fraction for the 2 cm ignition shows a strong incline which is associated with a successful spreading of the initial flame kernel, which does not apply to the 1 cm / 15 SLM case. An incline in the average fuel mass fraction can also be observed for the ignition at 1 cm for 10 SLM nozzle air flow.

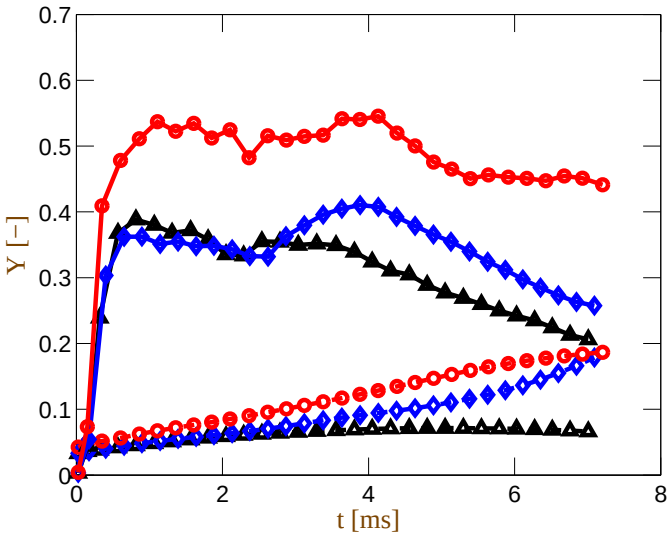

Figure 6.2.14.: **Maximum and mean fuel vapor mass fractions for the ignition taking place at 1 cm for the 10 SLM (successful) and 15 SLM (unsuccessful) setting and at 2 cm for the 15 SLM (successful) setting. Circles represent the ignition for 10 SLM at 1 cm position. Triangles correspond to the ignition for 15 SLM at 1cm position. Diamonds relate to the ignition for 15 SLM at 2 cm position. Solid lines are the maximum values. Dotted lines represent the mean value of the entire domain x 10^3.**

A second possible explanation for the different outcomes of the ignition events for the investigated configurations (Ignition location & SLM) is based on the impact of the Sauter mean diameter of the spray at the location of the ignition. Smaller SMDs in the vicinity of the ignition kernel could enhance the evaporation and consequently promote the growth of the flame. The derived Sauter mean diameters are therefore provided in Table 6.12. Note that for the 1 cm case insufficient droplets have passed at the ignition location to accomplish a

meaningful evaluation.

Table 6.12.: **Sauter Mean Diameter (SMD) at the ignition locations.**

	2 cm	3 cm	4 cm
SMD [μm]	35	30.5	28

Table 6.12 shows that the Sauter mean diameter tends to be more favorable for the ignition the further downstream which agrees with the ignition results for the 2 cm and 3 cm case. However, since the 4 cm ignition has a low ignitability in the simulation and in the experiment, albeit the most favorable SMD, this indicates that the SMD cannot be the crucial parameter governing the outcome of the ignition for this set-up.

In the following it is distinguished between the unsuccessful ignition at the near nozzle plane and the only partial ignition at the foremost ignition plane to offer a more comprehensive understanding of the causes. At first, the ignition at the near nozzle plane is elaborated.

Regarding the ignition at the near nozzle plane, it is pointed out in Fig. 6.2.14 that significant differences are present between the 10 SLM and 15 SLM case. In the 10 SLM case, due to the wider spray cone angle, a much higher maximum fuel vapor mass fraction is created by the ignition energy. The peak in the maximum fuel mass fraction plot is more prominent as compared to the two other depicted cases. The reason is that the ignition zone for the 10 SLM case touches a larger part of the initially high density spray cone than for the 15 SLM case. The schematic of the spray zones in Fig. 6.2.2 illustrates this point. The ignition at 1 cm is only partially located within the spray cone. In case the spray cone becomes wider, a greater part of the ignition zone is within the spray rich region. A second reason which improves the ignitability for a wider spray cone is the more homogeneous velocity distribution of the continuous phase. This is pointed out in Fig. 6.2.15 in which a comparison of the flow velocities of the continuous phase in the proximity of the ignition location is provided. The spray accelerates the continuous phase. Thus, for the 10 SLM case with the widest spray cone, the velocity is increased until 3.5 mm radial position with a more homogeneous velocity distribution (smaller velocity gradient) than for the other SLM configurations. This helps the deposited energy to remain long enough in the vicinity of the droplets to heat them sufficiently to promote the evaporation. In the case of a smaller spray cone angle and higher droplet velocities, the vaporized amount from the spray rich region within the ignition zone is too low to allow the flame kernel to grow. Furthermore, the ignition is affected by the fact that it encounters steeper velocity gradients which shear the ignition energy. In summary, the ignition for the 10 SLM case is successful for two reasons. The ignition location is sufficiently embedded within the spray cone and lower velocity gradients promote the generation of a flame kernel.

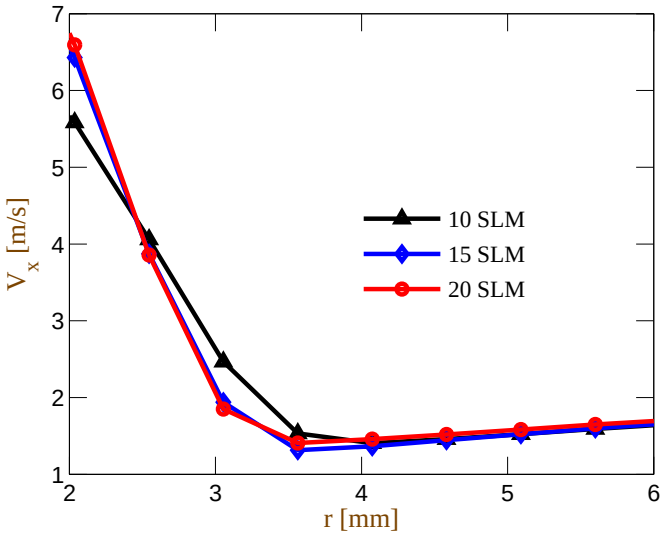

Figure 6.2.15.: **Flow velocities of the continuous phase at 1 cm distance from the injector plane. The larger spray cone angle for the 10 SLM case entails a smaller velocity gradient in the ignition region and accelerates the continuous phase until 3.5 mm radial position.**

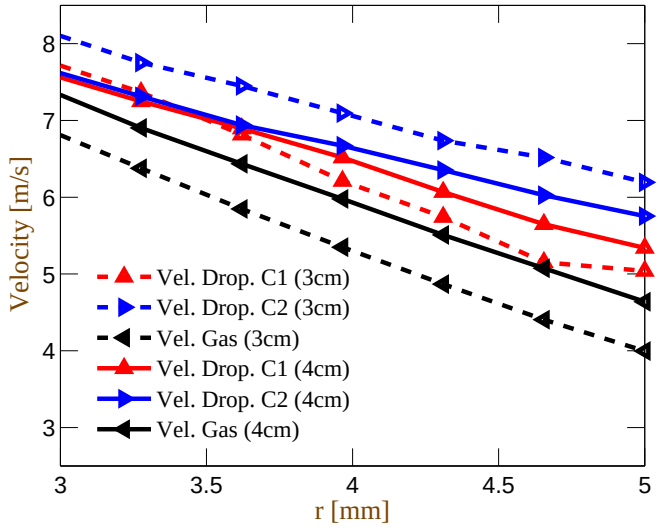

Figure 6.2.16.: **Gas and droplet velocities at 3 cm and 4 cm downstream of the nozzle exit plane. The droplets are grouped in classes. (C1** $\hat{=} D <$ 15μ**m, C2** $\hat{=} D < 40\mu$**m)**

Subsequently, the focus is on the question what causes the deterioration of the ignition probability from the 3 cm ignition to the 4 cm ignition. The total equivalence ratio which prevails at the ignition location under the assumption that all liquid droplets are vaporized amounts to approximately 3.8, see Table 6.11. Consequently, the lack of fuel cannot be the cause for the failed ignition. Therefore, another phenomena must be responsible for the different outcomes of both ignitions. It is found that the velocities of the liquid phase and the continuous

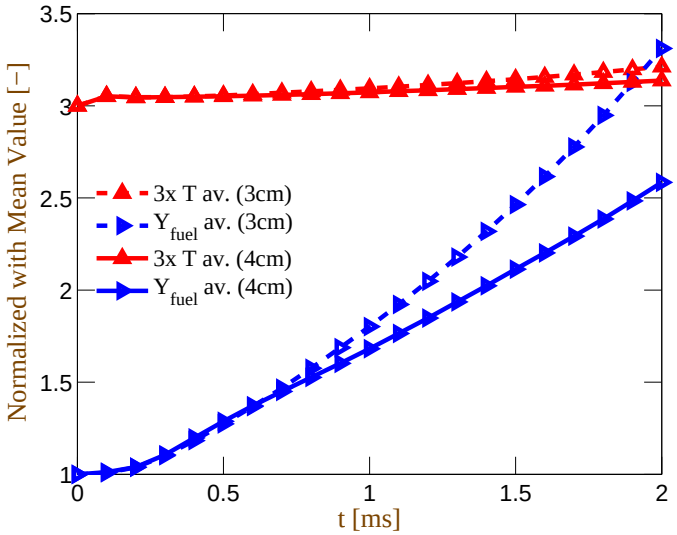

(a)

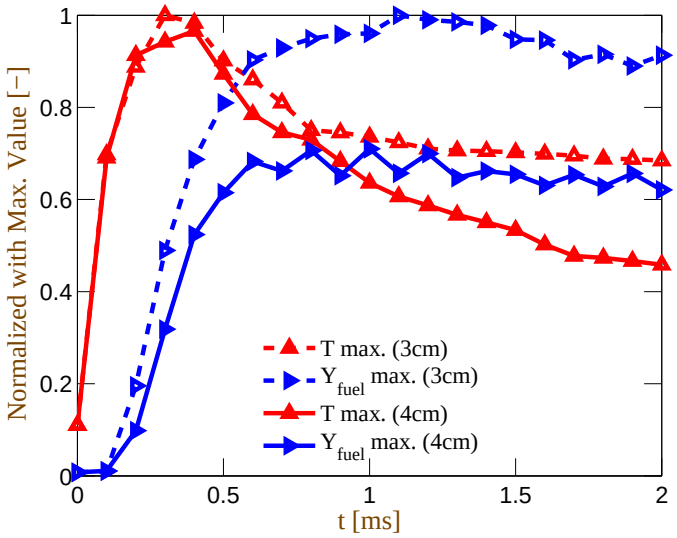

(b)

Figure 6.2.17.: **a) Averaged values of T and Y_{fuel} for the 3 cm and 4 cm ignition normalized with the averaged values of the initial conditions before ignition. The value for T is multiplied by 3 to emphasize the differences. b) Maximum values of T and Y_{fuel} for the 3 cm and 4 cm ignition normalized with the maximum value occurred.**

phase have a crucial influence.

For the ignition at 4 cm it is observed that the gas and the droplet velocities are very similar, as depicted in Fig. 6.2.16. This prevents new droplets from entering the hot ignition zone. As a consequence the fuel droplets already present in the initial volume burn up, whereas a supply with new droplets and fuel droplets leaving the volume is forestalled. In addition, since the total equivalence ratio is above the stoichiometric ratio, once the droplets have

fully evaporated, the source term of the flame progress variable is rather slow. This relates to reduced flame speeds associated with very rich conditions. For an ignition at the 3 cm location, the droplet velocities exceed the gas velocities. Hence, droplets are heated up in the initial hot volume, then, are able to pass the hot kernel and provide fuel vapor to regions in which no flame is present. This allows the reactions to continue in the newly generated vapor and enables the flame to grow.
Furthermore, the fuel vapor cannot accumulate as compared to the ignition at the 4 cm location. This is essential to sustain the flame. To elaborate this theory, at first the trends of the relevant quantities as depicted in Fig. 6.2.17 for the 15 SLM / 3 cm and 15 SLM / 4 cm cases are analyzed. The considered volume for the averages range from 0.34 m$< x <$ 0.38 m in axial direction and fulfills the condition $r <$ 0.1 m in radial direction. It is perceivable that the maximum and average temperature and fuel vapor mass fraction is considerably higher for the successful 3 cm ignition than for the 4 cm ignition. However, an interesting observation is made, when looking at the cross correlation of the temperature and the fuel vapor mass fraction. This is shown in Fig. 6.2.18. Although the values for the averaged and maximum temperature are always higher for the 3 cm ignition, the cross correlation between both quantities is surprisingly identical or even slightly higher for the 4 cm ignition event. This suggests indeed that vapor and heat are confined to the same volume in the 4 cm case which can be the reason for the impairment the flame growth.

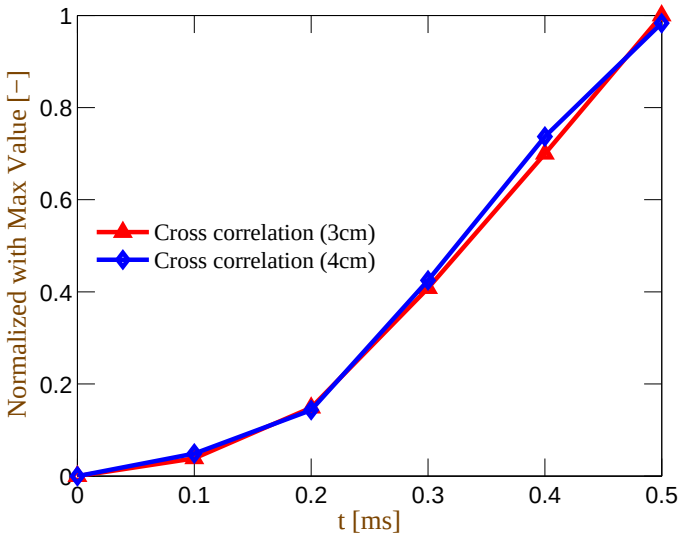

Figure 6.2.18.: **Cross correlation of temperature and fuel vapor mass fraction. The plot corresponds to the expression $y = \mathbf{max}(T-300{,}0.0)\cdot Y_{C_{10}H_{22}}$ within the investigated volume as specified. The values are normalized with the maximum value.**

The observation stemming from the experiment that the ignition probability is decreased to 40 % at the 4 cm location corresponds well with the finding from the simulation. The flame

establishment is impeded through the lack of droplets passing through the hot volume. It is also noticed that the flame is not entirely extinguished as for the ignition at 1 cm, however, exhibits a slower flame growth and lower temperatures.

At last, the role of the ignition energy is contemplated which is certainly a large influence factor. In this numerical study, the total effective energy is chosen to correspond to the estimated value from the experiment. This, however, includes several uncertainties, such as how much energy is contained in the shock-wave, how much of the laser energy leaves the domain to name only two. As aforementioned, the field of laser ignition is still a field of active research [29, 65] which is not fully understood yet. In conclusion, by prescribing a rather low total energy for the ignition, it is possible to observe the same effects and trends as measured. In case much higher ignition energies are employed which was done in a second simulation series for the 3 cm and 4 cm case, the difference between both locations vanishes. The experiment was only accomplished with a single ignition energy, thus, no additional data is available to compare to. That increasing the energy has a favorable effect on the resulting ignition probability was confirmed by other researchers [5]. A larger amount of energy spans a wider region which is more likely to contain areas in which ignition is promoted. In addition, the energy may be transported to favorable regions in which a sufficiently large remaining fraction is able to ignite the mixture. However, in order to study the causes which lead to a failure in ignition, a low ignition energy for which the specific phenomena become more pronounced, is necessary.

6.2.3.4. Conclusion

An ignition case study for a rectangular combustion channel which is equipped with a technical relevant fuel nozzle is presented. The investigation focuses on simulating specific ignition locations and determining which parameters influence the outcome of each respective ignition event in terms of successful and non-successful flame generation. It is found that the ignition is very sensitive to the initial conditions which surround the location of where the ignition energy is released. Especially for the ignition with a distance of 1 cm to the fuel nozzle exit plane, the prevailing conditions have a significant impact. No successful flame is generated if the ignition kernel is produced too far off of the spray cone edge as the very limited amount of available fuel droplets does not sustain the flame. Concerning different locations well inside the spray cone, major differences between the last successful ignition at 3 cm and the partially successful ignition at 4 cm are observed. This was due to the similarity of the velocities between the gas phase and the liquid phase. It prevents in case of the ignition being located 4 cm below the injector plane, the advection of new fuel droplets and the exit of heated up droplets in and from the flame. For locations further upstream, the velocity differences are higher which allows droplets to leave the flame and transport fuel vapor to the vicinity of the flame kernel. In summary, the measured ignition probabilities and the related trends are

Table 6.13.: **Test case identifier regarding the different fuels for the liquid and gas phase.**

Liquid Phase	Gas Phase	Test Case Identifier
Ethanol	Ethanol	F1
n-decane	n-decane	F2
Jet A-1, Single Component	n-decane	F3
Exxol D-80, 2 components mixture	n-decane	F4
Jet A-1, 3 components mixture	n-decane	F5

well captured, indicating the usefulness of numerical tools for the investigation of ignition phenomena.

6.2.4. Variations of Fuel and Ignition Parameters

Since the previous section only covered results which were intended for a direct comparison with experimental data, the range of parameters was restricted. Therefore, this part serves as an extension which delves further into aspects which were not part of the measurements such as investigating the impact of different fuels on the outcome or to modify the ignition parameters. Although the fuel was varied in the experiment, the different fuels have not been employed for identical boundary conditions to study the fuel specific influence. For example Jet A-1 was utilized for deriving the ignition probability map, however, was not taken into account for the flame propagation. To fill the gaps is a further objective of this chapter and to provide data for a direct comparison of different fuels. In addition, the question is explored how the ignition energy affects the probability of successfully lighting the domain.

6.2.4.1. Flame Propagation for Ethanol, n-Decane, Exxol D80, Jet A-1

In the context of fuel flexibility which will essentially play an important role in combustion systems in the future, being able to burn different fuels becomes a major requirement of aero-engine development. This stems from, on the one hand more stringent CO_2 emission regulations and, on the other hand, the general increasing demand for fuel which requires new ways of fuel production. This entails critical differences in the fuel composition. For this reason, the impact of different fuels and the evolving differences regarding the ignition spray flame test case are discussed in this paragraph. Table 6.13 contains the boundary conditions concerning the different fuels and provides an identification of the respective test case. Note that, although two fuel types similar to Jet A-1, namely Exxol D-80 and n-decane, are simulated, the modeling difference of those fuels lies in the multi-component fuel representation of the liquid phase only. On the gas phase the fuel vapor is treated as n-decane. The investigated quantities are the flame center speed and the flame edge speed.

The general boundary conditions concerning the fuel and air mass flows are listed in Table 6.14. The ignition is always carried out at the same position with a constant energy with-

Table 6.14.: **Common boundary conditions for the fuel and air mass flows.**

Air Mass Flow	40 m^3/h
Air Bulk Velocity	u_{air} = 1.92 m/s
Fuel Mass Flow	17.82 g/min
Droplet Velocities	u_{axis} = 35 m/s, u_{edge} = 15 m/s
Half Spray Angle	Half Spray Angle: 16.75°
Ignition Location	2cm Offset to Injector Plane
Ignition Energy	30 mJ, No Instantaneous Vapor
Ignition Shape	Sphere r = 3 mm

out the assumption of an instantaneous fuel vapor content. As the energy is chosen to be sufficiently high, an ignition kernel is generated for all fuels. That the ignition energy has a negligible effect on the subsequent flame propagation was shown earlier, see e.g. Fig. 6.2.6. Therefore, it is assumed that the absolute value of the effective ignition energy, also taking into account that always the same energy is employed, has only a minor influence on the study.

The derived velocities for the flame center and the flame edges are presented in Table 6.15. The results show primarily that the overall differences are not very large, even for two non-similar fuels as employed in F1 and F5, indicating that the flame movement is dominated by convection rather than chemical kinetics. The convection itself is governed by the flow-field which does not significantly change with each respective fuel.

The small deviations which occur shall be elaborated in the following. They can be contributed to the specific characteristics of the corresponding fuel. Ethanol has, in general, a lower flame velocity for similar conditions than higher hydrocarbons. Thus, this explains the lower values for the upper and lower flame edge speed for the case F1. In addition, the adiabatic temperature for an equal mixture fraction and ambient conditions is also below the value for higher hydrocarbons. The lower flame center velocity points out that the mean flow is affected by the higher density, a consequence of the lower combustion temperature, as compared to the other employed fuel combinations.

For the cases in which n-decane is used for the fuel representation in the gas phase, the discrepancy is a consequence of the differences in the liquid fuel treatment. The changes mostly depend on the flow-field and the evaporation which directly fuels the combustion processes. The flow-field is affected when using a different type of fuel due to differences in the fuel density. n-decane being one of the lighter components of Jet A-1 exhibits a lower mass density as compared to Jet A-1. This leads to an increased velocity of the liquid phase under the assumption that the mass flow rate is fixed. Since the droplets are faster than the surrounding gas, the acceleration of the gas phase by the liquid phase is enhanced. This explains the higher flame center velocity of n-decane, although at the same time the relative velocities of the flame edges are lower than for the Jet A-1 fuels. A high mean flame center

Table 6.15.: **Derived velocities for the investigated fuels. $\Delta u_{\mathbf{UEV}}$ represents the difference in velocity of the upper flame edge speed to the flame center speed. The value of $\Delta u_{\mathbf{LEV}}$ corresponds to the difference of the lower flame edge speed.**

Test Case Identifier	Flame Center Speed	Upper Flame Edge Speed	Lower Flame Edge Speed	Δu_{UEV}	Δu_{LEV}
F1	5.49 m/s	3.55 m/s	7.15 m/s	1.94 m/s	1.66 m/s
F2	5.86 m/s	3.77 m/s	7.67 m/s	2.09 m/s	1.81 m/s
F3	5.81 m/s	3.68 m/s	7.77 m/s	2.13 m/s	1.96 m/s
F4	5.77 m/s	3.73 m/s	7.56 m/s	2.04 m/s	1.79 m/s
F5	5.85 m/s	3.75 m/s	7.81 m/s	2.10 m/s	1.96 m/s

Table 6.16.: **Determination of the lowest ignition energy necessary to obtain a fully established flame.**

Test Case Identifier	F1	F2	F3	F4	F5
Minimum Ignition Energy	5 mJ	10 mJ	10 mJ	10 mJ	10 mJ

velocity in conjunction with increased relative velocities of the upper and lower flame edge is observable for the CTM Jet A-1 consisting of three component families. In this case, the evaporation is accelerated due to the modeling of whole component groups which also involve more volatile species. The more intense combustion promotes a velocity increase of the flow-field due to lower gas densities.

6.2.4.2. Ignitability for Ethanol, n-Decane, Exxol D80, Jet A-1

In the previous paragraph, the characteristics of the developing flame were simulated. The results provide insight in how fast the flame expands and where it is convected to by the mean flow. To know the differences which are intertwined with a change of fuel is essential for designing a combustor. It was shown that the results were quite similar in principle, yet, small deviations can occur. In some cases a small difference in the flame growth might decide whether the flame can expand to a stable anchoring position. A question of comparable importance is the probability of being able to generate a first flame kernel. Therefore, the same fuel types as employed in the previous paragraph are investigated with focus on their ignition performance. The parameter which is studied is the minimum ignition energy which has to be provided to the domain to light the test case. The same condition as specified in Table 6.14 with the identifiers as given in Table 6.13 are used. This time, the ignition energy is reduced in steps of 5 mJ until the ignition fails. This marks the lower bound for the ignition energy. The outcome of this parameter variation is provided in Table 6.16.

The results point out that the different modeling of the fuel in case of Jet A-1 does not lead to significant changes to the outcome of the ignition sequence for this set-up. The minimum

required amount of energy for all long hydrocarbon equals 10 mJ. A major difference occurs when ethanol is used as fuel. Since ethanol is more volatile than the other long hydrocarbons, the small amount of energy provided to the domain suffices to generate an initial flame kernel. The ethanol fuel droplets require shorter times to evaporate which leads to an increased fuel vapor production when the droplets encounter the heated laser breakdown region. The fuel droplets in the ignition zone are generally faster for this test case than the surrounding gas which renders it crucial that the short period in which the droplet crosses the hot air is sufficient for the evaporation.

6.2.4.3. Summary

In summary, this investigation shows that the model is able to capture differences in the flame behavior which result from variation of the employed fuel. At first, the characteristics of the developing flame are analyzed. It is elaborated that ethanol due to its lower flame speed leads to a slower spreading of the flame. For Jet A-1 fuels, the flame spreading is enhanced. It is observed that small disparities occur through the treatment of the liquid fuel as either a single or a multi-component fuel. These can be contributed to the characteristic properties of the additional component families which are included in a multi-component modeling. By also considering the more volatile components of the fuel, the evaporation is accelerated which entails slightly higher flame speeds. Concerning the minimum ignition energy, the study points out, that ethanol ignites with the least energy. This is due to the faster evaporation that allow droplets within the ignition zone to evaporate sufficient enough to generate viable conditions for an initial flame kernel. Without experimental data, a verification of the findings cannot be provided in the scope of this work.

7. Summary

The objective to simulate ignition problems numerically is accomplished for a number of test cases. At first, the numerical background is described in detail to allow a thorough understanding of the employed models and to highlight the requirements which have to be met in ignition simulations. The fundamental Navier-Stokes equations, the Lagrangian approach to track the particles, the turbulence model and the developed combustion model are introduced. The extended combustion model represents the main achievement of this work. It is an improved version of the original turbulent flame speed closure model. The advantage of the extended TFC model is that it spans the whole flame evolution from the initiation of a flame kernel until the stabilization of the flame for both, single- and multi-phase flows. It is shown that the modeling assumption of a heat source, representing the flame initiation mechanism gives satisfying results. The proposed second source term for the flame progress variables also allows a more physical and consistent method to prescribe ignition boundary conditions. The need for the substitution of the flame progress variable in order to adopt the model to multiphase flows is contemplated. Furthermore, it is demonstrated that the model improvements avoid pitfalls which are existent in the original model formulation concerning the mixing of burnt and unburnt gases.

Subsequently, as first step to verify the model extension, a series of elementary test cases are presented. These generic test cases serve as means to validate several aspects of the combustion model. The correct prediction of the flame shape which is governed by the laminar flame speed in the chosen set-ups is investigated first. A first comparison with experimental data for a shearless diffusion flame configuration which involves moderate turbulence levels shows the appropriate chemistry-turbulence interaction of the model as the experimental results are well captured by the simulation. A second benchmark test, this time for a configuration in which laminar flame speeds of a multiphase flow are evaluated, outlines the proper multiphase behavior of the model.

In the following, the model is applied to two set-ups for which ignition maps are available. These test cases are meant to assess the spark representation and the model ability to describe the flame evolution from an initial flame kernel to a self-sustained flame. The agreement between the numerical and experimental data underlines the adequacy of the chosen modeling approach and demonstrates the usefulness of the simulation to find favorable conditions for

the ignition. A key finding is that ignition can also be successful even if the energy deposition occurs away from burnable mixtures. The study of these scenarios is enabled through the proposed spark representation. The incorporation of heat as source for the flame progress allows the ignition in an arbitrary part of the domain. It is elaborated that the hot ignition zone gases can proceed to flammable mixture and light the domain.

A highly turbulent confined jet flame as a challenge regarding the embedded quenching mechanism represents the next investigated configuration. The major characteristics of the test case are well captured by the model. The flame is lifted as a consequence of the high strain rates which are present at the sides of the jet. Furthermore, the model correctly predicts that the flame cannot evolve at the narrower side of the channel as wall heat losses and detrimental turbulence effects suppress the combustion processes in this area. The core finding is that the model can distinguish correctly between favorable turbulence which enhances the combustion rate through the wrinkling of the flame front and unfavorable turbulence which can cause flame quenching through disturbing the inner reactions of the flame. A subsequent ignition case study shows the large variations in the flame development that can result from different igniter positions. Although the mixture in the entire channel is homogeneous, ignition above a certain height in the combustor does not lead to a stabilized flame as the flame kernel is convected outside the domain. The significance of knowing the location of the recirculation zone which allows a backward propagation of the flame is pointed out.

In the following, two DLR experiments of multiphase laboratory flames are studied numerically. For both test cases a broad basis of experimental data is available which allows an in-depth assessment of the obtained numerical results. The first test case concerns five parallel mono-dispersed droplet chains that are injected from a fuel lance in the domain middle. The chosen boundary conditions are very basic to facilitate the comparison between experiment and simulation. The cold flow evaluation shows that the droplets have a crucial influence on the flow field which is confirmed in the experiment. It is found that the probability of generating a flame is nearly independent of the chosen air co-flow which has only a minor impact. In contrast, the boundary conditions for the fuel flow have a large influence on the ignitability. A crucial observation is that the modeling of the liquid phase can be of large importance as it affects the characteristic evaporation length of a droplet. With the utilized Continuous Thermodynamics approach, the ignition probability map which is compiled in the experiment is well captured. The second aspect, the flame development in terms of flame size and flame location is also well described by the simulation. The flame center location as a quantity which is linked mainly to the mean flow characteristics shows a very satisfying agreement. The flame edge velocity which incorporates chemical effects through the local burning velocities is also reasonably predicted by the numerical approach.

The second multiphase-flow test case which involves a spray nozzle as fuel system exhibits

several relevant features of a real engine combustion chamber. The encountered velocities are higher than in the droplet stream test case and the spray offers a poly-dispersed character. Thus, the flame development is also influenced by parameter such as the mean droplet diameter and the prevailing shear stresses. A comparison of the flame evolution points out that the simulation delivers a very accurate picture of the flame. The flame center locations are well captured and also the flame edge velocities are in good agreement. This allows a thorough analysis of the ignition statistics of this configuration. In the experiment four different ignition locations in combination with three different boundary condition settings are investigated. The study reveals that ignition close to the nozzle on the spray cone edge fails for two of the three boundary condition settings. In the simulation the underlying causes are identified. It is discovered that a wider spray cone angle, which is induced by a lower assisting air mass flow in the nozzle, promotes the transport of the ignition energy within the spray. For the two other settings, the narrower spray cone exerts higher shear stresses on the ignition energy. As a consequence the remaining transported deposited heat does not suffice for the generation of a viable flame kernel. In the experiment it is also observed that the ignition probability rises first with increased distance to the nozzle exit plane, however reduces again for the furthest investigated location. In the simulation, an analysis identifies the probable cause. The fast spray leads an acceleration of the surrounding gas. For the closer ignition locations, the mean flow velocity of the gas remains reasonably lower than the droplet velocities which allows the droplets to enter the zone of hot gas stemming from the imposed ignition energy and to leave this zone. For the ignition at the furthest distance, the velocities of the gas and droplets have approached so much that most of the droplets are trapped within the ignition volume. This results in a confinement of the generated fuel vapor which eventually becomes too much and impedes the growth of the flame.

The last two configurations demonstrate the potential of the modeling approach. Underlying causes for a failed ignition which are often difficult to identify can be studied numerically. The simulation allows the generation of a comprehensive data set which largely facilitates the analysis. Furthermore, once the boundary conditions for the simulation are established, numerous ignition location can be evaluated which offers a fast and efficient way to locate favorable igniter locations in the combustor volume. The second significant contribution to the ignition probability concerns the influence of the flow field. Even without a reactive simulation, pre-obtained mean flow velocity magnitudes, prevailing turbulence levels and locations of for example the recirculation zones belong to the important parameter which can be determined beforehand.

All obtained results confirm the theory proposed by Levebvre [96] that the success or non-success of an ignition procedure is based upon the fulfillment of three phases. The deposition of a sufficient amount of energy to activate the primary chemical reactions is the first neces-

sary step. In the jet flame test case, the decline in the ignition probability is explained by the too fast dissipation of the available heat which forestalles the flame kernel generation. The second phase concerns the growth of the flame. In the spray nozzle configuration, the ignition fails as the flame is not able to grow in size due to the confinement of the fuel vapor generating droplets to the hot ignition zone. The last process, the stabilization of the flame cannot be achieved in the enclosed jet test case. Although a viable flame kernel and eventually a self-sustained flame is generated, the flame cannot propagate backwards and, thus, does not accomplish a fully lighted combustor. In conclusion, the developed extended TFC model demonstrates a very satisfying agreement for all investigated test cases. In the course of this thesis several causes for a failed ignition are identified numerically. These findings can be employed in the future to assess the appropriateness of certain boundary conditions or a certain igniter position for the generation of the flame. Furthermore, the results of the simulation show, on the one hand, the usefulness of numerical tools as an analysis tool to understand a problem and, on the other hand, point out the adequacy of the simulation to enhance design processes by allowing a parallel investigating of different potential configurations.

List of Figures

List of Tables

Bibliography

[1] B Abramzon and W. A. Sirignano. Droplet vaporization model for spray combustion calculations. *Int. J. Heat Mass Transfer*, 32:1605–1618, 1989.

[2] S. F. Ahmed, I. A. Bahane Ledezma, and E. Mastorakos. Spark ignition in a turbulent shearless fuel-air mixing layer: Average flame growth rates. *Proceedings of the 47th AIAA Aerospace Sciences Meeting, 2009, Orlando, FL (USA)*, 2009.

[3] S. F. Ahmed, R. Balachandran, T. Machione, and E. Mastorakos. Spark ignition of turbulent nonpremixed bluff-body flames. *Combust. Flame*, 151:366–385, 2007.

[4] S. F. Ahmed, R. Balachandran, and E. Mastorakos. Measurements of ignition probability in turbulent non-premixed counterflow flames. *Proc. Combust. Inst.*, 31:1507–1513, 2006.

[5] S. F. Ahmed and E. Mastorakos. Spark ignition of lifted turbulent jet flames. *Combust. Flame*, 146:215–231, 2006.

[6] S. F. A. F. S. Ahmed. *Spark Ignition of Turbulent Non-premixed Flames*. PhD thesis, University of Cambridge, 2006.

[7] J. D. Anderson. *Computational Fluid Dynamics*. McGraw-Hill, 1995.

[8] P. Bailly, M. Champion, and D. Garreton. Counter-gradient diffusion in a confined turbulent premixed flame. *Phys. Fluids*, 9:766–774, 1997.

[9] D. R. Ballal and A. H. Lefebvre. The influence of spark discharge characteristics on minimum ignition energy in flowing gases. *Combust. Flame*, 24:99–108, 1975.

[10] D. R. Ballal and A. H. Lefebvre. The influence of flow parameters on the minimum ignition energy and quenching distance. *Proc. Combust. Inst.*, 15:1473–1481, 1976.

[11] D. R. Ballal and A. H. Lefebvre. Ignition and flame quenching of flowing heterogeneous fuel-air mixtures. *Combust. Flame*, 34:155–168, 1979.

[12] D. R. Ballal and A. H. Lefebvre. A general model of spark ignition for gaseous and liquid fuel-air mixtures. *Proc. Combust. Inst.*, 18:1737–1746, 1980.

[13] A. D. Birch, D. R. Brown, and M. G. Dodson. Ignition probabilities in turbulent mixing flows. *Proc. Combust. Inst.*, 18:1775–1780, 1981.

[14] A. Bjoerck. *Numerical Methods for Least Squares Problems*. SIAM, 1996.

[15] T. Blacha, M. Di Domenico, P. Gerlinger, and M. Aigner. Soot predictions in premixed and non-premixed flames using a sectional approach for PAHs and soot. *Combust. Flame*, 2011.

[16] J. Boussinesq. Essai sur la théorie des eaux courantes. *Memoires presentes par divers savants á l'Académie des Sciences XXIII*, 1:1–680, 1877.

[17] J. M. Boyde, M. Di Domenico, B. E. Noll, and M. Aigner. Spark ignition simulations and the generation of ignition maps by means of a turbulent flame speed closure approach. *Proceedings of the ASME Turbo Expo*, GT2010-22211, 2010.

[18] J. M. Boyde, A. Fiolitakis, M. Di Domenico, and M. Aigner. Correlations for the laminar flame speed, adiabatic flame temperature and ignition delay time for methane, ethanol and n-decane. *Proceedings of the 49th AIAA Aerospace Sciences Meeting, 2011, Orlando, FL (USA)*, 2011.

[19] J. M. Boyde, P. Le Clercq, M. Di Domenico, T. Mosbach, G. Gebel, M. Rachner, and M. Aigner. Ignition and flame propagation along planar monodisperse droplet streams. *Proceedings of the 49th AIAA Aerospace Sciences Meeting, 2011, Orlando, FL (USA)*, 2011.

[20] J. M. Boyde, P. Le Clercq, M. Di Domenico, M. Rachner, G. C. Gebel, T. Mosbach, and M. Aigner. Validation of an ignition and flame propagation model for multiphase flows. *Proceedings of the ASME Turbo Expo*, GT2011-45104, 2011.

[21] J. M. Boyde, P. Le Clercq, M. Di Domenico, M. Rachner, G. C. Gebel, T. Mosbach, and M. Aigner. Numerical investigation of the parameter governing the ignitability of a spray flame. *Proceedings of the ASME Turbo Expo*, GT68181, 2012.

[22] J. M. Boyde, P. Le Clercq, M. Di Domenico, M. Rachner, G. C. Gebel, T. Mosbach, and M. Aigner. Numerical investigation of the parameter governing the ignitability of a spray flame. *Journal of Engineering for Gas Turbines and Power*, 135/1, 2013.

[23] J. M. Boyde, P. Le Clercq, G. C. Gebel, T. Mosbach, and M. Aigner. A numerical investigation of the ignition characteristics of a spray flame under atmospheric conditions. *Proceedings of the 50th AIAA Aeropsace Sciences Meeting, 2012, Nashville, TN (USA)*, 0174, 2012.

[24] J. M. Boyde, P. C. Le Clercq, M. Di Domenico, and M. Aigner. Extension of the turbulent flame speed closure model to ignition in multiphase flows. *Combust. Flame*, 2012.

[25] J. M. Boyde, Y. Schneider-Kühnle, and M. Aigner. Lufo IV project GerMaTec. Technical report, DLR-VT, 2011.

[26] D. Bradley, P. H. Gaskell, and Gu. Burning velocities, Markstein lengths, and flame quenching for spherical methane-air flames: A computational study. *Combust. Flame*, 104:1769–198, 1996.

[27] D. Bradley, M. Lawes, and M. S Mansour. Explosion bomb measurements of ethanol-air laminar gaseous flame characteristics at pressures up to 1.4 MPa. *Combust. Flame*, 156:1462–1470, 2009.

[28] D. Bradley and F. K-K. Lung. Spark ignition and the early stages of turbulent flame propagation. *Combust. Flame*, 69:71–93, 1987.

[29] D. Bradley, C. G. W. Sheppard, I. M. Suardjaja, and R. Woolley. Fundamentals of high-energy spark ignition with lasers. *Combust. Flame*, 156:55–77, 2009.

[30] K. N. C. Bray, P. A. Libby, G. Masuya, and J. B. Moss. Turbulence production in premixed turbulent flames. *Combust. Sci. Tech.*, 25:127–140, 1981.

[31] R. J. Cato, W. H. Gilbert, and J. M. Kuchta. Effect of temperature on upper flammability limits of hydrocarbon fuel vapors in air. *Fire Technology*, 3:14–19, 1967.

[32] Tuncer Cebeci, Jian. P. Shao, Fassi Kafyeke, and Laurendeau Eric. *Computational Fluid Dynamics for Engineers*. Horizons Publishing, Springer, 2008.

[33] N Chakraborty, E Mastorakos, and R. S. Cant. Effects of turbulence on spark ignition in inhomogeneous mixtures: a direct numerical simulation (DNS) study. *Combust. Sci. Tech.*, 179:293–317, 2007.

[34] R. H. Chen and J. F. Driscoll. Nitric oxide levels of jet diffusion flames: Effects of coaxial air and other mixing parameters. *Proc. Combust. Inst.*, 23:281–288, 1990.

[35] P. Cho, C. K. Law, R. K. Cheng, and I. G. Shepherd. Velocity and scalar fields of turbulent premixed flames in stagnation flow. *Proc. Combust. Inst.*, 22:739–745, 1988.

[36] R. Clift, J. R. Grace, and M. E. Weber. *Bubbles, drops and particles*. Academic Press, 1978.

[37] D. Cokljat, W. Polifke, and P. Wild. A non-adiabatic method for calculation of premixed flames using a turbulent flame speed closure. *7th Int. Conference on Numerical Combustion, 1998, York, UK*, 1998.

[38] M. Colket, T. Edwards, S. Williams, N. P. Cernansky, D. L. Miller, F. Egolfopoulos, P. Lindstedt, K. Seshadri, F. L. Dryer, C. K. Law, D. Friend, D. B. Lenhert, H. Pitsch, A. Sarofim, M. Smooke, and W. Tsang. Development of an experimental database and kinetic models for surrogate jet fuels. *Proceedings of the 45th AIAA Aerospace Sciences Meeting, 2007, Orlando, FL (USA)*, 2007.

[39] J. Contreras Espada. *Numerical Simulation of Reacting Flows under Laminar Conditions with Detailed Chemistry*. PhD thesis, Technische Universität Darmstadt, 2010.

[40] James Deardorff. A numerical study of three-dimensional turbulent channel flow at large reynolds numbers. *Journal of Fluid Mechanics*, 41 (2):453–480, 1970.

[41] P. E. DesJardin and S. H. Frankel. Large eddy simulation of a turbulent non-premixed reacting jet: Application and assessment of subgrid-scale combustion models. *Phys. Fluids*, 10:2298–2314, 1998.

[42] M. Di Domenico. Numerical simulations of soot formation in turbulent flows. Technical report, VT-Forschungsbericht 2008-01, Stuttgart, Germany, 2008.

[43] M. Di Domenico, C. Beck, O. Lammel, W. Krebs, and B. E. Noll. Experimental and numerical investiagtion of turbulent, lean high-strained, confined jet flames. *Proceedings of the 49th AIAA Aerospace Sciences Meeting, 2011, Orlando, FL (USA)*, 2011.

[44] M. Di Domenico, P. Gerlinger, and M. Aigner. Development and validation of a new soot formation model for gas turbine combustor simulations. *Combust. Flame*, 157:246–258, 2010.

[45] M. Di Domenico, P. Gerlinger, and B. E. Noll. Numerical simulations of confined turbulent, lean, premixed flames using a detailed chemistry combustion model. *Proceedings of the ASME Turbo Expo*, GT2011-45520, 2011.

[46] N. Doué, P. Le Clercq, and M. Aigner. Validation of a multicomponent-fuel droplet evaporation model bases on continuous thermodynamics. *Proceedings of the ICLASS*, 2006.

[47] N. Doué, P. Le Clercq, and M. Aigner. A new multicomponent-fuel droplet vaporization model based on continuous thermodynamics theory using Fourier series. *Proc. ECM*, 2007.

[48] J. F. Driscoll, R. H. Chen, and Y. Yoon. Nitric oxide levels of turbulent jet diffusion flames: Effects of residence time and Damköhler number. *Combust. Flame*, 88:37–49, 1992.

[49] J. K. Dukowicz. A particle-fluid numerical model for liquid sprays. *Journal of Computational Physics*, 35:229–253, 1980.

[50] M. P. Dunphy and J. M. Simmie. High-temperature oxidation of ethanol. Part 1. - lignition delays in shock waves. *Journal of Chem. Soc. Faraday Trans.*, 87:1691–1695, 1991.

[51] L. Durand. *Development, implementation and validation of LES models for inhomogeneously premixed turbulent combustion.* PhD thesis, University of Munich, 2007.

[52] T. Edwards and L. Q. Maurice. Surrogate mixtures to represent complex aviation and rocket fuels. *Journal of Propulsion and Power*, 17/2:461–466, 2001.

[53] F. N. Egolfopoulos, P. Cho, and C. K. Law. Laminar flame speeds of methane - air mixtures under reduced and elevated pressures. *Combust. Flame*, 76:375–391, 1989.

[54] F. N. Egolfopoulos, D. X. Du, and C. K. Law. A study on ethanol oxidation kinetics in laminar permixed flames, flow reactors and shock tubes. *Twenty-Fourth Symposium on Combustion*, 24:833–841, 1992.

[55] Y. Egorov, F. R. Menter, R. Lechner, and D. Cokljat. The scale-adaptive simulation method for unsteady turbulent flow predictions. Part 2: Application to complex flows. *Flow Turbulence Combust.*, 85:139–165, 2010.

[56] H. Eickhoff. Analysis of the turbulent burning velocity. *Combust. Flame*, 128:347–350, 2002.

[57] A. Favre. Statistical equations of turbulent gases. *Problems in hydrodynamics and continuum mechanincs*, pages 231–266, 1969.

[58] J. Ferziger. Large eddy simulation: An introduction and perspective. *New tools in turbulence modelling*, pages 29–47, 1997.

[59] J. H. Ferziger and M. Peric. *Numerische Strömungsmechanik.* Springer-Verlag, New York, 2008.

[60] P. Flohr and H. Pitsch. A turbulent flame speed closure model for LES of industrial burner flows. *Center of Turbulent Research. Proceedings of the Summer Program.*, pages 169–179, 2000.

[61] T. Frank. *Parellele Algorithmen für die numerische Simulation dreidimensionaler, disperser Merhphasenströmungen in der Verfahrenstechnik*. TU Chemnitz, Shaker Verlag, Aachen, 2002.

[62] D. J. Fyffe, J. Moran, K. Kumaran, A. Al-Sharshani, and R. Sadr. Effect of GTL-like jet fuel composition on GT engine altitude ignition performance. Part I: Combustor operability. *Proceedings of the ASME Turbo Expo*, GT2011-45487, 2011.

[63] H.-W. Ge, I. Düwel, H. Kronemayer, R. W. Dibble, E. Gutheil, C. Schulz, and J. Wolfrum. Laser based experimental and Monte Carlo pdf numerical investigation of an ethanol/air spray flame. *Combust. Sci. Tech.*, 180:1529–1547, 2008.

[64] G. C. Gebel, T. Mosbach, W Meier, and M. Aigner. Laser-induced ignition of kerosene in a model combustor. *Proceedings of the European Combustion Meeting, 2011, Cardiff, Ireland*, 2011.

[65] G. C. Gebel, T. Mosbach, W Meier, M. Aigner, and S. Le Brun. An experimental investigation of kerosene droplet breakup by laser-induced blast waves. *Proceedings of the ASME Turbo Expo*, GT2012-68963, 2012.

[66] Peter Gerlinger. *Numerische Verbrennungssimulation*. Springer-Verlag, Berlin, 2005.

[67] M. Germano, U. Piomelli, P. Moin, and W. H. Cabot. A dynamic subgrid scale eddy viscosity model. *Phys. Fluids*, 3:1760–1765, 1991.

[68] R. Günther and G Janisch. Messwerte der Flammegeschwindigkeit von Gasen und Gasmischen. *Chemie-Ing-Techn.*, 43:975–978, 1971.

[69] D. G. Goodwin. An open-source, extensible software suite for cvd process simulation. *Proceedings of the ECS*, pages 155–162, 2003.

[70] J. F. Grcar, K. J. Kee, M. D. Smooke, and J. A. Miller. A hybrid newton/time-integration procedure for the solution of steady, laminar, one-dimensional, premixed flames. *Twenty-First Symposium on Combustion*, pages 1773–1782, 1986.

[71] J. Gu, X., M. Z. Haq, M. Lawes, and R. Woolley. Laminar burning velocity and markstein length of methane-air mixtures. *Combust. Flame*, 121:41–58, 2000.

[72] H. C. Gupta and F. V. Bracco. Numerical computations of two-dimensional unsteady sprays for application to engines. *AIAA Journal*, 16/10:1053–1061, 1978.

[73] J. O. Hinze. *Turbulence*. McGraw-Hill, 1975.

[74] C. W. Hirt and B. D. Nichols. Volume of fluid (VOF) method for the dynamics of free boundaries. *Journal of Computational Physics*, 39:201–225, 1981.

[75] M. Ihme and H. Pitsch. Prediction of extinction and reignition in nonpremixed turbulent flames using a flamelet/progress variable model 1. A priori study and presumed PDF closure. *Combust. Flame*, 155:70–89, 2008.

[76] W. P. Jones and B. E. Launder. The prediction of laminarization with a two-equation model of turbulence. *Int. J. Heat Mass Transfer*, 15:301–314, 1972.

[77] W. P. Jones and R. P. Lindstedt. Global reaction schemes for hydrocarbon combustion. *Combust. Flame*, 73/3:233–249, 1988.

[78] T. Kariya and H. Kurata. *Generalized Least Squares*. Wiley, 2004.

[79] M. Kim, Y. Choi, J. Oh, and Y. Yoon. Flame-vortex interaction and mixing behaviors of turbulent non-premixed jet flames under acoustic forcing. *Combust. Flame*, 156/12:2252–2263, 2009.

[80] E. Knudsen and H. Pitsch. A dynamic model for the turbulent burning velocity for large eddy simulation for premixed combustion LES. *Combust. Flame*, 154:240–260, 2008.

[81] A. N. Kolmogorov. The local structure of turbulence in incompressible viscous fluid for very large Reynolds numbers. *Proceedings of the USSR Academy of Sciences*, 30:299–303, 1941.

[82] M. Kono, K. Niu, T. Tsukamoto, and Y. Ujiee. Mechanism of flame kernel formation introduced by short duration sparks. *Proc. Combust. Inst.*, 22:1643–1649, 1989.

[83] S. Kono, M.and Kumagai and T. Sakai. Ignition of gases by two successive sparks with reference to frequency effect of capacitance sparks. *Combust. Flame*, 27:85–98, 1976.

[84] T. Kravchik and E. Sher. Numerical modeling of spark ignition and flame initiation in a quiescent methane-air mixture. *Combust. Flame*, 99:635–643, 1994.

[85] K. Kumar, G. Mittal, and C.-J. Sung. Autoignition of n-decane under elevated pressure and low-to-intermediate temperature conditions. *Combust. Flame*, 156:1278–1288, 2009.

[86] K. Kumar and C.-J. Sung. Laminar flame speeds and extinction limits of preheated n-decane/O_2/N_2 and n-dodcane/O_2/N_2 mixtures. *Combust. Flame*, 151:209–224, 2007.

[87] G. Lacaze, B. Cuenot, T. Poinsot, and M. Oschwald. Large eddy simulation of laser ignition and compressible reacting flow in a rocket-like configuration. *Combust. Flame*, 156:1166–1180, 2009.

[88] G. Lacaze, E. Richardson, and T. Poinsot. Large eddy simulation of spark ignition in a turbulent methane jet. *Combust. Flame*, 156:1993–2009, 2009.

[89] O. Lammel, M. Stöhr, P. Kutne, C. Dem, W. Meier, and M. Aigner. Experimental analysis of confined jet flames by laser measurement techniques. *Proceedings of the ASME Turbo Expo*, GT2011-45111, 2011.

[90] B. E. Launder, A. P. Morse, W Rodi, and D. B. Spalding. The prediction of free shear flows - A comparison of six turbulence models. *NASE SP*, 311, 1972.

[91] B. E. Launder and B. I. Sharma. Application of the energy-dissipation model of turbulence to the calculation of the flow near spinning disc. *Lett. Heat Mass Transfer*, 1:131–138, 1974.

[92] P. Le Clercq and M. Aigner. Impact of alternative fuels physical properties on combustor performance. *Proceedings of the 11th ICLASS*, 2009.

[93] P. Le Clercq, M. Di Domenico, M. Rachner, E. Ivanova, and M. Aigner. Impact of Fischer-Tropsch fuels on aero-engine combustion performance. *Proceedings of the 48th AIAA Aerospace Sciences Meeting, 2010, Orlando, FL (USA)*, 613, 2010.

[94] P. Le Clercq, N. Doué, M. Rachner, and M. Aigner. Validation of a multicomponent-fuel model for spray computation. *Proceedings of the 47th AIAA Aerospace Sciences Meeting, 2009, Orlando, FL (USA)*, 2009.

[95] R. Lebas, T. Menard, P. A. Beau, A. Berlement, and F. X. Demoulin. Numerical simulation of primary break-up and atomization: DNS and modelling study. *International Journal of Multiphase Flows*, 35:247–260, 2008.

[96] A. H. Lefebvre. *Gas Turbine Combustion*. Hemisphere Publishing Corporation, Washington, USA, 1983.

[97] M. Lesieur. Recent approaches in large-eddy simulations of turbulence. *New tools in turbulence modelling*, pages 1–28, 1997.

[98] B. Lewis and von Elbe G. *Combustion, Flames and Explosion of Gases*. Academic Press, New York and London, 1961.

[99] X. Li and M. Soteriou. Prediction of high density-ratio liquid jet atomization in cross-flow using high fidelity simulations on HPC. *Proceedings of the 50th AIAA Aeropsace Sciences Meeting, 2012, Nashville, TN (USA)*, 0175, 2012.

[100] S. Y. Liao, D. M. Jiang, Z.H. Huang, K. Zeng, and Q. Cheng. Determination of the laminar burning velocities for mixtures of ethanol and air at elevated temperatures. *Alied Thermal Engineering*, 27:374–380, 2007.

[101] Michael Liberman. *Introduction to Physics and Chemistry of Combustion: Explosion, Flame, Detonation*. Springer-Verlag, Berlin, 2008.

[102] R. Maly. Ignition model for spark discharges and the early phase of flame front growth. *Proc. Combust. Inst.*, 18:1747–1754, 1981.

[103] R. Maly, H. Albrecht, W. H. Bloss, W. Herden, B. Saggau, and E. Wagner. Neue Ergebnisse über die Entflammung durch den elektrischen Funken. In *Kraftfahrzeuge und Strassenverkehrstechnik*, 1977.

[104] R. Maly, W. Herden, B. Saggau, E. Wagner, M. Vogel, G. Bauer, and W. H. Bloss. Die drei Phasen einer elektrischen Zündung und ihre Auswirkungen auf die Entlfammung-seinleitung. In *Kraftfahrzeuge und Strassenverkehrstechnik*, 1977.

[105] T. Marchione, S. F. Ahmed, and E. Mastorakos. Ignition of turbulent swirling n-heptane spray flames using single and multiple sparks. *Combust. Flame*, 156:166–180, 2009.

[106] E. Mastorakos. *Turbulent Combustion in Opposed Jet Flows*. PhD thesis, Imperial College, 1993.

[107] E. Mastorakos. Ignition of turbulent non-premixed flames. *Prog. Energy Combust. Sci*, 35:57–97, 2009.

[108] E. Mastorakos, A. M. K. P. Taylor, and J. H. Whitelaw. Extinction and temperature characteristics of turbulent counterflow diffusion flames with partial premixing. *Combust. Flame*, 91:40–54, 1992.

[109] E. Mastorakos, A. M. K. P Taylor, and J. H. Whitelaw. Scalar dissipation rate at the extinction of turbulent counterflow nonpremixed flames. *Combust. Flame*, 91:55–64, 1992.

[110] Bonnie J. McBridge, Micahel J. Zehe, and Sanford Gordon. NASA Glenn coefficients for calculating thermodynamic properties of individual species. Technical report, TP-2002-21155. NASA, 2002.

[111] J. J McGuirk and W Rodi. The calculation of three-dimensional turbulent free jets. *Proccedings of the 1st Symp. On Turbulent Shear Flows*, pages 71–83, 1979.

[112] I. C. McLean, D. B. Smith, and S. C. Taylor. The use of carbon monoxide/hydrogen burning velocities to examine the rate of the CO + OH reaction. *Proc. Combust. Inst.*, 25:749–757, 1994.

[113] P. A. McMurthy, S. Menon, and A. R. Kerstein. A linear eddy subgrid model for turbulent reacting flows. *Proc. Combust. Inst.*, 24:271–278, 1992.

[114] F. R. Menter and Y. Egorov. The scale-adaptive simulation method for unsteady turbulent flow predictions. Part 1: Theory and model description. *Flow Turbulence Combust.*, 85:113–138, 2010.

[115] F.R. Menter, M. Kuntz, and R. Bender. A scale-adaptive simulation model for turbulent flow prediction. *Proceedings of the 41th AIAA Aerospace Sciences Meeting*, 0767, 2003.

[116] B. Michaelis and B. Rogg. FEM-simulation of laminar flame propagation. I: Two-dimensional flames. *Journal of Computational Physics*, 196/2:417–447, 2004.

[117] J.-B. Michel, O. Colin, C. Angelberger, and D. Veynante. Using the tabulated diffusion flamelet model ADF-PCM to simulate a lifted methane-air jet flame. *Combust. Flame*, 156:1318–1331, 2009.

[118] P. Moin, K. Squires, W. Cabot, and S. Lee. A dynamic subgrid-scale model for compressible turbulence and scalar transport. *Phys. Fluids*, 3:2746–2757, 1991.

[119] A. P. Morse. *Axisymmetric Turbulent Shear Flows with and without Swirl*. PhD thesis, London University, 1977.

[120] T. Mosbach and G. C. Gebel. GerMaTec - Experimental investigation and validation measurements. Technical report, DLR Stuttgart, 2010.

[121] T. Mosbach and G. C. Gebel. Report on the experiments at the lab-scale combustor (D2.2.3b). Technical report, TIMECOP-AE Project no: AST5-CT-2006-030828, 2010.

[122] T. Mosbach, G. C. Gebel, P. Le Clercq, R. Sadr, K. Kannaiyan, and A. Al-Sharshani. Investigation of GTL-like jet fuel composition on GT engine altitude ignition and combustion performance. Part II: Detailed diagnostics. *Proceedings of the ASME Turbo Expo*, GT2011-45510, 2011.

[123] U. C. Müller, M. Bollig, and N. Peters. Approximations for burning velocities and Markstein numbers for lean hydrocarbon and methanol flames. *Combust. Flame*, 108:349–356, 1997.

[124] J. Natarajan. *Experimental and numerical investigation of laminar flame speeds of H2/CO/CO2/N2 mixtures.* PhD thesis, Georgia Institute of Technology, 2008.

[125] A. Neophytou and E. Mastorakos. Simulations of laminar flame propagation in droplet mists. *Combust. Flame*, 156:1627–1640, 2009.

[126] A Neophytou, E.S. Richardson, and E Mastorakos. Spark ignition of turbulent recirculating non-premixed gas and spray flames: A model for predicting ignition probability. *Combust. Flame*, 159:1503–1522, 2012.

[127] P. J. O'Rourke. *Collective Drop Effects on Vaporizing Liquid Sprays.* PhD thesis, Princeton University, 1981.

[128] N. Peters. Laminar diffusion flamelets models in non-premixed turbulent combustion. *Progress in energy and combustion science*, 10:319–339, 1984.

[129] N. Peters. The turbulent burning velocity for large-scale and small-scale turbulence. *J. Fluid Mech.*, 384:107–132, 1999.

[130] N. Peters. *Technische Verbrennung.* University of Aachen, Course Material, 2006.

[131] U. Piomelli and J. R. Chasnov. Large eddy simulations: Theory and applications. *Turbulence and Transition Modelling*, pages 269–336, 1996.

[132] Jean Piquet. *Turbulent Flows: Models and Physics.* Springer-Verlag, Berlin, 2001.

[133] S. Pischinger and J. B. Heywood. A model for flame kernel development in a sprak-ignition engine. *Proc. Combust. Inst.*, 22:1033–1040, 1990.

[134] T. Poinsot and D. Veynante. *Theoretical and numerical combustion.* Edwards, Philadelphia, USA, 2005.

[135] W. Polifke, P. Flohr, and M. Brandt. Modeling of inhomogeneously premixed combustion with an extended TFC model. *J. Eng. Gas. Turb. Power*, 124:58–65, 2002.

[136] S. B. Pope. An explanation of the turbulent round-jet/plane-jet anomaly. *AIAA Journal*, 16:279–281, 1978.

[137] S. B. Pope. Turbulent premixed combustion. *Ann. Rev. Fluid Mech.*, 19:237–270, 1987.

[138] S. B. Pope. *Turbulent Flows.* Cambridge University Press, UK, 2000.

[139] C. R. Rao, H. Toutenburg, A. Flieger, C. Heumann, T. Nittner, and S. Scheid. *Linear Models: Least Squares and Alternatives.* Springer Series in Statistics, 1999.

[140] B. Rauch, P. Le Clercq, M. Aigner, M. Rachner, R. Calabria, and P. Massoli. Jet A-1 fuel spray evaporation in a turbulent flow: Experimental investigations and validation of numerical models. *Proceedings of the 49th AIAA Aerospace Sciences Meeting, 2011, Orlando, FL (USA)*, 893915, 2011.

[141] R. D. Reitz. *Computer Modeling of Sprays.* Spray Technology Short Course, Pittsburgh, PA, 1994.

[142] C. Richards and W. Pitts. Global density effects on the self-preservation behavior of turbulent free jets. *Journal of Fluid Mechanics*, 254:417–435, 1993.

[143] E. Richardson. *Ignition Modelling for turbulent non-premixed flow.* PhD thesis, Cambridge University, 2007.

[144] E. Richardson and E Mastorakos. Numerical investigation of spark-ignition in a laminar methane-air counterflow. *Selected Papers from the Fourth Mediterranean Combustion Symposium*, 2005.

[145] P Sagaut and C. Meneveau. *Large Eddy Simulation for Incompressible Flow.* Springer, 2009.

[146] P. Saxena and F. A. Williams. Numerical and experimental studies of ethanol flames. *Proc. Combust. Inst.*, 31/1:1149–1156, 2007.

[147] H. Schmid, P. Habisreuther, and W. Leuckel. A model for calculating heat release in premixed turbulent flames. *Combust. Flame*, 113:79–91, 1998.

[148] P. Schmitt, T. Poinsot, B. Schuermans, and K. P. Geigle. Large-eddy simulation and experimental study of heat transfer, nitric oxide emissions and combustion instability in a swirled turbulent high-pressure burner. *Journal of Fluid Mechanics*, 570:17–46, 2007.

[149] T. G. Scholte and P. B. Vaags. Burning velocities of mixtures of hydrogen, carbon monoxide, and methane with air. *Combust. Flame*, 3:511–524, 1959.

[150] V. A. Sechenov, V. P. Starikovskii, and V. P. Zhukov. Methane-air mixtures ignition at high pressures. Moscow Institute of Physics and Technology.

[151] J. S. Seery and C. T. Bowman. An experimental and analytical study of methane oxidation behind shock waves. *Combust. Flame*, 14:37–48, 1970.

[152] R. Seiser, K Humer, K. Seshadri, and E. Pucher. Experimental investigation of methanol and ethanol flames in nonuniform flows. *Proc. Combust. Inst.*, 31/1:1173–1180, 2007.

[153] R. Seiser, K. Seshadri, E. Piskernik, and A. Liñán. Ignition in the viscous layer between counterflowing streams. Asymptotic theory with comparison to experiments. *Combust. Flame*, 122:339–349, 2000.

[154] L. Selle, G. Lartigue, T. Poinsot, R. Koch, K Schildmacher, and et al. Compressible large eddy simulation of turbulent combustion in complex geometry on unstructured meshes. *Combust. Flame*, 137 (4):489–505, 2004.

[155] J. A. Sethian. *Level Set Methods and Fast Marching Methods.* Cambridge University Press, 1999.

[156] W. A. Sirignano. *Fluid Dynamics and Transport of Droplets and Sprays.* Cambridge University Press, 1999.

[157] M. S. Skjoth-Rasmussen, M. Braun-Unkhoff, C. Naumann, and P. Frank. Experimental and numerical study of n-decane chemistry. *Proceedings of the European Combustion Meeting*, 2003.

[158] N. Slavinskaya. Skeletal mechanism for kerosene combustion with PAH production. *AIAA*, page 992, 2008.

[159] N. Slavinskaya, A. Zizin, M. Braun-Unkhoff, and C. Lefers. Skeletal mechanism for C12H4 combustion with PAH formation. *Proceedings of the ASME Turbo Expo*, 2008.

[160] J. Smagorinsky. General circulation experiments with the primitive equations. I. The basic experiment. *Mon. Weather Rev*, 91:99, 1963.

[161] G. P. Smith, M. Golden, D. M. Frenklach, N. W. Moriarty, B. Eiteneer, M. Goldenberg, C. T. Bowman, R. K. Hanson, S. Sond, W. C. jr. Gardiner, V. V. Lissianske, and Z. Qin. GRI 3.0. *http://www.me.berkely.edu/gri_mech/*, 2000.

[162] M. T. E. Smith, A. D. Birch, D. R. Brown, and M. Fairweather. Studies of ignition and flame propagation in the turbulent jets of natural gas, propane and a gas with a high hydrogen content. *Proc. Combust. Inst.*, 21:1403–1408, 1986.

[163] M. D. Smooke, J. Crump, K. Seshadri, and V. Giovangigli. Comparison between measurements and numerical calculations of the structure of counterflow premixed flames. *Proc. Combust. Inst.*, 21:463–471, 1990.

[164] M. D. Smooke, J. A. Miller, and R. J. Kee. Determination of adiabatic flame speeds by boundary value methods. *Combust. Sci. Tech.*, 34:79–90, 1983.

[165] M. D. Smooke, I. K. Puri, and K. Seshadri. A comparison between numerical calculations and experimental measurements of the structure of a counterflow diffusion flame. *Proc. Combust. Inst.*, 21:1783–1792, 1986.

[166] M. D. Smooke, I. K. Puri, and K. Seshadri. A comparison between numerical calculations and experimental measurements of the structure of a counterflow diffusion flame burning diluted methane in diluted air. *Proc. Combust. Inst.*, 21:1783–1792, 1986.

[167] P. R. Spalart. Detached-eddy simulation. *Annual Review of Fluid Mechanics*, 41:181–202, 2009.

[168] D. B. Spalding. Mixing and chemical reaction in steady confined turbulent flames. *Thirteenth Symposium (International) on Combustion*, 13:649–657, 1971.

[169] G. Stiesch. *Modeling Engine Spray and Combustion Processes*. Springer, 2003.

[170] Simon R. Stow, Marco Zedda, Antonios Triantafyllidis, Andrew Garmory, E. Mastorakos, and T. Mosbach. Conditional moment closure LES modelling of an aero-engine combustor at relight conditions. *Proceedings of the ASME Turbo Expo*, GT2011-46318, 2011.

[171] W. A. Strauss and R. Edse. Burning velocity measurements by the constant-pressure bomb method. *Proc. Combust. Inst.*, 7:377–385, 1958.

[172] H. Y. Sun, S. I. Yang, G. Jomass, and C. K. Law. High pressure laminar flame speeds and kinetic modeling of carbon monoxide/hydrogen combustion. *Proc. Combust. Inst.*, 31:439–446, 2006.

[173] G. C. Swett. Spark ignition of flowing gases using long-duration discharges. *Proc. Combust. Inst.*, 6:523–532, 1957.

[174] Zichao Tan and Rolf D. Reitz. An ignition and combustion model based on the level-set method for spark ignition engine multidimensional modeling. *Combust. Flame*, 145:1–15, 2006.

[175] H. Tennekes and J. L. Lumley. *A first course in turbulence*. M.I.T. Press, 1972.

[176] S. R. Tieszen, D. W. Stamps, and T. J. O'Hern. A heuristic model of turbulent mixing applied to blowout of turbulent jet diffusion flames. *Combust. Flame*, 106:442–466, 1996.

[177] E. Triantafyllidis, A.and Mastorakos. Large eddy simulation of forced ignition of a non-premixed bluff-body methane flame with conditional moment closure. *Combust. Flame*, 156:2328–2345, 2009.

[178] C. M. Vagelopoulos and F. N. Egolfopoulos. Laminar flame speeds and extinction strain rates of mixtures of carbon monoxide with hydrogen, methane, and air. *Proc. Combust. Inst.*, 25:1317–1323, 1994.

[179] J. A. van Oijen and L. P. H. de Goey. Modelling of premixed counterflow flames using the flamelet-generated manifold method. *Combust. Theory Modelling*, 6:463–478, 2002.

[180] D. Veynante, A Trouve, K. N. C. Bray, and T Mantel. Gradient and counter-gradient scalar transport in turbulent premixed flames. *J. Fluid Mech.*, 332:263–293, 1997.

[181] C. Wahl. Eu fp5 g4rd-ct-00075 final report. Technical report, DLR, German Aerospace Center, Institute of Combustion Technology, 2003.

[182] Y. Wan and N. Peters. Application of the cross-sectional average method to calculations for the dense spray region in a diesel engine. *SAE Paper*, 972866, 1997.

[183] Y. Wan and N. Peters. Scaling of spray penetration with evaporation. *Atomization and Sprays*, 9 (2):111–132, 1999.

[184] J Weckering, A Sadiki, J Janicka, E Mastorakos, and R. L. G. M. Eggels. A forced ignition probability analysis method using les and lagrangian particle monitoring. *Proc. Combust. Inst.*, 33:2919–2925, 2011.

[185] J. Weckering, A. Sadiki, J. Janickea, and E. Mastorakos. Investigations of ignition probability of a forced ignited turbulent methane jet using LES. *Proceedings of the V European Converence on Computational Fluid Dynamics*, 2010.

[186] C. K. Westbrook and F. L. . Dryer. Simplified reaction mechanisms for the oxidation of hydrocarbon fuels in flames. *Combust. Sci. Tech.*, 27:31–43, 1981.

[187] E. Wetzel, P. Habisreuther, and N. Zarzalis. Numerical investigation of lean blow out of a model gas turbine combustion chamber using a presumed jpdf-reaction model by taking heat loss processes into account. *Proceedings of the ASME Turbo Expo*, GT2006-90064, 2006.

[188] D. C. Wilcox. *Turbulence Modeling for CFD.* DCW Industries, Inc., 1998.

[189] F. A. Williams. *Turbulent Mixing in Nonreactive and Reactive Flows.* Plenum Press, 1975.

[190] F. A. Williams. *Combustion Theory.* Benjamin Cummings, 1985.

[191] J. P. Wood and J. B. Moss. Modelling partially premixed combustion using a turbulent burning velocity based closure. *Proceedings of the European Combustion Meeting, 2003, Orléans, France*, 2003.

[192] I. Wygnanski and H. Fiedler. Some measurements in the self-preserving jet. *Journal of Fluid Mechanics*, 38:577–612, 1969.

[193] B. Zamuner, P. Gilbank, D. Bissiéres, and C. Berat. Numerical simulation of the reactive two-phase flow in a kerosene/air tubular combustor. *Aerospace Science and Technology*, 6:521–529, 2002.

[194] S. M. Zenger. Numerische Erzeugung einer Zündkarte für eine verdrallte Spray Flamme. Master's thesis, DLR Stuttgart, Germany, 2012.

[195] M. Zhang, Z. Hu, G. He, and P. Liu. Large-eddy simulation of combustion of kerosene in a modern model scramjet chamber. *Proc. IMechE*, 224, 2010.

[196] V. L. Zimont. Theory of turbulent combustion of homogeneous fuel mixtures at high Reynolds numbers. *Comubstion, Explosion and Shockwaves*, 15/3:305–311, 1979.

[197] V. L. Zimont. Gas premixed combustion at high turbulence. Turbulent flame closure combustion model. *Experimental Thermal and Fluid Science*, 21:179–186, 2000.

[198] V. L. Zimont and F. Biagioli. Gradient, counter-gradient transport and their transition in turbulent premixed flames. *Combustion Theory and Modeling*, 6:79–101, 2002.

[199] V. L. Zimont and A. N. Lipatnikov. A numerical model of premixed turbulent combustion and its validation. *Chem. Phys. Reports*, 14(7):993–1025, 1995.

[200] V. L. Zimont, W. Polifke, M. Bettelini, and W. Weisenstein. An efficient computational model for premixed turbulent combustion at high Reynolds numbers based on a turbulent flame speed closure. *J. Eng. Gas. Turb. Power*, 120:526–533, 1998.

Appendices

The appendices contain data which would have impeded the readers flow if included in the related paragraphs. The first part comprises the methods employed to derive polynomials for the laminar flame speed, the ignition delay time and the adiabatic flame temperature of which the flame speed and the ignition delay time occur as model parameters in the extended TFC model formulation. The second part concerns a short guideline for the usage of the TFC model in the THETA code. The required input parameters are provided with a description of the corresponding meaning.

A. Least Squares Fit for the Derivation of Polynomials

A.1. General Derivation

The methods described in this section mostly belong to the category basic fundamental mathematical tools. Nevertheless, for completeness and for a thorough understanding of the origin of the polynomial coefficients the approach shall be shortly elucidated here. With the routines discussed in Sec. 2.2.5 which were dedicated to the generation of additional nodal points, it is, at this point, possible to perform a least squares fit. Some comprehensive literature on this topic can be found in [14], [78] and [139]. For each nodal point, the deviation between correlation and the correct value can be written as:

$$D_i = y_{e_i} - y_{a_i} \tag{A.1.1}$$

y_{a_i} represents the approximated node for which an appropriate approximation needs to be proposed. An evaluation pointed out that generic functions of the form: $y = f(\psi,\psi^2,\psi^3,\psi^4)$ are adequate. The employed function reads:

$$y = C_1 + C_2\psi + C_3\psi^2 + C_4\psi^3 + C_5 p\phi^4 \tag{A.1.2}$$

The objective is to determine the five unknown coefficients for each pair of T and p. For conciseness and in order to simplify the mathematical operations, matrix and vector notation are introduced. The coefficient and state vector can be expressed as:

$$\vec{C} = \begin{Bmatrix} C_1 \\ C_2 \\ C_3 \\ C_4 \\ C_5 \end{Bmatrix} \tag{A.1.3}$$

$$\vec{Z} = \begin{Bmatrix} 1 \\ \phi \\ \phi^2 \\ \phi^3 \\ \phi^4 \end{Bmatrix} \tag{A.1.4}$$

with any approximated node assembled as:

$$y_a = \vec{Z}'\vec{C} \tag{A.1.5}$$

For the entity of all deviations from the fixed nodal values it is written:

$$D_i = y_{e_i} - \vec{Z}_i'\vec{C} \tag{A.1.6}$$

which can be translated into a single expression:

$$\vec{D} = \vec{y}_e - \underline{\underline{Z}}\vec{C} \tag{A.1.7}$$

By taking the square of both sides, the initial formulation for the least square problem is accomplished. To derive the minimum of the least square function regarding the coefficient vector, the D^2 expression is differentiated once with respect to the coefficient vector. This yields:

$$\frac{\partial}{\partial \vec{C}} \vec{D}' \vec{D} = 0 = -\underline{\underline{Z}}\vec{y}_e + \underline{\underline{Z}}\underline{\underline{Z}}\vec{C} \tag{A.1.8}$$

with the final expression for $\vec{C}$:

$$\vec{C} = \underline{\underline{Z}}^{-1}\vec{y}_e \tag{A.1.9}$$

A.2. Methane

In the case of a methane flame the GRI3.0 [161] mechanism is employed for the calculation of additional nodal points.

A.2.1. Laminar Flame Speed

Figure A.2.1 shows the behavior of the laminar flame speed for a number of varied conditions. For different values of p and T, a good agreement is achieved for the entire equivalence ratio range. As the polynomial is established using nodal points in the lean and rich regime, the approximation is suitable for complex configurations covering a broad range of equivalence ratios. The final coefficients are provided in Table A.2.1.

A.2.2. Ignition Delay Time

A comparison between experimental data and calculated ignition delay times is presented in Fig. A.2.2 for two different pressures and equivalence ratios with varying temperature. The first curve demonstrates the good quality of the polynomial concerning the ignition delay time within the investigated temperature range for an equivalence ratio of 0.5 for a methane/air mixture at 3.3 bar. The second comparison contains data from Seery *et al.* [151] for a diluted methane/air/argon mixture which underlines the accuracy of the nodal points. Note that since diluted mixtures are not covered by the polynomial, only a comparison of the nodel points with the results from Seery *et al.* [151] can be accomplished. The derived coefficients are provided in Table A.2.2.

Table A.2.1.: **Coefficients of the polynomial concerning the laminar flame speed of methane.**

Coefficients for the Laminar Flame Speed

General Form: $S_L = C_1 + C_2\phi + C_3\phi^2 + C_4\phi^3 + C_5\phi^4$

Correlation for C_i

Formulation: $C_i = C^\star_{i,1} + C^\star_{i,2}T + C^\star_{i,3}T^2 + C^\star_{i,4}T^3 + C^\star_{i,5}T^4 + C^\star_{i,6}p + C^\star_{i,7}p\cdot T + C^\star_{i,8}p\cdot T^2 + C^\star_{i,9}p^2\cdot T^2$

Note, T/300 [K], p/1e5 [Pa].

$C^\star_{1,1}$:	1.80952e+01	$C^\star_{2,1}$:	-7.94577e+01	$C^\star_{3,1}$:	1.27177e+02	$C^\star_{4,1}$:	-8.76212e+01	$C^\star_{5,1}$:	2.18831e+01
$C^\star_{1,2}$:	-4.71247e+01	$C^\star_{2,2}$:	2.06418e+02	$C^\star_{3,2}$:	-3.29619e+02	$C^\star_{4,2}$:	2.27222e+02	$C^\star_{5,2}$:	-5.68799e+01
$C^\star_{1,3}$:	5.45663e+01	$C^\star_{2,3}$:	-2.41694e+02	$C^\star_{3,3}$:	3.89192e+02	$C^\star_{4,3}$:	-2.68602e+02	$C^\star_{5,3}$:	6.69844e+01
$C^\star_{1,4}$:	-2.65938e+01	$C^\star_{2,4}$:	1.17837e+02	$C^\star_{3,4}$:	-1.89151e+02	$C^\star_{4,4}$:	1.30348e+02	$C^\star_{5,4}$:	-3.25052e+01
$C^\star_{1,5}$:	4.46007e+00	$C^\star_{2,5}$:	-1.97134e+01	$C^\star_{3,5}$:	3.16725e+01	$C^\star_{4,5}$:	-2.18638e+01	$C^\star_{5,5}$:	5.46381e+00
$C^\star_{1,6}$:	-2.82275e−01	$C^\star_{2,6}$:	1.07488e+00	$C^\star_{3,6}$:	-1.70663e+00	$C^\star_{4,6}$:	1.27096e+00	$C^\star_{5,6}$:	-3.57336e−01
$C^\star_{1,7}$:	-4.80988e−01	$C^\star_{2,7}$:	2.53649e+00	$C^\star_{3,7}$:	-4.12943e+00	$C^\star_{4,7}$:	2.56811e+00	$C^\star_{5,7}$:	-5.22612e−01
$C^\star_{1,8}$:	1.02333e+00	$C^\star_{2,8}$:	-4.64311e+00	$C^\star_{3,8}$:	7.04341e+00	$C^\star_{4,8}$:	-4.58136e+00	$C^\star_{5,8}$:	1.08511e+00
$C^\star_{1,9}$:	-8.77924e−02	$C^\star_{2,9}$:	3.84077e−01	$C^\star_{3,9}$:	-5.72559e−01	$C^\star_{4,9}$:	3.76381e−01	$C^\star_{5,9}$:	-9.20466e−02

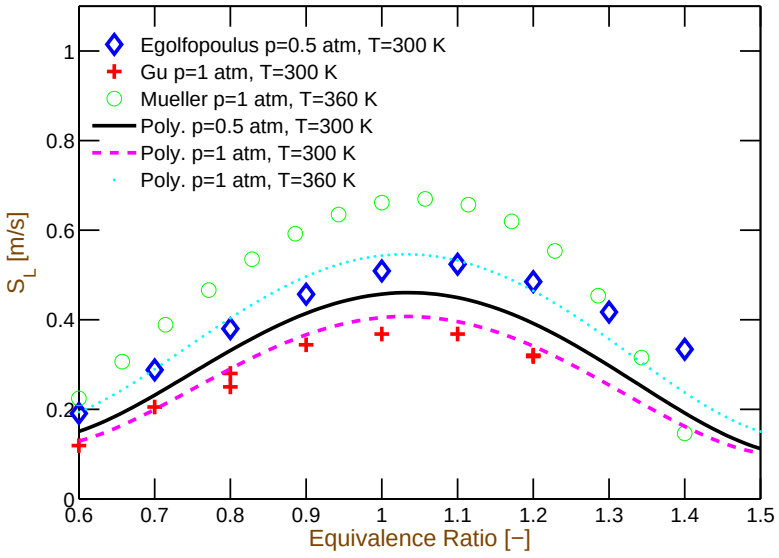

Figure A.2.1.: **Comparison of values derived with the polynomial with literature data. The first set of experimental values is taken from Egolfopoulus *et al.* [53]. The second data set originates from the work of Gu *et al.* [71]. The last set compares the polynomial proposed by Müller *et al.* [123], valid under lean conditions, with the present polynomial.**

Table A.2.2.: **Coefficients of the polynomial concerning the ignition delay time of methane.**

Coefficients for the Ignition Delay Time

General Form: $t_{\mathrm{i}} = C_1 + C_2\phi$

Correlation for C_i

Formulation: $C_i = C^\star_{i,1} + C^\star_{i,2}\cdot 1/T + C^\star_{i,3}\cdot 1/T^2 + C^\star_{i,4}\cdot 1/T^3 + C^\star_{i,5}\cdot 1/T^4 + C^\star_{i,6}\cdot 1/p + C^\star_{i,7}\cdot 1/(p\cdot T) + C^\star_{i,8}\cdot 1/(p\cdot T^2) + C^\star_{i,9}\cdot 1/(p\cdot T^3) + C^\star_{i,10}\cdot 1/(p\cdot T^4)$

Note, T/1000 [K], p/1e5 [Pa].

Note, coefficients are written in row formation.

$C^\star_{1,1}$:	2.39005e−02	$C^\star_{1,2}$:	-1.74903e−01	$C^\star_{1,3}$:	4.79014e−01	$C^\star_{1,4}$:	-5.82448e−01	$C^\star_{1,5}$:	2.65583e−01
$C^\star_{1,6}$:	3.39938e−01	$C^\star_{1,7}$:	-2.26768e+00	$C^\star_{1,8}$:	5.68183e+00	$C^\star_{1,9}$:	-6.34326e+00	$C^\star_{1,10}$:	2.66631e+00
$C^\star_{2,1}$:	1.75173e−02	$C^\star_{2,2}$:	-1.22666e−01	$C^\star_{2,3}$:	3.26076e−01	$C^\star_{2,4}$:	-3.90313e−01	$C^\star_{2,5}$:	1.77613e−01
$C^\star_{2,6}$:	4.27790e−01	$C^\star_{2,7}$:	-2.90319e+00	$C^\star_{2,8}$:	7.39537e+00	$C^\star_{2,9}$:	-8.38286e+00	$C^\star_{2,10}$:	3.56882e+00

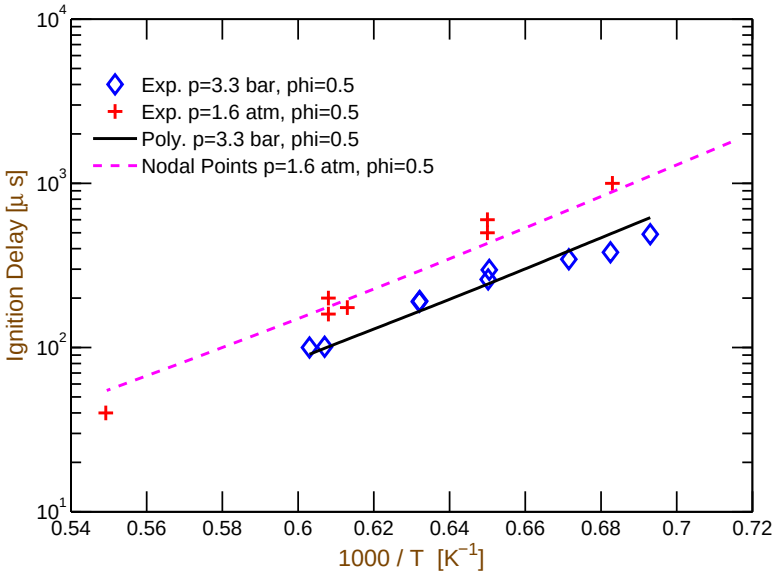

Figure A.2.2.: **The first comparison is based on methane-air ignition delay times measured by Sechenov *et al.* [150] with the polynomial. The second comparison which shows measurement data from Seery *et al.* [151] and the corresponding nodal points underlines the good performance of the GRI3.0 mechanism.**

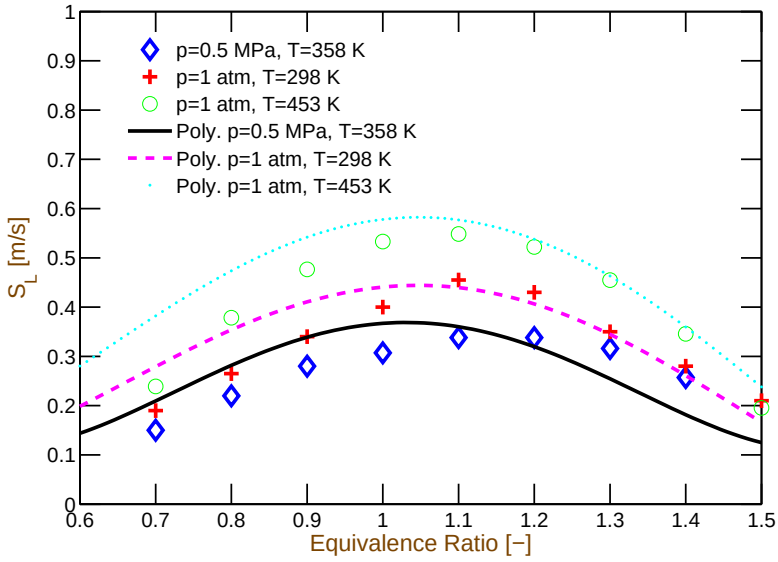

Figure A.3.1.: **Comparison of computed values by means of the polynomial with literature data. The first set of experimental values is taken from Bradley *et al.* [27]. The second data set originates from the work of Egolfopoulos *et al.* [54]. The last comparison includes computed data by an approximation of Liao *et al.* [100].**

A.3. Ethanol

In case ethanol is used as fuel, the reduced mechanism derived by Slavinskaya [159] is employed for the computation of additional nodal points. Note that the mechanism predicts slightly too high laminar flame speeds on the lean side, which, however, improves further towards the flammability limit.

A.3.1. Laminar Flame Speed

Figure A.3.1 presents a comparison of the approximated laminar flame speeds with the polynomial and experimental and numerical data available in the literature. The agreement is satisfying, except in the very lean regime where the flame speed is slightly over predicted. The laminar flame speed can be reproduced for all investigated conditions with good accuracy. The corresponding coefficients are listed in Table A.3.1.

A.3.2. Ignition Delay Time

The nodal points as the framework of the polynomial are also computed using the skeletal mechanism derived by Slavinskaya *et al.* [159]. The observed agreement between computed values and shock tube experiments is of good agreement as depicted in Fig. A.3.2. The computed coefficients are provided in Table A.3.2.

Table A.3.1.: **Coefficients of the polynomial concerning the laminar flame speed of ethanol.**

Coefficients for the Laminar Flame Speed

General Form: $S_L = C_1 + C_2\phi + C_3\phi^2 + C_4\phi^3 + C_5\phi^4$

Correlation for C_i

Formulation: $C_i = C^\star_{i,1} + C^\star_{i,2}T + C^\star_{i,3}T^2 + C^\star_{i,4}T^3 + C^\star_{i,5}T^4 + C^\star_{i,6}p + C^\star_{i,7}p \cdot T + C^\star_{i,8}p \cdot T^2 + C^\star_{i,9}p^2 \cdot T^2$

Note, T/300 [K], p/1e5 [Pa].

$C^\star_{1,1}$:	2.25141e+01	$C^\star_{2,1}$:	-9.14829e+01	$C^\star_{3,1}$:	1.33036e+02	$C^\star_{4,1}$:	-8.25485e+01	$C^\star_{5,1}$:	1.86148e+01
$C^\star_{1,2}$:	-6.04726e+01	$C^\star_{2,2}$:	2.43152e+02	$C^\star_{3,2}$:	-3.49015e+02	$C^\star_{4,2}$:	2.14113e+02	$C^\star_{5,2}$:	-4.78582e+01
$C^\star_{1,3}$:	6.24032e+01	$C^\star_{2,3}$:	-2.51639e+02	$C^\star_{3,3}$:	3.62718e+02	$C^\star_{4,3}$:	-2.22336e+02	$C^\star_{5,3}$:	4.94274e+01
$C^\star_{1,4}$:	-2.86708e+01	$C^\star_{2,4}$:	1.15686e+02	$C^\star_{3,4}$:	-1.66161e+02	$C^\star_{4,4}$:	1.01477e+02	$C^\star_{5,4}$:	-2.24833e+01
$C^\star_{1,5}$:	4.83125e+00	$C^\star_{2,5}$:	-1.93921e+01	$C^\star_{3,5}$:	2.77362e+01	$C^\star_{4,5}$:	-1.68625e+01	$C^\star_{5,5}$:	3.72008e+00
$C^\star_{1,6}$:	-8.14656e−01	$C^\star_{2,6}$:	3.39946e+00	$C^\star_{3,6}$:	-5.17077e+00	$C^\star_{4,6}$:	3.39903e+00	$C^\star_{5,6}$:	-8.15872e−01
$C^\star_{1,7}$:	1.47195e+00	$C^\star_{2,7}$:	-6.08923e+00	$C^\star_{3,7}$:	9.20348e+00	$C^\star_{4,7}$:	-6.10640e+00	$C^\star_{5,7}$:	1.49691e+00
$C^\star_{1,8}$:	-3.65180e−01	$C^\star_{2,8}$:	1.33738e+00	$C^\star_{3,8}$:	-2.07978e+00	$C^\star_{4,8}$:	1.41494e+00	$C^\star_{5,8}$:	-3.53490e−01
$C^\star_{1,9}$:	-1.08444e−02	$C^\star_{2,9}$:	5.94909e−02	$C^\star_{3,9}$:	-8.19545e−02	$C^\star_{4,9}$:	5.01443e−02	$C^\star_{5,9}$:	-1.16151e−02

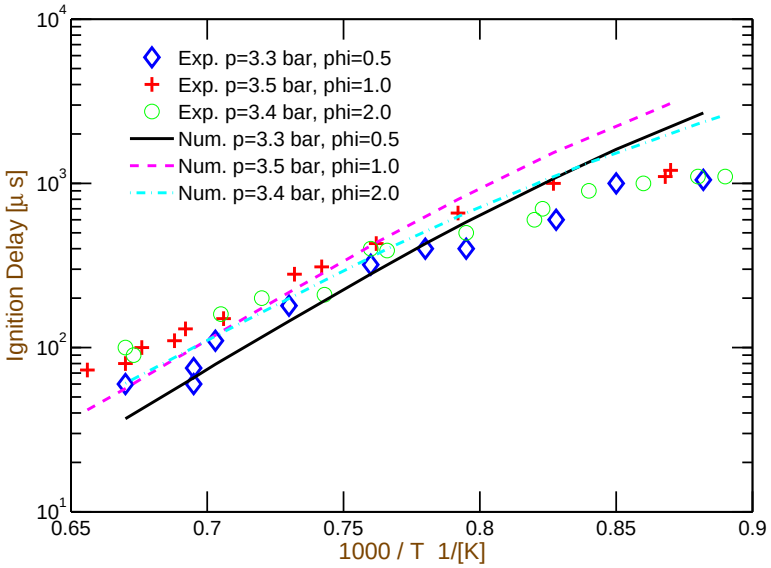

Figure A.3.2.: **Comparison of the experimental data derived by Dunphy and Simmie 1991 [50] with the results computed with the mechanism of Slavinskaya *et al.* [159]. A good agreement is achieved for the investigated conditions. The mixtures correspond to 91.25 %, 95.0 % and 93.25 % dilution with Argon.**

Table A.3.2.: **Coefficients of the polynomial concerning the ignition delay time of ethanol.**

Coefficients for the Ignition Delay Time
General Form: $t_{\mathrm{i}} = C_1 + C_2\phi$
Correlation for C_i
Formulation: $C_i = C^\star_{i,1} + C^\star_{i,2}\cdot 1/T + C^\star_{i,3}\cdot 1/T^2 + C^\star_{i,4}\cdot 1/T^3 + C^\star_{i,5}\cdot 1/T^4 + C^\star_{i,6}\cdot 1/p + C^\star_{i,7}\cdot 1/(p\cdot T) + C^\star_{i,8}\cdot 1/(p\cdot T^2) + C^\star_{i,9}\cdot 1/(p\cdot T^3) + C^\star_{i,10}\cdot 1/(p\cdot T^4)$
Note, T/1000 [K], p/1e5 [Pa].
Note, coefficients are written in row formation.

$C^\star_{1,1}$:	2.41696e−03	$C^\star_{1,2}$:	-1.71533e−02	$C^\star_{1,3}$:	4.57797e−02	$C^\star_{1,4}$:	-5.45203e−02	$C^\star_{1,5}$:	2.44813e−02
$C^\star_{1,6}$:	-4.44222e−03	$C^\star_{1,7}$:	1.89799e−02	$C^\star_{1,8}$:	-2.01369e−02	$C^\star_{1,9}$:	-8.80977e−03	$C^\star_{1,10}$:	1.70852e−02
$C^\star_{2,1}$:	-3.92147e−03	$C^\star_{2,2}$:	2.47697e−02	$C^\star_{2,3}$:	-5.88031e−02	$C^\star_{2,4}$:	6.22825e−02	$C^\star_{2,5}$:	-2.48767e−02
$C^\star_{2,6}$:	5.69187e−03	$C^\star_{2,7}$:	-3.17361e−02	$C^\star_{2,8}$:	6.41149e−02	$C^\star_{2,9}$:	-5.47150e−02	$C^\star_{2,10}$:	1.61056e−02

Table A.4.1.: **Coefficients of the polynomial concerning the laminar flame speed of n-decane.**

Coefficients for the Laminar Flame Speed
General Form: $S_{\mathrm{L}} = C_1 + C_2\phi + C_3\phi^2 + C_4\phi^3 + C_5\phi^4$
Correlation for C_i
Formulation: $C_i = C^\star_{i,1} + C^\star_{i,2}T + C^\star_{i,3}T^2 + C^\star_{i,4}T^3 + C^\star_{i,5}T^4 + C^\star_{i,6}p + C^\star_{i,7}p\cdot T + C^\star_{i,8}p\cdot T^2 + C^\star_{i,9}p^2\cdot T^2$
Note, T/300 [K], p/1e5 [Pa].

$C^\star_{1,1}$:	-6.09241e+01	$C^\star_{2,1}$:	2.60205e+02	$C^\star_{3,1}$:	-4.01296e+02	$C^\star_{4,1}$:	2.64740e+02	$C^\star_{5,1}$:	-6.32998e+01
$C^\star_{1,2}$:	1.86125e+02	$C^\star_{2,2}$:	-7.96783e+02	$C^\star_{3,2}$:	1.23133e+03	$C^\star_{4,2}$:	-8.12882e+02	$C^\star_{5,2}$:	1.94284e+02
$C^\star_{1,3}$:	-1.94090e+02	$C^\star_{2,3}$:	8.30943e+02	$C^\star_{3,3}$:	-1.28441e+03	$C^\star_{4,3}$:	8.49108e+02	$C^\star_{5,3}$:	-2.03377e+02
$C^\star_{1,4}$:	9.00070e+01	$C^\star_{2,4}$:	-3.86284e+02	$C^\star_{3,4}$:	5.98929e+02	$C^\star_{4,4}$:	-3.96813e+02	$C^\star_{5,4}$:	9.51801e+01
$C^\star_{1,5}$:	-1.56202e+01	$C^\star_{2,5}$:	6.72893e+01	$C^\star_{3,5}$:	-1.04651e+02	$C^\star_{4,5}$:	6.95071e+01	$C^\star_{5,5}$:	-1.67020e+01
$C^\star_{1,6}$:	1.35767e+00	$C^\star_{2,6}$:	-5.62723e+00	$C^\star_{3,6}$:	8.51518e+00	$C^\star_{4,6}$:	-5.58263e+00	$C^\star_{5,6}$:	1.33465e+00
$C^\star_{1,7}$:	-2.07916e+00	$C^\star_{2,7}$:	8.79306e+00	$C^\star_{3,7}$:	-1.34222e+01	$C^\star_{4,7}$:	8.73566e+00	$C^\star_{5,7}$:	-2.05006e+00
$C^\star_{1,8}$:	1.89322e+00	$C^\star_{2,8}$:	-7.95661e+00	$C^\star_{3,8}$:	1.16756e+01	$C^\star_{4,8}$:	-7.30360e+00	$C^\star_{5,8}$:	1.65391e+00
$C^\star_{1,9}$:	-1.99070e−01	$C^\star_{2,9}$:	8.24998e−01	$C^\star_{3,9}$:	-1.18174e+00	$C^\star_{4,9}$:	7.16808e−01	$C^\star_{5,9}$:	-1.57116e−01

A.4. n-decane

For the n-decane calculation of additional nodal points the reduced mechanism by Slavinskaya *et al.* [158] is utilized. The mechanism achieves a good agreement in terms of ignition delay times and laminar flame speeds throughout the entire investigated range.

A.4.1. Laminar Flame Speed

Figure A.4.1 contains a comparison of two different conditions for the laminar flame speed computed with the polynomial and experimental data. The agreement in both cases is satisfying. The laminar flame speed can be reproduced for all investigated conditions with good accuracy. The corresponding coefficients are listed in Table A.4.1.

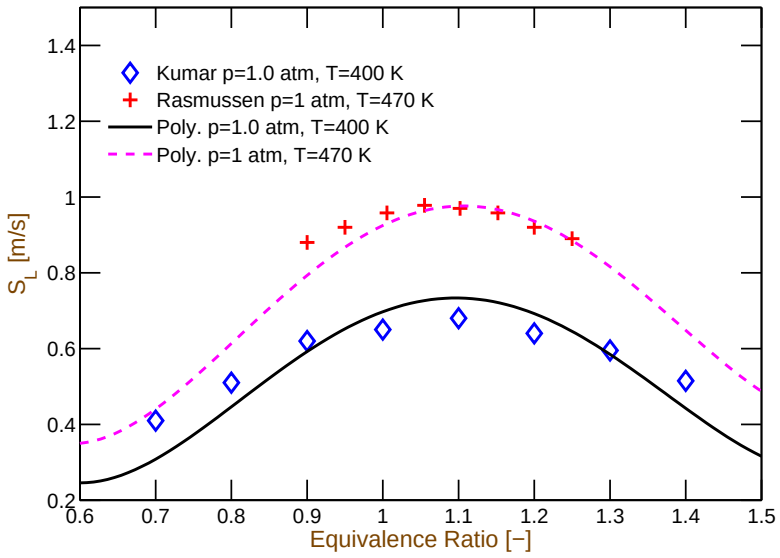

Figure A.4.1.: **Comparison of computed values by means of the polynomial with literature data. The first set of experimental values is taken from Kumar *et al.* [86]. The second data set originates from the work of Skjoth-Rasmussen *et al.* [157].**

A.4.2. Ignition Delay Time

The nodal points for the ignition delay time are derived with the mechanism proposed by Slavinskaya *et al.* [158]. The observed agreement between computed values and shock tube experiments is of good agreement as depicted in Fig. A.4.2, hence, providing credibility to the quality of the nodal points. The computed coefficients are given in Table A.4.2.

Table A.4.2.: **Coefficients of the polynomial concerning the ignition delay time of n-decane.**

Coefficients for the Ignition Delay Time

General Form: $t_i = C_1 + C_2\phi$

Correlation for C_i

Formulation: $C_i = C^\star_{i,1} + C^\star_{i,2}\cdot 1/T + C^\star_{i,3}\cdot 1/T^2 + C^\star_{i,4}\cdot 1/T^3 + C^\star_{i,5}\cdot 1/T^4 + C^\star_{i,6}\cdot 1/p + C^\star_{i,7}\cdot 1/(p\cdot T) + C^\star_{i,8}\cdot 1/(p\cdot T^2) + C^\star_{i,9}\cdot 1/(p\cdot T^3) + C^\star_{i,10}\cdot 1/(p\cdot T^4)$

Note, T/1000 [K], p/1e5 [Pa].

Note, coefficients are written in row formation.

$C^\star_{1,1}$:	5.41490e−02	$C^\star_{1,2}$:	-3.44915e−01	$C^\star_{1,3}$:	8.21339e−01	$C^\star_{1,4}$:	-8.67036e−01	$C^\star_{1,5}$:	3.42581e−01
$C^\star_{1,6}$:	-4.84663e−02	$C^\star_{1,7}$:	2.82626e−01	$C^\star_{1,8}$:	-6.05832e−01	$C^\star_{1,9}$:	5.61393e−01	$C^\star_{1,10}$:	-1.87151e−01
$C^\star_{2,1}$:	-6.57936e−02	$C^\star_{2,2}$:	4.16056e−01	$C^\star_{2,3}$:	-9.83080e−01	$C^\star_{2,4}$:	1.02895e+00	$C^\star_{2,5}$:	-4.02643e−01
$C^\star_{2,6}$:	7.31715e−02	$C^\star_{2,7}$:	-4.47257e−01	$C^\star_{2,8}$:	1.01743e+00	$C^\star_{2,9}$:	-1.01960e+00	$C^\star_{2,10}$:	3.79219e−01

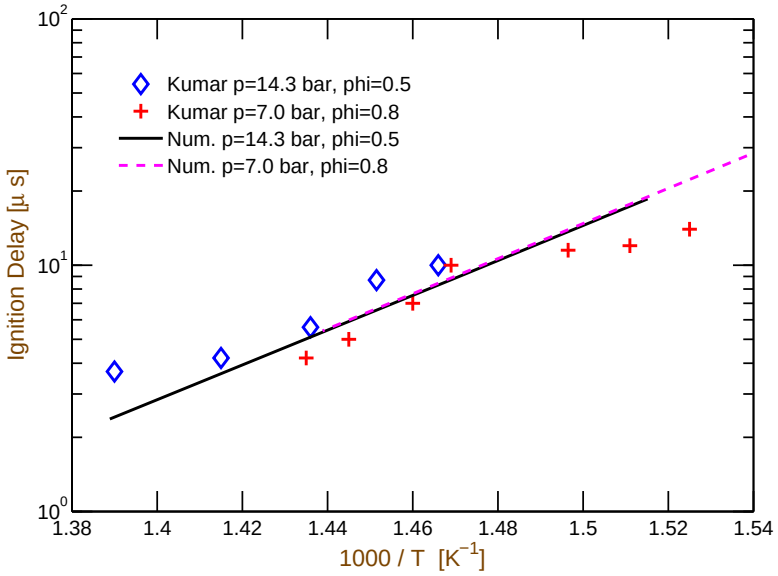

Figure A.4.2.: **Comparison of the experimental data derived by Kumar *et al.* [85] with the nodal points computed with the mechanism of Slavinskaya *et al.* [159]. A good agreement is achieved for the investigated conditions.**

B. Manual for the THETA TFC model

This section serves as manual of the extended TFC model when employed with THETA as CFD code. It is activated by putting "com_tfc" in the keyword:

```
Names of models to use:
```

The input parameter which need to prescribed are the main part of this manual. The TFC model relies on the species transport model "spc_tra" to incorporate transport equations for the major species and the enthalpy. For this reason, a mechanism file needs to be provided, in analogy to the FRC model, which determines the occurring species and the respective transport and thermodynamic properties of the species. The mechanism file can be left empty apart from the sections in which the species and elements are defined. Thus, the mechanism file has the following form:

```
ELEMENTS  H  O  C  N  AR  END
SPECIES
NmC10H22 O2 N2 H2O CO2 AR
END
REACTIONS
END
```

The transport and thermodynamic files are analog to the ones utilized with the FRC model. The fuels which are implemented are methane, ethanol, propane, iso-octane, n-decane. The input file part which is associated with the extended TFC model reads:

```
          Under-relaxation factor for TFC equation: 1.0
 Discretization scheme for TFC (UDS/CDS/LUDS/QUDS): QUDS
Use gradient limiter for TFC quantities (VENK/NVD): VENK
   NVD blending factor for TFC quantities (0.-0.5): 0.4
            Fuel Name (as termed in the mechanism): NmC10H22

                                Ignite Area (0/1): 0
```

```
            Ignition Delay / Ignition Iteration: 1.6
              Ignition Parameter (x,y,z,r,mode): 0.34 0.002 0.015 0.0025 4
Additional Ignition Parameter (E,dur,vap_frac): 0.06 30e-4 0.2
                           Domain Temperature: 293.15
                  TFC extended output (0/1/2): 2
                  Critical Strain Rate Factor: 1
```

The first four parameter are well-known from other models and relate to the solution scheme. The first new parameter is the fuel name string in which the user is requested to enter the fuel name as it appears in the mechanism file. This allows the model to compute the stoichiometric coefficients which are needed for the coupling of the species source term to the flame progress variable source term. The next parameter ignite area switches the spark on/off. This is helpful in case the user does not want to dismiss all the other parameters to supress an ignition. The next line corresponds to the ignition time or steady iteration when the time cannot be specified. Note that in a transient run, it is the time not the iteration which has to be prescribed. In the Ignition Parameter setting, the coordinates, the radius and the mode can be set. A mode of 1 sets the specified volume into a burnt state. This incorporates imposing a value of 1 for the flame progress variable and also sets the species mass fractions in accordance to a complete reaction at the local conditions. A value of 3 for the mode induces an enthalpy raise depending on the additional ignition parameter. A value of 4 also includes an instantaneous vaporization of the contained liquid fuel in the ignition volume. The additional ignition parameter determine the total enthalpy gain, the duration in which the energy source is active and the vaporization fraction of the liquid fuel. The parameter domain temperature initiates the temperature boundary condition in the domain. TFC extended output defines how many auxiliary variables are saved in the output file. The maximum value 2 comprises the gradient, the flammability areas to only name a few. A value of 0 deactivates most of the output. The critical strain rate factor relates to γ_q in Eq. (2.2.17) which scales the critical dissipation rate. This factor is essential for different fuels for which the exact dissipation rate is not known or a LES approach in which the flow field behaves differently.

Lebenslauf

Persönliche Daten

Name:	Jan Michael Boyde
Geburtstag:	28.04.1982
Geburtsort:	Rostock, Deutschland
Familienstand:	verheiratet, 1 Kind

Ausbildung

1992 - 2001:	Besuch des Friedrich Schiller Gymnasiums in Fellbach, Deutschland.
2002 - 2008:	Studium der Luft- und Raumfahrttechnik an der Universität Stuttgart, Deutschland. Vertiefungsrichtungen: Strömungslehre und Regelungstechnik. Studienarbeit: "Impedanzrandbedinungen", DLR Stuttgart, 2007. Diplomarbeit: "Fan Trim Balance as Means for Vibration Reduction", Rollsy Royce UK, 2008.
2008 - 2012:	Promotion am Deutschen Zentrum für Luft- und Raumfahrt, am Institut für Verbrennungstechnik, Stuttgart, Deutschland. Titel: Numerical Modeling of Ignition Processes in Single- and Multiphase Flows.

Berufliche Stationen

2001 - 2002	Zivildienst am Henry-Dunant Heim in Kiel, Deutschland.
2004 - 2005	Fachpraktikum bei Modine AG, Filderstadt, Deutschland. Abteilung Thermodynamik
2007 - 2008	Diplomarbeit bei Rolls Royce, plc, Derby, UK. Abteilung Regelung
2008 - 2012	Wissenschaftlicher Mitarbeiter am Deutschen Zentrum für Luft- und Raumfahrt am Institut für Verbrennungstechnik, Stuttgart, Deutschland. Abteilung Numerik
2012 - ...	Berechnungsingenieur bei der MTU Friedrichshafen, Friedrichshafen, Deutschland. Abteilung Vorentwicklung